

Resonance in swirling wakes and sloshing waves: non-normal and sublinear effects

THÈSE N° 7276 (2016)

PRÉSENTÉE LE 7 OCTOBRE 2016

À LA FACULTÉ DES SCIENCES ET TECHNIQUES DE L'INGÉNIEUR
LABORATOIRE DE MÉCANIQUE DES FLUIDES ET INSTABILITÉS
PROGRAMME DOCTORAL EN MÉCANIQUE

ÉCOLE POLYTECHNIQUE FÉDÉRALE DE LAUSANNE

POUR L'OBTENTION DU GRADE DE DOCTEUR ÈS SCIENCES

PAR

Francesco VIOLA

acceptée sur proposition du jury:

Prof. C. Ancey, président du jury
Prof. F. Gallaire, directeur de thèse
Prof. P. Huerre, rapporteur
Prof. L. Limat, rapporteur
Prof. F. Porté-Agel, rapporteur



ÉCOLE POLYTECHNIQUE
FÉDÉRALE DE LAUSANNE

Suisse
2016

Acknowledgements

I used to stay close to the Sea and far from the Alps but at some point these two distances happened to be inverted. Still, I quickly started to feel at home here in Lausanne, facing the marvelous lac Léman and surrounded by special people that I would like to briefly acknowledge here.

Thanks François to be my advisor and for the possibility to be part of the LFMI. Thanks for your continuous ideas, encouragement and infinite energy. With your positive attitude towards life and science, I have learned that is possible to be a gentleman in every situation. Thanks for sharing your incredible knowledge, for the never ending discussions on vortex breakdown and also for allowing me to travel on Friday afternoon (and Monday as well...). Thanks to let us grow as scientists and to create an ideal environment where is possible to learn and solve problems without competition and where people are friends more than colleagues. Like Gioele (better known as Mariano) who's always perfect and taking care of everything, Giacomo with whom I share daily jokes and fun, super-Vlado always smart and smiling (except when going by bike) and Laura, Mathias, Edouard, Andrea, Marc-Antoine, Isha, Simon, Nicolas, Yoan, Marta, Yves, Tobias, and Elise: all this *swirling* and *sloshing* would not have been possible without you, thank you all. Thanks Cristobal for answering all my questions with your deep understanding of fluid mechanics and for the thoughtful discussions. Thanks PT to be a continuous source of scientific curiosities and findings, I admire your original, creative and efficient approach to science and it has been great working together. Thanks Benjamin for your precise explanations about foam and wetting phenomena. Thanks Pierre-Yves for showing me the secrets of self-similarity and boundary layer theory. Thanks Petra for the technical and administrative help. Thanks Matteo for your versatile organization. Thanks to the students I had the pleasure to mentor and to learn with them, especially the brilliant and receptive Erica. And a special mention to Lailai, the most funny and unconventional office mate ever!

I am grateful to Simone who has been an *adjoint* guide throughout this thesis and introduced me to hydrodynamics stability in a 16 hours back and forth Pisa-Lausanne. A huge thanks to my older brother Valerio who believed in me and made everything to start: thanks for your (wise?) advices, for your intuitions, for your excellent experimental data and for your friendship.

I would like to acknowledge the members of my jury Patrick Huerre, Laurent Limat, Fernando Porté-Agel to have read this thesis with true interest and for the enriching discussion

Acknowledgements

they have stimulated with their questions, and Christophe Ancey for presiding over the jury.

And also thanks to the ECPS group, the WIRE group, "sexy body" Fernando, Marco, Topolone, the waterpolo team, the lunch-time volleyball teams Les Purées and Sfigatos, Andrea, Alessandra, Lorenzo and Giovanni, Stefano, Cecile.

Many thanks to the Italian crew which has been my family here in Lausanne: Pool, Frenkino, Biasiu, Masca, Spillo, Pisano, Milans, Giulio, Vale, Mattias, Silvia, Marti, Roby, Cara, Roby, Elena, Alessandra, Serdar, Enza, Lorenzo, Daniela, Daniela, Rossella, Carla, Gabriele, Creatura, Ferdinando e Tungo. There's not space to thank you one by one but you know how important is to enjoy and ski together and to have you here.

A deep thank to my Family, to my parents Teresa and Marco and to my sister Giulia for the continuous support and for making me feel at home as I never left every time I am back. Thanks also to Eliana, Sandro, Giulia and Zeno for welcoming me and taking care during the intense writing period. And finally thanks to you Silvia for always motivating me and for keeping close even when seemed so far.

Lausanne, 23 Septembre 2016

Francesco Viola

Abstract

Similarly to mechanical structures, stable flows can exhibit resonance when perturbed by an impulsive or harmonic forcing. Swirling wakes and sloshing waves belong to this kind of flows and manifest large energy response when excited close to their natural frequencies. Although these frequencies can be predicted by linear modal analysis, the full flow dynamics differs from the modal one because entailed by the mutual cooperation of the natural modes (non-normal effects) and dependent on the oscillation amplitude (nonlinear effects).

In this thesis, the response of swirling wakes subjected to a harmonic forcing is studied numerically and theoretically. Direct numerical simulations show that a large variety of helical modes can be excited and amplified in trailing vortices when a harmonic inlet or volume forcing is imposed, with the appearance of higher wavenumber modes at higher frequency. The mode-selection mechanism is shown to be directly connected to the local stability properties of the flow, and is simultaneously investigated by a WKB approximation, in the framework of weakly non-parallel flows, and by the global resolvent approach. This analysis is then extended to the case of turbulent swirling flows to investigate the physical origin of the meandering oscillations of the hub vortex, that is observed in wind turbine wakes experiments. We show as this low frequency spectral component is the result of a convectively unstable single-helix structure that oscillates at a frequency equal to one third the rotational frequency of the wind turbine rotor. Consequently, an adjoint-based technique for the passive control of these helical instabilities is proposed.

We then turn our attention towards the transient decay of sloshing waves affected by a viscous friction at the container's wall, that exhibits a sublinear dependence in the interface velocity, i.e. a power law with an exponent smaller than one. This capillary effect is exacerbated in our experiment by placing a thin layer of foam on the liquid phase that act as a collection of air-liquid interfaces. In contrast to classical theory, we uncover the existence of a finite-time singularity in our system yielding the arrest of the sloshing oscillations in a finite time and we propose a minimal theoretical framework to capture this effect. Using first principles, we then study the effect of contact angle hysteresis on sloshing waves. We show asymptotically that, in contrast to viscous damping where the wave motion decays exponentially, the contact angle hysteresis acts as Coulomb solid friction yielding the damping rate induced by the motion of the liquid meniscus to increase at small amplitude, consistently with the experimental observation.

Key words: hydrodynamic instability, vortex dynamics, vortex breakdown, turbulent flows, wind energy, adjoint methods, nonlinear dynamics, free-surface flows, contact lines, foams.

Riassunto

Come le strutture meccaniche, anche flussi stabili possono manifestare il fenomeno della risonanza se forzati impulsivamente o armonicamente. Scie vorticosi e onde di superficie appartengono a questa categoria di flussi e sono caratterizzati da una elevata risposta energetica quando eccitati vicino alle frequenze di risonanza. Sebbene queste frequenze possono essere determinate tramite l'analisi modale lineare, la dinamica reale del flusso differisce da quella modale poichè dipende dalla cooperazione dei modi naturali (effetto non-normale) e dall'ampiezza dell'oscillazione (effetto nonlineare).

In questa tesi, la risposta di scie vorticosi forzate armonicamente è studiata utilizzando un approccio sia numerico che teorico. Nel caso di vortici d'estremità aeronautici, le simulazioni numeriche mostrano che in presenza di una forzante armonica all'ingresso o nel volume del dominio, vari modi elicoidali sono eccitati e amplificati nel flusso; modi ad alto numero d'onda compaiono all'aumentare della frequenza. Il meccanismo di selezione dei modi è connesso con le proprietà di stabilità locale del flusso ed è studiato utilizzando simultaneamente un approccio WKB, nell'ipotesi di flussi che evolvono lentamente nella direzione assiale, e uno globale. L'analisi è quindi estesa al caso di scie vorticosi turbolente al fine di determinare l'origine delle oscillazioni trasversali del vortice posto al centro della scia delle giranti eoliche (hub-vortex). La componente di bassa frequenza, riscontrata sperimentalmente, risulta legata ad una instabilità convettiva del vortice di scia, caratterizzata da un modo a singola elica controrotante che oscilla ad una frequenza pari a circa un terzo della frequenza di rotazione del rotore della turbina. Inoltre, una tecnica per il controllo passivo delle instabilità elicoidali basata sul metodo dell'aggiunto è sviluppata in questa tesi.

Successivamente, si studia l'ammortizzamento nonlineare di onde di superficie soggette ad attrito viscoso alle pareti del recipiente. La forza di attrito ha una dipendenza sublineare con la velocità dell'interfaccia, cioè ha una dipendenza algebrica con un esponente minore di uno. Questo effetto nonlineare è enfatizzato nel nostro esperimento ponendo un sottile strato di schiuma sulla fase liquida, che agisce come una collezione di interfacce aria-liquido. A differenza del classico oscillatore smorzato, nel sistema è presente una singolarità che si manifesta ad un tempo finito, provocando l'arresto delle oscillazioni al pelo libero. Al fine di descrivere questo effetto nonlineare, viene proposto un semplice modello teorico che corregge il paradigmatico modello di oscillatore smorzato lineare. Utilizzando le equazioni secolari dei fluidi, si passa poi allo studio dell'effetto dell'isteresi dell'angolo di contatto sulle onde di superficie. Si dimostra con una procedura asintotica che, al contrario dello smorzamento viscoso che causa uno smorzamento esponenziale dell'ampiezza di oscillazione, l'isteresi

Acknowledgements

dell'angolo di contatto agisce come l'attrito solido di Coulomb, inducendo un fattore di smorzamento legato allo scivolamento del menisco dinamico. Tale smorzamento aumenta quando l'ampiezza di oscillazione diminuisce, in accordo con quanto osservato sperimentalmente.

Parole chiave: instabilità idrodinamica, dinamica dei vortici, vortex breakdown, flussi turbolenti, energia eolica, metodo dell'aggiunto, dinamica nonlineare, flussi a superficie libera, linee di contatto, schiume.

Contents

Acknowledgements	i
Abstract (English/Italian)	iii
1 Introduction	1
1.1 Fluid mechanics and hydrodynamic stability	1
1.2 Non-normal effects	4
1.2.1 Transient growth	4
1.2.2 Response to forcing	5
1.2.3 Sensitivity and passive control	6
1.2.4 In this thesis: The amplifier dynamics of swirling wakes	7
1.3 Nonlinear effects	13
1.3.1 Superlinear nonlinearities	13
1.3.2 Sublinear nonlinearities	16
1.3.3 In this thesis: Nonlinear friction in fluid-solid resonators	20
1.4 Foreword: Structure of the document and contribution of the author	23
Part I The amplifier dynamics of swirling wakes	25
2 Mode selection in trailing vortices	27
Paper: Mode selection in trailing vortices: harmonic response of the non-parallel Batchelor vortex	27
2.1 Introduction	28
2.2 Trailing-vortex prototype	31
2.3 Observation of the non-linear response to harmonic inlet forcing	33
2.4 Linear response to harmonic inlet forcing	34
2.4.1 WKB analysis	35
2.4.2 Global resolvent	37
2.4.3 Optimal forcing	40
2.5 Linear response to harmonic body forcing	42
2.5.1 Global resolvent	42
2.5.2 WKB analysis for volume forcing	44
2.6 Nonlinear response	45
	vii

Contents

2.6.1	Nonlinear gains	45
2.6.2	Nonlinear mode selection	48
2.7	Conclusions	49
2.8	Appendix: WKB formulation for swirling flows	52
2.8.1	WKB formulation for volume forcing	55
2.9	Appendix: Sensitivity to radial extension of the domain	55
3	Hub vortex instability	57
3.1	Paper: Linear stability analysis of wind turbine wakes performed on wind tunnel measurements	57
3.1.1	Introduction	58
3.1.2	Wind tunnel measurements of wind turbine wakes	61
3.1.3	Linear stability analysis: formulation of the numerical problem	65
3.1.4	Temporal stability analysis	68
3.1.5	Spatial stability analysis and characterization of the hub vortex instability	70
3.1.6	Discussion and final remarks	81
3.2	Paper: Prediction of the hub vortex instability in a wind turbine wake: stability analysis with eddy-viscosity models calibrated on wind tunnel data	84
3.2.1	Introduction	84
3.2.2	Problem formulation	85
3.2.3	Wind tunnel measurements	88
3.2.4	Eddy-viscosity models	89
3.2.5	Stability analysis results	92
3.2.6	Conclusions	94
3.2.7	A note on the mixing-length model	94
3.3	Conference Paper: Instability of wind turbine wakes immersed in the atmospheric boundary layer	96
3.3.1	Introduction	96
3.3.2	Experimental data	98
3.3.3	Stability analysis, turbulent model and numerical method	99
3.3.4	Hub vortex instability	101
3.3.5	Conclusions	105
3.4	Global stability and harmonic response to forcing of the hub vortex: an axisymmetric point of view	106
3.4.1	Introduction	106
3.4.2	Experiments	106
3.4.3	Global analyses	108
3.4.4	Conclusions	113
4	Flow control of weakly non-parallel flows	115
	Paper: Flow control of weakly non-parallel flows: application to trailing vortices . .	115
4.1	Introduction	115
4.2	Sensitivity of the local spatial stability spectrum	117

4.2.1	Generic sensitivity analysis of the local stability problem	118
4.2.2	Sensitivity of the local spatial stability properties to base flow modifications	119
4.3	Sensitivity of the integral growth factor in weakly nonparallel flows	120
4.3.1	Lagrangian formulation	121
4.3.2	Optimal inlet control	124
4.4	Conclusions	125
4.5	Local spatial stability of swirling flows	126
5	Axisymmetric vortex breakdown: linear and nonlinear mechanisms	127
5.1	Introduction	127
5.2	Governing equations and numerical method	128
5.3	Numerical results	130
5.4	Separation of the quasi-cylindrical equations	131
5.4.1	What is the missing term in the quasi-cylindrical equations?	135
5.5	Possible linear mechanisms	137
5.5.1	Local analysis: standing waves and subcritical state	137
5.5.2	Global analysis: instability	139
5.6	Possible nonlinear mechanisms	141
5.6.1	Weakly nonlinear resolvent: a regular asymptotic expansion approach	141
5.6.2	Weakly nonlinear stability: a compatibility condition approach	143
5.7	Appendix: Domain sensitivity	146
5.8	Appendix: Batchelor boundary layer equations	147
Part II	Nonlinear friction in fluid-solid resonators	149
6	The viscous torsional pendulum	151
6.1	Introduction	151
6.2	Problem description and governing equations	152
6.3	A fluid-solid oscillator	155
6.4	Nonlinear and linear regimes	157
6.4.1	Low amplitude model	158
6.4.2	High amplitude model	162
6.4.3	A phenomenological model for the amplitude decay	165
6.5	Conclusions	166
6.6	Appendix: Rosenblat's torque	169
7	Nonlinear friction in sloshing dynamics: total wetting	171
	Paper: Foam on troubled water: capillary induced finite-time arrest of sloshing waves	171
7.1	Introduction	172
7.2	Experiments	173
7.3	A nonlinear fluid oscillator	175
7.3.1	Equivalent mechanical system	175
7.3.2	Asymptotic solution and comparison to experiments	176

Contents

7.3.3	Sublinear friction and its finite-time arrest	177
7.4	Conclusions	178
7.5	Appendix: Asymptotic analysis	180
8	Nonlinear friction in sloshing dynamics: partial wetting	183
	Paper: Contact line hysteresis in sloshing dynamics yields finite time arrest	183
8.1	Introduction	184
8.2	Governing equations	187
8.3	Weakly nonlinear analysis	189
8.3.1	Order ϵ^0	189
8.3.2	Order ϵ	191
8.3.3	Order ϵ^2	193
8.3.4	Amplitude equation	196
8.4	Discussion	197
8.4.1	Effect of contact angle hysteresis	197
8.4.2	Time of arrest: parametric study	199
8.4.3	Comparison with the theory of Case & Parkinson (1957)	201
8.5	Conclusions	201
8.6	Appendix: Adjoint equations	203
8.7	Appendix: Numerical code	205
8.7.1	Static meniscus	205
8.7.2	Global stability analysis	205
9	Conclusions and perspectives	207
	Bibliography	228
	Curriculum Vitae	229

1 Introduction

1.1 Fluid mechanics and hydrodynamic stability

One of the most interesting and fascinating phenomena in fluid dynamics is the transition from one state to another with the eventual appearance of patterns or unsteadiness. A couple of representative examples are shown in Figure 1.1, namely (a) the Von Karman vortex street, that manifests in the lee of bluff bodies when the flow advection is high enough, (d) the single helical vortex breakdown state, observed when the flow rotational frequency is large enough and (g) the double helical mode at larger swirl.

As a branch of classical mechanics, fluid dynamics is governed by physical laws that explain empirical experience and, more importantly, predict future experiments. Thus, mass conservation and Newton's second law applied to an incompressible volume of fluid yield a set of governing equations for the velocity and pressure fields, \mathbf{u} , p

$$\frac{\partial \mathbf{u}}{\partial t} + \mathbf{u} \cdot \nabla \mathbf{u} = -\nabla p + Re^{-1} \Delta \mathbf{u}, \quad \nabla \cdot \mathbf{u} = 0, \quad (1.1)$$

where t is time and Re is the Reynolds number, a nondimensional number defined as the ratio between the advection and viscous forces at play in the flow. This system of equations is commonly referred to as the Navier-Stokes equations for incompressible flows, and it has been seen to govern fluids motion phenomena in a large variety of experiments and applications such as airplane, ship and car industries, biology and medicine, meteorology, oceanography and geology. See for instance in Figure 1.1 the (b) Von Karman wake and the (e) single and (h) double helical breakdown modes obtained by the direct numerical solution of equations 1.1.

However, due to their generality and the variety of their applications, the Navier-Stokes equations are complex and contain multiple physical mechanisms which can interplay at the same time such as advection, dissipation, body forces, turbulence, capillary effects, multi-phase fluids, complex geometries and others. For this reason, it is often arduous to isolate and understand the physical mechanism behind these state transitions.

The hydrodynamic stability theory is the most classical approach to understand and describe bifurcations, instability and eventual transition to turbulence in fluid dynamics (Huerre

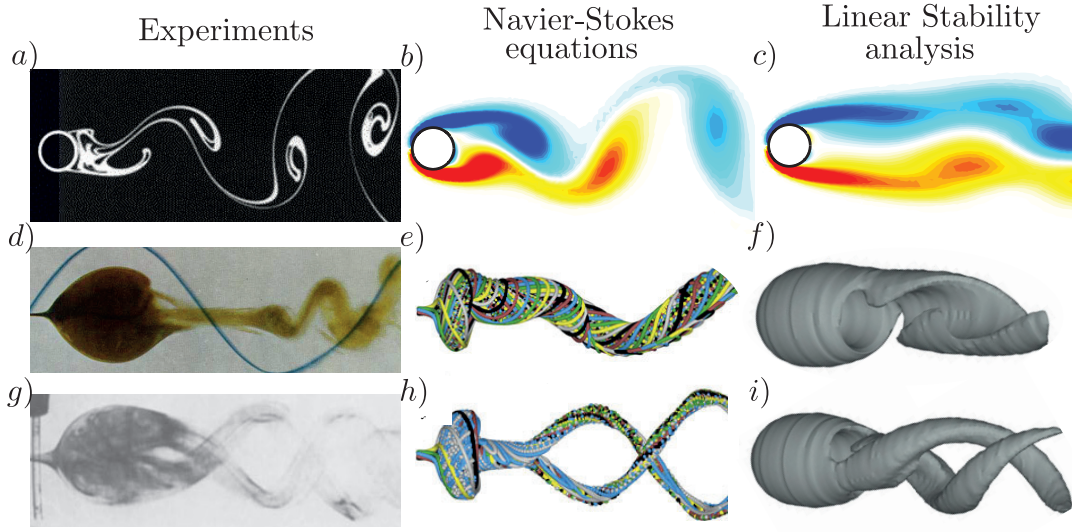


Figure 1.1: Archetipal examples of emerging unsteadiness and pattern formation in fluid mechanics. Experimental visualization of (a) vortex shedding in the cylinder wake (by Sadatoshy Taneda in Van Dyke (1982)), (d) single and (g) double helical vortex breakdown modes from Sarpkaya (1971) and Escudier & Zehnder (1982) respectively. The same flow configurations obtained by numerical solution of the Navier-Stokes equations (1.1) are shown in the central column, while the corresponding linear eigenmodes are reported in the right one. In (b,e) visualization from V. Mantič-Lugo (personal communications) while the ones in (e,f,h,i) are reproduced from Meliga *et al.* (2012a).

& Rossi, 1998; Drazin & Reid, 2004; Schmid & Henningson, 2001; Charru, 2011). Indeed, the transition affecting a flow when a control parameter is increased, can be investigated by computing the stability of the steady base flow, \mathbf{U} to infinitesimal perturbations. Let us suppose that at some threshold value of the Reynolds number, Re_{cr} , the system becomes unstable to infinitesimal velocity-pressure perturbations with growth rate, σ , and frequency, ω ,

$$(\mathbf{u}, p) = (\hat{\mathbf{u}}, \hat{p})e^{(\sigma - i\omega)t}. \quad (1.2)$$

For $Re > Re_{cr}$ we expect the unstable eigenmode $\hat{\mathbf{u}}$ centered around \mathbf{U} to grow exponentially in time, until it saturates to a macroscopic amplitude due to nonlinear effects. The dynamics of the perturbation is governed at leading order by the linearized Navier-Stokes equations around the base-state \mathbf{U}

$$(\sigma - i\omega)\hat{\mathbf{u}} = \hat{\mathbf{u}} \cdot \nabla \mathbf{U} + \mathbf{U} \cdot \nabla \hat{\mathbf{u}} + \nabla \hat{p} - Re^{-1} \Delta \hat{\mathbf{u}}, \quad \nabla \cdot \hat{\mathbf{u}} = 0, \quad (1.3)$$

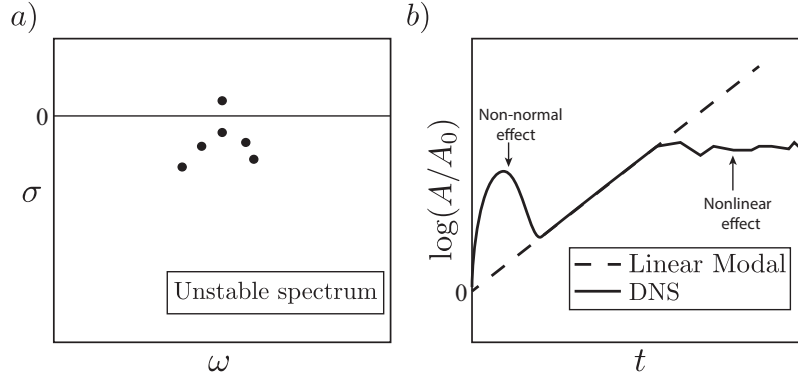


Figure 1.2: Schematics of non-normal and nonlinear effects in a linearly unstable flow. The stability spectrum in a) contains at least one eigenvalue with positive growth rate, σ , and b) the corresponding linear modal evolution prescribes the disturbance's amplitude, A , to grow exponentially in time (dashed line). However, the complete dynamics of the disturbance with initial amplitude A_0 (solid line) significantly differs from the modal solution at short time scale (non-normal effect) and at large amplitudes (nonlinear effect).

where the base-state is often chosen as a steady solution of the Navier-Stokes equations

$$\mathbf{U} \cdot \nabla \mathbf{U} = -\nabla P + Re^{-1} \Delta \mathbf{U}, \quad \nabla \cdot \mathbf{U} = 0. \quad (1.4)$$

The stability problem (1.3), together with the boundary conditions compelling the specific problem, can be rephrased as an eigenvalue problem of the type

$$(\sigma - i\omega)\hat{\mathbf{u}} = L\hat{\mathbf{u}}, \quad (1.5)$$

where the eigenvector $\hat{\mathbf{u}}$ belongs to the divergence-free vector space. The long term behaviour of the perturbation is then inferred by the eigenvalues and eigenmodes of the linear operator L . If an eigenvalue with positive growth rate, σ , exists, as in Figure 1.2(a), the associated eigenmode $\hat{\mathbf{u}}$ grows exponentially in time over the base-flow and dominates the linear dynamics. By naming, A , the perturbation's amplitude, the dashed line in Figure 1.2(b) depicts a typical exponential growth in time resulting from the linear modal analysis. Furthermore if the frequency, ω , differs from zero, the flow becomes unsteady and oscillates spontaneously: for this reason unstable flows are referred to as *oscillators* (Huerre & Rossi, 1998). As example, the right column in Figure (1.1) shows the unstable eigenmodes computed with linear stability analysis superimposed on the base flow in the case of (c) wake behind a cylinder and (g,i) helical instabilities in the lee of a vortex breakdown bubble. The spatial structure of the linear global eigenmode matches qualitatively the flow topology of the full nonlinear state. The natural frequency is also qualitatively well captured. In addition, the hydrodynamic stability predicts well the critical value of the control parameter (the Reynolds number or the swirl parameter), at which the bifurcation happens.

Nevertheless, the linear modal behaviour does not always fully capture the entire dynamics of the perturbation. Figure 1.2(b) shows by solid line the typical behaviour of the perturbation

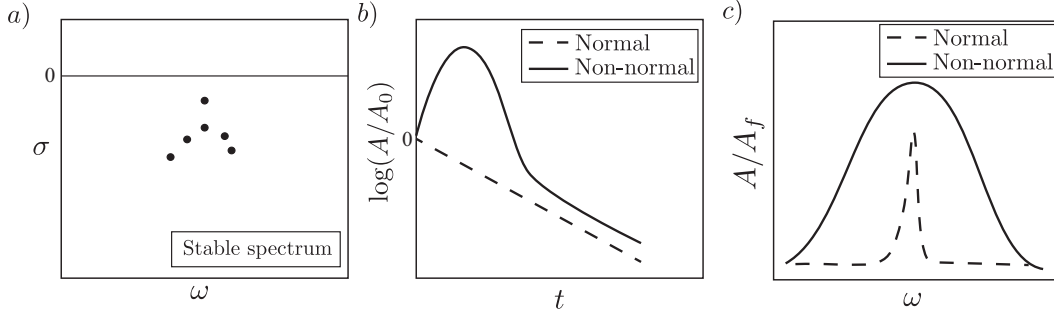


Figure 1.3: Schematics of non-normal effects on a linearly stable flow. a) All the eigenvalues in the spectrum have negative growth rate. b) If the system is normal, the perturbation’s amplitude, A , decays exponentially in time at a constant rate (dashed line). In contrast, if the system is non-normal the perturbation dynamics is described by the full modal basis and its amplitude, A , gets transiently larger than the initial amplitude, A_0 , before decaying (solid line). c) Moreover, in the case a harmonic forcing of amplitude A_f and frequency ω , the non-normality yields the system to a higher energy gain, A/A_f , even further from the resonance frequency.

amplitude in time for an unstable base-flow. Two main effects that are omitted by the linear stability can be distinguished: (i) Non-normal effects at short time scale and (ii) nonlinear effects at high amplitude. Their physical origin and their influence on fluid dynamics are discussed in the next two sections, along with the specific problems of interest studied in this thesis, which are progressively introduced.

1.2 Non-normal effects

1.2.1 Transient growth

The key-mechanism of the short-term amplification present in Figure 1.2(b), is in the non-normality of the linearized Navier-Stokes equations (Trefethen *et al.*, 1993; Chomaz, 2005; Schmid, 2007). This means that the eigenvectors of the linear operator L in equation (1.5) do not form an orthogonal set with respect to the energy scalar product. Hence, the linear evolution of a perturbation with initial amplitude, A_0 , which is given by the superposition of the eigenvectors, can produce a large transient of energy before decaying.

This phenomenon, which is known in literature as transient growth, non-modal, algebraic or short-term instability, has been widely studied over the last two decades especially to explain pattern formation and coherent fluctuation occurring in linearly stable flows. Indeed, even if the spectrum is stable and perturbations are damped as in Figure 1.3(a), some specific initial perturbations can be transiently amplified due to non-normality (Fig. 1.3(b)). If the amplification is large enough, the flow enters in the nonlinear regime and it can escape from the otherwise linearly stable solution (Schmid, 2007). This mechanism is particularly relevant in the case of parallel Couette and the plane Poiseuille flows, as well as Reynolds’ famous pipe flow experiment where the transition to turbulence is strongly dependent on the level of

external noise. Indeed, although stable, these flows are seen to exhibit a strong response to external disturbances and for this reason are named *amplifiers*, in opposition to previously described oscillator flows which display intrinsic dynamics that do not originate from external perturbations.

Calculations on transient growth have been first carried out by Butler & Farrell (1992) using a variational approach and by Corbett & Bottaro (2000) with direct-adjoint scheme. Two main mechanisms for the transient energy growth have been observed in parallel flows. In the (i) Orr mechanism, the initial disturbance has flow patterns oriented against the base flow shear. As time evolves the disturbance will tilt into the mean shear direction yielding transient energy amplification. Once the disturbance flow patterns is aligned to the base flow shear its energy decreases. The (ii) lift-up effect is induced by streamwise vortices superposed on a positive shear, that push down high velocity and lift up fluid at low velocity generating streaks. As time evolves, the vortices decay and the energy of the perturbation decays.

These studies have been extended to the case of open-flows where an additional source of non-normality is the spatial separation between direct and adjoint mode (Cossu & Chomaz, 1997; Chomaz, 2005) resulting from the convection of the perturbation by the mean flow. The global optimal perturbation have been computed by Ehrenstein & Gallaire (2005), Åkervik *et al.* (2008) and Monokrousos *et al.* (2010) for a Blasius boundary layer and by Ehrenstein & Gallaire (2008) and Alizard *et al.* (2009) for a separated boundary layer flow.

1.2.2 Response to forcing

The non-orthogonality of the linear eigenmodes not only affects the transient dynamics, but it also influences the response to a harmonic forcing. Similarly to stable mechanical systems, when a stable flow is perturbed it comes back to its rest-state after a transient time as in Figure 1.3 (b). However, when a sustained forcing is applied, the flow displays a sustained response. The ratio between the amplitude of the response, A , and the forcing amplitude, A_f , defines the resonance curve, see Fig. 1.3 (c). In particular, the frequency associated with the higher response defines resonance and it is also called the preferred frequency of the system.

As reviewed by Schmid & Henningson (2001) and Chomaz (2005), the non-normality of the linearized Navier-Stokes operator, L , also implies a high-sensitivity to external forcing. Figure. 1.3(c) shows schematically the resonance curve, A/A_f , in the case of a stable normal system (dashed-line) where the flow response is localized in frequency close to the eigenfrequency (resonance). In the case of non-normal system (solid line), the system exhibits larger amplitude response due to the cooperation between the non-normal eigenmodes, a property called convective non-normality (Cossu & Chomaz, 1997; Chomaz, 2005). In particular, strong response for excitation frequencies far from the eigenvalues is possible (pseudoresonance).

Therefore, due to the high sensitivity of non-normal systems to forcing, the appearance of large coherent structures in linearly stable system has been often explained in the literature as the result of external forcing acting on the flow. This is the case of isothermal jet flows, which are seen to support large-scale coherent structures developing in the outer shear layers as in Figure 1.4 (a,b). Crow & Champagne (1971) carried out forced and unforced experiments

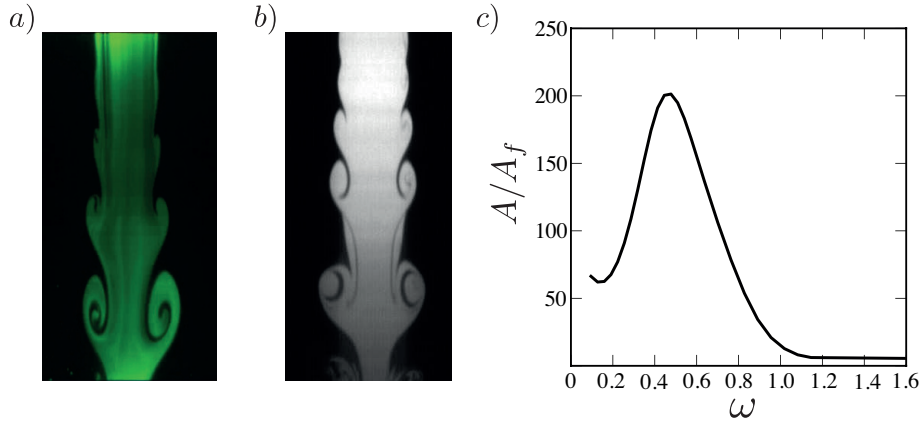


Figure 1.4: Experimental visualization of coherent structures in a jet by a) Billant *et al.* (1998) and b) Zaouali *et al.* (2011). In c) the resonance curve of an incompressible jet found by Garnaud *et al.* (2013) through global resolvent analysis: a preferred frequency it is observed for $\omega \approx 0.45$.

on a jet measuring the spatial structure of the coherent structure and their amplitude and frequency. The amplitude of the response was found to be significantly affected by the forcing frequency, which was imposed by using a loudspeaker at the jet exit.

In order to investigate theoretically the appearance of these large-scale eddies in jet flows, Crighton & Gaster (1976) carried out a quasi-parallel stability analysis using a mean flow which fits the measurements Crow & Champagne (1971) and Moore (1977). They observed that these structures were not self-sustained since a region of absolute stability is not present in the flow. On the contrary, the flow is convectively unstable downstream the nozzle. The downstream growth of the axisymmetric wave modes with prescribed real frequency was calculated numerically, on the basis on a WKB approach with multiple scale method which approximates the *slowly varying* mean-flow as a sequence of parallel flows. They found a good agreement on the wavelength measurements of Crow & Champagne (1971). More recently Garnaud *et al.* (2013) investigated the linear response of a jet to forcing in a global framework. They found the spectrum of the linearized Navier-Stokes equations to be stable and that no isolated or least stable eigenmode was present in order to justify a classical resonance mechanism. The resolvent analysis reported in Figure 1.4(c), enlightens the presence of a pseudo-resonant frequency that is in good agreement with experimental observation at low forcing intensity (Crow & Champagne, 1971; Moore, 1977)

1.2.3 Sensitivity and passive control

Modal and non-modal stability properties of the linearized Navier-Stokes operator L depend on multiple factors, such as the advection rate, the presence of localized forces, turbulence level, fluid properties, domain geometry, initial conditions and boundary conditions. Thus, a modification of one of these factor yields a variation of the linearized operator L . This turn in

a modification of the stability threshold for oscillator flows and of the transient or sustained energy amplification in amplifier flows. The dependence of these quantities on a modification of the operator L is called sensitivity.

Chomaz (2005) explained that the sensitivity may become large when the linearized operator L is non-normal, which is usually the case in hydrodynamics. For instance, Bottaro *et al.* (2003) showed how small variations of the parallel Couette flow may lead to a destabilization of the spectrum yielding large variations in the linear dynamics. In particular, they identified the flow regions where a base flow modification has the most significant effect on temporal stability. This analysis was extended to the local spatio-temporal analysis by Hwang & Choi (2006) who investigated the absolute instability of a two-dimensional wake. In a global framework Marquet *et al.* (2008) determined the sensitivity of the vortex shedding mode in the wake of a circular cylinder to a base-flow modification. Using a variational technique, these authors derived a general expression of the base-flow sensitivity valid for oscillator flows. Giannetti & Luchini (2007) defined the so-called structural sensitivity, which is the sensitivity to a spatially localized feedback and showed that the projection of the global mode associated with the Von-Karman instability in the cylinder flow on its adjoint mode identifies the wavemaker of the stability, i.e. the core region where the self-excited instability mechanism takes place. This analysis has been employed by other authors for different flows such as Qadri *et al.* (2013) in the case of spiral vortex breakdown and Giannetti *et al.* (2010) for a time periodic base-flow.

In the case of amplifiers, the flow response to an external forcing is given by the resolvent analysis as discussed above. Brandt *et al.* (2011) determined the sensitivity of the optimal forcing-response to a base-flow modification, extending the work Marquet *et al.* (2008) to amplifier flows. In particular, they focused on the variation of the resolvent norm in the case of the Blasius boundary layer subjected to a harmonic body force where both component-wise and convective non-normalities are active. This analysis was applied by Boujo & Gallaire (2015) to the backward-facing step flow and extended to the case of inlet forcing and time-stochastic perturbation.

These sensitivity analyses are then employed to design control strategy to reduce some quantities of interest such as the drag of a body, the flow separation or unsteadiness. We refer the interested reader to Sipp *et al.* (2010) and the recent review of Camarri (2015).

1.2.4 In this thesis: The amplifier dynamics of swirling wakes

Chapter 2: Mode selection in trailing vortices

In the literature, the stability of swirling flows behaving as oscillators, e.g. spiraling vortex breakdown, has been largely investigated, while the case of swirling flows acting as amplifiers is still poorly understood. A significant example of these kind of flows are the trailing vortices generated at the tips of a lifting wing, that manifest helical coherent structures even if globally stable as in Figure 1.5(a,b). These swirling flows are of fundamental importance in aeronautics because they persist for several minutes in the wake of aircrafts, thus creating a potential safety issue for following airplanes. For this reason, the minimum separation between aircrafts



Figure 1.5: Spatial amplification of helical disturbances in trailing vortices in a) military or b) civil aircraft, and in c) the 3D numerical simulations of a Batchelor vortex harmonically forced (isocontour of axial vorticity, see text and chapter 2).

is prescribed by the International Civil Aviation Organization (ICAO). In take-off conditions, the imposed separation distance limits the airport capacity. The commercial manufacturer Boeing is developing an active system to break up trailing vortices to safely reduce the required separation distances and reduce air-traffic delay. The idea is to trigger the vortex instabilities (Figure 1.5(a,b)) by periodically moving the control surfaces of a small fraction (Crouch & Spalart, 2000; Crouch *et al.*, 2001). Therefore, it is of primary importance to investigate the instability mechanisms occurring in trailing vortices and their characteristic frequencies as well.

In the literature a substantial body of work has been devoted to the understanding of the instability of columnar vortices, as carefully reviewed in section 2.1. However, real trailing vortices are non-parallel and the velocity profiles evolve in the streamwise direction due to viscous effects that slow down the tangential velocity inducing a positive axial pressure that favors the wake deficit to recover (Batchelor, 1964). Furthermore, wind tunnel experiments reveal that the wake defect in trailing vortices is typically less than 80% (Devenport *et al.*, 1996; Del Pino *et al.*, 2011), yielding the flow to be locally convectively unstable (Delbende *et al.*, 1998) and thus behaving as a noise amplifier.

In chapter 2 the response to harmonic forcing of a trailing vortex is investigated by combining local and global linear analyses along with fully nonlinear numerical simulations (DNS). Firstly, the response of a non-parallel Batchelor vortex to inlet harmonic forcing is carried out through DNS. A large variety of helical responses is seen to resonate by spanning the forcing frequency, see the single helical mode in Figure 1.5(c). Secondly, the mode-selection mechanism is investigated in a local framework, through spatial stability analysis and WKB (Wentzel, Kramers, Brillouin) approximation, and globally with a resolvent approach. Careful comparisons between local and global stability analyses are discussed, and the usual WKB formalism (Huerre & Rossi, 1998) is extended to a suitably chosen type of harmonic body forcing.

The effect of nonlinear saturation on the response is then investigated by comparing the linear and nonlinear energy gains as a function of the forcing frequency and amplitude. Finally, the mode selection observed in the DNS is compared with the one of the linear optimal response.

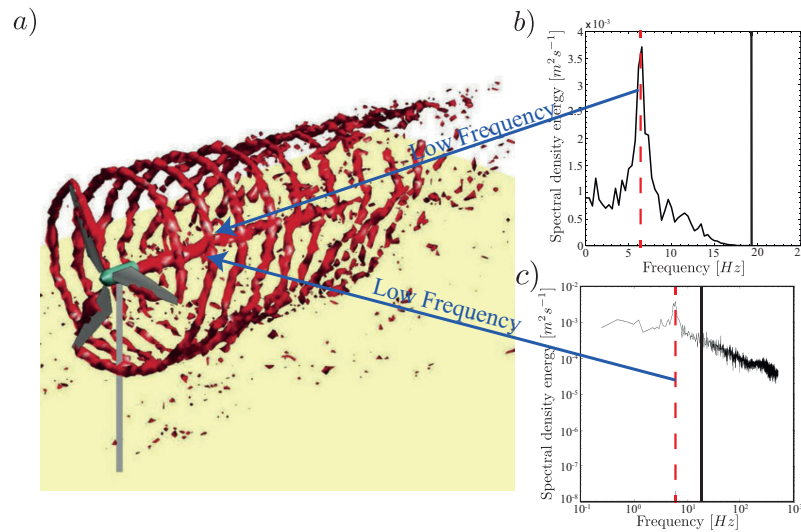


Figure 1.6: In a) isosurface of instantaneous vorticity of a wind turbine wake computed numerically (large-eddy simulations) by Lu & Porté-Agel (2011). Two main vorticity structures are present: the helicoidal tip vortices that shed from the blades' tip and the central hub vortex. The latter is found experimentally to oscillate at a frequency equal to 1/3 of the rotational frequency of the turbine as shown by the Fourier power spectral density of the velocity signals acquired experimentally by b) Chamorro & Porté-Agel (2010) and c) Zhang *et al.* (2012). The black vertical line refers to the rotational frequency of the turbine, whereas the red dashed one corresponds to the hub vortex instability frequency.

Chapter 3: The hub-vortex instability

Another example of swirling amplifier flow is present in wind energy, where wind turbines are used to convert the kinetic power of the wind into electricity. From the aerodynamic perspective, when the wind blows past a turbine the rotation of its blades produce a wake, which is the result of complex dynamics and interactions between different vorticity structures. Tip vortices are shed from the tip of each blade, which are then advected downstream forming a complex system of helicoidal vortices. At the wake center, the interaction between the root vortices shed from the blades and the boundary layer evolving over the turbine nacelle leads to the generation of the hub vortex, which is a vorticity structure mainly oriented in the streamwise direction.

Wind tunnel measurements in the wake of a down-scaled wind turbine immersed in a uniform flow have showed that these vorticity structures undergo to instabilities in the near-wake and are diffused downstream. As shown in Zhang *et al.* (2012), the near-wake dynamics is related with the far-wake dynamics. Thus, the physical understanding of the near-wake plays an important role on wind farm layout optimization. In particular, the tip-vortices instability is mainly driven by the mutual inductance between adjacent spirals, in cooperation with short-wave and long-wave instabilities which favorite the tip-vortices diffusion within one diameter past the turbine. Conversely, the hub vortex is characterized by oscillations of a frequency equal to roughly 0.34 times the rotational frequency of the wind turbine rotor which

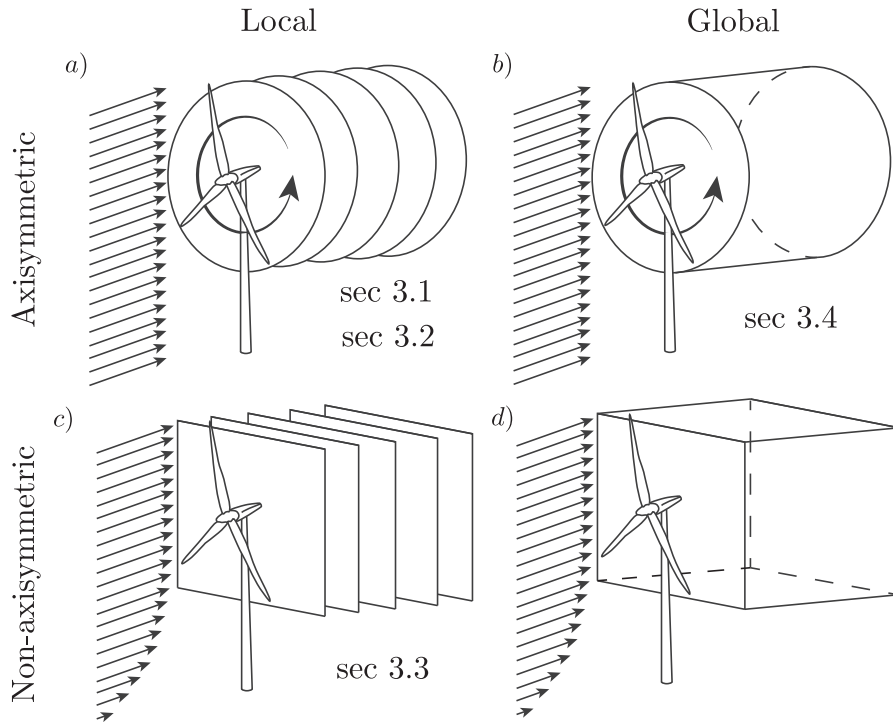


Figure 1.7: Illustrative plan of the possible linear stability analyses of the hub vortex. In the case the turbine is placed outside the boundary layer, the time averaged wake is 3D axisymmetric and its stability properties is studied as a a) set of 1D local problems (section 3.1 and 3.2) or a b) global 2D analysis (section 3.4). In contrast, the boundary layer breaks the axisymmetry of the wake and the computations gains one dimension: in a c) local approach a set of 2D stability analyses are solved (section 3.3), whereas in the d) global case a 3D analysis is necessary.

are detected up to two diameters downstream, see Figure 1.6.

In order to understand the origin of the low frequency oscillation of the hub vortex, in chapter 3 we carry out a stability analysis of the time averaged flow, measured in the wake of a down-scaled wind turbine model. In this work, the mean flow is used not only because the base-flow can not be measured experimentally, but also because it is expected to provide a better estimation of the dominant frequency and the associated unsteady mode, as discussed in section 1.3. Linear stability analysis on a time averaged flow obtained experimentally was applied by Oberleithner *et al.* (2011) to investigate the formation of large coherent structure in a turbulent swirling jet and by Camarri *et al.* (2013) to study the Von Karman wake behind a porous cylinder. Meliga *et al.* (2012b) analyzed the sensitivity of the turbulent mean wake of a D-shaped cylinder obtained through the numerical solution of the Reynolds-averaged Navier-Stokes equations (RANS).

We anticipate here that within the flow region where the experimental data are available, the wind turbine wake behaves as a noise amplifier because locally convectively unstable and globally stable. This motivates the investigation of the preferred frequency, defined as the frequency of the most amplified flow disturbance. The problem has been tackled with an

increasing level of complexity, as schematically reported in Figure 1.7.

In section 3.1 local temporal and spatial stability analyses are carried out on the mean wake flow measured in the wind tunnel, see Figure 1.7 (a). In the experiment the turbine model is mounted on a vertical support and placed outside the boundary layer. In this way, the oncoming flow was uniform yielding an axisymmetric mean wake with a frequency of oscillation of the hub vortex equal to the case of wind turbine immersed in the boundary layer. The nonparallel spatial mode that resonates at the hub vortex instability frequency measured in the wind tunnel is determined and its wavenumber is compared with the unsteady structure detected in the wind tunnel experiments.

In section 3.2 the stability analysis is reformulated by taking into account the turbulence nature of the flow. The Reynolds stresses in the perturbation dynamics are accounted by means of eddy-viscosity models, which are calibrated on the wind tunnel data. For the present investigation three eddy-viscosity models are considered: one model is based on the assumption of a uniform eddy viscosity for each streamwise location, whereas for the other two models a mixing length is estimated. It is shown that with the proposed improved formulation, stability analysis allows not only the identification of the hub vortex helical mode, but also the accurate prediction of its preferred frequency.

In section 3.3 the linear stability analysis has been extended to the case of wind turbines immersed in the atmospheric boundary layer, where the mean flow is not axisymmetric (Fig. 1.7 (c)). Specifically, a 2D local spatial stability analysis is developed in order to take into account typical flow features of real operating wind turbines, such as the presence of the atmospheric boundary layer and the turbulence heterogeneity in the oncoming wind. This stability analysis can be generally applied on either experimental measurements or numerical data.

In section 3.4 the hub vortex instability is investigated in a global framework as in Figure 1.7 (b). The global stability analysis of the time averaged hub vortex flow is carried out, showing that the global spectrum is stable. Consequently, the optimal response to a harmonic body forcing is studied by means of a resolvent analysis. The resulting preferred hub vortex frequency is determined and compared with the hub vortex frequency measured in the experiments, confirming the results obtained by weakly non-parallel stability analysis.

Chapter 4: Passive control of weakly non-parallel flows

The investigation on the mode selection in trailing vortices and in the hub vortex motivates the work presented in chapter 4 where a general formulation for a passive control design of weakly non-parallel amplifier flow is proposed. Our method generalizes the adjoint-based strategies usually employed to control oscillator flows (see Camarri (2015) for a review) to the case of weakly non-parallel amplifier flows. First, the sensitivity of the local spatial stability spectrum to a base-flow modification is determined, extending the results of Bottaro *et al.* (2006). Then, the Lagrangian multipliers theory is used to evaluate the sensitivity of the integrated amplification of disturbances in the streamwise direction to a modification of the inflow conditions. The resulting sensitivity map, depends on the local sensitivities of the

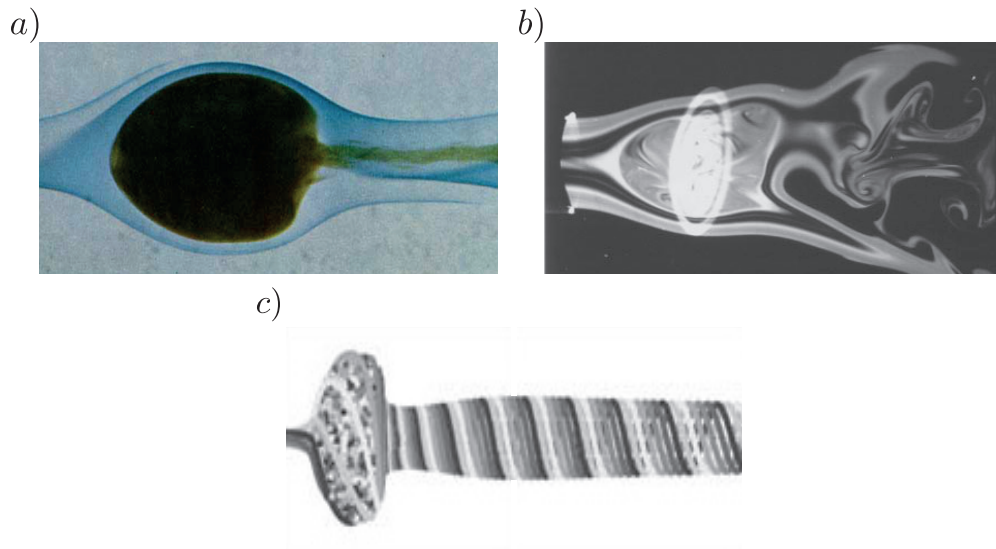


Figure 1.8: Visualizations of axisymmetric vortex breakdown obtained experimentally by a) Sarpkaya (1971) and b) Billant *et al.* (1998), and numerically by c) Ruith *et al.* (2003).

spatial stability, and indicates the optimal modification of the inlet flow condition to reduce the amplification of spatially growing perturbations. This method is applied to the case of a weakly non-parallel Batchelor vortex showing that the control, formulated using a single linearization of the flow dynamics carried out on the uncontrolled configuration successfully reduces the amplification of the helical modes.

Chapter 5: The axisymmetric vortex breakdown phenomenon

The spiral vortex breakdown phenomenon has been presented in section 1.1 as a prototype of oscillator flow (see see Figure 1.1(d,g)), i.e. resulting from a global instability of the flow. However, results obtained during the last decade suggest that breakdown itself does not result from the ultimate development of helical disturbances, but constitutes an independent phenomenon over which secondary helical disturbances may grow. This scenario, conjectured initially by Escudier & Zehnder (1982), has been confirmed by Ruith *et al.* (2003), who performed three-dimensional direct numerical simulations of a Grabovski and Berger vortex (Grabowski & Berger, 1976). Both studies clearly stress that the early stage of breakdown is axisymmetric, and that a finite time is needed at large swirl before this flow pattern is altered by the subsequent development of large-scale spiral waves, wrapped around and behind the axisymmetric bubble. Although numerous authors have carefully investigated this phenomenon, a clear and satisfactory explanation of the axisymmetric vortex breakdown state, that is shown in Figure 1.8, is still missing.

In chapter 5 the onset of the axisymmetric vortex breakdown state is carefully investigated by carrying out state-of-the-art numerical simulations, varying both the swirl, S , and Reynolds number, Re . Based on the DNS results, some classical explanations of the breakdown state are

discussed and revisited under a new light, and we propose a criterion for identification of the vortex breakdown as a transition state between two self-similar flow solutions.

We show that the breakdown state can not be explained as a standard supercritical bifurcation since the flow is seen to be globally stable. However, at a certain pre-breakdown swirl number (that depends on Re) we observe the presence of a weakly damped steady axisymmetric mode in the spectrum. This mode has a topology similar to the breakdown state and could be triggered by nonlinear effects even if linearly stable. Thus, we propose two possible weakly nonlinear mechanisms susceptible to trigger the weakly damped mode, which are based on a global resolvent and a global stability analysis.

Finally, inspired by the work of Lagr ee *et al.* (2005), we carry out *ad-hoc* numerical simulations in order to derive a set of reduced Navier-Stokes equations enabling to correctly account for the vortex breakdown state with a cheaper computational cost with respect to the full equations.

Many of the concepts and techniques developed in this thesis (such as oscillator and amplifier flows, non-normality and nonlinearity, global stability and global resolvent, temporal and spatial local analysis, DNS and weakly nonlinear analysis) are here applied in a renewed attempt to grasp new understanding on the fascinating vortex breakdown phenomenon.

1.3 Nonlinear effects

1.3.1 Superlinear nonlinearities

In Figure 1.2(c) a significant deviation of the full solution (solid line) from the linear modal solution (dashed line) is observed at large amplitude. Indeed, when the amplitude exceeds some level, the intrinsic nonlinearity of the Navier-Stokes equations (which is neglected in the linear analysis) kick in to play saturating the large amplifications of perturbations. The convective term, $\mathbf{u} \cdot \nabla \mathbf{u}$ in eq. 1.1, is a quadratic nonlinearity that becomes dominant at high amplitudes. This nonlinearity is defined as superlinear since it depends on the velocity with a power law with an exponent greater than one.

One example of superlinear nonlinearity is the supercritical Hopf bifurcation (Charru, 2011), where the amplitude of the unstable mode, A , initially grows exponentially in time accordingly to linear stability analysis, and then, when A is of order one, the exponential growth is perturbed by the convective nonlinear term leading to a periodic limit cycle with a finite amplitude. In the case of the first instability in the cylinder wake, Provansal *et al.* (1987) and Dušek *et al.* (1994) observed that the amplitude of the perturbation close to the bifurcation is governed by the Stuart-Landau equation

$$\dot{A} = \lambda A - \mu A |A|^2, \tag{1.6}$$

where the dot denotes derivation with respect to time and the Landau coefficients λ and μ were determined experimentally or numerically employing single-point measurements. More recently, these coefficients have been computed rigorously by Sipp & Lebedev (2007) using

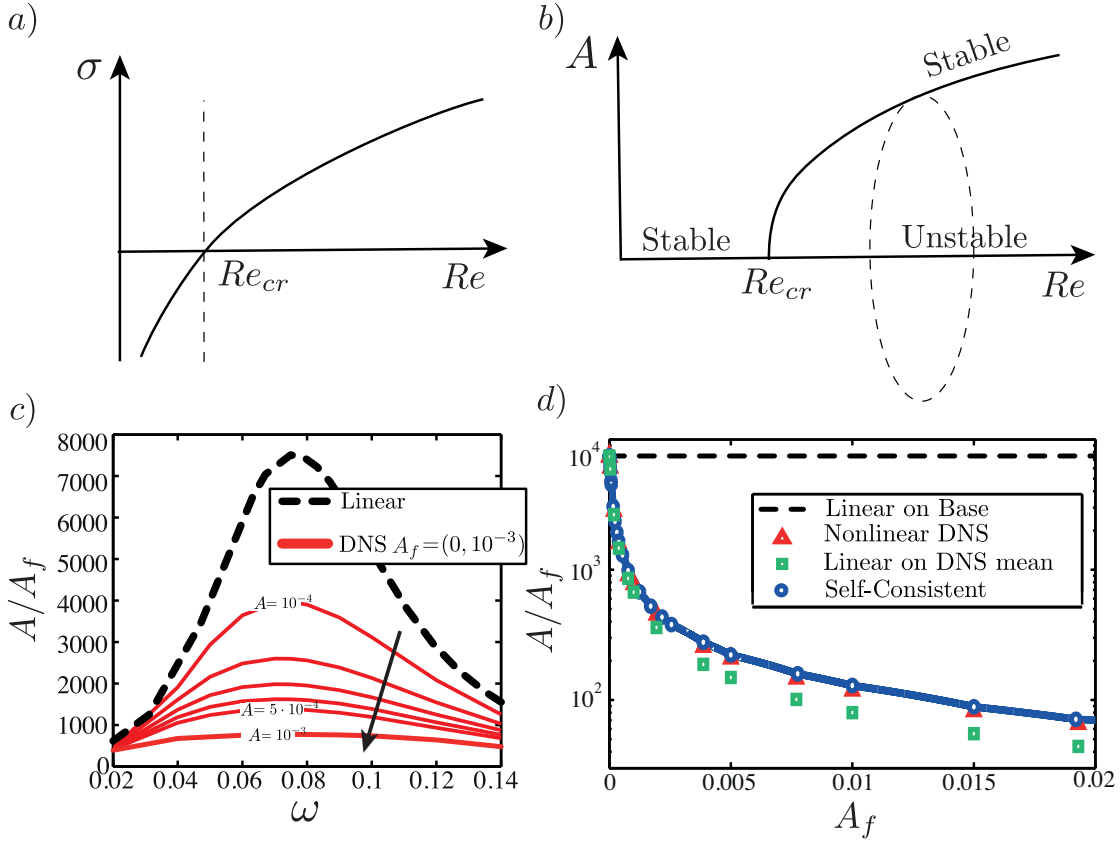


Figure 1.9: Linear growth and nonlinear saturation in (a,b) oscillator (c,d) and amplifier flows. In a) the transition from stable to unstable flow is given by the growth rate, σ , of the dominant eigenvalue that becomes positive for $Re > Re_{cr}$. The corresponding amplitude, A , of the nonlinearly saturated mode is shown in b) as a function of Re . c) The linear and nonlinear gain, A/A_f , as a function of frequency is shown in the case of amplifier flow over a backward-facing step (Mantič-Lugo & Gallaire, 2016). Each red line corresponds to a different forcing amplitude, A_f , ranging from 0 to 10^{-3} in equal intervals. d) The gain saturation as a function of the forcing amplitude, A_f , is well predicted by the linear resolvent over the mean flow (green symbols) and by the nonlinear self-consistent model proposed by Mantič-Lugo *et al.* (2015) (blue symbols).

adjoint methods and a weakly nonlinear analysis for the Navier-Stokes equations in the neighborhood of the critical Reynolds number, Re_{cr} , following the approach of Stuart (1958). They showed that the Stuart-Landau equation (1.6) naturally appears as a compatibility condition in their asymptotic scheme based on global stability. Together with Chomaz (2005), let us note here that the Landau constant μ actually links nonlinearity and non-normality, the two main points of focus of this thesis. Indeed, in the calculation procedure by Stuart (1958), μ depends on the scalar product of the direct and adjoint fields and it increases with increasing non-normality which requires nonlinear front theories for very non-normal globally unstable flows.

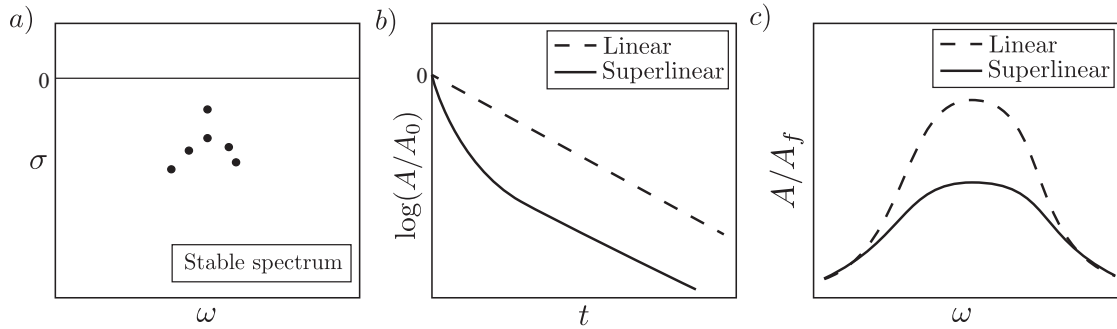


Figure 1.10: Schematics of superlinear effects on a linearly stable flow. a) All the eigenvalues in the spectrum have negative growth rate, σ . b) If the initial perturbation amplitude, A_0 , is small, the flow comes back to equilibrium following an exponential decay (dashed line). In contrast, if A_0 is large, the free decay of the system is nonlinear before entering in the linear regime when the amplitude, A , gets small enough (solid line). c) In the case of response to forcing the nonlinear response (solid line) differs significantly from the linear response (dashed line) when the gain A/A_f is large, due to nonlinear saturation. Far enough from resonance the amplification is less and the flow response is in the linear regime (plane and dashed lines overlap).

As discussed in the previous section, globally stable amplifier flows may also undergo large linear amplification when a sustained forcing is applied. More precisely, when the forcing frequency is close to resonance or pseudo-resonance the amplitude of the response becomes large and nonlinear saturation occurs, as schematically shown in Figure 1.10(c). The saturation dynamics in the response to harmonic forcing has been studied by Mantič-Lugo & Gallaire (2016) for the stable laminar flow over a backward-facing step. They observed that when a sustained forcing with increasing amplitude is imposed, the response experiences a strong nonlinear saturation when compared to the linear estimation and that the energy gain of the response significantly reduces when the amplitude of the forcing is increased, see Figure 1.9 (c,d). Furthermore, they showed as in the backward-facing step flow, the linear response around the mean flow computed by DNS provides a very good estimation of the saturated energy gain as shown in Figure 1.9(d). This means that the linear response analysis over the saturated mean flow already includes a significant part of the nonlinearity effects. This result is in line with the work of Barkley (2006) and Sipp & Lebedev (2007) who obtained good estimation on the vortex-shedding frequency in the cylinder flow by performing linear stability analysis on the mean flow.

On the other hand, also the short term dynamics of stable systems is affected by nonlinear effects when the initial amplitude of the perturbation is large. Figure 1.10(b) shows by a dashed line the logarithmic decrement of small perturbations: the mode is damped with a uniform damping rate. In the case of large initial amplitude A_0 (solid line), the dynamics is initially nonlinear with the damping rate depending on the oscillation amplitude. At later stage, A gets small enough to *turn off* the nonlinear term and the perturbation follows the linear dynamics decaying exponentially.

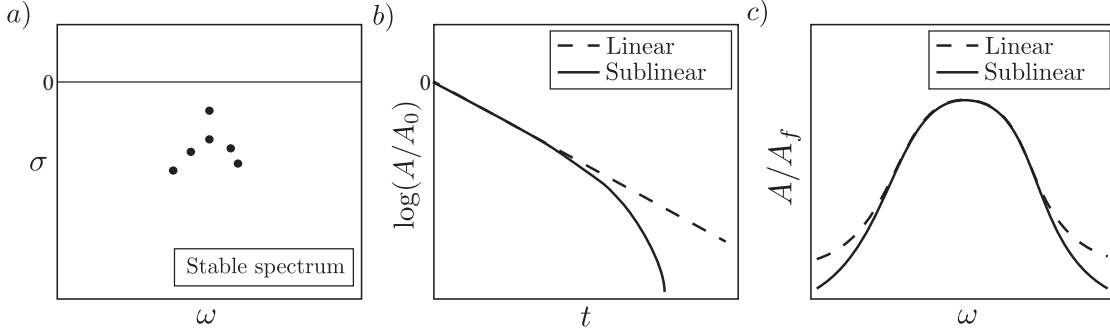


Figure 1.11: Schematics of sublinear effects on a linearly stable flow. a) All the eigenvalues in the spectrum have negative growth rate, σ . b) At large amplitude, the free decay of the nonlinear problem (solid line) follows the exponential decay of the linearized problem (dashed line). When the amplitude is small, the relative importance of sublinear friction terms increases and the logarithmic decay is concave down since the damping rate increases as the amplitude of oscillations decreases. c) Similarly, in the case of response to forcing the nonlinear response (solid line) follows the linear response (dashed line) when the gain A/A_f is large and sublinear effects are expected to become important far from resonance when the amplitude is small.

1.3.2 Sublinear nonlinearities

The convective term in the Navier-Stokes equations is an intrinsic nonlinearity of fluid dynamics that appears in the governing equations. However, in presence of a free surface or in the case of fluid-structure interaction, other nonlinearities may appear. For the Euler’s disk, Moffatt (2000) for instance identified a viscous Stokes layer friction scaling like the inverse of the absolute angular velocity of the disk. In this case, when the nonlinearity follows a power law with an exponent smaller than one, we define it as sublinear.

In stark contrast to the case of superlinear nonlinearity, a stable system subjected to a sublinearity exhibits nonlinear behaviour at small amplitudes since the sublinear term dominates the linear and superlinear terms when the amplitude A approaches zero. This behaviour is schematically depicted in Figure 1.11(b), where the logarithmic decay of a linear system (dashed line) is seen to be modified at small amplitudes when a sublinear term is added (solid line). Similarly, in the response to harmonic forcing the resonance curve is modified far from the resonance frequency where the amplitude A is small, while close to the natural frequency, the sublinear term is small compared to the other terms and the system response linearly (dashed and solid lines overlap in Fig. 1.11(c)).

As often the case for oscillating systems, an easy and meaningful representation can be obtained through a simple mass-spring oscillator. It is evident that the dynamics of

$$\ddot{A} + A = -\dot{A}^\alpha. \tag{1.7}$$

is non linear when the ratio A^α/A is large. As shown in Figure 1.12, two scenarios are possible depending on the magnitude of the amplitude A and on the value of the coefficient α . If $\alpha > 1$ the nonlinear term dominates the dynamics at high amplitude (as for the convective term

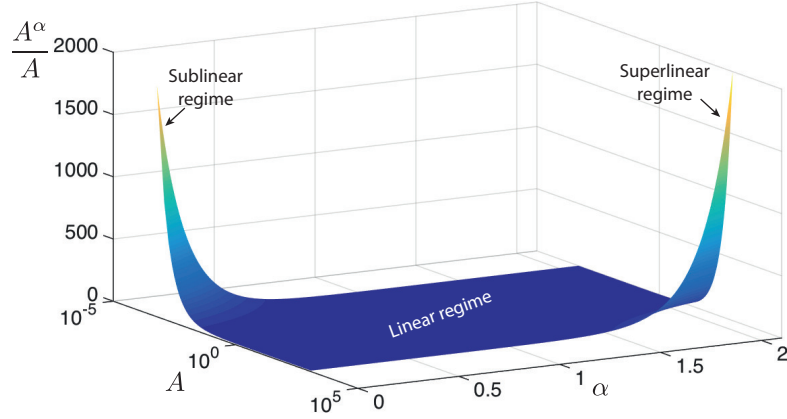


Figure 1.12: Ratio between a generic algebraic nonlinearity A^α and the oscillation amplitude A . Depending on the exponent of the power law, α , and the oscillation amplitude, A , the system is governed by linear or nonlinear dynamics. Specifically if $A \gg 1$ and $\alpha > 1$ the system experiences a superlinear nonlinearity, whereas if $A \ll 1$ and $\alpha < 1$ sublinear effects dominate. The linear regime takes place when the ration A^α/A is small: $A \ll 1$, $\alpha > 1$ and $A \gg 1$, $\alpha < 1$, while in the case $\alpha = 1$ the term A^α is trivially linear.

in Navier-Stokes equations). Vice versa the nonlinear effects are more significant when the amplitude is small in the case $\alpha < 1$.

In the following we consider the case of a liquid meniscus sliding over a solid substrate, where sublinear terms are seen to appear.

Dynamic meniscus: Total wetting

Let us consider a liquid wedge with surface tension, γ , and fluid viscosity, μ , which advances over a precursor wetting film as in Figure 1.13(a). The dynamical contact angle, θ is different from the one at equilibrium θ_s and it depends on the wedge's advancing velocity, U . The relation between θ and U results from the balance of the traction force pulling the liquid toward the wetting film and the viscous force $\gamma(1 - \cos(\theta)) \sim \mu U/\theta$. In the limit of small angles we get

$$\theta^3 \sim Ca = \frac{\mu U}{\gamma}. \quad (1.8)$$

where the capillary number $Ca = \mu U/\gamma$ is the nondimensional number of the problem that measures the relative importance of viscosity to surface tension forces. The relation (1.8) is known as Tanner's law and has been experimentally validated as shown in Figure 1.13(b).

More than that, this motion induces a specific friction force, F_f , that has a visco-capillary origin and exhibits a nonlinear dependency in the meniscus velocity. Indeed, by injecting Tanner's law (1.8) in the expression of the viscous force, $\mu U/\theta$, it is found that

$$F_f \sim \gamma Ca^{2/3} = \gamma^{1/3} \mu^{2/3} U^{2/3}. \quad (1.9)$$

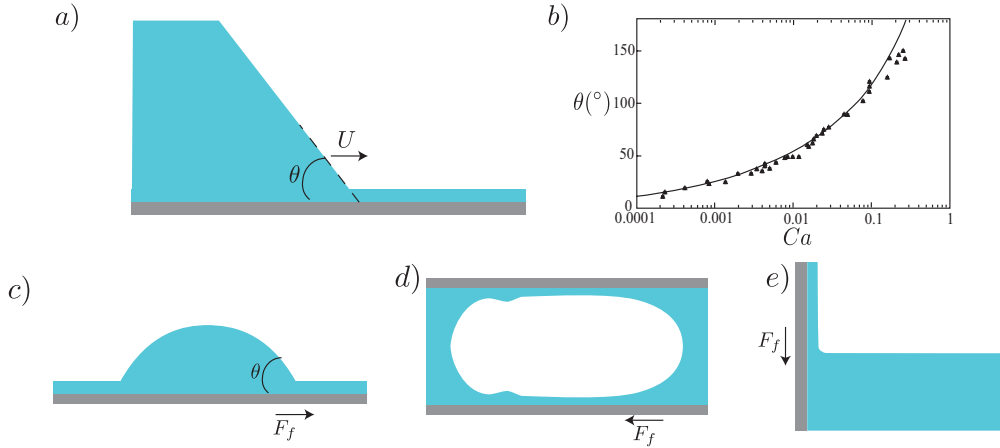


Figure 1.13: a) A liquid wedge advancing over a wet substrate. The apparent dynamic contact angle, θ , depends on the sliding velocity, U , according to Tanner's law (1.8) that has been verified experimentally as reported in b) for the case of a moving of silicone oil meniscus inside a capillary tube (Petit *et al.*, 2012). Next, three famous total wetting problems where the friction force, F_f , scales as $F_f \sim U^{2/3}$ are sketched: c) a droplet spreading (Tanner's problem), d) a bubble moving in a tube (Bretherton's problem) and e) a plate pulled out of a liquid bath (Landau-Levich-Derjaguin problem).

As reviewed in Stone (2010), this sublinear relation of friction force on the capillary number is typical of total wetting diphasic flows such as droplet spreading on a wet plate (Tanner's problem, Fig. 1.13(c)), a bubble moving in a tube (Bretherton's problem, (d)) or a solid plate pulled out of a liquid bath (Landau-Levich-Derjaguin problem, (e)).

It should be noted that the relation differs from the force scalings encountered in classical hydrodynamic such as the linear force-velocity dependence $F \sim U$ in the Stokes flow and Stokes oscillating boundary layer. Or the nonlinear scalings $F \sim U^{3/2}$ in the laminar boundary layer and $F \sim U^2$ typical of the separated flows. Hence, in the case of an oscillating flow over a steady base-state the friction force (1.9) is expected to dominate the linear and superlinear terms at small enough values of U .

Dynamic meniscus: Partial wetting

When a liquid meniscus is moving on a dry surface, an air-liquid-solid interface is present and other kinds of nonlinearities enter in the system. Let us consider a drop sliding on an inclined dry plate. It has been observed experimentally (Dussan, 1979; Rio *et al.*, 2005; Le Grand *et al.*, 2005) that the dynamic advancing, θ_1 , and receding, θ_2 , contact angles change from their static values depending on the velocity of displacement of the advancing/receding meniscus, see Figure 1.14(b). Furthermore, it exists a range $[\theta_R, \theta_A]$ such that if θ lies within this interval then the contact line does not appear to move (contact-angle hysteresis).

Various models have been proposed in literature to relate the nonlinear dependance of the dynamic contact angles (θ) on the capillary number based on the drop velocity, U . A simple

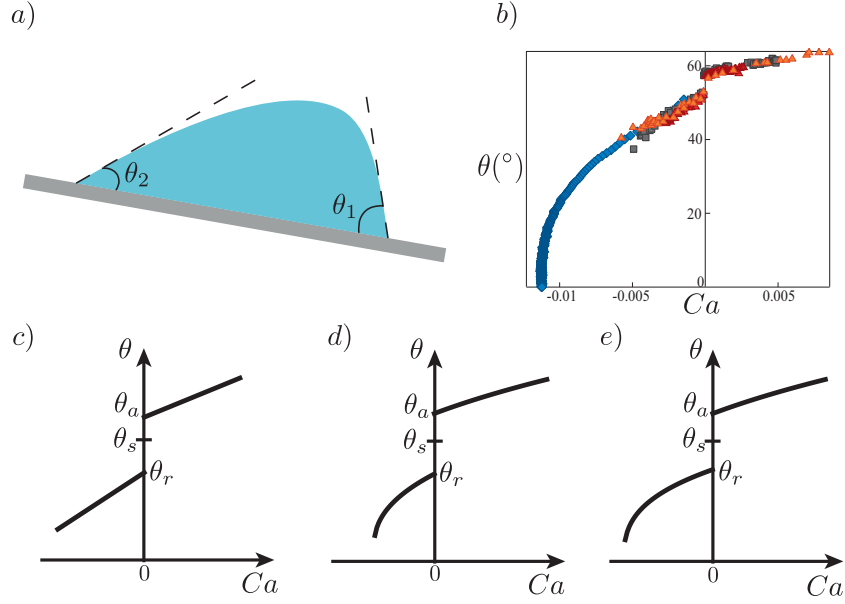


Figure 1.14: a) Advancing, θ_1 , and receding, θ_2 , contact angles in a droplet which slides with velocity U over a dry substrate. The dynamic contact angle is seen experimentally to depend on the capillary number $Ca = \mu U / \gamma$ as reported in b), where a hysteresis range for $Ca = 0$ is present (figure adapted from Snoeijer & Andreotti (2013)). The dependence of the dynamic contact angle, θ , on the capillary number, Ca , is modeled in the literature by the c) linear Dussan d) de Gennes and e) Cox-Voinov models with hysteresis.

phenomenological model inspired by experiments on a unidirectional flow over a flat plate, was proposed by Dussan (1979) imposing a linear relation between the dynamic contact angle and the capillary number

$$\theta - \theta_s \sim Ca \quad (1.10)$$

where θ_s is the static contact angle.

An analytic law linking θ , θ_s and Ca was derived by De Gennes (1985) extending the Tanner's law 1.8 to the case of partial wetting. The traction force to pull the liquid is now $\gamma(\cos(\theta_s) - \cos(\theta))$ and the viscous force scales as $\mu \frac{U}{\theta} \ln(x_M / x_m)$. Here, x_M is a macroscopic characteristic length and x_m is a microscopic cut-off length which is needed to avoid stress singularity (Snoeijer & Andreotti, 2013). In the limit of small static and dynamic contact angle we have

$$\theta(\theta^2 - \theta_s^2) = \pm 6Ca \ln(x_M / x_m) \quad (1.11)$$

where the \pm distinguishes the advancing from the receding contact line motion.

Cox (1986) and Voinov (1976) determined a similar but different relation by solving lubrication equations for weakly curved air-liquid interfaces. Similar to the approach of de Gennes,

the solution is truncated at molecular and macroscopic dimensions, giving the following law

$$\theta^3 - \theta_s^3 = \pm 9Ca \ln(x_M/x_m). \quad (1.12)$$

As pointed out by Le Grand *et al.* (2005), although these models match well the contact line dynamics observed in the experiments, they all neglect the wetting hysteresis. For this reason when comparing the models with the experiments, the static contact angle in the equations (1.10), (1.11) and (1.12) is replaced by the limit static angle θ_a for the advancing branch and by θ_r for the receding one. Figure 1.14 shows the resulting $\theta(Ca)$ dependence for the c) linear Dussan d) de Gennes and e) Cox-Voinov models with hysteresis.

Mathematically the hysteresis of the contact angle is sublinear because it only depends on the sign of the contact line rather than on its amplitude. This means that the hysteresis contribution to the dynamics is not amplitude-dependent and it will become dominant when the other linear and superlinear terms get smaller at small amplitude. For example, in the case of an oscillating flow about a rest state, the liquid meniscus will always experience the same hysteresis range $[\theta_R, \theta_A]$ over one period, no matter what the amplitude of oscillation is.

1.3.3 In this thesis: Nonlinear friction in fluid-solid resonators

Chapter 6: The viscous torsional pendulum

The transition from the high-amplitude nonlinear regime to the low-amplitude linear regime is here instigated by considering a fluid-solid oscillator: a torsional pendulum immersed in a fluid. The system is made by a thin disk connected to a perfect torsional spring (the spring always obeys Hooke's law). The disk can only rotate about its axis and when it is twisted from its equilibrium position the restoring force of the spring results in an oscillatory motion. However, the system relaxes to equilibrium due to the viscous dissipation exerted by the surrounding fluid which damps the oscillations.

In this work, we have carried out direct numerical simulations of the coupled fluid-disk system in order to investigate the damping rate of decay. We have observed that if the twisting angle is large the damping rate is not uniform in time but depends on the oscillation amplitude due to the superlinear effect of the convective term in the Navier-Stokes equations, which is the only nonlinearity in the system. However, when the amplitude of oscillation is small the nonlinear contribution becomes negligible and the disk's oscillation amplitude decays exponentially with a constant damping rate. Some insight about the nonlinear and the linear regimes is gained by writing the boundary layer equations in the limit of high and low amplitude regimes. Finally, an analytical and predictive model for the free oscillation decay of the viscous torsional pendulum is proposed.

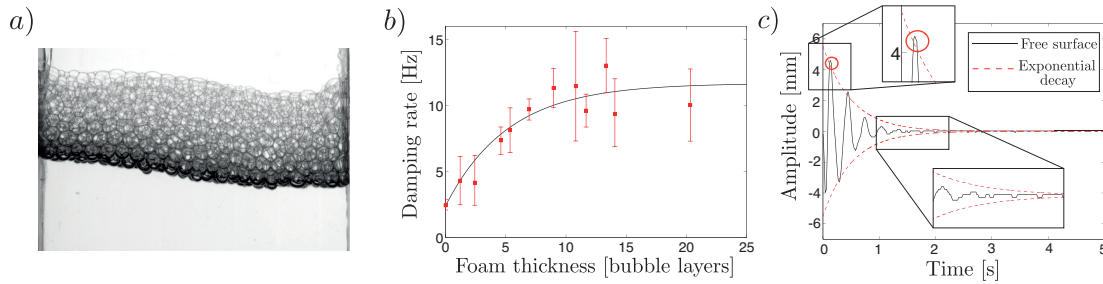


Figure 1.15: a) Sloshing wave with a thin layer of foam placed on top of the water column. The b) damping rate measured experimentally increases with the foam thickness. However, c) the corresponding exponential decay is seen to underestimate the surface elevation at high oscillation amplitude and to overestimate it in the low amplitude regime. Figures from Sauret *et al.* (2015).

Chapter 7: Sloshing with foam

The transition between the linear to the sublinear regime is here studied considering the sloshing phenomenon. This phenomenon is well known from everyday's life. Whenever one moves or agitates a glass of liquid, capillary-gravity waves at the liquid-air interface are excited and the deformations of the free-surface are progressively relaxed: the excess of gravitational potential energy is periodically turned into kinetic energy and dissipated by viscosity. Due its regular motion, small amplitude sloshing constitutes an archetypal damped oscillator in fluid mechanics, with frequency derived in the potential flow limit (Lamb, 1932). The damping rate results from the viscous dissipation at the wall, in the bulk and at the free surface and was determined analytically by Case & Parkinson (1957) for a cylindrical container. However, this classic theoretical prediction significantly underestimates the damping rate measured in experiments (Cocciaro *et al.*, 1991). In particular, (Keulegan, 1959) found that the damping depends on the material of the container pointing to the key-role of capillary effects at the interface on the waves attenuation, which was neglected in the theory of Case & Parkinson (1957).

In order to enhance the capillary effect in the sloshing dynamics, we propose in chapter 7 an experiment that introduces a small modification to the classical sloshing problem placing a thin layer of foam on a volume of water, and we explored the dramatic change in its mechanistic properties. It has recently been shown independently that a thin layer of foam placed on top of a liquid strongly damps its sloshing motion (Sauret *et al.*, 2015), see Figure 1.15. Here, we focus our attention on the nonlinear nature of the dissipation in the collection of moving lines present in the foam structure. In fact, these surface Plateau borders induce a viscous friction that sublinearly depends on their sliding velocity (Denkov *et al.*, 2005; Cantat, 2013). We show experimentally and theoretically that, due to this nonlinear friction, the sloshing of the liquid phase does not relax exponentially. The damping rate increases catastrophically at small amplitude and yields a finite-time arrest of the fluid's motion. This result is in strong contrast with the classical linear exponential relaxation ending at infinite time. We rationalize

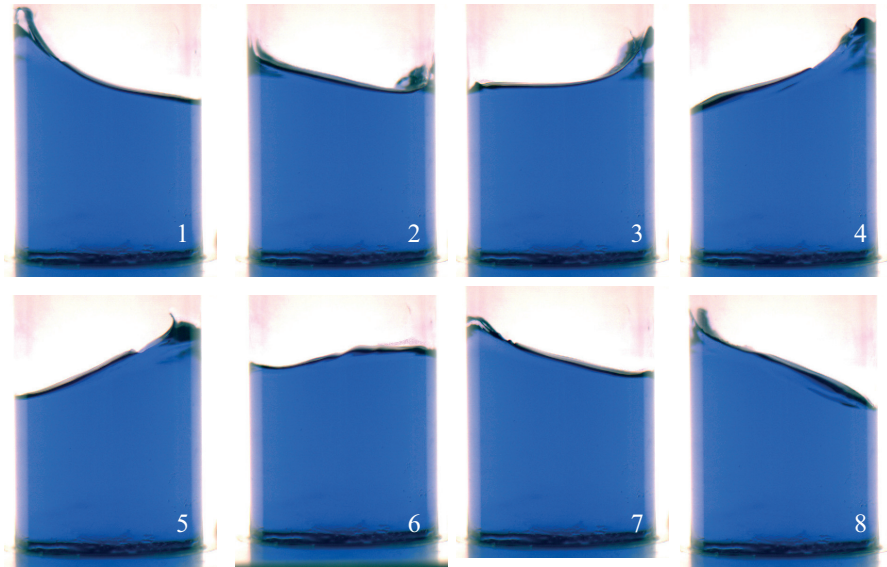


Figure 1.16: Images of the fundamental sloshing mode in a circular cylinder with partial wetting conditions at the wall. The eight images represent slightly more than one wave period which is equal to 290 ms.

our observations deriving a minimal theoretical model accounting for the sublinear interfacial effects in the total wetting regime.

Chapter 8: Contact line hysteresis in sloshing dynamics

In chapter 8 the dynamics of sloshing water waves in the partial wetting regime is studied. In this case the oscillating interface is effectively in contact with the container without any precursor film along the container's wall, see Figure 1.16. To this end, we carry out a weakly nonlinear analysis and investigate the dynamics of inviscid waves subjected to a contact line law presenting an hysteresis (Dussan, 1979; Rio *et al.*, 2005). We show theoretically that capillary effects have a dramatic influence on the damping rate. Specifically, the damping rate induced by the motion of the liquid meniscus depends on the wave amplitude, consistently with the experimental observation (Keulegan, 1959; Cocciaro *et al.*, 1991). This rate is practically uniform when the wave amplitude is large and increases significantly at small amplitudes due to the presence of the sublinear hysteretic behavior of the contact line motion. Similarly to the foam case, we unravel the existence of a finite time singularity in this problem.

1.4 Foreword: Structure of the document and contribution of the author

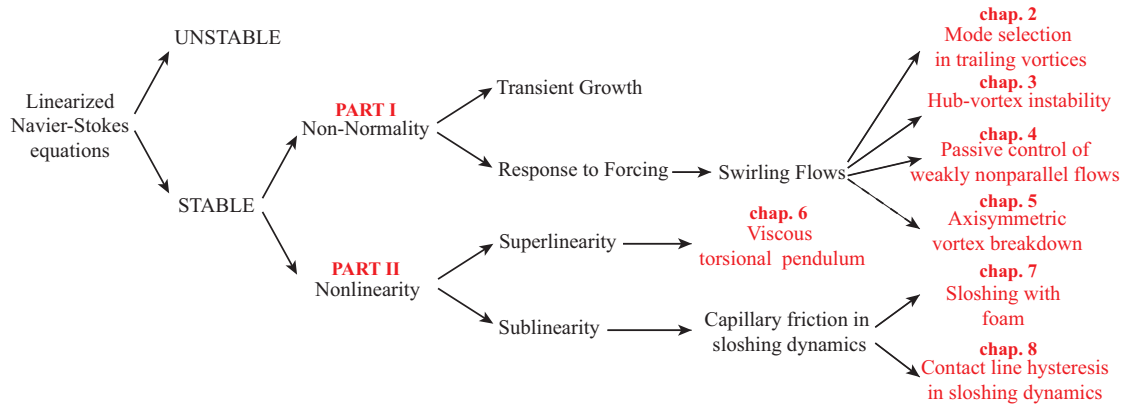


Figure 1.17: Original contributions of this work inserted in the graph of hydrodynamic stability.

Note that the thesis is organized as in Figure 1.17 and contains published or submitted material carried out in collaboration with other experienced researchers as well as my supervisor. I fundamentally contributed to all parts of the papers, including the writing phase, as detailed below.

PART I: Non-modal effects in swirling flows

In **chapter 2** the harmonic response to inlet and body forcing of a non-parallel Batchelor vortex is investigated through DNS and linear WKB and global resolvent analyses. I have built up the numerical models for local and global stability analysis of non-parallel swirling flows from scratch and performed the nonlinear numerical simulations within the frame provided by Nek5000. I have written the paper with input from the coauthors.

In **chapter 3** the hub vortex instability in wind turbine wakes is studied by carrying out local and global stability analyses on the time-averaged flow acquired in wind-tunnel experiments. In the papers contained in this chapter, I have carried out the local and global stability analysis and fundamentally contributed to the formulation accounting for turbulence effects in the stability analysis. I contributed in writing the first paper, especially in sections two to five devoted to stability analysis, and wrote the other two papers with input from the coauthors. The experimental data reported in section 3.1 and 3.2 was acquired by G. V. Iungo at the Wind Engineering and Renewable Energy Laboratory (WIRE) at EPFL directed by Prof. F. Porté-Agel whereas those in section 3.3 have been kindly provided by W. Zhang, C. D. Markfort and F. Porté-Agel.

In **chapter 4** a strategy for the design of passive control of weakly non-parallel amplifiers flow is proposed. In the paper contained in this chapter, I developed the sensitivity of the

Chapter 1. Introduction

spatial stability analysis to a base flow modification. I have also developed the DNS code for steady axisymmetric solutions from scratch and built up the numerical models for local stability analysis and inlet sensitivity together with Erica Pezzica (master student from the University of Pisa). I wrote the manuscript with input from the coauthors.

In **chapter 5** the axisymmetric vortex breakdown phenomenon is revisited with new perspectives. This chapter has greatly benefited from a collaboration with Prof. Pierre-Yves Lagr e, initiated during his visit at EPFL.

PART II: Nonlinear effects in solid-fluidic oscillators

In **chapter 6** the linear and superlinear friction regimes of a viscous torsional pendulum are studied.

In **chapter 7** the nonlinear friction induced by moving contact lines is investigated experimentally by means of a liquid-foam sloshing system. We then propose an equivalent mechanical system mimicking the nonlinear dynamics. In the paper contained in this chapter I have carried out the sloshing experiments with fast camera and analyzed the data acquired. I fundamentally contributed to the formulation of the equivalent mechanical model and developed the asymptotic solution. I wrote the second and third section of the paper (with input of the coauthors) and contributed in writing the first and the fourth sections.

In **chapter 8** the effect of contact angle hysteresis in sloshing dynamics is studied in a global framework by means of a weakly nonlinear analysis. In the paper contained in this chapter I fundamentally developed the weakly nonlinear analysis and built up the numerical models for the computation of the global sloshing modes. I wrote the paper with input from the coauthors.

In **chapter 9** conclusions are drawn and possible future works are described.

The amplifier dynamics of Part I
swirling wakes

2 Mode selection in trailing vortices

Mode selection in trailing vortices: harmonic response of the non-parallel Batchelor vortex

F. Viola¹, C. Arratia^{1,2} and F. Gallaire¹

¹ Laboratory of Fluid Mechanics and Instabilities, École Polytechnique Fédérale de Lausanne, Lausanne, CH-1015, Switzerland

² Departamento de Física, FCFM, Universidad de Chile, Casilla 487-3, Santiago, Chile

Journal of Fluid Mechanics 790 (2016): 523-552.

In the present study, the response of model trailing vortices subjected to a harmonic forcing is studied. To this purpose, a globally stable non-parallel Batchelor vortex is considered as the base-flow. Direct numerical simulations (DNS) show that a large variety of helical responses can be excited and amplified through the domain when an harmonic inlet forcing is imposed. The spatial shape of the responses strongly depends on the forcing frequency, with the appearance of modes with progressively higher azimuthal wavenumber m as the frequency increases. The mode selection mechanism is shown to be directly connected to the local stability properties of the flow, and is simultaneously investigated by a WKB approximation in the framework of weakly-non-parallel flows and by the global resolvent approach. In addition to the excellent agreement between the two (local and global) approaches for the computation of the linear response to harmonic forcing at the inlet, the usual WKB analysis is extended to a suitably chosen type of harmonic body forcing, showing also good agreement with the corresponding global results. As expected, the gain of the nonlinear response is significantly lower than that of the linear response, but the mode selection observed in the DNS as a function of the forcing frequency can be predicted fairly accurately by the linear analysis. Finally, by comparing the linear and nonlinear results in terms of energy content for different m , we suggest that the origin of the meandering observed in trailing vortex experiments could be due to a nonlinear excitation stemming consistently at $m = 1$ from the competition between the leading linear modes.

2.1 Introduction

In aeronautics, trailing vortices occur behind the wing of an aircraft due to the variation of the lift along the wing span. These vortices are characterized by strong axial velocity and relatively small-wake deficit, which is recovered downstream due to the positive axial pressure gradient induced by the slowing-down of the tangential motion caused by viscous effects. The analysis of their stability with respect to infinitesimal disturbances is important to better understand their lifetime as well as contrail formation. The tip-vortices are accountable for the proper evaluation of aerodynamic loads and for the induced drag, which represents about one third of the total drag of a civil aircraft. Its reduction, even by a small percentage, would correspond to a significant decrease in fuel consumption. Furthermore the persistence of the trailing wake shed by an aircraft represents a source of risk for aircrafts that follow in its wake, especially in takeoff and landing operations. For this reason, the minimum separation between aircrafts in the different operating conditions is prescribed by the International Civil Aviation Organization (ICAO).

Batchelor (1964) derived an asymptotic solution for trailing vortices by adopting boundary layer assumptions in incompressible axisymmetric Navier-Stokes equations, which rely on the slow variation of the flow in the streamwise direction. This solution is commonly referred to as a *Batchelor vortex*, which in dimensional variables (r^*, x^*) reads:

$$\begin{aligned} U_x^*(r^*, x^*) &\sim U_\infty + (U_c(x^*) - U_\infty)e^{-(r^*/R(x^*))^2}, \\ U_\theta^*(r^*, x^*) &\sim C_0 \frac{1 - e^{-(r^*/R(x^*))^2}}{r^*}, \end{aligned} \quad (2.1)$$

where U_x^* and U_θ^* are the axial and azimuthal velocity components, and U_∞ is the freestream velocity. $U_c(x^*)$ and C_0 are respectively the axial velocity at the centerline and the circulation divided by 2π , and $R(x^*)$ is the vortex radius at the streamwise position x^* . For large Reynolds number, $Re = \frac{U_\infty R(0)}{\nu}$, the radial velocity, $U_r^*(r^*, x^*) \sim U_\infty/Re$, which is negligible at leading order and results in a slow evolution of the flow in the streamwise direction. This allows Batchelor (1964) to determine analytically the asymptotic streamwise evolution of $R(x^*)$ and $U_c(x^*)$.

At a given downstream location, equations (2.1) can be made non dimensional by choosing as length scale the radius core of the vortex, $R(x^*)$, and as velocity scale the velocity defect, $\Delta U_x(x^*) = U_c(x^*) - U_\infty$, see Delbende *et al.* (1998). Consequently, the so called *a-q* formulation is obtained:

$$U_x(r, x) \sim a(x) + e^{-r^2}, \quad U_\theta(r, x) \sim q(x) \frac{1 - e^{-r^2}}{r}, \quad (2.2)$$

where $a \equiv U_\infty/\Delta U$ is the external flow parameter, $q \equiv C_0/(R\Delta U)$ the swirl number and the local Reynolds number is defined as $Re_D(x) = |\Delta U(x)|R(x)/\nu$. In contrast, if the freestream velocity, U_∞ , and the initial vortex radius, $R(0)$, are chosen as reference velocity and reference length, the following expressions are obtained, as in Heaton *et al.* (2009), which we will refer to

as α - δ formulation:

$$U_x(r, x) \sim 1 - \alpha(x)e^{-r^2/\delta^2(x)}, \quad U_\theta(r, x) \sim k \frac{1 - e^{-r^2/\delta^2(x)}}{r}, \quad (2.3)$$

where α is the non-dimensional wake defect $-\Delta U/U_\infty$, k is the non-dimensional circulation $k \equiv C_0/(R(0)U_\infty)$, and $\delta(x)$ is the non dimensional vortex radius $\delta(x) \equiv R(x)/R(0)$. Consequently the local Reynolds number is defined as $Re_H = U_\infty R(0)/\nu$. The relations among the quantities introduced in the two non-dimensionalizations are:

$$q = -\frac{k}{\alpha\delta}, \quad a = -\frac{1}{\alpha}, \quad Re_D = \alpha Re_H. \quad (2.4)$$

The parameters a - q and α - δ vary along the streamwise direction and mimic the vortex core spreading and the recovery of the wake deficit in the trailing vortex evolution. By keeping these parameters constant the *parallel* Batchelor-vortex is obtained, which is a family of columnar vortices identified by swirl number, wake deficit and Reynolds number.

The linear stability of the parallel Batchelor vortex has been widely studied in the literature. Taken in isolation, the tangential velocity profile is stable, since it does not satisfy Rayleigh's criterion, while the axial velocity profile is only unstable to mode $m = 1$ (Batchelor & Gill (1962)) as a consequence of a shear instability. However, the addition of both velocity components leads to a massive destabilization for virtually any azimuthal mode when the swirl number is less than $q \approx 1.5$ (Mayer & Powell (1992); Leibovich & Stewartson (1983); Delbende *et al.* (1998)), the only cut-off mechanism being viscous damping. The mechanism underlying this destabilization is a generalized centrifugal instability unravelled by Ludwig (1962); Leibovich & Stewartson (1983); Eckhoff (1984). This general picture does not hold close to the stability bound $q = \sqrt{2}/2$ where weakly amplified modes have been detected. In addition, viscous core modes could also be identified numerically and asymptotically (Khorrami (1991); Heaton (2007); Fabre & Jacquin (2004); Fabre *et al.* (2006)).

Besides these temporal stability analyses, Delbende *et al.* (1998); Olendraru *et al.* (1999); Olendraru & Sellier (2002) carried out a spatio-temporal analysis as a function of swirl and wake parameters, showing that for relatively large wake deficits the flow can be absolutely unstable, as seen in figure 2.2 of the present work. For coflowing wakes, the wake defect needed to trigger an absolute instability depends on the swirl number and the lower bound is approximately $a = -1.25$ corresponding of a wake deficit of 80% of the external flow. Conversely, in the case of strong advection and moderate wake deficit, the flow is convectively unstable, with perturbations growing in space as they are simultaneously amplified and advected away. While Delbende *et al.* (1998) used the linear impulse response method, Olendraru *et al.* (1999); Olendraru & Sellier (2002) used the pinch-point diagnostic for the transition from convective to absolute instability and carried out a spatial stability analysis computing the spatial growth rate as a function of the forcing frequency and the azimuthal wavenumber. In convectively unstable situations, they found that the helical symmetry of the most amplified mode changed drastically, when spanning the forcing frequency, ω_f . This suggests that the mode-selection in convectively unstable swirling flows strongly depends on the frequency spectrum of the

incoming perturbations.

Delbende & Rossi (2005) more recently also investigated the nonlinear response to the harmonic forcing of modes on an artificially maintained parallel swirling jet flow. They found that for low swirl ($q \leq 0.6$), the flow saturates as an array of dipoles which cause an increase of the vortex core size. At intermediate values, $q \sim 0.8$, the vortex breaks in an array of equal sign vortices and for high swirl $q \geq 1$ the increase of the instantaneous swirl induced by the accelerated diffusion of the axial core velocity favors the flow relaminarization.

Although these results strictly apply for the parallel Batchelor vortex, they are of fundamental importance for real non-parallel flows, because it is known that the global stability features are related to the local stability properties, see Huerre & Monkewitz (1990) and Chomaz (2005) for a comprehensive discussion. In the non-parallel framework, Heaton *et al.* (2009) carried out a global analysis, considering the base flow resulting from the imposition of a 90% wake deficit at inlet, i.e. $\alpha(0) = 0.9$. As the wake deficit is progressively recovered downstream, the flow turns convectively unstable, but for the chosen inlet parameters and Reynolds number, the flow exhibits a sufficiently extended absolutely unstable region to become globally unstable. The frequency of the most unstable global mode is indeed observed to match the absolute frequency prevailing at inlet, as long as the domain is short enough for an accurate resolution of the resulting eigenvalue problem. However, typical trailing vortices have a rather strong axial velocity component, as experimentally measured by Devenport *et al.* (1996) and more recently by Del Pino *et al.* (2011), with wake deficits typically less than 80%. These flows are locally convectively unstable everywhere and behave as noise amplifiers. In this work the mode selection in an harmonically forced non-parallel Batchelor vortex is considered, and the capability to predict the amplitude and spatial shape of the response by linear analyses is investigated.

The objective of this work is to analyse the mode selection in a non-parallel spatially evolving Batchelor vortex subjected to harmonic in time but random in space perturbations. After the introduction of the prototype trailing-vortex used throughout the work in section 2.2, the observation of the non-linear response to an harmonic inlet forcing computed by three-dimensional (3D) direct numerical simulation (DNS) is briefly reported in section 2.3. In section 2.4, the linear flow response to boundary forcing is investigated using the WKB (Wentzel, Krammers, Brillouin) asymptotic analysis in the framework of weakly-non parallel flow. The asymptotic results are then compared to the results of a global analysis, which relaxes the weakly non-parallel assumption. The optimal inlet forcing, which maximize the linear energy amplification of the response, is thus determined through global resolvent. In section 2.5, the flow response to a volume forcing is computed using both the global resolvent approach and a generalized WKB analysis. The effect of nonlinearity on the response is investigated in section 2.6 in the case of inlet forcing. The nonlinear gains are computed through DNS as a function of the forcing frequency and for increasing forcing amplitudes. The mode selection observed in the DNS is compared to the one of the linear optimal response. Finally, conclusions are outlined.

Several sets of equations, all derived from Navier-Stokes equations, are used in this study to conduct the different steps of the analysis, which all require adequate numerical methods.

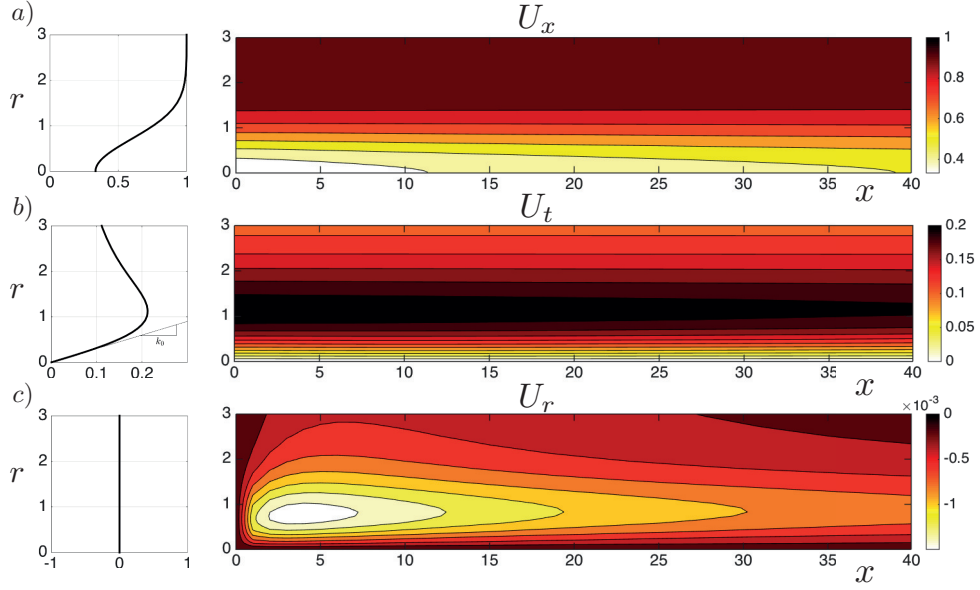


Figure 2.1: (a) Streamwise, (b) azimuthal and (c) radial velocity components of the axisymmetric Navier-Stokes steady solution obtained by setting at the inlet a parallel Batchelor profile with $\alpha(0) = 0.667$, $\kappa(0) = 0.333$, which is depicted in the left column.

We have chosen to describe briefly these methods when the corresponding equations are progressively introduced.

2.2 Trailing-vortex prototype

In the present work a typical trailing vortex is considered and used as test-case. This prototype flow satisfies the steady axisymmetric Navier-Stokes equations

$$\begin{aligned}
 \mathbf{U}_b \cdot \nabla \mathbf{U}_b &= -\nabla P_b + \frac{1}{Re} \Delta \mathbf{U}_b, \\
 \nabla \cdot \mathbf{U}_b &= 0, \\
 \mathbf{U}_b &= \mathbf{U}_0 \quad \text{on} \quad \Gamma_i.
 \end{aligned} \tag{2.5}$$

A parallel Batchelor profile, \mathbf{U}_0 , in the α, δ formulation is imposed at the inlet, Γ_i , as a Dirichlet boundary condition with $\alpha = 0.667$, $\kappa = 0.333$. A free-stress boundary condition is imposed at the outlet, Γ_o and lateral boundary, Γ_l , while symmetry conditions are imposed on the axis. The Reynolds number is defined using as reference length the size of the vortex core at the inlet and is equal to $Re_H = 1000$ ($Re_D = 667$). Taking advantage of the local stability of Batchelor vortices with respect to $m = 0$ axisymmetric perturbations, this steady solution is obtained by time-marching an axisymmetric simulation with the spectral element code Nek5000 (Fischer *et al.* (2008)). The flow is considered steady when the L^2 -norm of the difference between two consecutive solutions is less than 10^{-12} . The computational domain

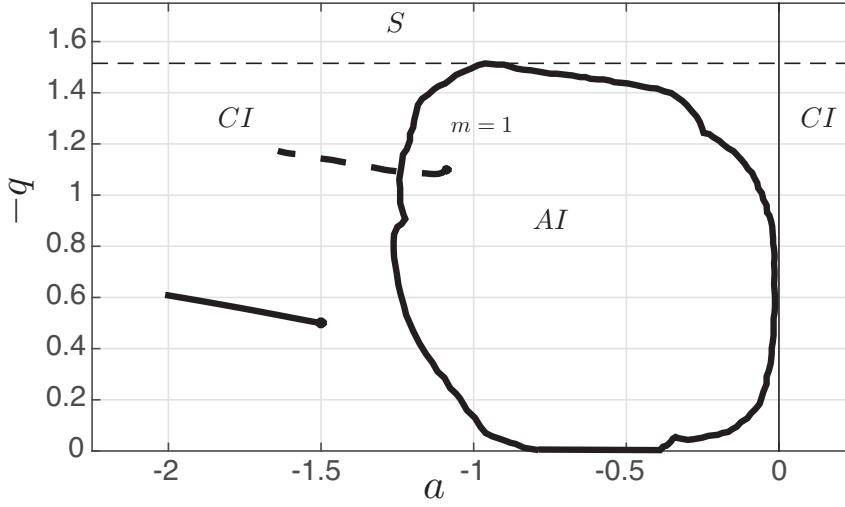


Figure 2.2: Figure adapted from Delbende *et al.* (1998). The regions of absolute (AI) and convective (CI) instability are reported in the (a, q) parameter space for the Reynolds number $Re_D = 667$. The path in solid-line depicts the local properties of non-parallel trailing vortex studied in this work. The dashed line identifies the globally unstable non-parallel Batchelor vortex investigated in Heaton *et al.* (2009).

is $0 \leq x \leq 40$ and $0 \leq r \leq 10$ (see appendix 2.9 for discussion of the influence of the radial extension of the domain). The resulting steady-flow, \mathbf{U}_b , is reported in figure 4.2 as (a) axial (b) azimuthal and (c) radial velocity components, showing the gradual recover of the wake deficit, as one proceeds downstream, and the diffusion of the vortical core. The radial velocity is significantly smaller than the other two velocity components thus validating the boundary layer assumptions adopted by Batchelor. This is due to the fact that the streamwise evolution of a trailing vortex is governed by viscous effects, which operate at a slower time scale with respect to advection. The present flow can be qualified as weakly non-parallel, meaning that at first order the flow field $\mathbf{U}(x, r)$ can be seen as a sequence of parallel Batchelor vortices. Hence, the streamwise evolution of the trailing vortex can be represented as a path in the (a, q) plane, starting at $a = -1.5$ and $q = -0.5$, see figure 2.2.

The present choice of prototype trailing vortex has been motivated by the fact that for higher or lower swirl numbers the flow is close to neutral stability conditions and perturbations are less amplified. With this choice of negative but large amplitude advection parameter at the inlet, the locus of the local base-flow characteristic parameters in the (a, q) plane does not penetrate into the absolutely unstable region. This flow is therefore globally stable and behaves as a noise amplifier. The stability of the base-flow has been checked numerically using the discretization method discussed in section 2.4, and the least stable eigenvalue is found to be $\omega = 0.5609 - 0.202i$ corresponding to the azimuthal wavenumber $m = 1$. As a comparison, the dotted path intersecting the region of absolute instability in figure 2.2 corresponds to the globally unstable non-parallel swirling flow considered by Heaton *et al.* (2009).

2.3 Observation of the non-linear response to harmonic inlet forcing

In this section the non-linear response of a trailing vortex to an harmonic forcing is investigated by full 3D DNS. Specifically, an harmonic inlet forcing acting on the three velocity components has been considered. The forcing adopted is chosen random in space in order to better enlighten the role of the forcing frequency on the change of the structure of the response.

The unsteady Navier-Stokes equations

$$\begin{aligned} \frac{\partial \mathbf{U}}{\partial t} + \mathbf{U} \cdot \nabla \mathbf{U} &= -\nabla P + \frac{1}{Re} \Delta \mathbf{U}, \\ \nabla \cdot \mathbf{U} &= 0, \end{aligned} \quad (2.6)$$

are solved in a cylindrical domain of radius $r_{max} = 10$ and length $x_{max} = 40$, complemented with free stress boundary conditions on all domain boundaries except at the inlet Γ_i , where an unsteady Dirichlet boundary condition fluctuating around the base flow inlet profile is imposed

$$\mathbf{U} = \mathbf{U}_0 + a_\zeta \boldsymbol{\zeta} \cos(\omega_f t) \quad \text{on } \Gamma_i. \quad (2.7)$$

A random inlet field concentrated in the region $r \leq 5$ is generated off-line before the first time step and saved in memory invoking the MATLAB function *rand* which returns pseudorandom numbers uniformly distributed between 0 and 1. These fields are then loaded in Nek5000 and projected in the space of continuous functions, obtaining the fields $\boldsymbol{\zeta} = (\zeta_x(y, z), \zeta_y(y, z), \zeta_z(y, z))$. Three forcing amplitude have been considered, $a_\zeta = 0.01, 0.05$ and 0.1 . The Navier-Stokes equations are solved in Cartesian coordinates using Nek5000 spectral elements solver, while the time-discretization is ensured using a Crank-Nicolson scheme. Convergence is attained with 2.2 million degrees of freedom and the code is parallelized. The integration time was equal is 400 time units, sufficiently large to capture the flow dynamics of the permanent regime. The time evolution of the energy of the flow was used to assess that a periodic permanent regime was indeed reached.

The forcing frequency ω_f ranges from 0.1 to 5 and the spatial structure of the response is monitored by observing its azimuthal symmetries. Figure (2.3) reports isosurfaces of axial vorticity at the streamwise section $x = 30$ for different values of the forcing frequency. At low frequency, low azimuthal wavenumbers are the most amplified, while at higher frequency, higher wavenumbers are excited by the forcing. For instance, at frequency $\omega_f = 0.50$, a single spiral mode is excited, while for $\omega_f = 1.00$ the response is dominated by a double helical structure. When increasing further the forcing frequency, triple ($\omega_f = 1.80$), quadruple ($\omega_f = 2.40$) or higher helical structures appear. In this swirling flow, the spatial shape of the response is found to be very sensitive to the forcing frequency, calling for a detailed understanding of the mode selection mechanism.

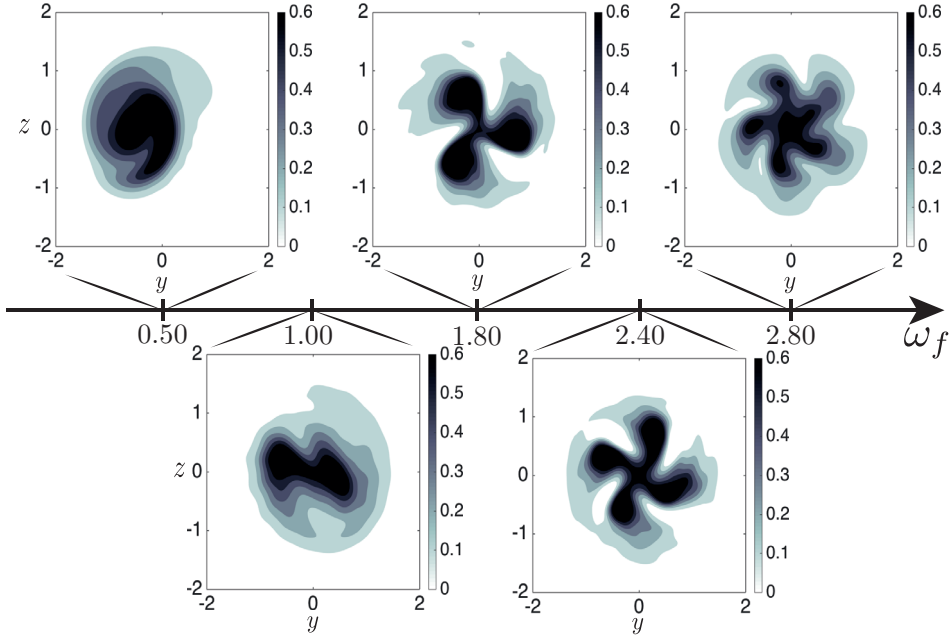


Figure 2.3: Isocontours of the axial vorticity at the streamwise section $x = 30$ for different forcing frequencies. The amplitude of the forcing was set equal to $a_\zeta = 0.01$.

2.4 Linear response to harmonic inlet forcing

In a parallel convectively unstable flow, the spatial stability branches fully describe the response to an harmonic forcing at any point of the domain, see Huerre & Rossi (1998). The spatial analysis provides the amplification in space, $-k_i$, and the axial wavenumber, k_r , of a downstream propagating perturbation with frequency ω_f . In this framework, k is the complex eigenvalue of the polynomial eigenvalue problem obtained from the linearized stability equations after the introduction of a normal mode expansion $\exp(i(kx + m\theta - \omega_f t))$. Following Jungo *et al.* (2013), the corresponding stability equations in primitive variables around a parallel base flow $U_\theta(r), U_x(r)$ are:

$$\begin{aligned}
 -i\omega_f u_r + \Gamma_{m,k} u_r - 2\Omega u_\theta &= -\frac{\partial p}{\partial r} + \frac{1}{Re} \left[\left(\Delta_{m,k} - \frac{1}{r^2} \right) u_r - \frac{2im u_\theta}{r^2} \right], \\
 -i\omega_f u_\theta + \Gamma_{m,k} u_\theta + u_r \frac{\partial U_\theta}{\partial r} + \Omega u_r &= -\frac{imp}{r} + \frac{1}{Re} \left[\left(\Delta_{m,k} - \frac{1}{r^2} \right) u_\theta + \frac{2im u_r}{r^2} \right], \\
 -i\omega_f u_x + \Gamma_{m,k} u_x + u_r \frac{\partial U_x}{\partial r} &= -ikp + \frac{1}{Re} \Delta_{m,k} u_x, \\
 \frac{1}{r} \frac{\partial(r u_r)}{\partial r} + \frac{im u_\theta}{r} + ik u_x &= 0,
 \end{aligned} \tag{2.8}$$

where $\Omega = U_\theta/r$, $\Gamma_{m,k} = im\Omega + ikU_x$ and $\Delta_{m,k} = \frac{1}{r} \frac{\partial}{\partial r} \left(r \frac{\partial}{\partial r} \right) - \frac{m^2}{r^2} - k^2$. Homogeneous Neumann conditions are imposed at r_{max} , as well as regularity conditions on the axis, see Batchelor &

Gill (1962):

$$\begin{aligned}
 u_r = u_\theta = \frac{\partial u_x}{\partial r} &= 0 \text{ for } m=0 \\
 \frac{\partial u_r}{\partial r} = \frac{\partial u_\theta}{\partial r} = u_x &= 0 \text{ for } |m| = 1 \\
 u_r = u_\theta = u_x &= 0 \text{ for } |m| > 1,
 \end{aligned} \tag{2.9}$$

where $m = 1$ is the only positive azimuthal mode to admit a displacement from the centerline, and is called the displacement mode. The discretization is ensured through a Chebyshev spectral collocation technique including an algebraic mapping of the domain, as detailed in Viola *et al.* (2014), where the influence of r_{max} is discussed in appendix 2.9. To capture the amplified k^+ spatial branches, the Gaster transformation of the temporal stability analysis is used to obtain a target for the complex wavenumber k , as explained in detail in Iungo *et al.* (2013).

Figure 2.4 reports the spatial growth rates as a function of the frequency ω_f , and each branch corresponds to a different azimuthal wavenumber, m . Figure 2.4(a) pertains to the flow prevailing at the inlet section, while (b) considers the flow at the section $x = 30$. Observe that, in both cases, a large number of helical modes have positive spatial growth-rates, as a consequence of the generalized centrifugal instability (Ludwig (1962); Leibovich & Stewartson (1983)) which selects only the angular pitch of the unstable modes m/k . However, a detailed inspection shows that the local stability properties differ at both streamwise locations. While at the inlet section the most amplified mode is the single helical mode, $m = 1$, further downstream in the wake the double helix $m = 2$ becomes the most amplified mode. In addition, the frequency corresponding to the maximum amplification for a given mode is seen to be slightly shifted as one proceeds downstream.

2.4.1 WKB analysis

In order to take into account the weak non-parallelism of the baseflow the WKB formalism introduced by Gaster *et al.* (1985) and Huerre & Rossi (1998) for a spatial mixing layer has been here extended to the case of swirling flows with axial velocity. A fast, x , and a slow, $X = \epsilon x$, streamwise scale are introduced, where the baseflow depends only on X , and ϵ is a measure of the weak non-parallelism. The global response to a boundary forcing then takes the following modulated wave form:

$$\mathbf{q}(r, \theta, X; t) \sim A(X) \hat{\mathbf{q}}(r, X) \exp \left[i \left(\frac{1}{\epsilon} \int_0^X k(X', \omega_f) dX' + m\theta - \omega_f t \right) \right], \tag{2.10}$$

where $\hat{\mathbf{q}} = (\hat{\mathbf{u}}, \hat{p})$ is a column vector. $k(X', \omega_f)$ is the local complex wavenumber at section X' and frequency ω_f , and $A(X)$ is the envelope function which smoothly connects the slices of parallel spatial analyses. The local eigenfunction $\hat{\mathbf{q}}(r, X)$ is normalized by imposing $\int_0^\infty \hat{\mathbf{q}}^H \cdot \hat{\mathbf{q}} r dr = 1$, where $(\cdot)^H$ is the tranconjugate, and the phase angle is set to zero at a given radial position. A systematic asymptotic expansion, including a compatibility condition, de-

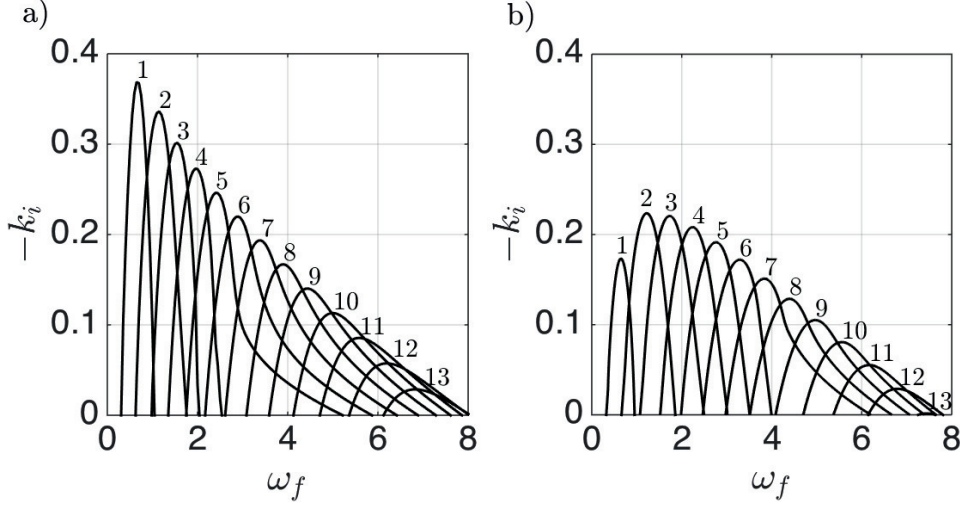


Figure 2.4: Spatial growth rate, $-k_i$ versus frequency ω_f , of the locally unstable helical perturbations. In (a) the results of the local spatial analysis at the inlet, while in (b) at the streamwise section $x = 30$.

tailed in appendix 2.8, shows that the local spatial analysis (2.8) is recovered at zero order in ϵ while an amplitude equation (8.43) is obtained at order ϵ :

$$M(X) \frac{dA(X)}{dX} + N(X)A(X) = 0, \quad (2.11)$$

where the operators $M(X)$ and $N(X)$ are defined in the Appendix 2.8.

The solution is $A(X) = A_0 \exp\left(-\int_0^X \frac{N(X')}{M(X')} dX'\right)$. Setting the amplitude at the inlet to one $A(0) = 1$, this yields the response associated to forcing at the inlet with the local normalized direct mode, i.e.:

$$\mathbf{f}(r, 0) = \hat{\mathbf{u}}(r, 0) \exp(i(m\theta - \omega_f t)). \quad (2.12)$$

The spatial branches, $k(X, \omega_f)$, and the corresponding eigenfunctions, $\hat{\mathbf{q}}$, are obtained by solving the local spatial analysis problem.

The kinetic energy gain of the response respect to the forcing is defined as:

$$G_{bnd}^2(m, \omega) = \frac{\|\hat{\mathbf{q}}\|_E^2}{\|\hat{\mathbf{f}}\|_f^2} = \frac{\int_0^x A^H(x')A(x') \left(\int_0^\infty \hat{\mathbf{u}}^H(r, x') \hat{\mathbf{u}}(r, x') r dr \right) \left(e^{\int_0^{x'} -2k_i(x'') dx''} \right) dx'}{\int_0^\infty \hat{\mathbf{u}}^H(r, 0) \hat{\mathbf{u}}(r, 0) r dr}. \quad (2.13)$$

The global gains of the response excited by forcing at the inlet at each frequency and azimuthal wavenumber with the local eigenmode, are reported in figure 2.5. Full lines correspond to the gains obtained at first order (eq. (2.13)), i.e. by solving both the weakly non parallel linear spatial stability analysis and the amplitude equation. In contrast, the dashed line report the results obtained by setting the amplitude $A(X) = 1$. These zero-order solutions are seen to

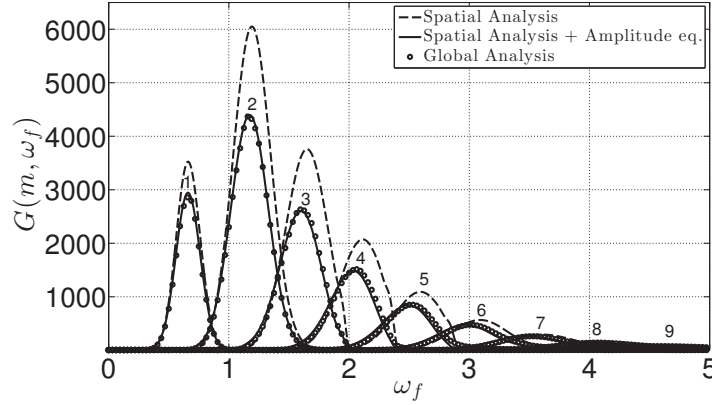


Figure 2.5: Global gains of the responses excited by forcing at the inlet with the local direct mode. The solid black lines depict the result of WKB analysis, conversely dashed lines correspond to the gains obtained by a zero order analysis, i.e. imposing the amplitude unitary. The results obtained through global resolvent are reported with circle marks.

differ significantly with respect to the first-order results at low frequency.

In order to verify the accuracy of the WKB analysis and the ability of the amplitude equation to properly take into account the non-parallelism of the flow, the same problem can be tackled in a global framework using the resolvent operator, i.e. dealing with the flow as fully non-parallel.

2.4.2 Global resolvent

Let us consider the linearized Navier-Stokes equations on the axisymmetric steady base-flow, \mathbf{U}_b subjected to an harmonic forcing with frequency ω_f imposed at the inlet through a non-homogenous Dirichlet boundary condition. The linear response, \mathbf{u} is thus governed by:

$$\begin{aligned} \frac{\partial \mathbf{u}}{\partial t} + \mathbf{U}_b \cdot \nabla \mathbf{u} + \mathbf{u} \cdot \nabla \mathbf{U}_b &= -\nabla p + \frac{1}{Re} \nabla^2 \mathbf{u}, \\ \nabla \cdot \mathbf{u} &= 0, \\ \mathbf{u} &= \mathbf{f} \quad \text{on } \Gamma_i, \\ \frac{\partial \mathbf{u}}{\partial x} &= ik_o \mathbf{u} \quad \text{on } \Gamma_o. \end{aligned} \tag{2.14}$$

Free-stress boundary conditions are imposed on the lateral boundary Γ_l . In order to mimic an infinite vortex flow, a non-homogenous Neumann condition is imposed at the outlet as in equation (2.14), where k_o is the local axial wavenumber according to local spatial analysis. This boundary condition is similar to the one adopted by Ehrenstein & Gallaire (2005) in the global analysis of a boundary layer flow. In situations like the present one where the flow is still convectively unstable at the outlet section, the imposition of a free-stress boundary condition at the outlet is not appropriate.

As usual in the case of steady and axisymmetric base-flows, an expansion of the perturbation

in azimuthal modes is considered:

$$\begin{aligned}\mathbf{f}(x, r, \theta, t) &= \hat{\mathbf{f}}(0, r) e^{i(m\theta - \omega t)}, \\ (\mathbf{u}, p)(x, r, \theta, t) &= (\hat{\mathbf{u}}, \hat{p})(x, r) e^{i(m\theta - \omega t)},\end{aligned}\tag{2.15}$$

where $m \in \mathbb{Z}$ is the azimuthal wavenumber and $\omega \in \mathbb{R}$ is the frequency.

Equations (2.14) together with modal expansion (3.36) are discretized using a staggered pseudospectral Chebyshev-Chebyshev collocation method. The three velocity components are defined at the Gauss-Lobatto-Chebyshev (GLC) nodes, whereas the pressure is staggered on a different grid, which is generated with Gauss-Chebyshev nodes (GC). Specifically, the momentum equation is collocated at the GLC nodes, and the pressure is interpolated from GC points to GLC points. Conversely the continuity equation is enforced on the GC grid and the velocity components are interpolated from the GLC grid. Consequently the two grids are mapped in the physical domain $0 \leq r \leq r_{max} = 10$ and $0 \leq x \leq x_{max} = 30$, where the equality holds only for the velocity grid, since the GC grid is not defined on the boundaries. In the radial direction the algebraic mapping with domain truncation is used $r = L(1 + s)/(s_{max} - s)$ where s are GLC and GC nodes, L is a mapping parameter to cluster the points close to the origin and set equal to 3, and s_{max} is defined as $(2L + R_{max})/R_{max}$, (see Canuto *et al.* (2007)). In the axial direction the physical space is mapped with a linear mapping $x = (1 + s)x_{max}/2$. $P_n - P_{n-2}$ formulation has been used in order to avoid spurious pressure modes by simply setting $N_{GC} = N_{GLC} - 2$, see Canuto *et al.* (2007) for a comprehensive discussion. The code used is a two-dimensional generalization of the one-dimensional code documented in Malik *et al.* (1985) and Khorrami (1991) used for local stability analysis in cylindrical coordinates. In the present work $N_x = 80$ and $N_r = 40$ points are used in the axial and radial direction respectively, having shown to provide the desired convergence of the amplification factors.

Introducing the state vector $\hat{\mathbf{q}} = (\hat{\mathbf{u}}, \hat{p})$, the linearized system of equations with embedded boundary conditions reads:

$$-i\omega_f \mathbf{B} \hat{\mathbf{q}} = \mathbf{L} \hat{\mathbf{q}} + \mathbf{B}_f \hat{\mathbf{f}},\tag{2.16}$$

where \mathbf{B} is the mass matrix, \mathbf{L} is the linearized Navier-Stokes operator and \mathbf{B}_f is a so-called prolongation operator (Garnaud *et al.* (2013); Boujo & Gallaire (2014)) that maps the boundary forcing onto the interior degrees of freedom. The response to a given forcing $\hat{\mathbf{f}}(x = 0, r)$ pushing at the inlet harmonically with frequency ω_f is directly obtained by solving the linear system in equation (2.16). Note that in principle the matrix $(-i\omega_f \mathbf{B} - \mathbf{L})$ can be inverted as long as ω_f is not an eigenvalue of the non-forced system.

As for the WKB, we define the energy gain, $G_{bnd}(m, \omega_f)$, as the measure of the amplification of the perturbation due to an externally applied boundary forcing:

$$G_{bnd}^2(m, \omega_f) = \frac{\int_{\Omega} |\hat{\mathbf{u}}|^2 r dr dx}{\int_{\Gamma_i} |\hat{\mathbf{f}}|^2 r dr} = \frac{\|(\mathbf{L} + i\omega_f \mathbf{B})^{-1} \mathbf{B}_f \hat{\mathbf{f}}\|_E^2}{\|\hat{\mathbf{f}}\|_f^2},\tag{2.17}$$

2.4. Linear response to harmonic inlet forcing

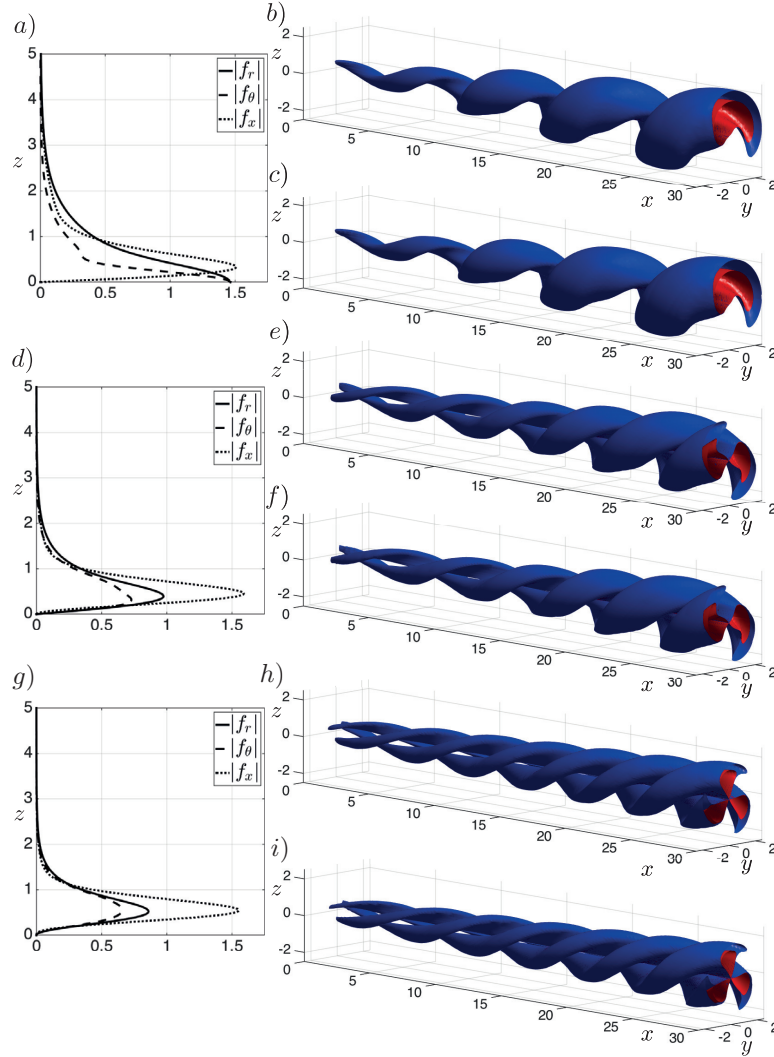


Figure 2.6: Three components of the direct mode forcing at the inlet (a) and associated response computed with WKB analysis (b) and global resolvent (c) at forcing frequencies $\omega_f = 0.65$. In (d-e-f) and (g-h-i) the same quantities are reported for the frequencies $\omega_f = 1.15$ and $\omega_f = 1.6$ respectively.

where $(\mathbf{L} + i\omega_f \mathbf{B})^{-1}$ is known as the resolvent. The calculation of the energy gains requires one-dimensional and two-dimensional numerical integrals, here computed with Clenshaw-Curtis quadrature formula. In order to achieve a better accuracy the quadrature weights are computed for the particular integration weight which depends on the mappings used, following the method presented in Sommariva (2013). For a comprehensive discussion on the accuracy of Clenshaw-Curtis quadrature compared to Gaussian quadrature we refer to Trefethen (2008).

The global energy gains, as computed from the global resolvent analysis, to harmonic forcing at the inlet with the local direct modes, are superimposed on the results of the WKB analysis with circle markers in figure 2.5. The agreement is stunning, confirming the excellent accuracy of WKB analysis to study weakly non-parallel flows. In contrast, the zero-order

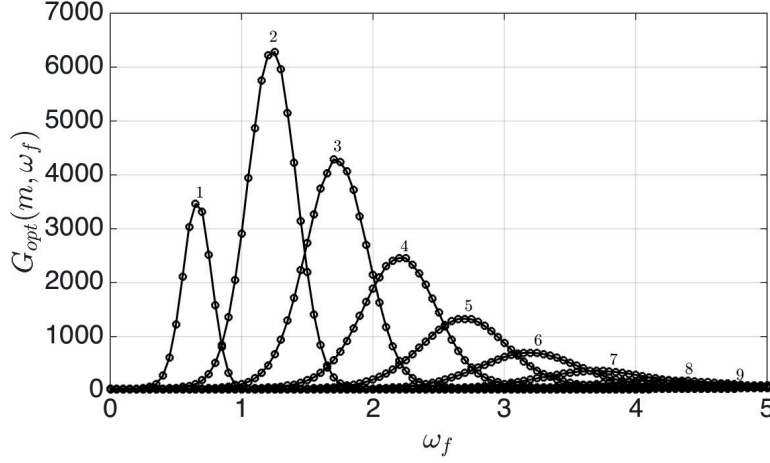


Figure 2.7: Optimal gains for boundary forcing as a function of the forcing frequency ω_f . Each branch corresponds to a different azimuthal wavenumber.

approximation overestimates the global gains, since the amplitude $A(x)$ is in general less than unity, as a consequence of the streamwise evolution of the local eigenmode. This agreement also represents a convincing validation of the local and global numerical tools. Also the axial wavelength of the response is very well captured by WKB analysis, as shown in figure 2.6 where isosurfaces of the axial vorticity of the responses calculated with WKB and global analysis are reported in the right column, while the corresponding inlet forcings are depicted in the left column. In figure 2.6 (a-b-c) the forcing frequency $\omega_f = 0.65$ strongly excites a single-helical mode. The double-helical mode reported in (d-e-f) emerges at frequency $\omega_f = 1.15$. In the case of higher forcing frequency higher wavenumber modes arise, as the three-helical structure resulting for $\omega_f = 1.6$. In a very similar way to the first DNS observations of section 2.3, different azimuthal wavenumbers, m , yield large responses when spanning ω_f . Figure 2.6 also clearly shows that the helical structures are counterwinding. Considering their time dependence, one can deduce their co-rotation. These results perfectly match the literature of parallel swirling wakes (Delbende *et al.* (1998); Gallaire & Chomaz (2003)).

It is interesting to observe that, due to the azimuthal symmetry, the displacement mode $m = 1$ is the only one to have a non-zero forcing at the centerline, see figure 2.6(a). This indicates that the displacement mode is the most sensitive one to perturbations forcing the flow at the vortex center.

2.4.3 Optimal forcing

In principle, by forcing randomly in space in the numerical experiment presented in section 2.3, all the competing modes are excited. Thus, the dominant helical mode which resonates at a given frequency, see figure 2.3, is expected to correspond to the most amplified one. When the amplitude of the perturbation is small, the mode having the highest energy amplification can be determined via the analysis of the linear optimal response to an harmonic forcing.

2.4. Linear response to harmonic inlet forcing

Given the forcing frequency, ω_f , and the azimuthal wavenumber, m , the optimal forcing corresponding to the maximum energy amplification is defined in discrete form as:

$$G_{opt}^2(\omega_f, m) = \max_{\hat{\mathbf{f}}} \frac{\|\hat{\mathbf{q}}\|_E^2}{\|\hat{\mathbf{f}}\|_f^2} = \max_{\hat{\mathbf{f}}} \frac{\|(\mathbf{L} + i\omega_f \mathbf{B})^{-1} \mathbf{B}_f \hat{\mathbf{f}}\|_E^2}{\|\hat{\mathbf{f}}\|_f^2}, \quad (2.18)$$

As explained in detail in Marquet & Sipp (2010) and Garnaud *et al.* (2013) the optimization defined in equation (3.50) is equivalent to the following eigenvalue problem, where $G_{opt}^2(\omega_f)$ corresponds to the eigenvalue λ :

$$\mathbf{Q}_f^{-1} \mathbf{B}_f^H (\mathbf{L} + i\omega_f \mathbf{B})^{-H} \mathbf{Q}^H (\mathbf{L} + i\omega_f \mathbf{B})^{-1} \mathbf{B}_f \hat{\mathbf{f}} = \lambda \hat{\mathbf{f}}, \quad (2.19)$$

\mathbf{Q} and \mathbf{Q}_f are the weight matrices of the discretized energy norm and the norm of the forcing, respectively. The previous eigenvalue problem is solved using the UMFPACK library available in MATLAB.

In figure 2.7 the optimal gains, $G_{opt}(\omega_f, m)$, are shown as a function of the forcing frequency, where each branch corresponds to a different azimuthal wavenumber. The results are presented optimizing the amplification of the perturbation in the domain $0 \leq x \leq 30$. The high energy response observed is related to the strong non-normality of the damped operator \mathbf{L} . In fact, when the global modes are not self-adjoint the flow is usually extremely sensitive to forcing, and the energy gain is inversely proportional to the smallest value for which the pseudospectrum crosses the neutral axis, (Trefethen *et al.* (1993); Chomaz (2005)). Here, the optimal inlet forcing is seen to yield less than 20% more amplification for some frequency than using the eigenfunction at the inlet. This relatively weak net increase shows that in these instabilities, there is little potential for intense local non-normality effects (as lift-up or Orr mechanisms). The dominant non-normality of the global operator \mathbf{L} is the convective non-normality, which is the global counterpart of the local convective instability (Cossu & Chomaz (1997); Chomaz (2005); Marquet *et al.* (2009)). In fact, the spatial mode used as inlet forcing in figure 2.5 excites the most convectively unstable spatial branch which is the main contribution to the optimal response, since the other spatial branches are either damped or less unstable.

Spanning the forcing frequency, the spatial shape of the most amplified mode drastically changes. The largest energy gain occurs at a forcing frequency $\omega_f \approx 1.15$ and the associated mode is a double helix. However, when varying ω_f , the most amplified azimuthal mode increases from $m = 1$ to $m = 9$. Specifically, at lower ω_f , lower m are more amplified (see figure 2.13 left column for isocontours of the optimal responses at $x = 30$). Since the helical perturbations are convectively unstable in all the flow domain, they are continuously amplified while propagating. For this reason the maximum amplification of the perturbation is encountered at the outlet, after a continuous amplification throughout the domain.

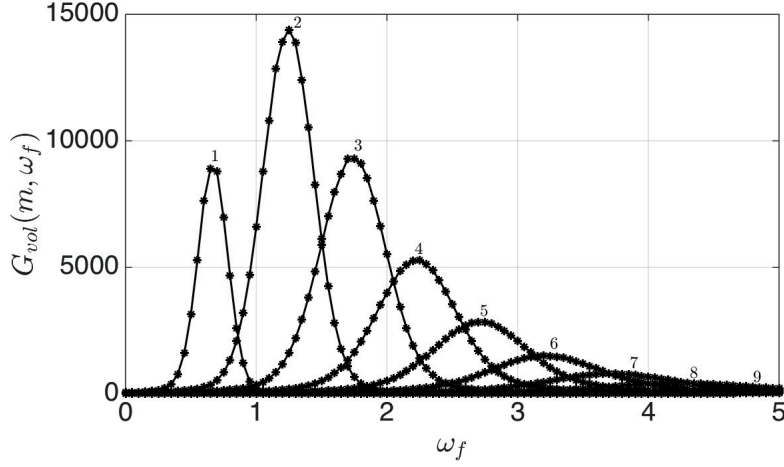


Figure 2.8: Optimal gains for volume forcing versus forcing frequency ω_f . Each branch corresponds to a different azimuthal wavenumber.

2.5 Linear response to harmonic body forcing

Rather than the response to a forcing acting at the inlet, the effect of a body forcing is now considered. As in the previous section the problem is assessed both in the global and the local framework.

2.5.1 Global resolvent

The linear response, \mathbf{u} , due to an harmonic body forcing, \mathbf{f} , acting on the axisymmetric base-flow \mathbf{U}_b is given by:

$$\begin{aligned}
 \frac{\partial \mathbf{u}}{\partial t} + \mathbf{U}_b \cdot \nabla \mathbf{u} + \mathbf{u} \cdot \nabla \mathbf{U}_b &= -\nabla p + \frac{1}{Re} \nabla^2 \mathbf{u} + \mathbf{f}, \\
 \nabla \cdot \mathbf{u} &= 0, \\
 \mathbf{u} &= \mathbf{0} \quad \text{on } \Gamma_i, \\
 \frac{\partial \mathbf{u}}{\partial x} &= ik_0 \mathbf{u} \quad \text{on } \Gamma_o,
 \end{aligned} \tag{2.20}$$

as in the case of inlet forcing, the local spatial growth rate is imposed as inhomogeneous Neumann conditions in order to better mimic the amplification of the perturbation at the outlet. A normal mode expansion is used similar to equation (3.36). However, the energy gain is now defined as the ratio among the kinetic energy of the response and of the forcing integrated in the domain:

$$G_{vol}^2(m, \omega_f) = \frac{\int_{\Omega} |\hat{\mathbf{u}}|^2 r dr dx}{\int_{\Omega} |\hat{\mathbf{f}}|^2 r dr}. \tag{2.21}$$

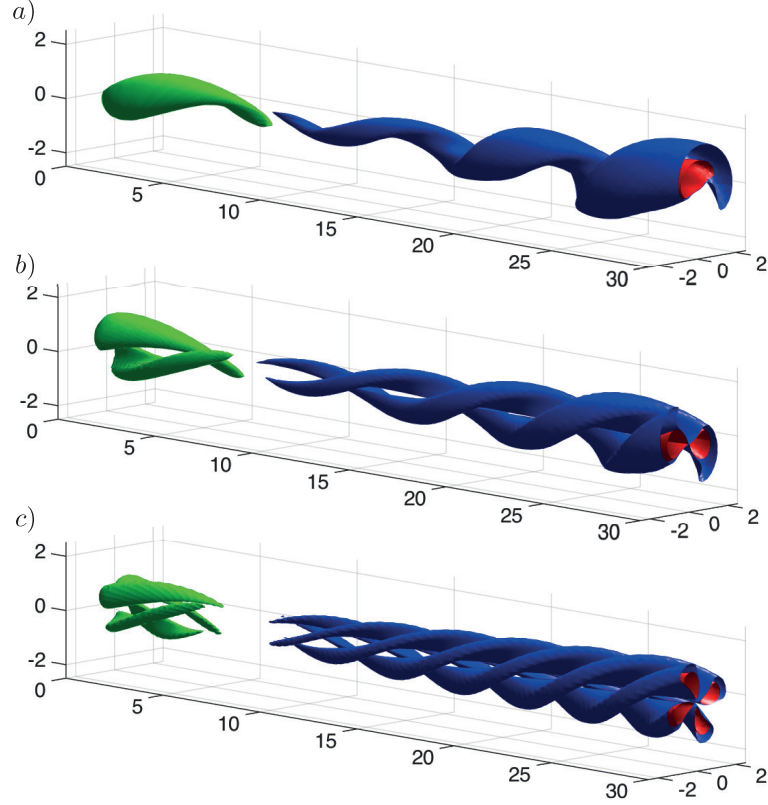


Figure 2.9: Isosurfaces of the axial vorticity of the optimal volume forcings (green) and the associated responses (blue and red) for different values of ω_f : 0.65 (a), 1.25 (b) and 2.20 (c).

In a similar fashion to inlet forcing, the optimization of the body forcing yields to the eigenvalue problem (3.51), where now Q_f is the weight matrix of the energy norm of the forcing in the volume, and the prolongation operator is non-null in correspondence of all the internal nodes. And the eigenmode $\hat{\mathbf{f}}$ associated with the largest eigenvalue corresponds to the optimal volume forcing.

Figure 2.8 shows the energy gain when forcing at each ω_f with the optimal body forcing. The domain length is equal to $x_{max} = 30$, and each branch refers to a different azimuthal wavenumber. As in the case of inlet forcing, the variation of the forcing frequency results in a different azimuthal wavenumber mode selection. Due to the non-normality of the system, the response is strongly amplified, where the maximum gain corresponds to the double-helical mode at $\omega_f = 1.20$. However, it should be reminded that these very high values of the amplification factors pertain to a linear stability analysis where nonlinear saturation mechanisms are not at play.

Isosurfaces of the axial vorticity of typical optimal forcings are reported in figure 2.9, together with the corresponding responses. In (a) at a forcing frequency $\omega_f = 0.65$, the most amplified mode is $m = 1$, while at (b) $\omega_f = 1.25$ and (c) $\omega_f = 2.20$ the most amplified modes are $m = 2$ and $m = 4$ respectively. The forcing is located close to the inlet, in order to excite the mode,

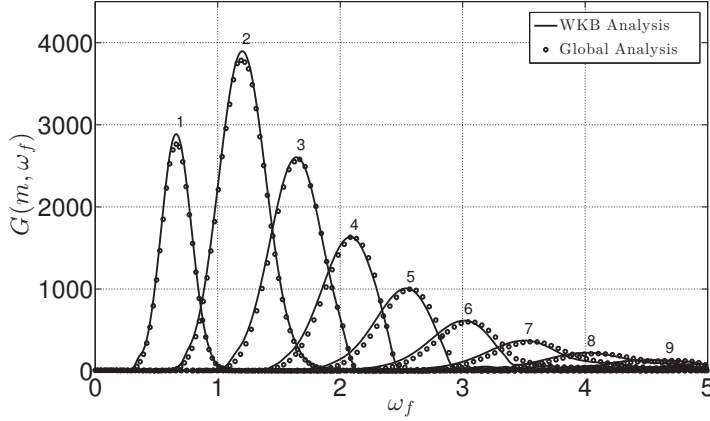


Figure 2.10: Global gains of the reponses excited by a given volume forcing versus forcing frequency. The solid black lines depict the result of WKB analysis, conversely circle marks corresponds to the gains obtained by global resolvent.

which propagates and amplifies inside the domain, reaching the maximum amplification at the outlet. In the single-helix mode the optimal forcing is located at the vortex center. For this reason, similarly to the case of inlet forcing, the displacement mode is more sensitive to disturbances forcing at the centerline.

2.5.2 WKB analysis for volume forcing

The global resolvent with a generic body forcing, \mathbf{f} , can be approximated by a generalized WKB analysis, through the technique presented in Arratia & Gallaire (2013) and here outlined in appendix 2.8.1. The response to a body forcing of this type is considered:

$$\mathbf{f}(r, x) \sim \epsilon F(x) \hat{\mathbf{u}}(r, x) \exp \left[i \left(\int_0^x k(x') dx' + m\theta - \omega_f t \right) \right], \quad (2.22)$$

where $F(x)$ is the slowly-varying *amplitude* of the forcing. In this formulation the forcing term enters only at order ϵ , thus at order ϵ^0 the local spatial problem persists. As before the response is asymptotic to:

$$\mathbf{u}(r, x) \sim A(x) \hat{\mathbf{u}}(r, x) \exp \left[i \left(\int_0^x k(x') dx' + m\theta - \omega_f t \right) \right]. \quad (2.23)$$

Consequently, at first order a modified amplitude equation is retrieved:

$$M(X) \frac{dA(X)}{dX} + N(X)A(X) = H(X)F(X), \quad (2.24)$$

where $M(X)$ and $N(X)$ are the same operators as in the case of inlet forcing and $H(X)$ is a diagonal matrix with the scalar products among direct and adjoint modes, see appendix 2.8. Equation (2.24) is discretized in the streamwise direction using spectral methods and $A(X)$

is obtained by solving the subsequent linear system. For each given forcing frequency and azimuthal wavenumber, (ω_f, m) , the volume forcing is fixed once $F(x)$ is set. Note as the response to a generic forcing term $F(X)$ can be computed *online*, if the outcomes of the local spatial analysis were computed previously *offline*, since only linear systems with the size of the number of streamwise sections considered have to be solved. In other words the response can be calculated with a cheap and fast computation if the spatial growth rates, the direct modes together with the operators $M(X)$ and $N(X)$ are available.

As test case, figure 2.10 reports the gains corresponding to forcing in the volume with the global mode weighted with an arbitrary weight function $F(x) = \left[-\left(\frac{x}{5} - 1\right)^2 + 1 \right] \Pi\left(\frac{x-5}{10}\right)$, where $\Pi(x)$ is the rectangular function. The results are compared with the ones of global resolvent, where the expression (2.22) has been set as volume forcing: the WKB analysis correctly predicts the linear kinetic energy amplification in all the frequency band. The agreement is good also in terms of axial wavenumber of the responses, which are not reported for the sake of brevity.

2.6 Nonlinear response

The linear investigation carried out in the previous sections describes the flow response in the hypothesis of small amplitude forcing and response. However, the helical perturbations propagating in the trailing vortex grow exponentially in space according to their spatial growth rate, $-k_i(x)$. Hence, after a finite distance from the inlet, which depends on the frequency, the response is no longer small and nonlinearity starts to play. Thus, after having described the effect of nonparallelism in the response to forcing of a trailing vortex, we explore here the effect of nonlinearity, focusing on the case of inlet forcing.

2.6.1 Nonlinear gains

The 3D DNS presented in section 2.3 yields the nonlinear response, $\tilde{\mathbf{u}}$, which is here defined as the difference between the velocity and the base-flow $\tilde{\mathbf{u}}(t) = \mathbf{U}(t) - \mathbf{U}_b$. Similarly to the previous section we define the energy gain, $G_{DNS}(\omega_f; a_\zeta)$, as the ratio between the time-averaged energy of the perturbation and the one of the boundary forcing:

$$G_{DNS}^2(\omega_f; a_\zeta) = \frac{\overline{\int_{\Omega} \tilde{\mathbf{u}}^2 r dr dx}}{a_\zeta^2 \overline{\int_{\Gamma_i} \zeta^2 r dr}} \quad (2.25)$$

where the overline denotes time-averaging. In this case, the energy gain does not depend explicitly on the azimuthal wavenumber since no modal expansion is carried out in the DNS. In figure 2.11, the G_{DNS} , connected by a spline interpolation, are reported as a function of ω_f for the three forcing amplitudes $a_\zeta = 0.01, 0.05$ and 0.1 . In order to explore the nonlinear gain sensitivity to the inlet spatial random forcing, two additional DNSs have been carried out at $a_\zeta = 0.1$ using two other independently drawn random inlet forcing fields. The effects on G_{DNS} are seen in the inset of figure 2.11, where the mean value of G_{DNS} is reported, together

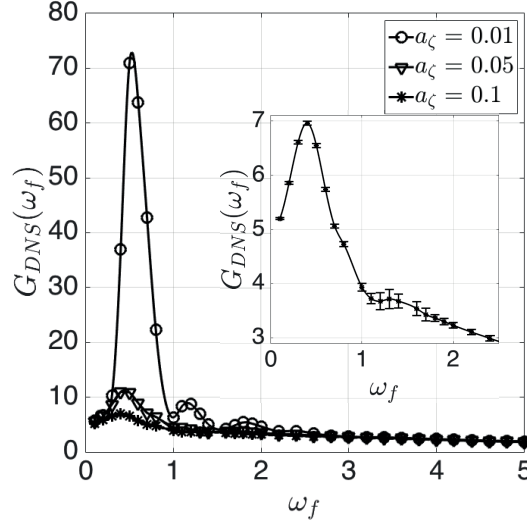


Figure 2.11: Non-linear energy gains of the responses excited by the random inlet forcing computed with DNS. Three values of the forcing amplitude have been considered: $a_\zeta = 0.01, 0.05$ and 0.1 . In the inset is reported in detail the G_{DNS} at $a_\zeta = 0.1$ averaged for three different realizations of inlet random forcing. The errorbars represent the standard deviation.

with the errorbars representing the standard deviations. The deviations remain very small among the three realizations, except in the medium frequency range, $\omega_f \approx 1.2$, where we will see in section 2.6.2 that a strong competition between the helical modes sets in.

When compared to figure 2.7, the G_{DNS} are two order of magnitude smaller than the linear gains. This might result from two possible effects: first, part of the forcing energy is lost as the random noise is projected on the optimal forcing. Second, nonlinearities become important and lead to saturation, in contrast to the linear prediction where the base flow distortion and mode interactions are neglected. The low-frequency peak is robustly observed in the forcing amplitude range considered: the energy of the response is seen to saturate and the gain therefore strongly depends on the forcing amplitude, decreasing when increasing a_ζ . In the low amplitude forcing case, $a_\zeta = 0.01$, the nonlinear gain exhibits two additional peaks in the energy gain ($\omega_f \approx 1.1$ and 1.8), which are associated to higher azimuthal wavenumbers (namely $m = 2$ and 3) in a similar fashion to the linear case, where higher wavenumbers are excited at higher frequencies. These peaks are no longer present when the forcing amplitude and, consequently, nonlinear effects, are increased. In the high frequency region, G_{DNS} does finally not depend significantly on the forcing amplitude, because the amplification is not strong enough to trigger significant nonlinear saturation processes. In summary, when a_ζ increases, the nonlinear saturation is more pronounced in the frequency band which is the most amplified according to linear analysis. The same phenomenon has been observed in Mantič-Lugo *et al.* (2015). Observe that the most non-linearly amplified frequency is $\omega_f \approx 0.50$ which correspond to a single helix perturbation, as will be discussed in figure 2.13.

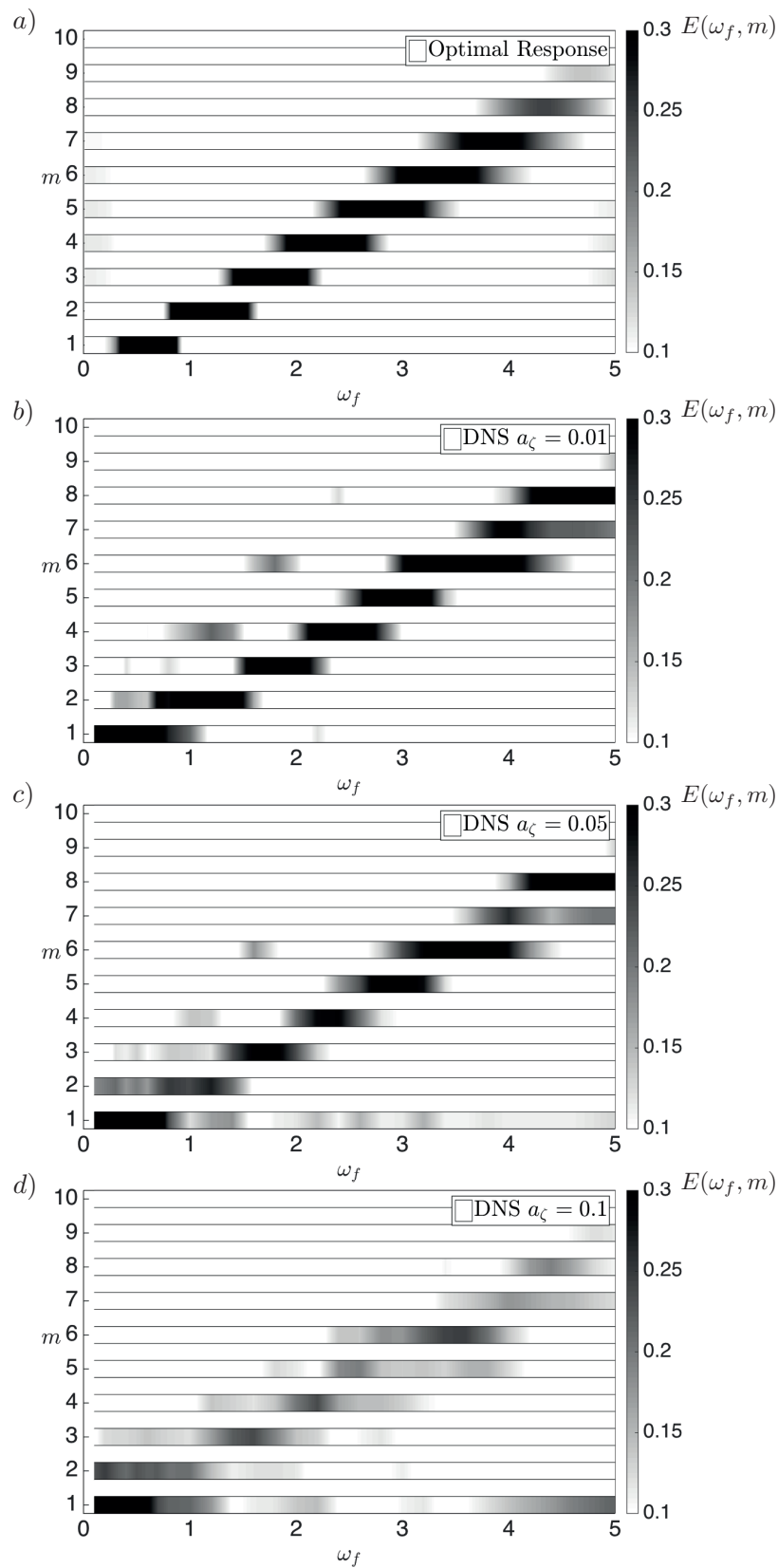


Figure 2.12: Linear (a) and nonlinear (b-c-d) mode selection. The horizontal bars depict in grey scale the normalized energies, $E(\omega_f, m)$, of the azimuthal Fourier components of the response. In (a) the $E(\omega_f, m)$ of the linear optimal response are shown. In the same fashion (b), (c) and (d) represent the normalized energies of the nonlinear responses computed through DNS for $a_\zeta = 0.01$ in (b), 0.05 in (c) and 0.1 in (d).

2.6.2 Nonlinear mode selection

Mode selection in swirling flows denotes the dominant helical symmetry of the response which resonates at a given forcing frequency. By forcing randomly in space in our numerical experiment, a competition is set-up between the modes which are convected and amplified in the wake until nonlinear saturation occurs. In order to assess whether the linear mode selection holds in the nonlinear case, the dominant azimuthal mode appearing in the full non-linear response has been computed as a function of the forcing frequency. Specifically, the axial vorticity at a certain downstream section, $\Omega_x(r, \theta, x = 30, t; \omega_f)$, has been decomposed into Fourier series. The obtained Fourier components have been integrated in the radial direction and time averaged, according to eq. (2.26):

$$C(\omega_f, m) = \frac{1}{2\pi} \overline{\int_0^{R_c} \int_{-\pi}^{\pi} \Omega_x(r, \theta, t; \omega_f) e^{im\theta} d\theta dr}, \quad (2.26)$$

where R_c is an arbitrary radial distance set here equal to 2, and the overline denotes time averaging. The modulus of $C(\omega_f, m)$ is a measure of the energy of the corresponding Fourier mode and $E(\omega_f, m) = |C(\omega_f, m)| / \sum_m |C(\omega_f, m)|$ are the normalized energies. Figure 2.12(a) depicts $E(\omega_f, m)$ in the case of linear optimal response, where the horizontal bars show the intensity of the various azimuthal components as a function of ω_f . The stair-like graph reflects that a change in forcing frequency induces a change in the most energetic mode, as already shown in figure 2.7.

In order to investigate the role of non-linearity on the mode selection, the normalized energies, $E(\omega_f, m)$ are reported in figure 2.12 for three forcing amplitudes: $a_\zeta = 0.01$ in (b), 0.05 in (c) and 0.1 in (d). It results that the dominant azimuthal Fourier mode resonating at frequency ω_f is maintained when the amplitude forcing increases and generally corresponds to the one of linear stability mode selection. As typical in non-linear systems, higher harmonics are excited, for instance at $\omega_f \approx 1.15$, where $m = 2$ is the most energetic component, $m = 4$ is also present. In the same way for $\omega_f \approx 2$ the second harmonic $m = 6$ is superimposed to the fundamental $m = 3$. However when increasing the amplitude forcing the mode selection is less sharp and the energy more distributed among the different harmonics.

In particular, the strong competition between neighboring helical modes, m and $m + 1$, generally leads to a forcing on the component $m = 1$ through the quadratic nonlinear term. Thus, the staircase structure of the optimal gains shown in figure 2.12(a), through the competition of consecutive modes, yields an intense $m = 1$ response at various frequencies, as is particularly visible in figure 2.12(b) and (c). As a consequence, due to the symmetry properties of the displacement mode, $m = 1$, the response meanders around the centerline in a frequency band which is much broader than the one of linear amplification of $m = 1$.

In figure 2.13 isocontours of the axial vorticity of the response are reported as a function of the forcing frequency, ω_f , and amplitude, a_ζ . Each row corresponds to a different forcing frequency: $\omega_f = 0.50, 1.20, 2.20, 3.60, 4.60$ and 5.00 . In the first column the axial vorticity of the linear optimal response is shown. While in the following columns, the nonlinear responses with respect to the mean flow $\mathbf{U}(t) - \bar{\mathbf{U}}$ are considered, namely $a_\zeta = 0.01$ in the second, 0.05

in the third and 0.1 in the last column. Although the nonlinear response is given by the cooperation of several Fourier components, as depicted in figure 2.12, the dominant helical shape corresponds to the one predicted by linear analysis. Interestingly, in the case of very intense amplitude of the forcing strong nonlinear interactions are seen in the frequency region $\omega_f \approx 1.20$ with competition among double- and triple helical responses, as shown in figures 2.12(d) and 2.13.

2.7 Conclusions

In this work the response to forcing of a trailing vortex has been investigated by non-linear and linear analyses. At first the non-linear three-dimensional response of a prototype spatially developing Batchelor vortex has been determined by directly simulating the effect of an inlet forcing harmonic in time and random in space. We observed that several helical modes respond to the forcing, with the most resonating azimuthal wavenumber increasing with frequency. Three forcing amplitude in the DNS were considered equal to 1%, 5%, and 10% of the freestream velocity, which corresponds roughly to 5%, 25%, and 50% the maximum azimuthal velocity at the inlet section. The corresponding flow perturbations, starting from the inlet, grow in amplitude proceeding downstream until they undergo nonlinear saturation, manifesting an helical symmetry.

It has been shown that the appearance of these helical shapes is related to the local stability properties of the base-flow, which is everywhere locally convectively unstable. Moreover, since the local stability properties of the flow vary along the streamwise direction, a WKB analysis has been used for the first time to the case of swirling flows. Specifically an amplitude equation is obtained in order to take into account the non-parallelism of the flow. The response to forcing has also been computed by global resolvent, finding excellent agreement with the WKB results.

Consequently, to further investigate whether the linear analysis is able to predict the mode selection observed in the DNS, the optimal response to forcing has been performed, which is more suitable to detect the most amplified mode by a random forcing. It results that the helical symmetry of the most amplified mode, excited by the associated optimal forcing, in general fits well with the geometrical structure of the response computed with DNS. This shows that the linear resolvent analysis is applicable in this flow, and allows to explain the mode-selection experienced in the non-linear flow.

On the other hand, the energy gains provided by the linear analysis significantly overestimate the ones computed by DNS in all the frequency range. It results that the nonlinear gains strongly depend on the forcing amplitudes in the frequency band which is the most amplified according to linear analysis. In contrast, at higher frequency, where the linear amplification is smaller, the nonlinear gains do not depend significantly on the forcing amplitude.

The preferred nonlinear frequency is $\omega_f \approx 0.50$, which is significantly lower than the one predicted through a global resolvent analysis, $\omega_f \approx 1.20$. Accordingly, the associated most nonlinearly amplified perturbation to a spatially random inlet forcing is the single-helix. Due

to its peculiar azimuthal symmetry, the single-helix mode is the most sensitive to disturbances forcing the flow at the centerline and resonates in a broader frequency range due to nonlinear interaction mechanism between neighboring modes, as discussed in the sections 2.4.2 and 2.6.2. These conclusions could give a possible interpretation of the vortex meandering phenomenon which consists in random-like precession of the vortex core observed in trailing vortex experiments, see Devenport *et al.* (1996); Jacquin *et al.* (2001). In particular, Roy & Leweke (2008) carried out PIV measurements of a trailing vortex generated by a half-wing in a water channel in nine configurations involving different free-stream velocities and angles of attack. By carrying out a Proper Orthogonal Decomposition (POD) of the vorticity at a given downstream section, they observed as the most energetic helical perturbation was the single-helix displacement mode. These authors related their observations to the theoretical result of transient growth in a parallel Gaussian vortex without axial flow, which was triggered by the background noise in the flow or by turbulence in the wake of the wing. Here we may only speculate that the precession of the vortex core could be the result of the convectively amplification of the perturbations present in the incoming turbulent flow. In a first approximation, the turbulent fluctuations can be viewed as broad band perturbations that are amplified by the flow in accordance with the mechanisms explained in the present work, where the single-helix mode is the nonlinear preferred mode.

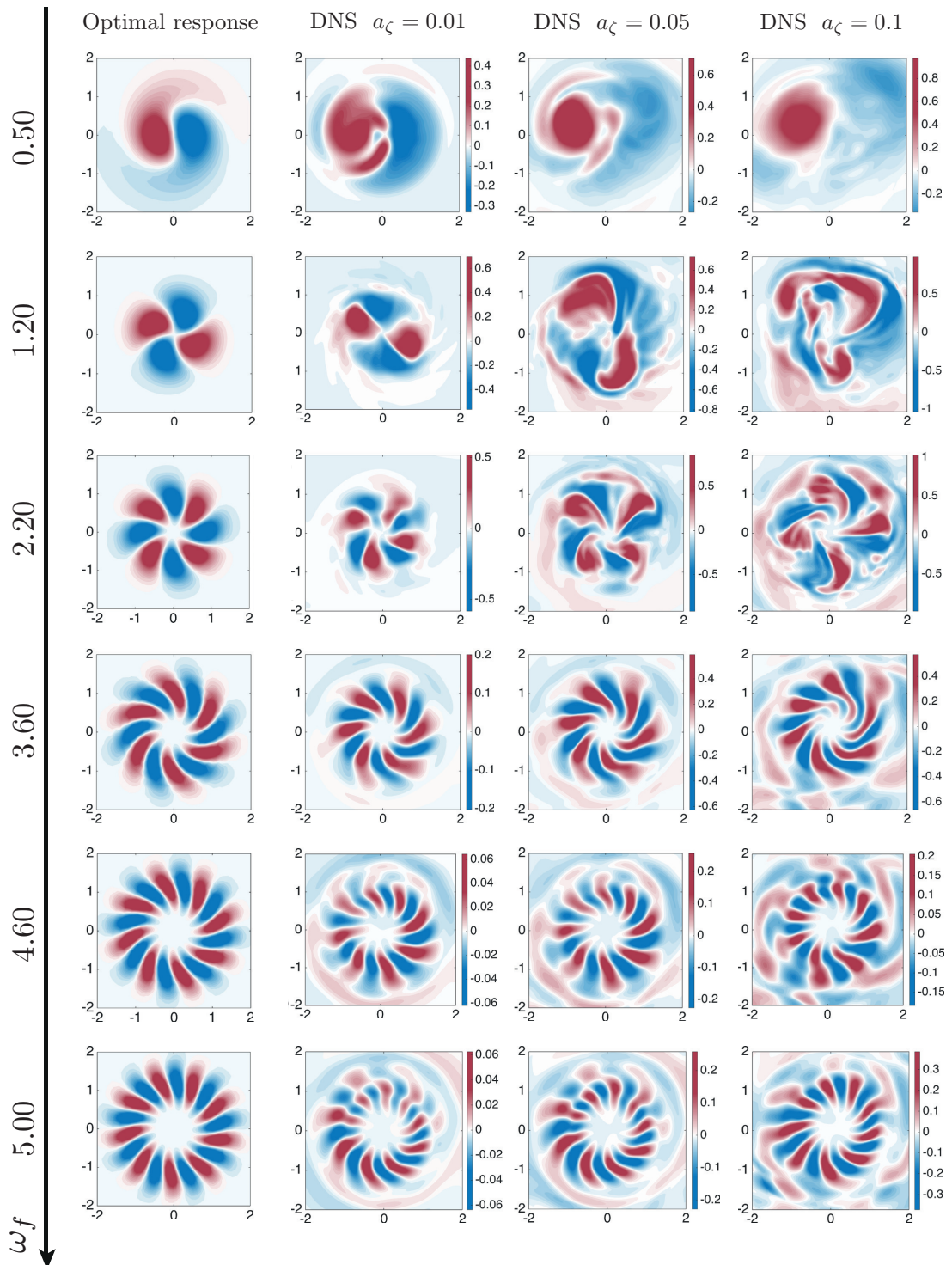


Figure 2.13: In the first column isocontours of the axial vorticity of the linear optimal response at the streamwise position $x = 30$, are shown as a function of the forcing frequency, ω_f . Similarly, isocontours of the nonlinear responses obtained through DNS with $a_\zeta = 0.01$, 0.05 and 0.1 , are reported in the successive columns.

2.8 Appendix: WKB formulation for swirling flows

The linearized Navier-Stokes equations on a 3D axisymmetric base-flow, (U_r, U_θ, U_x) , in cylindrical coordinates read:

$$\begin{aligned} \frac{\partial u_r}{\partial t} + \Gamma u_r + u_r \frac{\partial U_r}{\partial r} + u_x \frac{\partial U_r}{\partial x} - 2\Omega u_\theta &= -\frac{\partial p}{\partial r} + \frac{1}{Re} \left[\left(\Delta - \frac{1}{r^2} \right) u_r - \frac{2}{r^2} \frac{\partial u_\theta}{\partial \theta} \right], \\ \frac{\partial u_\theta}{\partial t} + \Gamma u_\theta + u_r \frac{\partial U_\theta}{\partial r} + u_x \frac{\partial U_\theta}{\partial x} + \Omega u_r + U_r \frac{u_\theta}{r} &= -\frac{1}{r} \frac{\partial p}{\partial \theta} + \frac{1}{Re} \left[\left(\Delta - \frac{1}{r^2} \right) u_\theta + \frac{2}{r^2} \frac{\partial u_r}{\partial \theta} \right], \\ \frac{\partial u_x}{\partial t} + \Gamma u_x + u_r \frac{\partial U_x}{\partial r} + u_x \frac{\partial U_x}{\partial x} &= -\frac{\partial p}{\partial x} + \frac{1}{Re} \Delta u_x, \\ \frac{1}{r} \frac{\partial r u_r}{\partial r} + \frac{1}{r} \frac{\partial u_\theta}{\partial \theta} + \frac{\partial u_x}{\partial x} &= 0, \end{aligned} \quad (2.27)$$

where (u_r, u_θ, u_x) are the velocity components of the perturbation, Ω is the angular velocity of the base-flow and the convective and laplacian operators are defined as:

$$\begin{aligned} \Gamma &= U_r \frac{\partial}{\partial r} + \Omega \frac{\partial}{\partial \theta} + U_x \frac{\partial}{\partial x}, \\ \Delta &= \frac{1}{r} \frac{\partial}{\partial r} \left(r \frac{\partial}{\partial r} \right) + \frac{1}{r^2} \frac{\partial^2}{\partial \theta^2} + \frac{\partial^2}{\partial x^2}. \end{aligned} \quad (2.28)$$

As usual in multiple scales, two spatial scales are introduced, a fast one, x , and a slow one, $X = \epsilon x$. The base-flow depends only on X , and from the continuity equation:

$$\frac{1}{r} \frac{\partial r U_r}{\partial r} + \frac{\partial U_x}{\partial x} = 0 \Rightarrow \frac{1}{r} \frac{\partial r U_r}{\partial r} + \epsilon \frac{\partial U_x}{\partial X} = 0 \Rightarrow U_r = \epsilon U_r' \Rightarrow \frac{1}{r} \frac{\partial r U_r'}{\partial r} + \frac{\partial U_x}{\partial X} = 0. \quad (2.29)$$

Let consider the following normal modes expansion for the perturbation:

$$\mathbf{u}(r, \theta, X; t) = \hat{\mathbf{u}}(r, X) \exp \left[i \left(\frac{1}{\epsilon} \int_0^X k(X', \omega_f) dX' + m\theta - \omega_f t \right) \right]. \quad (2.30)$$

By injecting the transformations (2.31) in equations (2.27), the linearized Navier-Stokes on a 3D axisymmetric weakly non-parallel base-flow equations (2.32) are obtained:

$$\frac{\partial}{\partial t} \rightarrow -i\omega_f \quad \frac{\partial}{\partial \theta} \rightarrow im \quad \frac{\partial}{\partial x} \rightarrow ik + \epsilon \frac{\partial}{\partial X} \quad \frac{\partial^2}{\partial x^2} \rightarrow -k^2 + \epsilon i \left(k \frac{\partial}{\partial X} + \frac{\partial k}{\partial X} \right) + \epsilon^2 \frac{\partial^2}{\partial X^2}. \quad (2.31)$$

$$\begin{aligned}
 & -i\omega_f u_r + \Gamma_{m,k} u_r - 2\Omega u_\theta + \epsilon \left(U_x \frac{\partial}{\partial X} + U_r' \frac{\partial}{\partial r} \right) u_r + \epsilon \frac{\partial U_r'}{\partial r} u_r = \\
 & \quad - \frac{\partial p}{\partial r} + \frac{1}{Re} \left[\left(\Delta_{m,k} - \frac{1}{r^2} \right) u_r - \frac{2im}{r^2} u_\theta + \epsilon i \left(k \frac{\partial}{\partial X} + \frac{\partial k}{\partial X} \right) u_r + \epsilon^2 \frac{\partial^2 u_r}{\partial X^2} \right], \\
 & -i\omega_f u_\theta + \Gamma_{m,k} u_\theta + \left(2\Omega + \frac{\partial \Omega}{\partial r} r \right) u_r + \epsilon \left(U_x \frac{\partial}{\partial X} + U_r' \frac{\partial}{\partial r} \right) u_\theta + \epsilon \frac{\partial U_\theta}{\partial X} u_x + \epsilon \frac{U_r'}{r} u_\theta = \\
 & \quad - \frac{im}{r} p + \frac{1}{Re} \left[\left(\Delta_{m,k} - \frac{1}{r^2} \right) u_\theta + \frac{2im}{r^2} u_r + \epsilon i \left(k \frac{\partial}{\partial X} + \frac{\partial k}{\partial X} \right) u_\theta + \epsilon^2 \frac{\partial^2 u_\theta}{\partial X^2} \right], \quad (2.32) \\
 & -i\omega_f u_x + \Gamma_{m,k} u_x + \frac{\partial U_x}{\partial r} u_r + \epsilon \left(U_x \frac{\partial}{\partial X} + U_r' \frac{\partial}{\partial r} \right) u_x + \epsilon \frac{\partial U_x}{\partial X} u_x = \\
 & \quad - ikp - \epsilon \frac{\partial p}{\partial X} + \frac{1}{Re} \left[\Delta_{m,k} u_x + \epsilon i \left(k \frac{\partial}{\partial X} + \frac{\partial k}{\partial X} \right) u_x + \epsilon^2 \frac{\partial^2 u_x}{\partial X^2} \right], \\
 & \frac{1}{r} \frac{\partial r u_r}{\partial r} + \frac{im}{r} u_\theta + ik u_x + \epsilon \frac{\partial u_x}{\partial X} = 0.
 \end{aligned}$$

Where $\Gamma_{m,k}$ and $\Delta_{m,k}$ are the convective and laplacian operators for a parallel flow:

$$\begin{aligned}
 \Gamma_{m,k} &= im\Omega + ikU_x, \\
 \Delta_{m,k} &= \frac{1}{r} \frac{\partial}{\partial r} \left(r \frac{\partial}{\partial r} \right) - \frac{m^2}{r^2} - k^2. \quad (2.33)
 \end{aligned}$$

Considering now the asymptotic expansion:

$$\hat{\mathbf{u}}(r, X) \sim A(X) \hat{\mathbf{u}}^{(1)}(r, X) + \epsilon \hat{\mathbf{u}}^{(2)}(r, X) + \dots \quad (2.34)$$

At zero order in ϵ the local stability problem is retrieved:

$$\boxed{\epsilon^0} \quad L[\hat{\mathbf{u}}^{(1)}] = 0, \quad (2.35)$$

where the operator L contains the linearized Navier-Stokes equation on a parallel base flow $U_\theta(r)$, $U_x(r)$:

$$\begin{aligned}
 & -i\omega_f u_r + \Gamma_{m,k} u_r - 2\Omega u_\theta = - \frac{\partial p}{\partial r} + \frac{1}{Re} \left[\left(\Delta_{m,k} - \frac{1}{r^2} \right) u_r - \frac{2imu_\theta}{r^2} \right], \\
 & -i\omega_f u_\theta + \Gamma_{m,k} u_\theta + u_r \frac{\partial U_\theta}{\partial r} + \Omega u_r = - \frac{imp}{r} + \frac{1}{Re} \left[\left(\Delta_{m,k} - \frac{1}{r^2} \right) u_\theta + \frac{2imu_r}{r^2} \right], \quad (2.36) \\
 & -i\omega_f u_x + \Gamma_{m,k} u_x + u_r \frac{\partial U_x}{\partial r} = - ikp + \frac{1}{Re} \Delta_{m,k} u_x, \\
 & \frac{1}{r} \frac{\partial r u_r}{\partial r} + \frac{im u_\theta}{r} + ik u_x = 0.
 \end{aligned}$$

At a given ω_f the spatial branches $q(k, X')$ are the solutions of equation (2.36).

Chapter 2. Mode selection in trailing vortices

At first order in ϵ we get:

$$\boxed{\epsilon^1} \quad L[\hat{\mathbf{u}}^{(2)}] = Q[A\hat{\mathbf{u}}^{(1)}]. \quad (2.37)$$

Hence, the operator Q can be split in two parts:

$$Q[A\hat{\mathbf{u}}^{(1)}] = R[\hat{\mathbf{u}}^{(1)}] \frac{dA}{dX} + S[\hat{\mathbf{u}}^{(1)}]A, \quad (2.38)$$

where R and S are defined as:

$$R[\hat{\mathbf{u}}^{(1)}] = \begin{bmatrix} -U_x + \frac{ik}{Re} & 0 & 0 & 0 \\ 0 & -U_x + \frac{ik}{Re} & 0 & 0 \\ 0 & 0 & -U_x + \frac{ik}{Re} & -I \\ 0 & 0 & -I & 0 \end{bmatrix} \begin{pmatrix} \hat{u}_r^{(1)} \\ \hat{u}_\theta^{(1)} \\ \hat{u}_x^{(1)} \\ \hat{p}^{(1)} \end{pmatrix}, \quad (2.39)$$

$$S[\hat{\mathbf{u}}^{(1)}] = \begin{bmatrix} C(U_x, U'_r, k) - \frac{\partial U'_r}{\partial r} & 0 & 0 & 0 \\ 0 & C(U_x, U'_r, k) - \frac{U'_r}{r} & -\frac{\partial U_\theta}{\partial X} & 0 \\ 0 & 0 & C(U_x, U'_r, k) - \frac{\partial U_x}{\partial X} & -\frac{\partial}{\partial X} \\ 0 & 0 & -\frac{\partial}{\partial X} & 0 \end{bmatrix} \begin{pmatrix} \hat{u}_r^{(1)} \\ \hat{u}_\theta^{(1)} \\ \hat{u}_x^{(1)} \\ \hat{p}^{(1)} \end{pmatrix},$$

with:

$$C(U_x, U'_r, k) = -U_x \frac{\partial}{\partial X} - U'_r \frac{\partial}{\partial r} + \frac{1}{Re} \left(ik \frac{\partial}{\partial X} + i \frac{\partial k}{\partial X} \right). \quad (2.40)$$

In order to have solutions of the inhomogeneous equation $L[\hat{\mathbf{u}}^{(2)}] = Q[A\hat{\mathbf{u}}^{(1)}]$, the forcing term Q should be in the image of the operator L . This means that Q should be orthogonal to the corresponding adjoint eigenfunction $\tilde{\mathbf{u}}$ of the adjoint operator \tilde{L}_w with respect to the defined inner product, see Huerre & Rossi (1998):

$$\underbrace{\int_0^\infty R[\hat{\mathbf{u}}^{(1)}] \tilde{\mathbf{u}} w(r) dr}_{M(X)} \frac{dA}{dX} + \underbrace{\int_0^\infty S[\hat{\mathbf{u}}^{(1)}] \tilde{\mathbf{u}} w(r) dr}_{N(X)} A = \int_0^\infty L[\hat{\mathbf{u}}^{(2)}] \tilde{\mathbf{u}} w(r) dr = \int_0^\infty \hat{\mathbf{u}}^{(2)} \tilde{L}_w[\tilde{\mathbf{u}}] w(r) dr = 0, \quad (2.41)$$

where $w(r)$ is the weight of the scalar product, yielding to the amplitude equation:

$$M(X) \frac{dA}{dX} + N(X)A = 0. \quad (2.42)$$

Thus at first order the response is given by:

$$\mathbf{u}(r, x) \sim A(x) \hat{\mathbf{u}}(r, x) \exp \left(\int_0^x -k_i(x') dx' \right) \exp \left[i \left(\int_0^x k_r(x') dx' + m\theta - \omega t \right) \right], \quad (2.43)$$

where $A(x)$ is the solution of equation (2.42).

2.9. Appendix: Sensitivity to radial extension of the domain

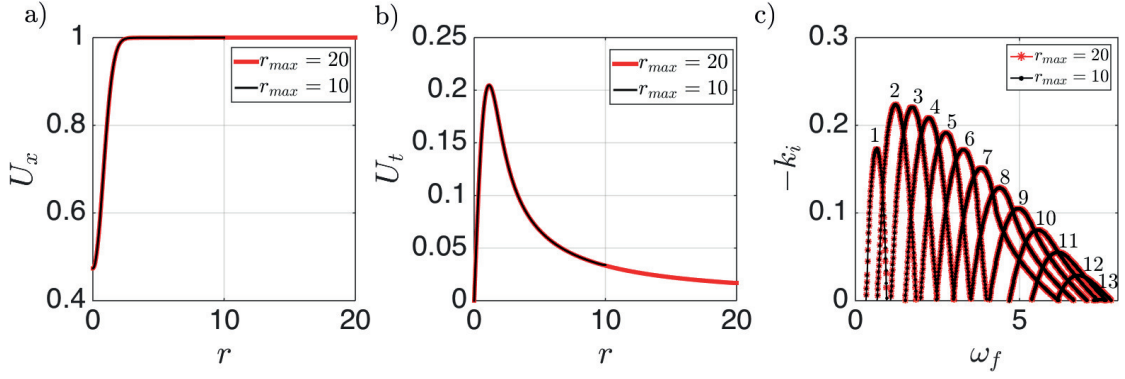


Figure 2.14: (a) Streamwise and (b) azimuthal velocity components of the base flow at $x = 30$ computed with $r_{max} = 10$ (black line) and $r_{max} = 20$ (red line). The corresponding spatial growth rate, within the same streamwise position, are showed in (c).

2.8.1 WKB formulation for volume forcing

In the case of volume forcing the following first order term is included in the linearized Navier-Stokes equation (2.27):

$$\mathbf{f}(r, x) \sim \epsilon F(x) \hat{\mathbf{u}}(r, x) \exp\left(\int_0^x -k_i(x') dx'\right) \exp\left[i\left(\int_0^x k_r(x') dx' + m\theta - \omega t\right)\right]. \quad (2.44)$$

As for the signaling problem the response is expressed as in equation (2.43). Consequently at zero order the local spatial problem of equation (2.35) is retrieved. The forcing term appears only at first order in equation (2.45):

$$L[\hat{\mathbf{u}}^{(2)}] + F(X) \hat{\mathbf{u}}^{(1)} = R[\hat{\mathbf{u}}^{(1)}] \frac{dA(X)}{dX} + S[\hat{\mathbf{u}}^{(1)}] A(X). \quad (2.45)$$

By projecting on the adjoint mode a non-homogeneous amplitude equation is now obtained:

$$\underbrace{\int_0^\infty R[\hat{\mathbf{u}}^{(1)}] \tilde{\mathbf{u}} w(r) dr}_{M(X)} \frac{dA}{dX} + \underbrace{\int_0^\infty S[\hat{\mathbf{u}}^{(1)}] \tilde{\mathbf{u}} w(r) dr}_{N(X)} A = \underbrace{\int_0^\infty \hat{\mathbf{u}}^{(1)} \tilde{\mathbf{u}} w(r) dr}_{H(X)} F. \quad (2.46)$$

where $H(X)$ is a diagonal matrix defined as $H_{ii} = \langle \tilde{\mathbf{u}}(x_i), \hat{\mathbf{u}}^{(1)}(x_i) \rangle$. If the adjoint modes are normalized by $\tilde{\mathbf{u}} / (\langle \tilde{\mathbf{u}}, \hat{\mathbf{u}}^{(1)} \rangle_W)^H$, $H(X)$ corresponds to the identity matrix. Of course the results are not affected by the choice of the normalization of the adjoint field.

2.9 Appendix: Sensitivity to radial extension of the domain

The very good agreement between WKB and global resolvent analysis discussed in section 2.4.2 represents a significant convergence test since both the theoretical approach, the numerical method and the grids are different.

We show here the independence of the results from the radial extension of the domain.

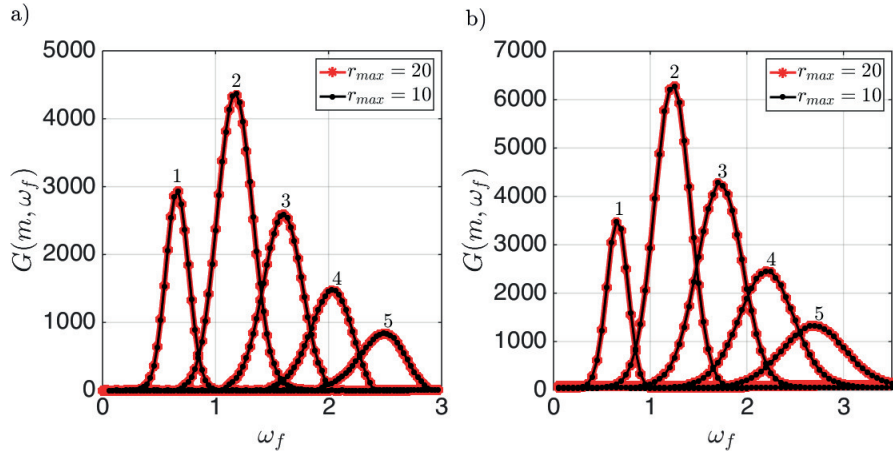


Figure 2.15: In (a) the global gains of the first five helical responses excited by forcing at the inlet with the local direct mode computed by WKB analysis are shown. Similarly, the optimal gains for inlet forcing computed through global resolvent are reported in (b).

The results for $r_{max} = 10$ and $r_{max} = 20$ are depicted in this section by black and red line, respectively. In figure 2.14 the (a) axial and (b) azimuthal velocity profiles of the base flow at $x = 30$ reveal the null influence of the radial extension of the domain and of the free-stress constraint at the boundary. The corresponding spatial gains, $-k_i(x = 30)$, are reported in (c) for the two domain size. Similar results are found for the other streamwise positions. As a consequence, also the global gains carried out with WKB approach result insensitive to the radial domain extension, see figure 2.15(a). In addition, the optimal gains to inlet forcing are reported in figure 2.15(b). Similar independence on the radial extension of the domain is found for the case of volume forcing. Since in both WKB and global resolvent analyses the baseflow is used, figure 2.15 represents a further validation test for the baseflow.

3 Hub vortex instability

3.1 Linear stability analysis of wind turbine wakes performed on wind tunnel measurements

G.V. Iungo¹, F. Viola^{1,2}, S. Camarri³, F. Porté-Agel¹ and F. Gallaire²

¹ Wind Engineering and Renewable Energy Laboratory, École Polytechnique Fédérale de Lausanne, Lausanne, CH-1015, Switzerland

² Laboratory of Fluid Mechanics and Instabilities, École Polytechnique Fédérale de Lausanne, Lausanne, CH-1015, Switzerland

³ Department of Civil and Industrial Engineering, University of Pisa, Pisa, 56122, Italy

Journal of Fluid Mechanics 737 (2013): 499-526.

Wind tunnel measurements were performed for the wake produced by a three-bladed wind turbine immersed in uniform flow. These tests show the presence of a vorticity structure in the near wake region mainly oriented along the streamwise direction, which is denoted as hub vortex. The hub vortex is characterized by oscillations with frequencies lower than the one connected to the rotational velocity of the rotor, which have been ascribed to wake meandering by previous works. This phenomenon consists in transversal oscillations of the wind turbine wake, which might be excited by the vortex shedding from the rotor disc acting as a bluff body. In this work temporal and spatial linear stability analyses of a wind turbine wake are performed on a base flow obtained through time-averaged wind tunnel velocity measurements. This study shows that the low-frequency spectral component detected experimentally matches the most amplified frequency of the counter-winding single-helix mode downstream of the wind turbine. Then, simultaneous hot-wire measurements confirm the presence of a helicoidal unstable mode of the hub vortex with a streamwise wavenumber roughly equal to the one predicted from the linear stability analysis.

3.1.1 Introduction

Wind turbine blade rotation produces a wake, which is the result of complex dynamics and interactions between different vorticity structures. The near wake is dominated by vortex roll-up, which is strongly dependent on blade characteristics; its characterization is fundamental for optimization of rotor aerodynamics, to analyse vortex induced vibrations on blade structure and to reduce noise production typically connected to the shedding of the tip vortices. Conversely, in the far-wake concentrated vorticity structures are no longer observed and investigations are mainly focused on wake recovery and small-scale turbulent structures. Characterization of the far wake is fundamental for wind farm design and for evaluation of fatigue loads on downstream turbines. The connection between the vorticity structure formation in the near wake and the turbulence decay in the far wake is still an open question, as highlighted in Sørensen (2011).

The near wake of a wind turbine is characterized by the presence of counter-rotating helicoidal vorticity pairs shed from the tip and root of each blade. Furthermore, a system of trailing vortices is produced as a consequence of the varying circulation distribution along the blade span, see Sherry *et al.* (2010). Helicoidal tip-vortices shed from a rotor have been characterized through different experimental works, e.g. PIV measurements in Whale *et al.* (1996), Massouh & Dobrev (2007), or through hot-wire anemometry in Chamorro & Porté-Agel (2009, 2010) and Zhang *et al.* (2012). However, the only experimental work dealing with a detailed characterization of wind turbine near-wake vortex system, i.e. helicoidal tip and root vortices and trailing vortices, is carried out in Sherry *et al.* (2010), where PIV measurements in a water tunnel are performed. Tip and root vortices are simultaneously shed from each blade, whereas at a very early stage trailing vortices are also detected. Tip vortices are rapidly convected downstream because located in a wake region with higher streamwise velocity with respect to the hub region, which is characterized by a strong velocity deficit. The helicoidal root-vortices practically surround the wind turbine nacelle with a relatively small radius of curvature. This geometric feature and a reduced streamwise distance between adjacent vortex helices promote a faster diffusion of the root vortices with respect to the tip vortices. In Sherry *et al.* (2010) root vortices are completely diffused at a downstream distance smaller than 0.5 rotor diameters (d). Furthermore, interaction of root vortices with the nacelle boundary layer and wind turbine stem can further anticipate their diffusion. Diffusion of both root and tip vortices is found to be enhanced by increasing wind turbine tip speed ratio, which is due to the decreased helical pitch of the vortices, thus to the increased mutual induction between adjacent vortices (Widnall, 1972).

Root and tip vortices have been also investigated in the near-wake through Direct Numerical Simulations (DNS) of the Navier-Stokes equations in Ivanell *et al.* (2009). However, the main shortcoming of the numerical simulations of wind turbines consists in not resolving the boundary layer flow over the blades and their induced loads are simulated through the actuator disc or actuator line models; thus, near wake vorticity structures cannot be characterized with a very high accuracy (Porté-Agel *et al.*, 2011).

By moving downstream root vortices are rapidly diffused, whereas a system of helicoidal

3.1. Linear stability analysis of wind turbine wakes

tip-vortices is still present; indeed, their signature in the velocity signals has been clearly detected through both numerical simulations, see e.g. Lu & Porté-Agel (2011), and experimental investigations, like in Medici & Alfredsson (2006), Chamorro & Porté-Agel (2009, 2010) and Zhang *et al.* (2012).

Regarding the central part of the wake, root vortices are found to rapidly diffuse in proximity of the wind turbine hub; however, a vorticity structure mainly oriented along the streamwise direction, which is denoted as hub vortex, is still present several diameters downstream. The hub vortex is clearly visualized in the wake of a marine propeller by Felli *et al.* (2011); regarding wind turbine wakes, the hub vortex is detected in Schito (2012) through smoke visualizations. With the PIV measurements carried out in Zhang *et al.* (2012) the hub vortex is observed up to a downstream distance of $1.5 d$.

Further downstream several instabilities of wind turbine wakes are observed, see e.g. Medici & Alfredsson (2008) and Felli *et al.* (2011), which can affect the wake recovery and increase fatigue loads for downstream wind turbines within a wind farm. In the so-called transitional region, the helicoidal tip-vortices show an instability that is mainly driven by the mutual inductance between adjacent spirals. With the theoretical instability model of a helical vortex filament proposed by Widnall (1972), three instability modes are predicted, which are a short-wave instability, a long-wave instability and a mutual-inductance instability. In Felli *et al.* (2011), through water tunnel visualizations of a marine propeller wake, all these three instability modes are found to be superimposed.

In Joukowski (1912) a wake produced from a blade with a constant circulation along the blade span is considered, which is composed of helicoidal tip-vortices and root vortices. This vortex system is found to be unconditionally unstable, but it becomes stable if the trailing vortex sheet is also considered. In Okulov & Sørensen (2007) a linear stability analysis of helicoidal tip-vortices is performed also including a vorticity field mimicking the presence of the hub vortex. These authors found that the stability of the tip vortices is strongly affected by the radial extent of the hub vortex and by its vorticity distribution. Furthermore, it is shown that the interaction between the hub vortex and the helicoidal tip-vortices stabilizes the latter, otherwise they are always unstable and not affected by the number of blades and by the characteristics of the vorticity structures (see e.g. Levy & Forsdyke (1928), Widnall (1972), Gupta & Loewy (1974), Okulov (2004), Okulov & Sørensen (2007)). In Ivanell *et al.* (2010) stability analysis of helicoidal tip-vortices is carried out with Large Eddy simulations (LES) of the Navier-Stokes equations using the actuator line model, and introducing small harmonic perturbations close to the blade tips. They found dispersive instabilities at several specific frequencies and vortex pairing was also detected. Typically helicoidal tip-vortices diffuse faster if immersed in a boundary layer flow, see e.g. Porté-Agel *et al.* (2011) and Lu & Porté-Agel (2011). In Zhang *et al.* (2012) the helicoidal tip-vortices are detected up to a distance of $2 d$.

Downstream with respect to the destabilization of the helicoidal tip-vortices, the hub vortex is also found to become unstable by Felli *et al.* (2011). By proceeding further downstream, the hub vortex starts oscillating sinusoidally, according to a spiral geometry, until breakdown occurs. This oscillation occurs with a frequency equal to the one of the rotor and is found to be independent on the number of blades. These authors hypothesize that the hub vortex instabil-

ity can be excited by the perturbations produced by the instability of the helicoidal tip-vortices. A low-frequency instability is also detected from wind tunnel tests of wind turbine models, see e.g. Medici & Alfredsson (2006, 2008), Chamorro & Porté-Agel (2010) and Zhang *et al.* (2012). In Medici & Alfredsson (2008) this low-frequency instability, denoted as wake meandering or wandering, is equal to 0.29 times the hub rotational frequency and is ascribed to transversal oscillations of the wind turbine wake, which may be excited by the vortex shedding from the rotor disc in a similar way as for bluff bodies. This low frequency is found to decrease with increasing tip speed ratio of the turbine and with increasing thrust coefficient. In Chamorro & Porté-Agel (2010) and Zhang *et al.* (2012) the low-spectral component connected to wake meandering is equal to 0.34 times the hub rotational frequency and it can be detected up to a downstream distance of $1.5 d$.

Further downstream, the hub vortex breakdown occurs, as documented in Klein *et al.* (1995) and Ortega *et al.* (2003). In Sarpkaya (1971) and Felli *et al.* (2011) the hub vortex breakdown is found to occur as a double helix with the same rotation sense of the rotor.

In the far wake the helicoidal tip-vortices and the hub vortex are completely diffused and the streamwise velocity field shows a smooth quasi gaussian-like shape, with the peak of the streamwise velocity deficit located in correspondence of the hub height. Due to this wake feature several analytical wake models are proposed for the far wake, see e.g. Burton *et al.* (2001), which are mainly used for wind farm design. For cases of a wind turbine immersed in the boundary layer, the mean streamwise velocity component is skewed due to the oncoming boundary layer flow, but it recovers to an axisymmetric shape if the oncoming wind is subtracted, as shown in Chamorro & Porté-Agel (2009). By moving downstream the wake gradually recovers with increasing wake width and decreasing velocity deficit.

In the present work linear stability analysis of wind turbine wakes is performed by using velocity measurements averaged in time as a base flow, which were carried out in a wind tunnel for a down-scaled wind turbine model. The main goal of this work is the physical characterization of the hub vortex low-frequency instability observed experimentally in the near wake. Both temporal and spatial linear stability analyses were performed; moreover, the Gaster transformation was also considered in order to produce a first approximation of the results then obtained through the spatial stability analysis. The stability properties of the experimental mean flow have been investigated in details, and the results are used to reconstruct the mode associated with the instability of the hub vortex. The reconstructed mode has been successively assessed through further dedicated wind tunnel tests.

The work is organized as follows. Wind tunnel velocity measurements of wakes produced by a down-scaled wind turbine model invested by a uniform flow are described in §3.1.2. The numerical formulation of the linear stability analysis is presented in §3.1.3, while results of the temporal stability analysis are reported in §3.1.4. The spatial linear stability analysis is then described in §3.1.5. Concluding, final remarks are presented in §3.1.6.

3.1. Linear stability analysis of wind turbine wakes

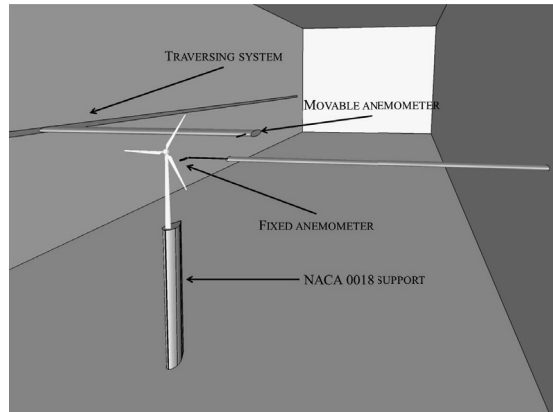


Figure 3.1: Sketch of the experimental setup.

3.1.2 Wind tunnel measurements of wind turbine wakes

Set-up

Velocity measurements of wind turbine wakes were performed in the boundary layer wind tunnel of the Wind Engineering and Renewable Energy Laboratory (WIRE) of the École Polytechnique Fédérale de Lausanne (EPFL), Switzerland. The facility is an open loop wind tunnel with an inlet providing a contraction with 4:1 area ratio. Several turbulence devices consisting of coarse meshes and honeycomb flow straighteners are used to increase flow quality. The wind tunnel consists of three different test sections; the one used for this work is the first one downstream to the inlet, which has a length of 28 m, width of 2.5 m and height of 2 m. This testing chamber provides an adjusting ceiling in order to eventually change pressure gradient along the streamwise direction; for this work the pressure gradient was negligible ($dC_p/dx \approx -0.1\% \text{ m}^{-1}$). The flow is produced by a single fan with a power of 90 kW producing a maximum velocity of about 7 m/s with a minimum turbulence level of 2%. A three degree of freedom traversing system allows probes to be positioned with an accuracy higher than 0.1 mm.

The used wind turbine down-scaled model is a 3-bladed GWS/EP-6030x3 counter-clockwise. The rotor, with a diameter, d , of 152 mm, is connected to a DC motor with a diameter of 10 mm. The wind turbine model is mounted with a stem of 127 mm height, which is in turn placed on a vertical support with a NACA 0018 cross-section and height of 500 mm. This set-up enables placing the turbine outside of the boundary layer, thus allowing the turbine to be invested by a uniform flow. A sketch of the experimental setup is reported in figure 3.1. Typically for the tests considered here the tip speed ratio of the turbine (TSR), which is the ratio between the speed of the blade tip and the oncoming velocity at hub height, U_{hub} , is 4.7. The turbine rotational velocity was monitored through a laser tachometer manufactured by Monarch with an accuracy of about 10 RPM. For these tests the mean rotational frequency was 57 Hz, with average fluctuations of 2.7% of the mean value. The velocity at hub height is 5.8 m/s and the turbulence level is equal to 7%, which was obtained by removing one of the

Chapter 3. Hub vortex instability

three turbulence screens located in the wind tunnel relaxation chamber. A Reynolds number of 60800 is obtained by considering U_{hub} as reference velocity, and the rotor diameter, d , as reference length.

Wind tunnel flow velocity was measured through two Pitot static tubes located in proximity of the entrance and end of the testing chamber; the Pitot tubes were in turn connected to two transducers SETRA 239. Atmospheric pressure into the testing chamber was measured with a transducer SETRA 276, while the static temperature with a Pt100 Eliwell SN206000. All the analog signals were acquired with three NI PXI-6143 data acquisition systems.

Measurements of three components of the velocity were performed through a customized Cobra probe produced by Turbulent Flow Instrumentation, which is a four-hole pressure-probe. This probe, with an external diameter of 1.5 mm, can measure velocity fluctuations characterized by frequencies lower than 300 Hz. The maximum admissible angle between the probe stem and the wind direction is about 45° . This miniaturized version of the Cobra probe allows obtaining an accuracy higher than 2% in the velocity module and about 1° for pitch and yaw. Cobra measurements were typically carried out with a sampling frequency of 5 kHz and a number of samples equal to 2^{19} .

Wake measurements were also performed through hot-wire anemometers, both single-component (DANTEC 55P11) or cross-wire probes (DANTEC 55P61). For the simultaneous hot-wire measurements presented in §3.1.5, hot-wire probes with right-angled prongs and with the sensor perpendicular to the probe axis were used (DANTEC 55P14). These probes were introduced from the wake side in order to reduce intrusiveness of the measuring system. The hot-wire anemometers were connected to an A.A. Lab Systems AN-1003. Their calibration was performed by setting the probes on a StreamLine Pro Automatic Calibrator manufactured by Dantec, which guarantees an accuracy of the flow higher than 1%. Hot-wire measurements were typically carried out with a sampling frequency of 20 kHz and a number of samples equal to 2^{21} . Statistics of the hot-wire measurements were generally in good agreement with the ones performed with the Cobra probe (see figure 3.2); however, their higher frequency resolution allowed the performance of more accurate spectral analyses.

The used reference frame has its origin placed just behind the hub of the wind turbine, x -axis corresponds to the streamwise direction, positive by pointing downstream. The z -axis is along the vertical direction, positive from the bottom towards the top, while y -axis is along the spanwise direction oriented in a way to produce a right-handed Cartesian coordinate system.

Velocity measurements were performed from a downstream distance of $0.125 d$ up to $20 d$. For each considered downstream location, 2D maps were measured with an area of $1.5 d \times 1.5 d$ with a spatial spacing between adjacent points of about $0.025 d$. Moreover, measurements over the horizontal and vertical planes passing through the hub location were performed with a higher resolution along the streamwise direction.

Velocity measurements

As already proved from previous experimental and numerical works (Alfredsson & Dahlberg, 1979; Vermeer *et al.*, 2003; Medici & Alfredsson, 2006) and confirmed from the present experimental campaign, the wake velocity field produced from a wind turbine immersed in a uniform flow can be considered to be axisymmetric with respect to the axis passing through the hub location and directed along the oncoming wind direction, i.e. the x -axis. 2D measurements performed over transversal planes located at different downstream locations, not reported here for the sake of brevity, confirmed that velocity profiles are invariant for different azimuthal orientations of the traverses. A small wake produced by the wind turbine stem is detected in the very near-wake; however, it is completely recovered at the downstream locations considered for this investigation. Moreover, the radial velocity is also found to be practically negligible, as shown in figure 3.2(a). Therefore, the wake flow can be completely characterized through the axial and azimuthal velocities as a function of the radial and streamwise positions. In figure 3.2 the radial velocity, U_r , the mean azimuthal velocity, U_θ , the non-dimensional axial vorticity, ω_x , and the axial velocity, U_x , are shown as a function of the radial position and for several downstream locations considered for the linear stability analysis. For the sake of brevity, only the mean velocity obtained through the Cobra probe measurements is presented; however, the one obtained from the two component hot-wire anemometry is practically equal, i.e with differences lower than 1% for each location, as shown in figure 3.2 for the measurements carried out at the downstream location $x/d = 0.5$.

In figure 3.2(b) significant peaks of the azimuthal velocity are detected for radial positions $r/d \approx 0.15$, which are connected to the rotational velocity induced by the hub vortex, which is a vorticity structure mainly oriented along the streamwise direction. Indeed, a dominant peak of the axial vorticity is typically detected in figure 3.2(c) in correspondence of the wake centre, and it is shielded by a ring-like negative vorticity structure, which is the result of the time-averaging of the helicoidal tip-vortices. The hub vortex produced from a rotor has been already detected in the near wake by several experimental works, e.g. Felli *et al.* (2011) and Zhang *et al.* (2012). The azimuthal velocity connected to the hub vortex and its related axial vorticity are rapidly reduced by moving downstream and the hub vortex can be considered as completely diffused for downstream distances larger than $4d$. Secondary peaks of the azimuthal velocity are also observed for radial positions approximately equal to $r/d \approx 0.5$, which are related to the presence of the helicoidal tip-vortices. Also the azimuthal velocity connected to the tip vortices is decreased by moving downstream and at $x/d = 4$ it is practically diffused.

In figure 3.2(d) the axial velocity field shows a significant deficit in correspondence of the wake centre, which gradually recovers by moving downstream, while wake width increases. A velocity deficit connected to the presence of the helicoidal tip-vortices is also observed in the near wake at $r/d \approx 0.5$, but it disappears as the helicoidal tip-vortices diffuse.

Spectral analysis of the velocity signals acquired in the wind turbine wake clearly shows the presence of two main spectral components, as presented in figure 3.3: a low frequency, which is typically detected in correspondence of the wake core within a radial distance of

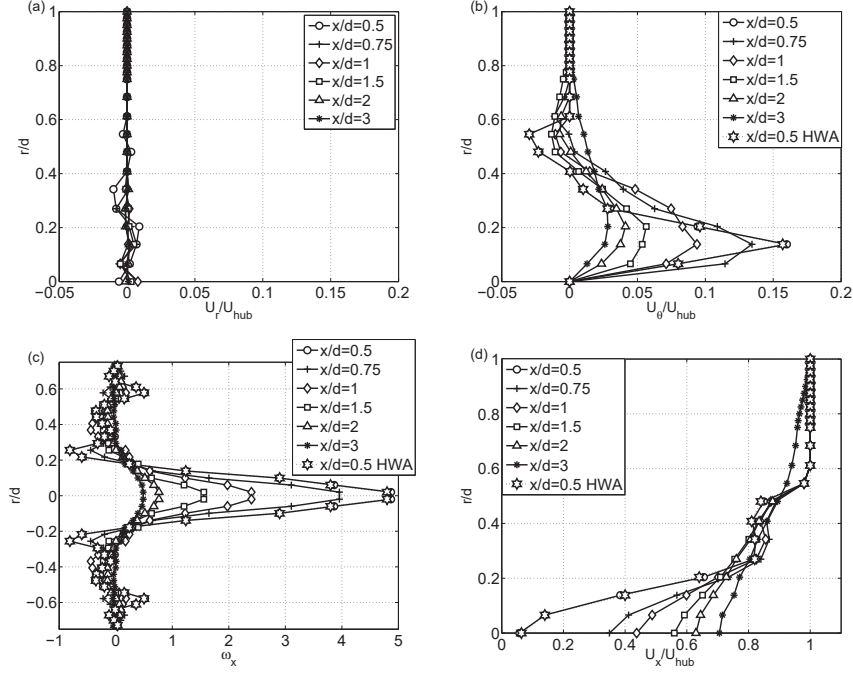


Figure 3.2: Mean velocity field of the wind turbine wake: (a) radial velocity, U_r ; (b) azimuthal velocity, U_θ ; (c) non-dimensional axial vorticity, ω_x ; (d) axial velocity, U_x . These data are obtained with the Cobra probe, but the ones $x/d = 0.5$ HWA with hot-wire anemometry.

about $r/d \approx 0.2$, and a high frequency related to the shedding of the tip vortices. In the present investigation the high frequency connected to the tip vortices shedding is 171 Hz, which is equal to three times the rotational frequency of the turbine (a three-bladed model was tested). On the other hand, the spectral energy detected in the central part of the wake has a frequency about 20 Hz. This frequency, which could be connected to the hub vortex oscillations, is equal to 0.34 times the hub rotational frequency, which is in strong agreement with results of previous works, like e.g. Medici & Alfredsson (2008), Chamorro & Porté-Agel (2010) and Zhang *et al.* (2012). This low-frequency spectral contribution corresponds to a non-dimensional frequency of $\omega = 2\pi f d / U_{hub} = 3.18$. In figure 3.4 the average power spectral density obtained from 2D measurements performed in the wake core within a radial distance of $r/d = 0.2$ is reported for several downstream locations. It is shown that the spectral energy connected to this low-frequency component increases by moving downstream up to $x/d = 1$, then further downstream its energy starts decreasing.

Tests were also performed by setting different values of the tip speed ratio (TSR). Spectral analysis of the velocity signals, briefly summarized in table 3.1, shows that both the frequency connected to the helicoidal tip-vortices and the one related to the hub vortex vary roughly linearly with the rotational frequency of the rotor, f_{hub} . This result indicates that dynamics of these vorticity structures are dependent on the wake swirl, and confirms an outcome presented in Felli *et al.* (2011) where an invariant hub vortex frequency was detected by changing the tip-vortex frequency by mean of a different number of rotor blades.

3.1. Linear stability analysis of wind turbine wakes

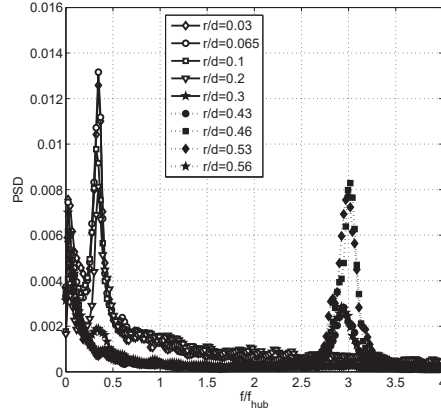


Figure 3.3: Fourier power spectral density of the velocity signals acquired at $x/d = 0.5$, $z/d = 0$, and different radial locations.

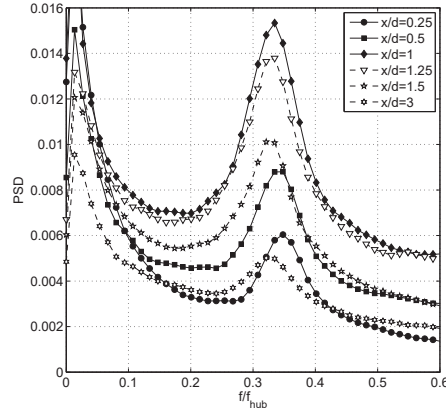


Figure 3.4: Average power spectral density obtained from 2D velocity measurements performed within the wake core with a radius of $r/d = 0.2$, and evaluated for different downstream locations.

Case	$U_{hub}[m/s]$	TSR	$f_{hub}[Hz]$	$f_{tip\ vortices}[Hz]$	$f_{hub\ vortex}[Hz]$
1	5.8	7.6	92	276	31.5
2	5.8	5.3	65	195	21.5
3	5.8	4.7	57	171	20
4	5.8	3.2	39	118	17

Table 3.1: Spectral analysis for the tests performed with different TSR values.

3.1.3 Linear stability analysis: formulation of the numerical problem

In this section the classical local linear stability theory of shear flows is presented, which is related to the development in space and time of infinitesimal perturbations on a given base flow. The base flow is assumed to be quasi-parallel and slowly evolving along the streamwise direction. Flow fluctuations are typically decomposed into elementary instability waves of

Chapter 3. Hub vortex instability

axial and azimuthal wavenumbers k and m , respectively, and frequency ω . The perturbations satisfy an ordinary differential equation of Orr-Sommerfeld type. Enforcement of appropriate boundary conditions then leads to an eigenvalue problem, whereby eigenfunction solutions for the perturbations exist only if k , m and ω satisfy a dispersion relation of the form:

$$D[k, m, \omega] = 0. \quad (3.1)$$

Temporal modes refer to cases where the complex frequency ω is determined as a function of real wavenumbers k and m . Conversely, spatial branches are obtained by solving the dispersion relation with complex wavenumbers k , whereas m and ω are real numbers.

The base flow used for the linear stability analysis was obtained by averaging in time the above-mentioned wind tunnel velocity measurements, as done in Oberleithner *et al.* (2011) for the study of breakdown of swirling jets. Although the mean flow does not represent an equilibrium point for the system, accurate results can be obtained through a stability analysis, as proved e.g. in Barkley (2006), Leontini *et al.* (2010) and Camarri *et al.* (2013). The relevance of considering the stability of the time-averaged flow was assessed by Sipp & Lebedev (2007) theoretically close to onset of instability. In presence of background turbulence, despite the lack of a solid theoretical framework, stability analyses of mean flows were observed to accurately compare with experimental observations by Monkewitz (1988) or Meliga *et al.* (2009) for instance.

The wind turbine wake flow is practically axisymmetric and with a negligible radial velocity, see §3.1.2. Moreover, according to the local nature of the present stability analysis, for each section the flow is considered as invariant for translations along the x -axis. Let us consider the base flow expressed in cylindrical coordinates:

$$U = \begin{pmatrix} U_r \\ U_\theta \\ U_x \\ P \end{pmatrix} = \begin{pmatrix} 0 \\ r\Omega(r) \\ W(r) \\ P(r) \end{pmatrix} \quad (3.2)$$

where U_x is the streamwise velocity, U_θ is the azimuthal velocity, U_r the radial velocity and P is the pressure field. The radial velocity, U_r , is identically null, while the azimuthal velocity, U_θ , is proportional to the the angular velocity, Ω .

Accordingly to the linear stability analysis, the evolution of small perturbations can be described by the Navier-Stokes equations linearized on the base flow. Let us consider the normal modes expansion of the perturbation:

$$\mathbf{u}(r, \theta, x, t) = \hat{\mathbf{u}}(r, t) e^{i(m\theta + kx)} \quad (3.3)$$

where k is the axial wavenumber, m is the azimuthal wavenumber and i is the imaginary unit. The expansion in normal modes imposes a helicoidal symmetry on the perturbation allowing to investigate separately each Fourier component by solving the corresponding monodimensional problem for each pair (k, m) . The continuity equation and the momentum

equations in cylindrical coordinates are the following ones:

$$\begin{aligned}
 & \frac{1}{r} \frac{\partial(r u_r)}{\partial r} + \frac{i m}{r} u_\theta + i k u_x = 0 \\
 & \left(\frac{\partial}{\partial t} + \Gamma_{m,k} \right) u_r - 2\Omega u_\theta = -\frac{\partial p}{\partial r} + \frac{1}{Re} \left(\Delta_{m,k} u_r - \frac{u_r}{r^2} - \frac{2im}{r^2} u_\theta \right) \\
 & \left(\frac{\partial}{\partial t} + \Gamma_{m,k} \right) u_\theta + \left(r \frac{\partial \Omega}{\partial r} + 2\Omega \right) u_r = -\frac{im}{r} p + \frac{1}{Re} \left(\Delta_{m,k} u_\theta - \frac{u_\theta}{r^2} + \frac{2im}{r^2} u_r \right) \\
 & \left(\frac{\partial}{\partial t} + \Gamma_{m,k} \right) u_x + \frac{\partial W}{\partial r} u_r = -i k p + \frac{1}{Re} (\Delta_{m,k} u_x)
 \end{aligned} \tag{3.4}$$

where $\Gamma_{m,k}$ and $\Delta_{m,k}$ are expressed as follows:

$$\begin{aligned}
 \Gamma_{m,k}(r) &= i m \Omega(r) + i k W(r) \\
 \Delta_{m,k} &= \frac{1}{r} \frac{\partial}{\partial r} \left(r \frac{\partial}{\partial r} \right) - \frac{m^2}{r^2} - k^2
 \end{aligned} \tag{3.5}$$

In order to solve numerically the equation system (3.4), a reduced formulation is obtained by using the variable $\mathbf{v} = (u_r, u_\theta)^T$:

$$F(\mathbf{v}) = L \frac{\partial \mathbf{v}}{\partial t} + C \mathbf{v} - \frac{1}{Re} D \mathbf{v} = 0 \tag{3.6}$$

Where the operators are defined as follows:

$$\begin{aligned}
 L &= \begin{pmatrix} 1 & 0 \\ 0 & 1 \end{pmatrix} + b_1 b_2^T \\
 C &= \begin{pmatrix} \Gamma_{m,k} & -2\Omega \\ r \frac{\partial \Omega}{\partial r} + 2\Omega & \Gamma_{m,k} \end{pmatrix} + b_1 \Gamma_{m,k} b_2^T - b_1 \left(\frac{\partial W}{\partial r}, 0 \right) \\
 D &= \begin{pmatrix} \Delta_{m,k} - \frac{1}{r^2} & -\frac{2im}{r^2} \\ \frac{2im}{r^2} & \Delta_{m,k} - \frac{1}{r^2} \end{pmatrix} + b_1 \Delta_{m,k} b_2^T \\
 b_1^T &= \frac{1}{ik} \left(\frac{\partial}{\partial r}, \frac{im}{r} \right) \\
 b_2^T &= \frac{1}{ik} \left(\frac{\partial}{\partial r} + \frac{1}{r}, \frac{im}{r} \right)
 \end{aligned} \tag{3.7}$$

For the stability analysis, a code based on a Chebyshev spectral collocation method is used, see Antkowiak (2005) for more details. The Gauss-Lobatto-Chebyshev collocation grid is mapped into the infinite physical space through algebraic map $r = L\zeta / \sqrt{1 - \zeta^2}$ (Canuto *et al.*, 2007), where the parameter L is set in order to fix the second to last and the second point to r_{max} and $-r_{max}$, respectively. Moreover, taking into account the parity of the functions in the expression of the derivatives (Kerswell & Davey, 1996), and imposing the boundary conditions at infinity, the equations are discretized in the finite domain $]0, r_{max}[$. The computational sensitivity related to the number of collocation points, N , and the size of the physical domain

was investigated, but these results are not reported here for the sake of brevity. The selected settings with $N = 120$ and $r_{max} = 50$ are seen to provide the convergence of the most unstable eigenvalue with a five-digit accuracy, which is deemed to be sufficient for the present purposes. For the stability analysis the same Reynolds number of the experimental measurements was used, i.e. 60800; indeed the used equations were made non-dimensional by using U_{hub} and d as reference dimensions.

The experimental data were fitted with spline functions in order to produce an adequate spatially resolved base flow for the stability analysis. Different fitting methods were tested, which do not affect the results of the stability analysis.

3.1.4 Temporal stability analysis

Temporal stability analysis allows the investigation of the temporal evolution of disturbances on a base-flow within a volume large enough to include the complete disturbance, see Schmid & Henningson (2001). After a transient period the evolution of the perturbations is dominated by the less damped mode, which is in the form $e^{-i\omega t}$ with $\omega \in \mathbb{C}$. In particular if $\omega_i = \text{Im}(\omega) > 0$ the corresponding mode is unstable with a growth rate equal to ω_i , while $\omega_r = \text{Re}(\omega)$ is the frequency related to the propagating harmonic mode (Lighthill, 1978). Considering harmonic perturbations in time equation (3.6) becomes:

$$F_\omega(\mathbf{v}) = -\omega i L \mathbf{v} + C \mathbf{v} - \frac{1}{Re} D \mathbf{v} = 0 \quad (3.8)$$

In order to carry out the temporal stability analysis, equation (3.8) is integrated with $k \in \mathbb{R}$, $m \in \mathbb{R}$ and $\omega \in \mathbb{C}$. By considering normal mode expansion, as in (3.3), positive values of m correspond to modes winding in the opposite direction with respect to the rotation inferred by the hub vortex; see Gallaire & Chomaz (2003) for a more detailed discussion. For each couple (k, m) solving equation (3.8) is equivalent to solve the following generalized eigenvalue problem:

$$A(k)\mathbf{v} = \omega B(k)\mathbf{v} \quad (3.9)$$

where, referring to equation (3.8):

$$A(k) = C - \frac{1}{Re} D \quad B(k) = iL \quad (3.10)$$

The growth rates $\omega_{m,i}(k)$ of the unstable modes calculated as a function of the axial wavenumber, k , and different m are reported in figure 3.5. For the considered downstream location $x/d = 1$, the modes are unstable for $k \leq 82$ and for values of m up to 42. The maximum growth rate connected to the most unstable mode is in good agreement with the value predicted through the Leibovich-Stewartson instability criterion. The latter is a generalization of the Rayleigh criterion and provides a necessary instability condition for a rotating inviscid vortex with the presence of axial flow (Leibovich & Stewartson, 1983). As for the above-mentioned

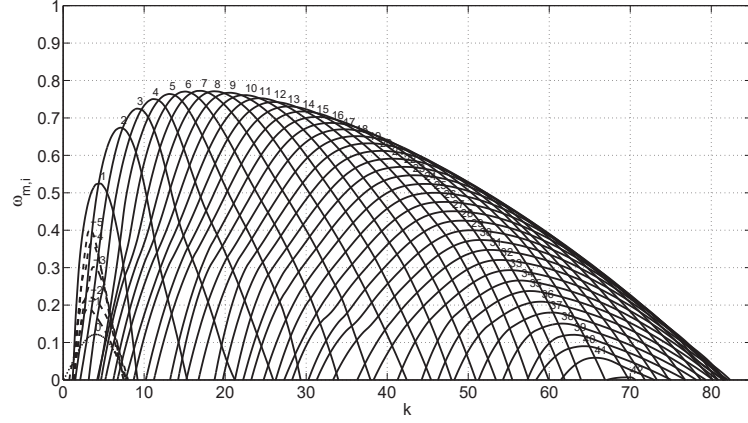


Figure 3.5: Growth rates ($\omega_{m,i}$) of the unstable modes as a function of the axial wavenumber k for the downstream location $x/d = 1$.

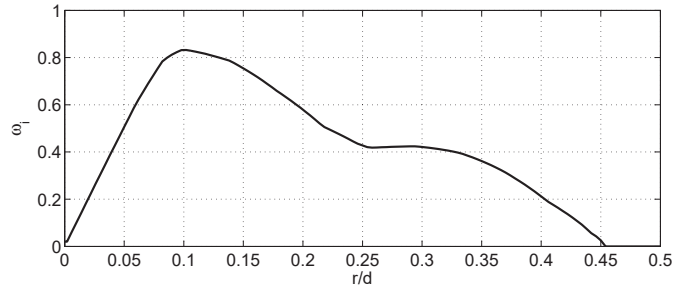


Figure 3.6: Growth rate predicted through the Leibovich-Stewartson instability criterion for the measurements carried out at $x/d = 1$.

criterion the vortex is unstable when the following sufficient condition is satisfied:

$$\omega_i^2 = \frac{2U_\theta(rDU_\theta - U_\theta)(U_\theta^2/r^2 - (DU_\theta)^2 - (DU_x)^2)}{(rDU_\theta - U_\theta)^2 + r^2(DU_x)^2} > 0 \quad (3.11)$$

where D is the spatial first derivative along the radial direction. Moreover, when the inequality (3.11) is satisfied for a certain value of r , that relation provides the square of the growth rate of the most unstable mode corresponding to an eigenfunction with a certain characteristic size, r (see Gallaire & Chomaz (2003) for details). Figure 3.6 shows that the Leibovich-Stewartson instability criterion, evaluated for the measurements carried out at $x/d = 1$, predicts instability for every radial position with the highest values in proximity of the azimuthal velocity peak connected to the hub vortex (see figure 3.2(a)). The growth rate of the most unstable mode predicted through the Leibovich-Stewartson criterion is about 0.8, which confirms the result obtained with the temporal stability analysis shown in figure 3.5. The main goal of the present work is the characterization of the low-frequency spectral component detected through the wind tunnel velocity measurements carried out into the core of the wind turbine wake, which

is reasonable to interpret as the effect of an instability of the hub vortex. To this aim the growth rate, ω_i , is plotted as a function of the non-dimensional frequency, ω_r , in figures 3.7 and 3.8 for the different analysed downstream locations. In these figures the non-dimensional frequency related to the above-mentioned low-frequency instability is highlighted through a vertical dashed line in correspondence of the value 3.18, which has been obtained from the spectral analysis of the velocity signals (see figures 3.3 and 3.4).

Starting from the location $x/d = 0.5$, the selected unstable mode corresponding to the non-dimensional frequency related to the hub vortex instability is $m = 1$, i.e. a counter-winding single-helix mode. However, the unstable mode $m = 1$ is not the one with the highest growth rate overall. Concerning the unstable high-frequency modes, diffusive contribution of the turbulent fluctuations, which is neglected in the present stability analysis, is expected to significantly damp them, in particular as m increases, so as to change the picture given in figure 3.5. Indeed, one among the simplest ways to take into account this effect in the stability analysis might be the inclusion of an eddy viscosity turbulence model in equations (3.4). Assuming, in the simplest form, to use a constant eddy viscosity, the adoption of such a model would be equivalent to reduce the effective Reynolds number of the stability analysis and, in turn, this would decrease the growth rate of the unstable modes depending on m ; indeed, the viscous terms scale as m^2 . This aspect, which is delicate and mentioned here only very briefly, is the object of on-going investigations of the authors, and at present the provided interpretation is confirmed by preliminary results. By moving downstream, the scenario remains practically unchanged with a general reduction of the growth rate for all unstable modes. However, at the downstream position of $x/d = 2.5$, the non-dimensional frequency corresponding to the hub vortex instability starts selecting the mode $m = 2$, i.e. the counter-winding double-helix mode. For the location $x/d = 4$ the mode $m = 4$ is selected. In order to provide a physical interpretation of this stability analysis several factors should be considered: first, the growth rates generally reduce by moving downstream, as shown in figure 3.9 for the mode $m = 1$. Moreover, the hub vortex diffuses rapidly by moving downstream, as reported with the experimental measurements in figure 3.2. Therefore, the unstable mode with $m = 1$ should dominate because it is the mode selected through the hub vortex instability frequency ($\omega_r = 3.18$) in the very near-wake, which is a wake region where the hub vortex has a significant vorticity.

The temporal analysis suggests that in the near wake the hub vortex is characterized by a single-helix counter-winding instability, i.e. $m = 1$. Furthermore, by considering that ω_r is positive, the helicoidal unstable mode is rotating in the same direction of the hub vortex. By moving downstream the hub vortex diffuses and unstable modes with higher values of m could be selected, even with decreasing growth rates. This mode competition will be better investigated in the following section through the spatial stability analysis.

3.1.5 Spatial stability analysis and characterization of the hub vortex instability

This section is devoted to the spatial stability analysis of disturbances generated at a fixed position within a wind turbine wake and evolving downstream. In the temporal setting of §3.1.4, the mode $m = 1$ could not be singled out, although it was seen to “resonate” well at

3.1. Linear stability analysis of wind turbine wakes

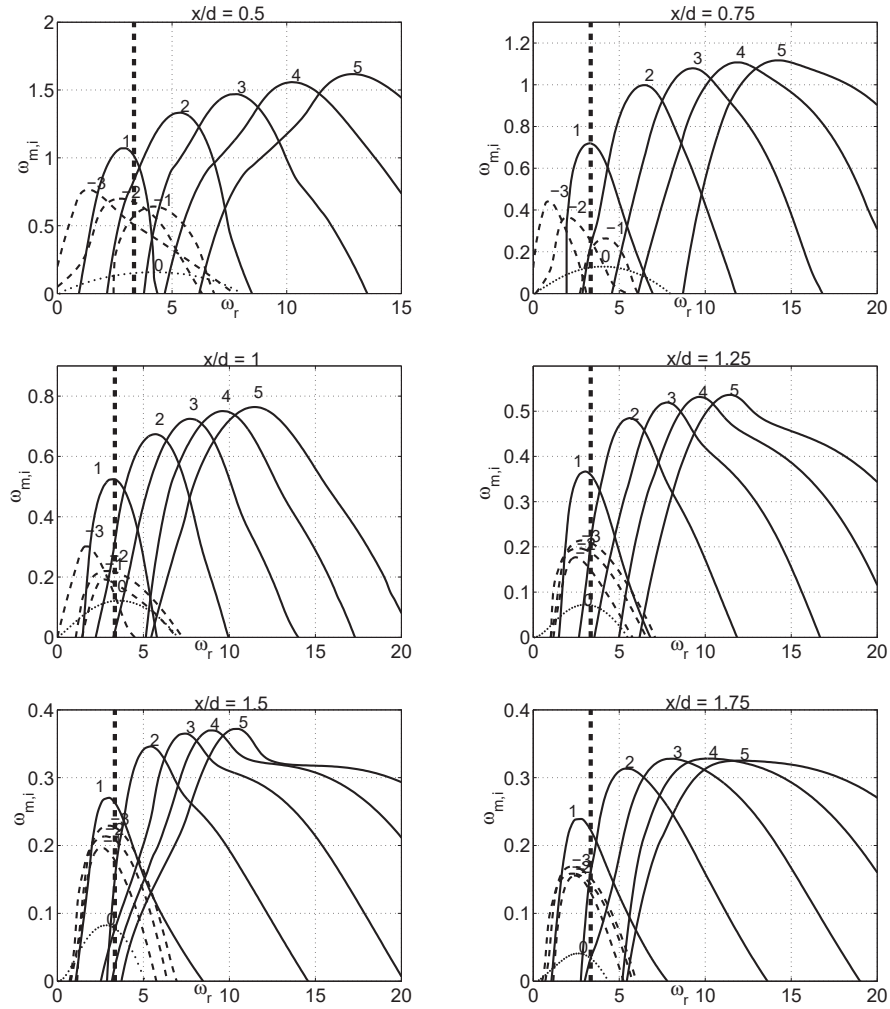


Figure 3.7: Growth rate as a function of the non-dimensional frequency for downstream locations from $x/d = 0.5$ up to $x/d = 1.75$. The vertical dashed line corresponds to the non-dimensional frequency measured experimentally and related to the hub vortex instability.

the frequency observed in the experiments. In order to better elucidate this mode selection, a spatial stability analysis is more suitable, since it is adapted to convectively unstable flows submitted to incoming noise. These flows are known to act as selective amplifiers. The weakly non-parallel spatial stability theory is the preferred analysis tool to better understand this selection.

Note however that a spatial stability analysis is only justified if the flow is convectively unstable. We have therefore checked that the flow is not absolutely unstable for $x/d > 0.5$ where the present analysis applies. The presented measurements do not allow us to determine the nature of the instability closer to the hub, where a backflow region could be expected. We can therefore only speculate on a sufficiently extended pocket of absolutely unstable flow in the very near wake region as the origin of the sharp frequency selection observed at

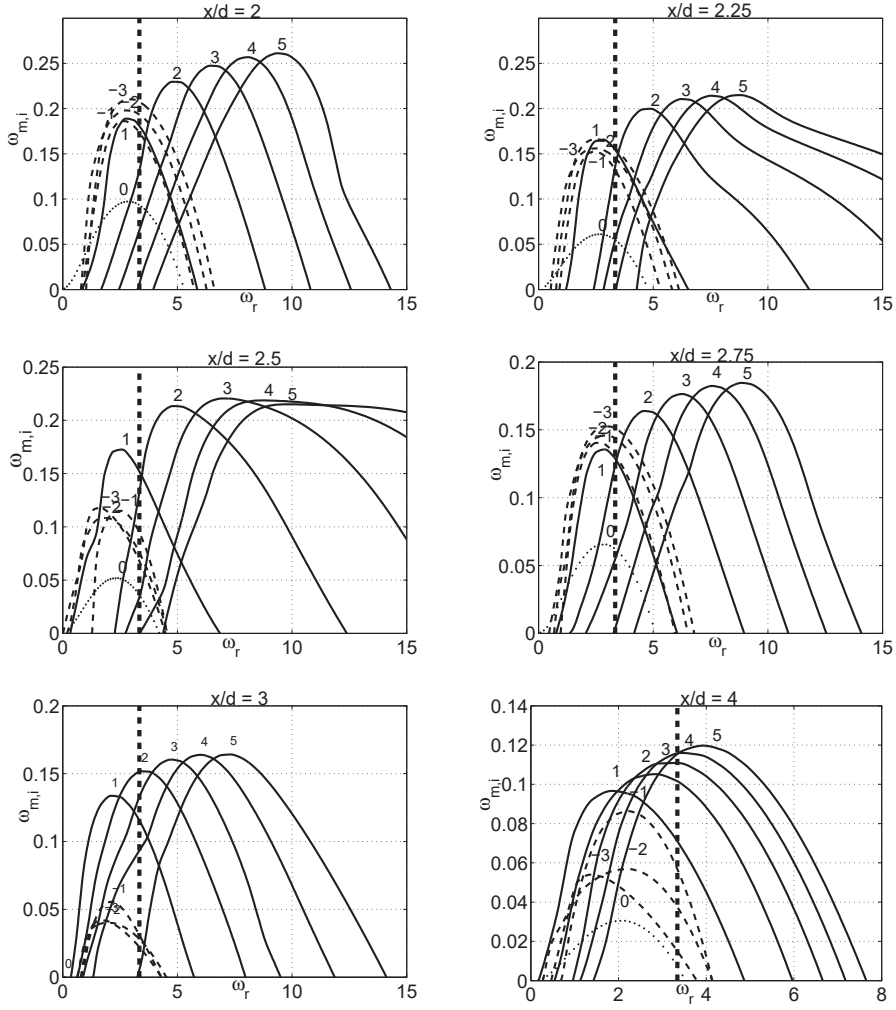


Figure 3.8: Growth rate as a function of the non-dimensional frequency for downstream locations from $x/d = 2$ up to $x/d = 4$. The vertical dashed line corresponds to the non-dimensional frequency measured experimentally and related to the hub vortex instability.

$x/d = 0.5$ and beyond, through the development of a self-sustained steep nonlinear global mode (Chomaz (2005), Pier & Huerre (2001)). While it cannot elucidate the detailed origin of the spectral signature, the spatial stability analysis of the convective region is perfectly valid: it will be seen to be very useful to characterize the spatial structure of the mode.

The numerical formulation of the spatial stability analysis is analogous to the one of the temporal analysis, see Eq. 3.8, with the exception that a complex streamwise wavenumber, k , and a real frequency, ω , are now considered. Therefore, the spatial stability analysis consists in a non-linear polynomial eigenvalue problem, as follows:

$$A_0(\omega)\mathbf{v} + kA_1(\omega)\mathbf{v} + k^2A_2(\omega)\mathbf{v} + k^3A_3(\omega)\mathbf{v} + k^4A_4(\omega)\mathbf{v} = 0 \quad (3.12)$$

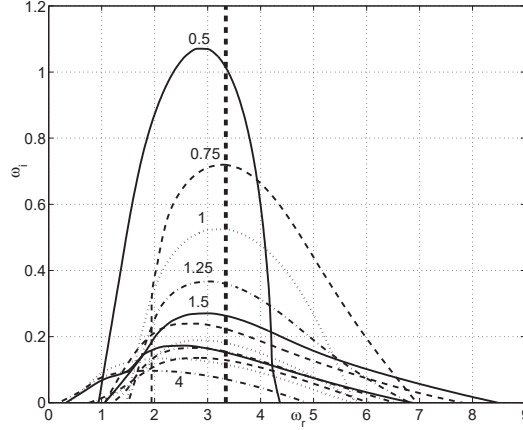


Figure 3.9: Growth rate as a function of the non-dimensional frequency for the mode $m = 1$ and different downstream locations. The vertical dashed line corresponds to the non-dimensional frequency measured experimentally and related to the hub vortex instability.

The opposite of imaginary part of k , $-k_i$, is the spatial amplification rate, whereas its real part, k_r corresponds to the streamwise wavenumber of the travelling wave, whose frequency is given by ω .

The solution of the equation (3.12) leads to a blow-up of spurious eigenvalues due to numerical discretization, which makes difficult the detection of the right eigenvalue with a physical significance. However, unstable waves propagating downstream are characterized by a positive axial phase velocity, $c_\phi = \omega/k_r$, and a negative growth rate, k_i . Thus, for positive ω the eigenvalues of interest are located in the fourth quadrant, i.e. with $k_r > 0$ and $k_i < 0$. To overcome issues related to the detection of the right eigenvalue between many spurious ones, the solution of equation (3.12) is evaluated by searching the closest eigenvalue to the one predicted through the Gaster transformation. The Gaster relation allows relating the temporal growth rate to the spatial growth rate in the vicinity of marginal stability, see Gaster (1962). In fact, the same dispersion relation is considered for the temporal analysis and spatial analysis, but it is solved for different variables. On the neutral curves temporal and spatial results are coincident, since $k_i = \omega_i = 0$ and $(k, \omega) \in \mathbb{R}$. For small imaginary parts a Taylor series expansion in the neighborhood of the neutral curves is used. The Gaster relation is the following:

$$\omega_i^{(T)} = -c_g k_i^{(S)} \quad (3.13)$$

stating that in the limit of small imaginary parts the temporal growth rate, $\omega_i^{(T)}$, and the spatial growth rate, $-k_i^{(S)}$, are related by the group velocity, c_g . Therefore, an approximation of the spatial instability results can be obtained from the the temporal analysis through the Gaster transformation.

For the spatial stability analysis, growth rates $-k_i(\omega_r, m)$ of the unstable spatial modes are represented as a function of the non-dimensional frequency, ω_r , for different m and down-

stream locations. In figures 3.10 and 3.11 the dashed lines represent the results of the Gaster approximation, whereas the solid lines correspond to the values $-k_i$ obtained from the spatial stability analysis. For downstream locations $x/d \geq 1.75$ the dashed and solid lines in figures 3.10 and 3.11 are practically coincident; in fact, the Gaster transformation and the spatial stability analysis produce roughly the same results, despite the large values of the spatial growth rate, $-k_i$. For the downstream location $x/d = 0.5$ the Gaster relation underestimates significantly the growth rate obtained with the spatial analysis. This discrepancy is mainly due to the large values of k_i and to the strong wake velocity deficit observed at this downstream location. Indeed, the Gaster transformation produces more accurate results for high convective flows, see e.g. Olendraru *et al.* (1999), Schmid & Henningson (2001) and Olendraru & Sellier (2002). Furthermore, as mentioned above, it has been verified that the strong peak of the spatial growth rate for $m = 1$ at $x/d = 0.5$, obtained from the spatial stability analysis, is not related to an absolute instability; indeed, no intersection in the complex plane $k_r - k_i$ between the positive and negative branches, k^+ and k^- , was detected (see Huerre & Rossi (1998), Olendraru *et al.* (1999), Schmid & Henningson (2001) and Olendraru & Sellier (2002) for details).

The results obtained with the spatial stability analysis are qualitatively similar to the ones obtained through the temporal stability analysis presented in §3.1.4. By considering the low-frequency instability connected the hub vortex, highlighted in figures 3.10 and 3.11 through a vertical dashed line in correspondence of $\omega_r = 3.18$, it is evident that for downstream locations from $x/d = 0.5$ up to $x/d = 2.75$ the selected unstable mode is the one with $m = 1$. Further downstream, i.e. at $x/d \approx 3$, the most unstable mode switches to $m = 2$ but with a much smaller spatial growth rate. At $x/d = 4$ the selected mode is the one with $m = 4$.

In order to determine the dominant unstable mode related to the low frequency instability of the hub vortex, the growth rates corresponding to $\omega_r = 3.18$ for the modes with $m = 1$ and $m = 2$ are plotted in figure 3.12 as a function of the streamwise location. Then, the integral amplification factor is evaluated for the two modes $m = 1$ and $m = 2$, as proposed by Oberleithner *et al.* (2011) and Juniper *et al.* (2011), according to:

$$G(\omega, m) = \exp\left(\int_{X_0}^{X_S} -k_i(\omega, m, X') dX'\right) \quad (3.14)$$

X_S is the streamwise position where the flow reenters in a stable domain. $G(\omega, m)$ represents the overall amplification of the mode m at the frequency ω within the wake, after it has gone through its entire amplification process. This integral amplification factor, computed from the position $x/d = 0.5$ up to $x/d = 4$, for the unstable mode with $m = 1$ is equal to 6.6, whereas for the one with $m = 2$ is 2.47, thereby suggesting the predominance of the $m = 1$ mode, i.e. a counter-winding single-helix structure. Using this simple procedure, the integral amplification factor can be systematically determined as a function of the frequency for the single helical mode, as shown in figure 3.13. It is striking to observe that the counter-winding single-helix mode is not only the most amplified in this frequency range, but it reaches its maximum amplification at a frequency very close to the one observed experimentally. While the present analysis does not reveal the origin of the sharp frequency selection mechanism observed in

3.1. Linear stability analysis of wind turbine wakes

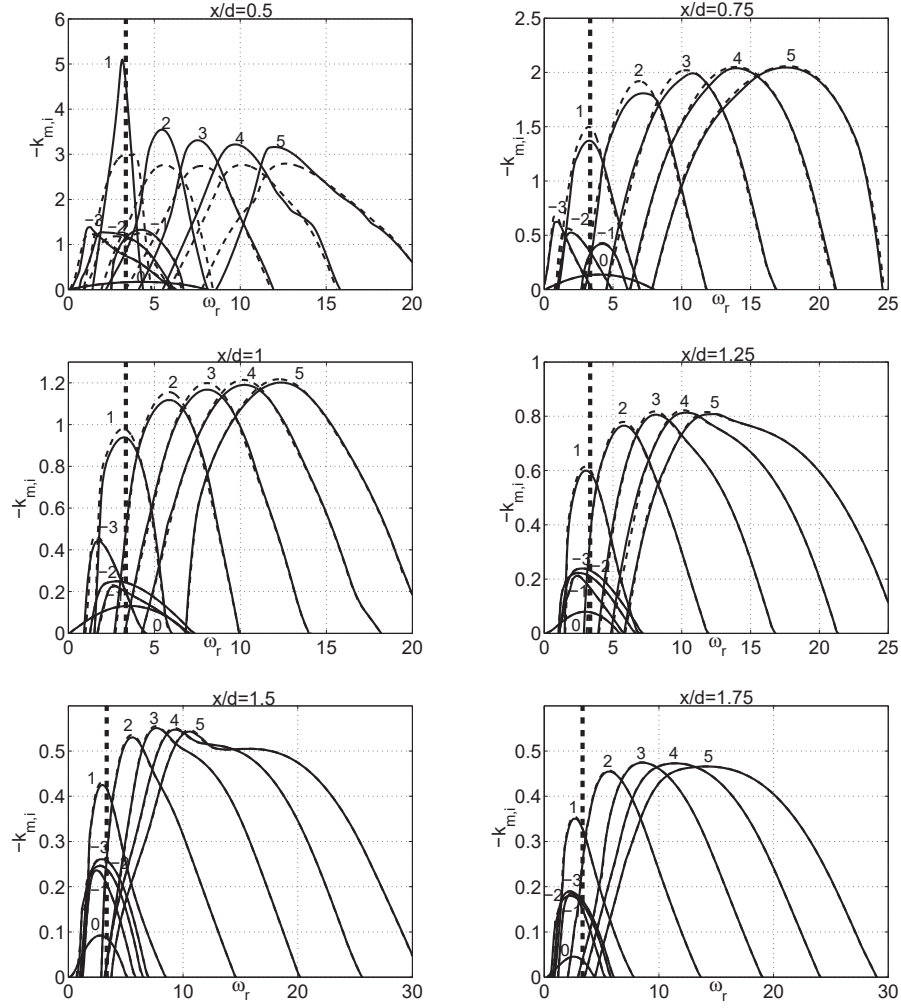


Figure 3.10: Growth rate evaluated through the Gaster approximation (dashed line) and spatial stability analysis (solid line) as a function of the non-dimensional frequency for downstream locations from $x/d = 0.5$ up to $x/d = 1.75$. The vertical dashed line corresponds to the non-dimensional frequency measured experimentally and related to the hub vortex instability.

the experiments, this shows that the most amplified frequency downstream from $x/d = 0.5$ matches the one measured in our experiments.

With the spatial stability analysis the real part of k , k_r , represents the axial wavenumber of the respective unstable mode. In figure 3.14 k_r is plotted as a function of the non-dimensional frequency, ω_r , for several downstream locations, considering different values of m . For the selected mode with $m = 1$ representing the hub vortex instability, the axial growth rate is about 4.5 and it is slightly reduced by moving downstream, except for the position $x/d = 0.5$ where $k_r = 6.31$ is obtained. Therefore, the single-helix instability of the hub vortex is characterized by an axial wavelength, $\lambda/d = 2\pi/k_r$, of about 1 at $x/d = 0.5$, then it is increased by moving downstream with a value of 1.65 at the location $x/d = 4$.

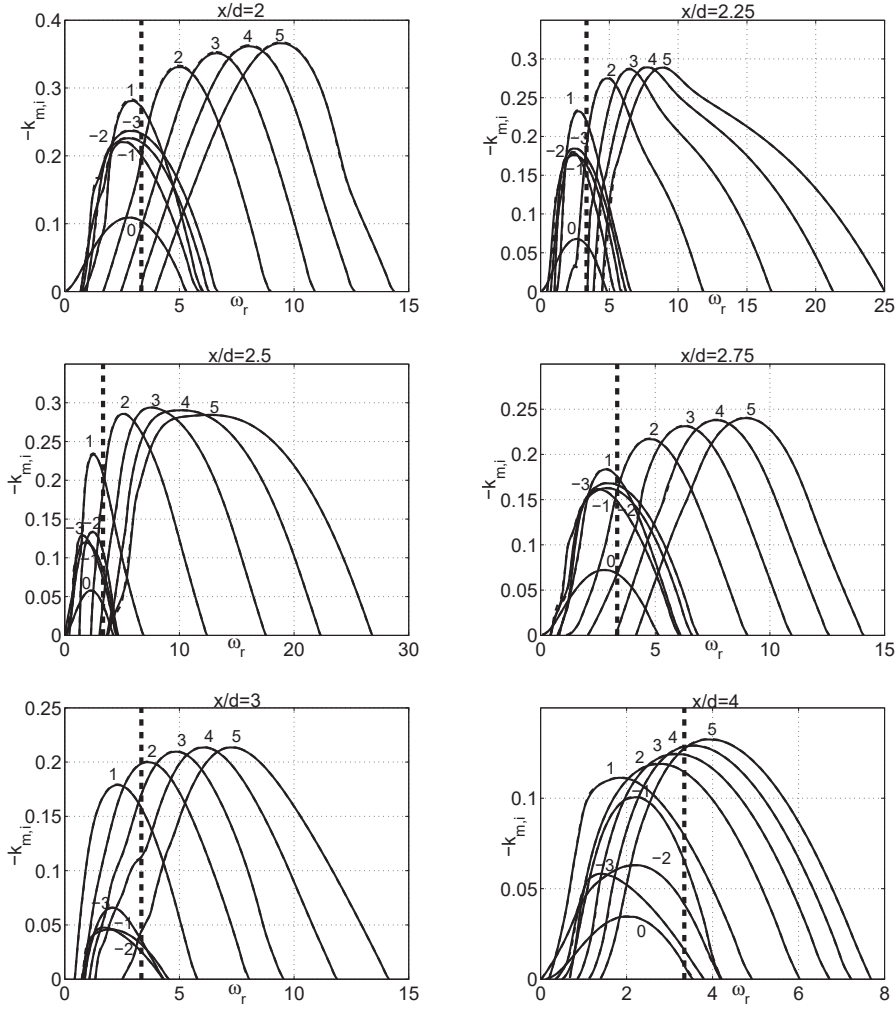


Figure 3.11: Growth rate evaluated through the Gaster approximation (dashed line) and spatial stability analysis (solid line) as a function of the non-dimensional frequency for downstream locations from $x/d = 2$ up to $x/d = 4$. The vertical dashed line corresponds to the non-dimensional frequency measured experimentally and related to the hub vortex instability.

It is now possible to perform the reconstruction of the single helix global mode representing the hub vortex instability by integrating the unstable eigenmode $m = 1$ in the x -direction, in agreement with equation (3.15) (see Oberleithner *et al.* (2011) and Juniper *et al.* (2011)):

$$u(x, r, \theta, t) \approx \text{Re} \left\{ A_0(X) \hat{u}(r, X) \exp \left[i \left(\int_{X_0}^X k(X', \omega) dX' + m\theta - \omega t \right) \right] \right\} \quad (3.15)$$

where k is the complex wavenumber, ω is the instability frequency and \hat{u} are the eigenmodes at the X -position normalized using the Euclidean norm, and phase-aligned at the characteristic vortex radius. The slowly varying amplitude $A_0(X)$ could be considered as uniform at the first order, in agreement with the WKBJ formulation. The axial vorticity of the local unstable mode

3.1. Linear stability analysis of wind turbine wakes

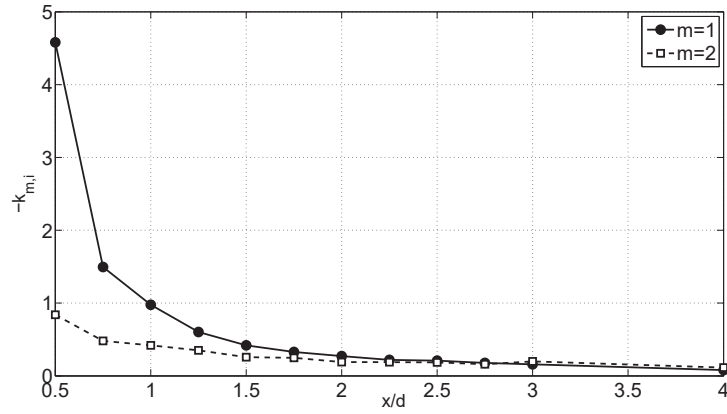


Figure 3.12: Spatial growth rates of the unstable modes with $m = 1$ and $m = 2$ as a function of the downstream location, x , corresponding to the non-dimensional frequency $\omega_r = 3.18$.

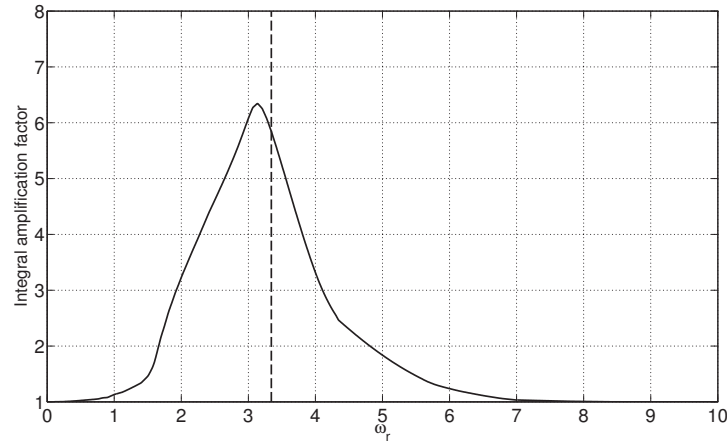


Figure 3.13: Integral amplification factor of the unstable mode with $m = 1$ as a function of the pulsation ω_r .

with $m = 1$ is plotted in figure 3.15. These vorticity structures clearly represent a coherent evolution of a single-helix unstable mode, although these eigenfunctions were obtained from experimental data acquired at different downstream locations. Finally, the global unstable mode with $m = 1$ is reconstructed along the x -direction, as for the axial vorticity reported in figure 3.16.

Further wind tunnel measurements were performed in order to provide an experimental evidence of this outlined helicoidal mode structure and in particular to assess the axial wavenumber predicted by the local stability analysis. To this goal, simultaneous measurements with two single-component hot-wire anemometers were carried out. For these tests one probe was placed at the fixed location $x/d = 0.13$, $y/d = 0.1$, $z/d = 0$ and another probe was set on the traversing system, which allows displacements of the probe along the x -direction, and at the transversal position $y/d = -0.1$ and $z/d = 0$. In other words the two probes were

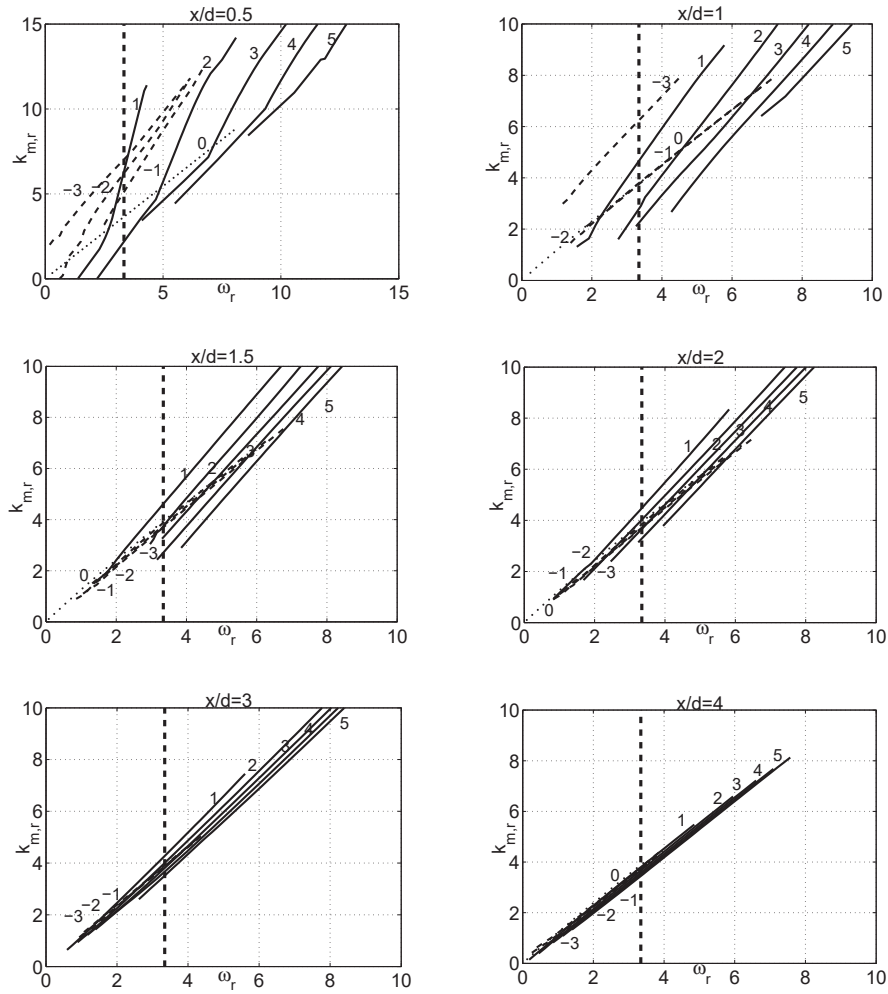


Figure 3.14: Axial wavenumber, k_r , evaluated through the spatial stability analysis as a function of the non-dimensional frequency. The vertical dashed line corresponds to the non-dimensional frequency measured experimentally and related to the hub vortex instability.

symmetrically located with respect to the wake centre and at a transversal distance where the spectral component related to the hub vortex instability was typically detected with maximum energy. For each acquired velocity signal, the spectral component of interest was extracted by using a filtering technique based on Proper Orthogonal Decomposition proposed in Iungo & Lombardi (2011), by using a frequency resolution of 5 Hz. This technique presents the advantage to automatically detect and extract the dominant spectral component, thus to emphasize the correlation between simultaneous signals by removing experimental noise and other spectral contributions.

The cross-correlation coefficient between the extracted components from the velocity signals acquired simultaneously on the two sides of the wake was then calculated for different downstream locations. These tests were driven by the idea that in case the hub vortex is

3.1. Linear stability analysis of wind turbine wakes

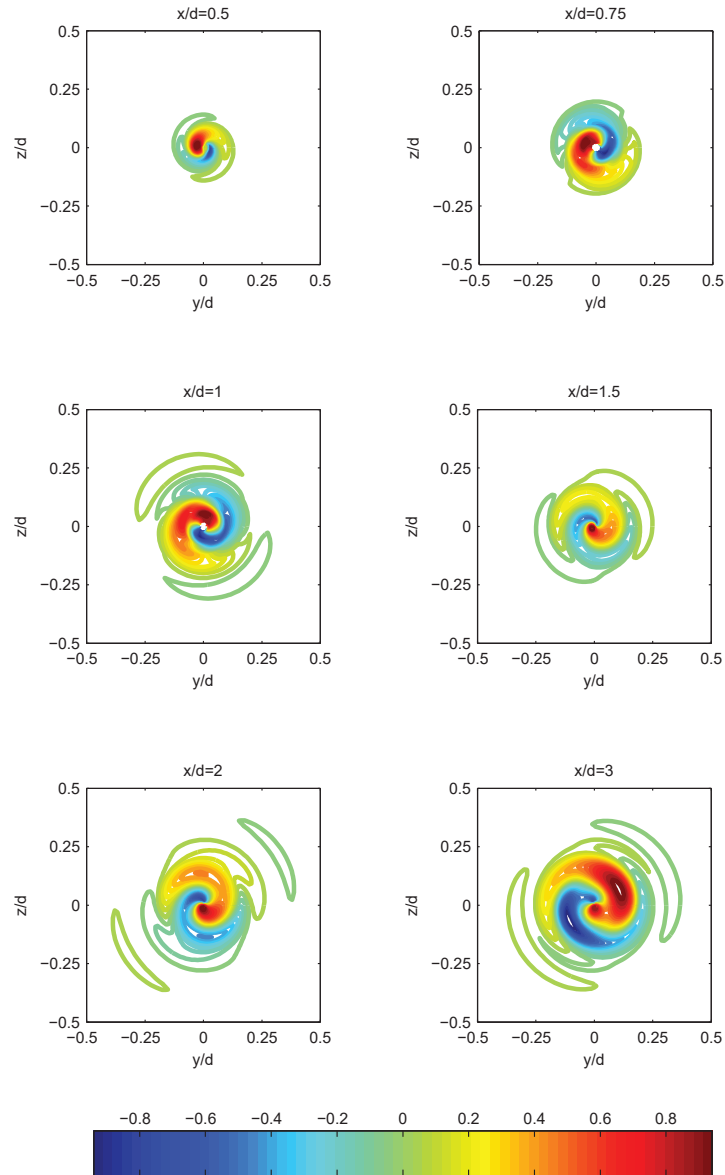


Figure 3.15: Axial vorticity of the selected unstable eigenmode with $m = 1$ reconstructed through the spatial stability analysis.

characterized by helicoidal instability, the cross-correlation coefficient between the time series acquired on the two sides of the wake should follow a harmonic function when one probe is placed at a fixed position and the other one is moved downstream. Furthermore, the wavelength of the harmonic function detected through the cross-correlation coefficient should reproduce the same axial wavenumber of the helicoidal structure. Indeed, the cross-correlation coefficient evaluated for different downstream locations clearly reproduces a

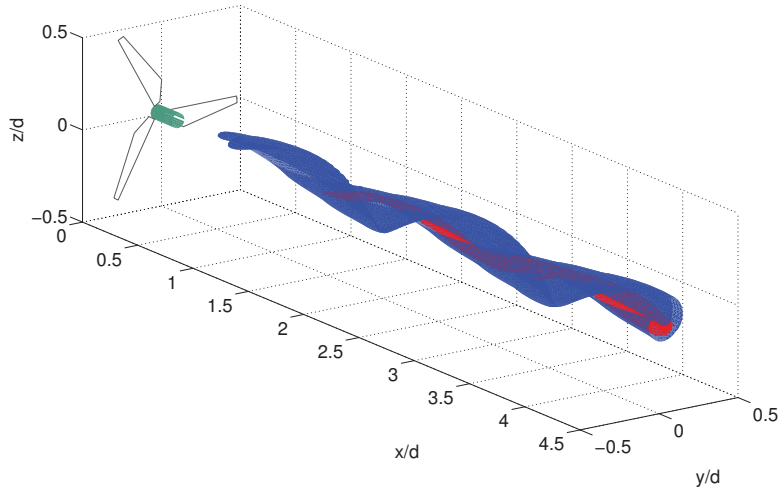


Figure 3.16: Reconstruction of the hub vortex instability corresponding to the mode with $m = 1$. Iso-surface of the axial vorticity.

harmonic trend, as shown in figure 3.17, with a slightly reducing amplitude and frequency by moving downstream, which can be connected to the diffusion of the hub vortex. Therefore, the simultaneous hot-wire measurements confirm the presence of a helicoidal instability of the hub vortex predicted through the linear stability analysis.

Moreover, the instantaneous wavelength of the cross-correlation coefficient as a function

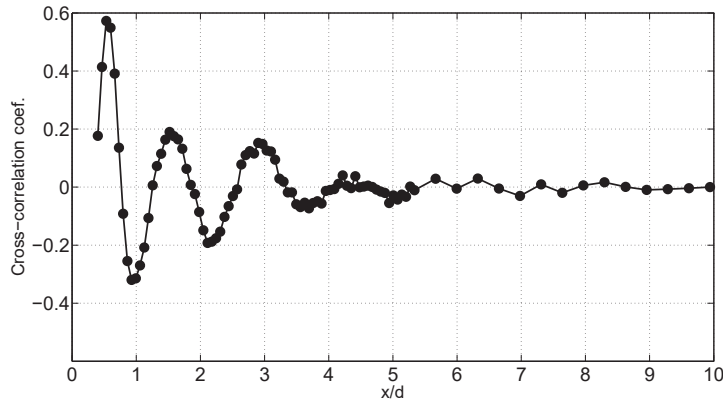


Figure 3.17: Cross-correlation coefficient between hot-wire time-series acquired simultaneously at $y/d = \pm 0.1$ and $z/d = 0$ as a function of the streamwise location.

of the downstream location is then computed through the Hilbert transform, see Iungo & Lombardi (2011) for details. This parameter is plotted in figure 3.18 and compared to the results obtained through the spatial stability analysis, i.e. with $2\pi/k_r$ corresponding to the unstable mode with $m = 1$ and at the non-dimensional frequency corresponding to the hub vortex instability, $\omega_r = 3.18$. The experimental results generally confirm the data obtained through the linear stability analysis, i.e. the hub vortex is characterized by a helicoidal instability with a wavelength $\lambda/d = 1$ at the downstream location $x/d = 0.5$. Then, it is gradually increased

3.1. Linear stability analysis of wind turbine wakes

by moving downstream up to a value $\lambda/d \approx 1.6$ at $x/d = 4$. Slightly different results are found for the locations $0.5 < x/d < 1.5$, where the wavelength varies more rapidly. However, both experimental data and linear instability results show a good agreement and a gradual increase of the streamwise wavelength with increasing streamwise distance from the turbine location. By moving downstream an increase of the wavelength of the unstable mode related to the hub vortex is connected to the diffusion of the hub vortex and the imminent breakdown of this vorticity structure, which compares well with previous works like e.g. Sarpkaya (1971) and Felli *et al.* (2011). Furthermore, from figure 3.17, and also from the Fourier spectra reported in figure 3.4, the energy content connected to the hub vortex instability decays in the downstream direction, whereas the linear stability analysis predicts a growth. This feature can be ascribed to the linearity of the stability analysis, which does not take the non-linear saturation of the mode into account. Indeed, diffusive effects caused by Reynolds stresses are neglected, which affects the estimated growth rates.

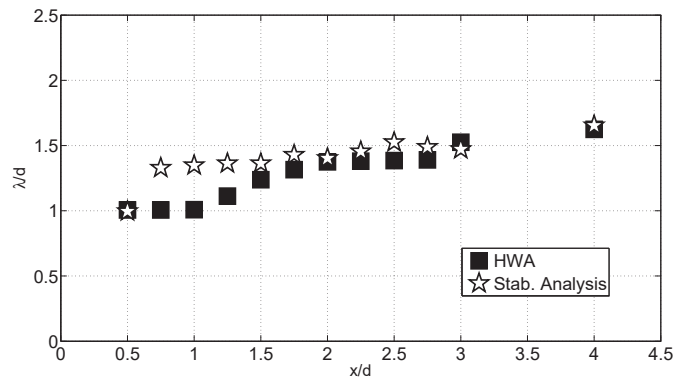


Figure 3.18: Comparison of the axial wavelength of the global unstable mode evaluated through the linear stability analysis and the simultaneous hot-wire measurements, *HWA*.

3.1.6 Discussion and final remarks

Wind tunnel measurements of a wake produced by a wind turbine immersed in uniform flow showed the presence of an axial vorticity structure in the very near wake, which is denoted as hub vortex. The hub vortex is characterized by oscillations with a frequency equal to 0.34 times the rotational frequency of the wind turbine rotor. In previous works these flow fluctuations were ascribed to wake wandering or meandering, which consists in transversal oscillations of the wind turbine wake. Wake meandering was investigated in details in Medici & Alfredsson (2008); in fact, these authors stated that this phenomenon is mainly excited by the shedding of vorticity structures from the rotor disc acting as a bluff body.

To further investigate the above-mentioned low-frequency wake instability detected experimentally, linear stability analysis has been performed. The evolution of perturbations acting on a mean flow obtained through wind tunnel velocity measurements has been investigated. The temporal stability analysis has shown that the most unstable mode corresponding to the low-frequency instability of the hub vortex is characterized by a single-helix counter-winding

mode and rotating in the same direction of the hub vortex. This result is obtained in the near wake up to a downstream distance of 2.5 rotor diameters. Further downstream unstable modes with a higher azimuthal wavenumber, m , start to be dominant. However, by moving downstream a reduction of the growth rates of the unstable modes has been generally observed. Therefore, a possible competition between different unstable modes can take place by moving downstream, while the hub vortex is rapidly diffusing. It should be pointed out that the single-helix counter-winding unstable mode ($m = 1$) is not always the one with the highest growth rate, but it is generally the one corresponding to the experimentally measured frequency of the spectral component connected to the hub vortex instability. This suggests that for the wind turbine wake flow produced in the wind tunnel, unstable modes with a higher azimuthal wavenumber are damped, thus the dominating mode results to be the one with $m = 1$. This reduction of the growth rates related to unstable modes with a higher azimuthal wavenumber could be due to diffusive effects connected to turbulent fluctuations, which are not taken into account for the linear stability analysis.

In order to deeper investigate on a possible competition between unstable modes with a different azimuthal wavenumber, m , a spatial stability analysis has been performed, which is more suitable for convectively unstable flows. The spatial stability analysis has confirmed the results obtained from the temporal analysis, and in addition it has allowed determining through the evaluation of the integral growth rate that the dominant unstable mode has an azimuthal wavenumber equal to one ($m = 1$). The global unstable mode characterized by a single-helix counter-winding structure has been reconstructed, in particular characterizing the evolution of the axial wavelength by moving downstream. Further hot-wire measurements were then performed to assess experimentally the presence of a helicoidal instability of the hub vortex. To this goal simultaneous hot-wire measurements were performed by placing two probes at hub height, on the two side of the wake and with the same spanwise distance from the hub, i.e. where the frequency connected to the hub vortex instability has the maximum energy. During the tests one probe was placed at a fixed location, while the other one was moved downstream. The spectral component connected to the hub vortex instability was then extracted from the velocity signals. The cross-correlation coefficient between the signals acquired simultaneously, evaluated as a function of the streamwise location, has shown a harmonic trend confirming the presence of a helicoidal instability of the hub vortex. Furthermore, the local axial wavelength of this harmonic function obtained from the cross-correlation coefficient accurately confirms the evolution of the axial wavenumber of the most unstable mode predicted through the linear stability analysis.

The single-helix counter-winding unstable mode of the hub vortex obtained through this linear stability analysis is in strong agreement with the instability of the hub vortex produced by a marine propeller visualized in Felli *et al.* (2011). The main difference with the present work is that for the case of the marine propeller the frequency related to hub vortex instability is equal to the rotational frequency of the rotor, whereas for the present experimental case this frequency is 0.34 times the rotational frequency of the rotor, which is in good agreement with previous wind tunnel investigations of wind turbine models, like e.g. Medici & Alfredsson (2008), Chamorro & Porté-Agel (2010) and Zhang *et al.* (2012).

3.1. Linear stability analysis of wind turbine wakes

While it is very tempting to attribute the sharp frequency selection typical of an oscillator behaviour to an absolutely unstable region in the near wake region, this could not be confirmed experimentally with the presently used measurement techniques. Still, our study has revealed:

(i) that the most amplified frequency downstream of $x/d = 0.5$ matches the one measured in our experiments. This might be a pure coincidence or point to a selective noise amplification mechanism to be further identified.

(ii) that, in contrast to most commonly accepted nonlinear global mode shapes predicted from nonlinear front theories (see Chomaz (2005) for a review and Couairon & Chomaz (1999) for a detailed analysis), the coherent structure observed in this study does not display a sharp front located at the convective to absolute transition location. The spectral energy associated to the hub vortex is seen to increase up to $x/d = 1$ before it starts to decay, as readily seen in figure 3.4. This observation is consistent with the study of Felli *et al.* (2011) who have also observed that the hub vortex instability starts only at a downstream distance of few rotor diameters.

Unravelling the detailed origin of the sharp frequency selection through precise measurements in the very near wake region constitutes therefore both a natural continuation of this study as well as a formidable experimental challenge.

Currently further wind tunnel tests and respective linear instability analyses are under-way in order to bring this study to more practical applications, as the case of a wind turbine immersed in a boundary layer flow or the case of interaction of wind turbine wakes within a wind farm.

3.2 Prediction of the hub vortex instability in a wind turbine wake: stability analysis with eddy-viscosity models calibrated on wind tunnel data

F. Viola¹, G.V. Iungo², S. Camarri³, F. Porté-Agel² and F. Gallaire¹

¹ Laboratory of Fluid Mechanics and Instabilities, École Polytechnique Fédérale de Lausanne, Lausanne, CH-1015, Switzerland

² Wind Engineering and Renewable Energy Laboratory, École Polytechnique Fédérale de Lausanne, Lausanne, CH-1015, Switzerland

³ Department of Civil and Industrial Engineering, University of Pisa, Pisa 56122, Italy

Journal of Fluid Mechanics 750 (2014): R1.

The instability of the hub vortex observed in wind turbine wakes has been recently studied by Iungo *et al.* (2013) via local stability analysis of the mean velocity field measured through wind tunnel experiments. This analysis was carried out by neglecting the effect of turbulent fluctuations on the development of the coherent perturbations. In the present paper, we perform a stability analysis taking into account the Reynolds stresses modeled by eddy-viscosity models, which are calibrated on the wind tunnel data. This new formulation for the stability analysis leads to the identification of one clear dominant mode associated with the hub vortex instability, which is the one with the largest overall downstream amplification. Moreover, this analysis also predicts accurately the frequency of the hub vortex instability observed experimentally. The proposed formulation is of general interest for the stability analysis of swirling turbulent flows.

3.2.1 Introduction

The flow past a wind turbine is characterized by two main large-scale vorticity structures: the helicoidal tip vortices, which detach from the tip of each turbine blade, and the hub vortex, which is a streamwise-oriented vorticity structure approximately located at the wake centre. Several wind tunnel experiments of down-scaled wind turbine models showed that, besides the frequency connected with the shedding of tip vortices, wake velocity signals can present a different spectral contribution with a frequency lower than the one of the rotor rotation. In Medici & Alfredsson (2006, 2008); Chamorro & Porté-Agel (2009); Zhang *et al.* (2012), this low-frequency instability was typically ascribed to a global meandering of the wind turbine wake. In LES simulations using actuator disc and actuator line turbine models the far-wake is simulated with sufficient accuracy to reproduce wake meandering (see for instance Wu & Porté-Agel (2011) and España *et al.* (2011)). More recently Iungo *et al.* (2013) showed, via local stability analysis performed on the time-averaged wind tunnel velocity measurements, that the low-frequency clearly detected in the near-wake, is related to a single-helix counter-

winding instability of the hub vortex, which can also affect the meandering phenomenon in the far-wake. Kang *et al.* (2014) confirmed the results in Iungo *et al.* (2013) by carrying out LES simulations which include all geometrical details of the wind turbine by a curvilinear immersed boundary method.

The main limitation of the analysis presented in Iungo *et al.* (2013), which is focused on the hub vortex instability, is that the instability observed experimentally was not predicted through the local stability analysis as the unstable mode with the largest growth rate. Indeed, it was necessary to use the instability frequency of the hub vortex, which was determined via wind tunnel measurements, as an additional input for the stability analysis in order to detect the mode associated with the hub vortex instability. The main reason for difficulties in the identification of the dominant unstable mode by the sole stability analysis was attributed to the neglecting of the Reynolds stresses in the Orr-Sommerfeld equations.

In this paper, a stability analysis is performed by taking into account the effects of the Reynolds stresses by means of eddy-viscosity models, which are calibrated on the wind tunnel data. Other studies in the literature considered eddy-viscosity models to close the linearized equations for the coherent velocity field in a turbulent flow (see, e.g., Reynolds & Hussain, 1972; Bottaro *et al.*, 2006; Crouch *et al.*, 2007; Cossu *et al.*, 2009; Meliga *et al.*, 2012a). A similar but more sophisticated closure is proposed in Kitsios *et al.* (2010, 2011). For the present investigation three eddy-viscosity models are considered: one model based on the assumption of a uniform eddy-viscosity for each streamwise location, whereas for the other two models a mixing-length is estimated. In this paper it is shown that with the proposed improved formulation, stability analysis allows not only the unambiguous identification of the hub vortex instability, but also the accurate prediction of its instability frequency.

The paper is organized as follows: the formulation of the stability analysis by taking into account the Reynolds stresses is presented in §2. The wind tunnel data are then described in §3, while the three eddy-viscosity models and their calibration against the wind tunnel data are reported in §4. The characterization of the hub vortex instability is presented in §5. Finally, conclusions are drawn in §6.

3.2.2 Problem formulation

Triple decomposition and linearized equations for the coherent perturbation

Following the approach proposed in Reynolds & Hussain (1972), the unsteady flow, $\mathbf{U}(\mathbf{x}, t)$, is decomposed in the time-averaged base-flow, $\overline{\mathbf{U}}(\mathbf{x})$, the coherent fluctuation, $\tilde{\mathbf{u}}(\mathbf{x}, t)$, and the turbulent motion, $\mathbf{u}'(\mathbf{x}, t)$:

$$\mathbf{U} = \overline{\mathbf{U}} + \tilde{\mathbf{u}} + \mathbf{u}'$$

where the sum of the time-averaged flow and the coherent fluctuation coincides with the ensemble averaged flow $\langle \mathbf{U} \rangle = \overline{\mathbf{U}} + \tilde{\mathbf{u}}$ (see also Reau & Tumin (2002)).

The stability of the flow is given by the tendency of $\tilde{\mathbf{u}}$ to grow (unstable) or decay (stable) in time and space. Thus, stability can be verified by a modal analysis of the linearized dynamics of $\tilde{\mathbf{u}}$. To this purpose the non-linear evolution of the coherent perturbation for an incompressible

Chapter 3. Hub vortex instability

flow can be written as (see, e.g., Reynolds & Hussain, 1972):

$$\begin{aligned} \nabla \cdot \tilde{\mathbf{u}} &= 0 \\ \frac{\partial \tilde{\mathbf{u}}}{\partial t} + \nabla \tilde{\mathbf{u}} \cdot \bar{\mathbf{U}} + \nabla \bar{\mathbf{U}} \cdot \tilde{\mathbf{u}} &= -\nabla \bar{p} + \frac{1}{\text{Re}} \Delta \tilde{\mathbf{u}} - \nabla \cdot [\tilde{\mathbf{u}}\tilde{\mathbf{u}} - \overline{\tilde{\mathbf{u}}\tilde{\mathbf{u}}}] - \nabla \cdot [\langle \mathbf{u}'\mathbf{u}' \rangle - \overline{\mathbf{u}'\mathbf{u}'}] \end{aligned} \quad (3.16)$$

In the framework of a linear analysis with respect to the coherent fluctuations $\tilde{\mathbf{u}}$, the third term of the rhs is neglected. However, the system of equations is not closed and the last term of the rhs, related to the turbulent diffusion, has to be modeled. As in Reynolds & Hussain (1972) and Cossu *et al.* (2009), the linear relationship between the strain rate and the Reynolds stresses is considered here. In the following two equations, the Boussinesq hypothesis is written using time and ensemble averaging, respectively:

$$\begin{cases} -\overline{\mathbf{u}'\mathbf{u}'} + \frac{2}{3}\bar{q}I \simeq \nu_t^m[\nabla + \nabla^T]\bar{\mathbf{U}} \\ -\langle \mathbf{u}'\mathbf{u}' \rangle + \frac{2}{3}\langle q \rangle I \simeq \nu_t^e[\nabla + \nabla^T]\langle \mathbf{U} \rangle \end{cases} \quad (3.17)$$

where q is the turbulent kinetic energy (TKE) and I is the 3x3 identity matrix. The eddy-viscosity depends on $\bar{\mathbf{U}}$ (i.e. $\nu_t^m(\bar{\mathbf{U}})$) in the case of time averaging and on $\langle \mathbf{U} \rangle$ (i.e. $\nu_t^e(\langle \mathbf{U} \rangle) = \nu_t^e(\bar{\mathbf{U}} + \tilde{\mathbf{u}})$) in the case of ensemble averaging. By linearizing ν_t^e at first order with respect to $\tilde{\mathbf{u}}$, it is possible to rewrite it as the sum of one function of the mean flow and one linear function of the coherent fluctuation, $\nu_t^e(\bar{\mathbf{U}} + \tilde{\mathbf{u}}) \simeq \nu_t^e(\bar{\mathbf{U}}) + \nabla_{\mathbf{U}}\nu_t^e(\bar{\mathbf{U}}) \cdot \tilde{\mathbf{u}}$, (see Appendix 3.2.7). In order to determine the relation between $\nu_t^m(\bar{\mathbf{U}})$ and $\nu_t^e(\bar{\mathbf{U}})$, the second equation in (3.17) is averaged in time. Since time average of ensemble average corresponds to time average itself ($\overline{\langle \cdot \rangle} = \langle \cdot \rangle$), we obtain the following set of identities:

$$\begin{aligned} -\overline{\mathbf{u}'\mathbf{u}'} + \frac{2}{3}\bar{q}I &= -\overline{\langle \mathbf{u}'\mathbf{u}' \rangle} + \frac{2}{3}\overline{\langle q \rangle} I \simeq \overline{\nu_t^e(\langle \mathbf{U} \rangle)[\nabla + \nabla^T]\langle \mathbf{U} \rangle} \simeq \\ &\overline{\nu_t^e(\bar{\mathbf{U}})[\nabla + \nabla^T]\bar{\mathbf{U}} + (\nabla_{\mathbf{U}}\nu_t^e(\bar{\mathbf{U}}) \cdot \tilde{\mathbf{u}})[\nabla + \nabla^T]\bar{\mathbf{U}} + \nu_t^e(\bar{\mathbf{U}})[\nabla + \nabla^T]\tilde{\mathbf{u}}} \\ &+ \overline{(\nabla_{\mathbf{U}}\nu_t^e(\bar{\mathbf{U}}) \cdot \tilde{\mathbf{u}})[\nabla + \nabla^T]\tilde{\mathbf{u}}} \simeq \nu_t^e(\bar{\mathbf{U}})[\nabla + \nabla^T]\bar{\mathbf{U}} \end{aligned} \quad (3.18)$$

where second and third terms of rhs in the last identity are rigorously null because the averaged quantities depend linearly on $\tilde{\mathbf{u}}$. The fourth term is neglected since it is of higher order in $\tilde{\mathbf{u}}$. Consequently, the last (quasi-)identity follows and, together with the first equation in (3.17), it leads to the result: $\nu_t^e(\bar{\mathbf{U}}) = \nu_t^m(\bar{\mathbf{U}})$.

According to the previous results, the term $\langle \mathbf{u}'\mathbf{u}' \rangle - \overline{\mathbf{u}'\mathbf{u}'}$ can be modeled as:

$$\begin{aligned} \langle \mathbf{u}'\mathbf{u}' \rangle - \overline{\mathbf{u}'\mathbf{u}'} &\simeq -\nu_t^e(\bar{\mathbf{U}} + \tilde{\mathbf{u}})[\nabla + \nabla^T]\langle \mathbf{U} \rangle + \nu_t^m(\bar{\mathbf{U}})[\nabla + \nabla^T]\bar{\mathbf{U}} + \frac{2}{3}\langle q \rangle I - \frac{2}{3}\bar{q}I \simeq \\ &-\nu_t^e(\bar{\mathbf{U}})[\nabla + \nabla^T]\bar{\mathbf{U}} - (\nabla_{\mathbf{U}}\nu_t^e(\bar{\mathbf{U}}) \cdot \tilde{\mathbf{u}})[\nabla + \nabla^T]\bar{\mathbf{U}} - \nu_t^e(\bar{\mathbf{U}})[\nabla + \nabla^T]\tilde{\mathbf{u}} \\ &\quad - (\nabla_{\mathbf{U}}\nu_t^e(\bar{\mathbf{U}}) \cdot \tilde{\mathbf{u}})[\nabla + \nabla^T]\tilde{\mathbf{u}} + \nu_t^m(\bar{\mathbf{U}})[\nabla + \nabla^T]\bar{\mathbf{U}} + \frac{2}{3}\langle q \rangle I - \frac{2}{3}\bar{q}I \end{aligned} \quad (3.19)$$

3.2. Prediction of the hub vortex instability

The first and fifth terms in the last identity cancel out since $v_t^e(\bar{\mathbf{U}}) = v_t^m(\bar{\mathbf{U}})$. The fourth term is neglected because it is of higher order in $\tilde{\mathbf{u}}$, yielding:

$$\langle \mathbf{u}'\mathbf{u}' \rangle - \overline{\mathbf{u}'\mathbf{u}'} \simeq -(\nabla_{\mathbf{U}} v_t^e(\bar{\mathbf{U}}) \cdot \tilde{\mathbf{u}})[\nabla + \nabla^T]\bar{\mathbf{U}} - v_t^e(\bar{\mathbf{U}})[\nabla + \nabla^T]\tilde{\mathbf{u}} + \frac{2}{3} \langle q \rangle I - \frac{2}{3} \bar{q} I \quad (3.20)$$

As in Reynolds & Hussain (1972) and Kitsios *et al.* (2010) we assume that the phase-averaging process affects the turbulence structure but not the energy, i.e. $\langle q \rangle \simeq \bar{q}$, obtaining:

$$\langle \mathbf{u}'\mathbf{u}' \rangle - \overline{\mathbf{u}'\mathbf{u}'} \simeq -(\nabla_{\mathbf{U}} v_t^e(\bar{\mathbf{U}}) \cdot \tilde{\mathbf{u}})[\nabla + \nabla^T]\bar{\mathbf{U}} - v_t^e(\bar{\mathbf{U}})[\nabla + \nabla^T]\tilde{\mathbf{u}} \quad (3.21)$$

The term $v_t^e(\bar{\mathbf{U}}) = v_t^m(\bar{\mathbf{U}})$ in Eq. (3.21) can be evaluated from the statistics of the experimental data, as in Kitsios *et al.* (2010), while the term $\nabla_{\mathbf{U}} v_t^e(\bar{\mathbf{U}}) \cdot \tilde{\mathbf{u}}$ is obtained by the linearization of the turbulence model used to close the equations, as detailed in Appendix 3.2.7. When Eq. (3.21) is substituted in Eq. (3.32), the linear evolution of the coherent perturbation $\tilde{\mathbf{u}}$ with modeled Reynolds stresses is retrieved:

$$\frac{\partial \tilde{\mathbf{u}}}{\partial t} + \nabla \tilde{\mathbf{u}} \cdot \bar{\mathbf{U}} + \nabla \bar{\mathbf{U}} \cdot \tilde{\mathbf{u}} = -\nabla \tilde{p} + \frac{1}{\text{Re}} \Delta \tilde{\mathbf{u}} + \nabla \cdot (v_t(\bar{\mathbf{U}})[\nabla + \nabla^T]\tilde{\mathbf{u}}) + \nabla \cdot ((\nabla_{\mathbf{U}} v_t(\bar{\mathbf{U}}) \cdot \tilde{\mathbf{u}})[\nabla + \nabla^T]\bar{\mathbf{U}}) \quad (3.22)$$

Equation (3.52) is analogous to the one used in Reynolds & Hussain (1972); Cossu *et al.* (2009); Del Álamo & Jimenez (2006), but the last term in the rhs is included to take the linearization of the turbulence model into account. This corresponds to a generalization of the formulation of Crouch *et al.* (2007) and Meliga *et al.* (2012a) based on the Spalart-Allmaras model. From now on the suffix for the eddy-viscosity, e and m , will not be specified any longer because they are redundant.

Application to parallel flow

In the framework of weakly-non-parallel stability analysis, Eq. (3.52) is now applied to a parallel flow $\bar{\mathbf{U}} = (\bar{U}_x, \bar{U}_\theta, 0)$ extracted at a given streamwise location, since experiments showed a negligible radial velocity component (Iungo *et al.* (2013)). This allows for a modal expansion of the coherent fluctuation in the following form:

$$\tilde{\mathbf{u}}(x, \theta, r, t) = \hat{\mathbf{u}}(r) \exp(ikx + im\theta - i\omega t) \quad (3.23)$$

where k and m are the axial and azimuthal wavenumber respectively, and ω is the frequency. When this modal form is substituted in Eq. (3.52), an eigenvalue problem is obtained. In the temporal stability analysis k is real and assigned, while ω is the complex eigenvalue of the problem. The opposite choice is done for the spatial stability analysis. In both cases, m is a free integer parameter.

For the stability analysis, equation (3.52) together with continuity equation are discretized using a code based on a Chebyshev spectral collocation method. In the present analysis the number of collocation points is $N = 120$ and the size of the domain in the radial direction is

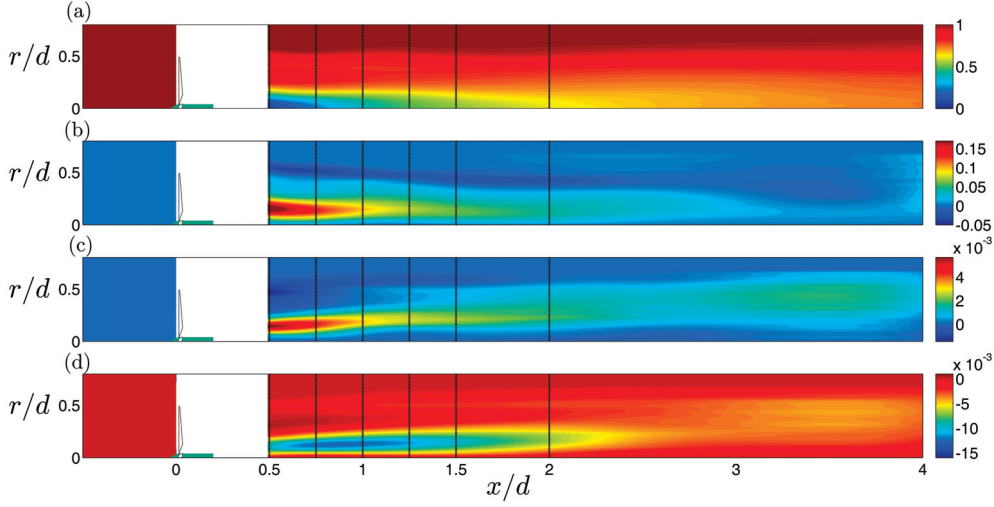


Figure 3.19: Nondimensional mean velocity components and tangential Reynolds stresses acquired in the wind tunnel. (a) Axial \overline{U}_x/U_{hub} and (b) azimuthal $\overline{U}_\theta/U_{hub}$ velocities, (c) $\overline{u'_r u'_\theta}/U_{hub}^2$ and (d) $\overline{u'_r u'_x}/U_{hub}^2$. Vertical lines depict the streamwise positions where local stability analysis has been carried out. In the white region measurements are not available.

$r_{max}/d = 50$. This choice provides the convergence of the most unstable eigenvalue with a five-digit accuracy, which is sufficient for the present purposes.

3.2.3 Wind tunnel measurements

Velocity measurements of the wake produced by a down-scaled three-bladed wind turbine were performed in the boundary layer wind tunnel of the Wind Engineering and Renewable Energy Laboratory (WIRE) of the École Polytechnique Fédérale de Lausanne (EPFL). For details on the experimental setup and measurement techniques we refer to Iungo *et al.* (2013). The tip speed ratio of the turbine (TSR), which is the ratio between the speed of the blade tip and the oncoming velocity at hub height ($U_{hub} = 6.9 \text{ ms}^{-1}$) is equal to 4.6 with a freestream turbulence level equal to 6%. The stability equations and the subsequent results are normalized using U_{hub} as the reference velocity and the rotor diameter, $d = 0.152 \text{ m}$, as the reference length, leading to a flow Reynolds number equal to 72000. For these tests the mean rotational frequency was $f_{hub} \approx 66 \text{ Hz}$ and the frequency connected to the tip vortex shedding was equal to three times f_{hub} , i.e. $f_{tip \text{ vortices}} \approx 198 \text{ Hz}$. The frequency related to the hub vortex instability was 21 Hz, i.e. approximately equal to $0.32 f_{hub}$. This instability frequency corresponds to a non-dimensional pulsation of $\omega_{hub \text{ vortex}} = 2\pi d f_{hub \text{ vortex}}/U_{hub} = 2.9$.

Since the turbine is placed outside the boundary layer and invested by a uniform oncoming flow, the produced mean wake flow is axisymmetric. Experiments show also a negligible radial component of the velocity, which is thus completely characterized by the axial, \overline{U}_x , and azimuthal, \overline{U}_θ , velocity components. The experimental time-averaged velocity field and the Reynolds stresses used for the stability analysis are plotted in figure 3.19. Velocity mea-

measurements cannot be performed at a downstream distance smaller than $0.5 d$ with hot-wire anemometers and Cobra probes. Indeed, at those locations the strong axial velocity deficit and the large tangential velocity produce an angle between the probe axis and the velocity vector larger than 45° , which is the acceptance angle to perform velocity measurements with an acceptable accuracy. Besides this technical limitation, in the very near-wake the roll-up of the wake vorticity structures produces strong velocity gradients along the streamwise direction, thus the weakly non-parallel assumption adopted for the stability analysis cannot be ensured. The reported vertical lines correspond to the sections where local stability analysis was carried out, i.e. $x/d = 0.5, 0.75, 1, 1.25, 1.5, 2$. On the other hand, sections at $x/d > 2$ are not considered here since in that region the growth rates are significantly smaller in comparison with the ones evaluated for the upstream locations (see Iungo *et al.* (2013)).

3.2.4 Eddy-viscosity models

Description of the considered turbulence closure models

As already pointed out, the Boussinesq hypothesis yields:

$$\overline{R} = \overline{\mathbf{u}'\mathbf{u}'} \approx -2\nu_t \overline{S} + \frac{2}{3} \overline{q} I \quad (3.24)$$

where R is the Reynolds stress tensor and S is the strain rate tensor. In the framework of a local stability analysis of a wind turbine wake flow, we have $\overline{U}_r = 0$ and $\partial \overline{\mathbf{U}} / \partial \theta = \partial \overline{\mathbf{U}} / \partial x = \mathbf{0}$, which implies that the term $\overline{R}_{x\theta} = \overline{u'_\theta u'_x}$ is null, and the model leads to null normal stresses (see Kitsios *et al.* (2010)). Consequently, the only non-null components of the modeled tensor \overline{R} are $\overline{R}_{r\theta}$, \overline{R}_{rx} , and their symmetric counterparts.

Three different turbulence models are considered here, which are concisely described in the following. The first is a uniform eddy-viscosity model, in which the eddy-viscosity, ν_t , in equation (3.24) is assumed to be only a function of the streamwise location, and it is the only unknown closure parameter of the resulting model. The other two turbulence models are based on the concept of a mixing-length, l_m , in order to define the eddy-viscosity. The mixing-length, l_m , is a function of the streamwise position and it is the only unknown parameter of the turbulence closure model. The second considered model is the classical mixing-length model, in which ν_t is related to l_m as follows:

$$\nu_t(r) = l_m^2 \left| \frac{\partial \overline{U}_x}{\partial r} \right| \quad (3.25)$$

The third model is a generalized mixing-length model for swirling-flows (see Appendix 3.2.7 and Pope (2000) for more details):

$$\nu_t(r) = l_m^2 (2\overline{S} : \overline{S})^{1/2} = l_m^2 \left[\left(r \frac{\partial}{\partial r} \left(\frac{\overline{U}_\theta}{r} \right) \right)^2 + \left(\frac{\partial \overline{U}_x}{\partial r} \right)^2 \right]^{1/2} \quad (3.26)$$

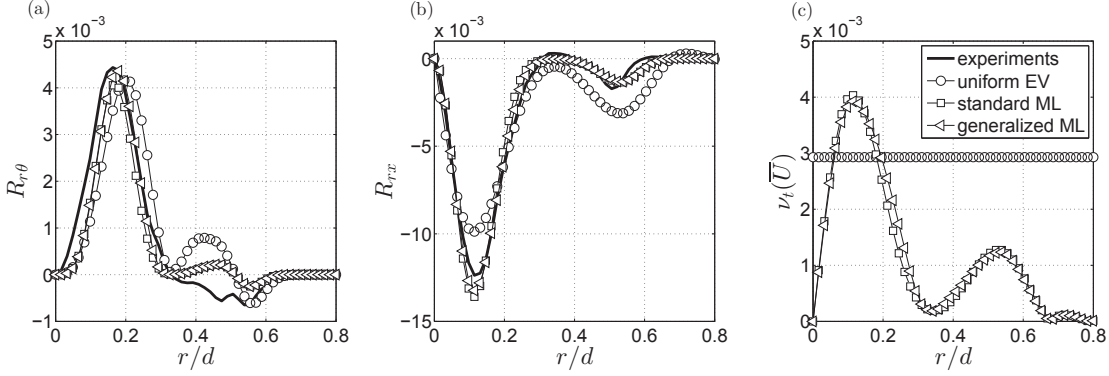


Figure 3.20: Calibration of the closure turbulence models against the wind tunnel data (plane line) for the downstream position $x/d = 0.75$. The Reynolds stresses (a) $\overline{R}_{r\theta}$ and (b) \overline{R}_{rx} are shown. The symbols refer to the three calibrated models, detailed in the legend. The resulting eddy viscosities obtained for the different models are then reported in (c). The *uniform* EV appears in a straight line.

Calibration of the turbulence closure models against wind tunnel data

The free parameters of the eddy-viscosity models are calibrated by using the statistics of the experimental velocity data at each streamwise section. Specifically, a *best fit* strategy between the measured Reynolds stresses and the modeled ones, minimizing the norm of the residuals of equation (3.24), has been adopted. For the uniform eddy-viscosity model, the value of ν_t , which is independent of r , is estimated at each streamwise location minimizing the functional:

$$\nu_t(x) : \min_{\nu_t} \sum_j \left\| \left(\overline{R}(r_j, x) - 2/3 \overline{q}(r_j, x) l - (-2\nu_t(x) \overline{S}(r_j, x)) \right) \right\|^2 \quad (3.27)$$

where r_j are the discrete radial position where experimental data are acquired.

In the case of mixing-length turbulence models, at a given x -location the function to minimize is obtained substituting in equation (3.27) the mixing-length models expressions for ν_t (eqs. (3.25) and (3.26)) and optimizing with respect to the scalar l_m , which varies with x and is independent of r . Note that using directly the statistics of the experimental velocity field needs a further assumption, since measurements include the saturated coherent fluctuation $\overline{\tilde{u}_i \tilde{u}_j}$, which cannot be modelled using the Boussinesq approximation. Thus the used best-fit strategy requires that the stresses $\overline{\tilde{u}_i \tilde{u}_j}$ are small in comparison to $\overline{u'_i u'_j}$ (see for instance Kitsios *et al.* (2010)). This assumption is very reasonable for high-Reynolds-number turbulent flows, as for the considered case, and it is supported a-posteriori by the accuracy of the obtained stability results (see § 3.2.5).

An example of the calibration fitting procedure performed for all the considered models is shown in figure 3.20 for the measurements acquired at $x/d = 0.75$. In figures 3.20(a-b) the Reynolds stresses modeled from the experimental strain rate tensor through the calibrated turbulence closure models are compared with the ones directly measured through the wind

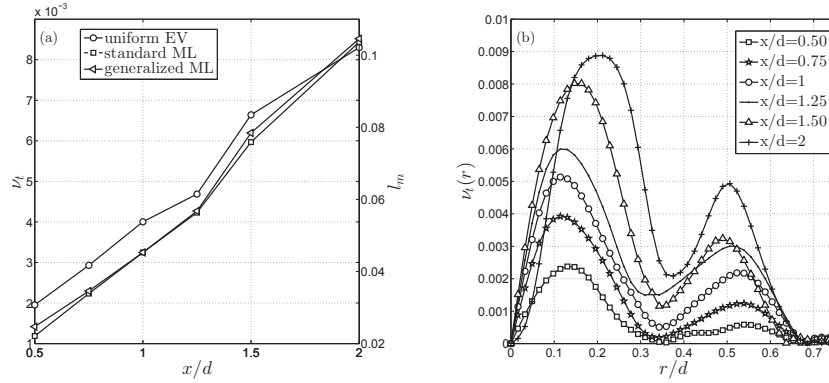


Figure 3.21: Calibration of the closure turbulence models: (a) superposition of ν_t in the case of *uniform* EV (left ordinate axis) and l_m for *standard* and *generalized* ML (right ordinate axis), as a function of the streamwise position x/d . (b) Radial profiles of ν_t evaluated via *generalized* mixing-length model for different streamwise locations.

tunnel tests. It is evident that a fair accuracy is generally achieved through the fitting procedure. Specifically, the Reynolds stress peaks connected to the presence of the hub vortex, observed at $r/d \approx 0.15$ for both $R_{r\theta}$ and R_{rx} , are well reproduced by the models. However, some differences can be observed in correspondence of the tip vortex location at $r/d \approx 0.5$, especially as concerns $R_{r\theta}$. This feature suggests that the turbulence closure models and the calibration fitting procedure could be improved. However, in §5 we will show that results of the stability analysis are very robust with respect to the differences in the calibrated ν_t , which arise from the use of different closure models and/or due to the accuracy of the calibration procedure.

Figure 3.20(c) represents the tuned eddy-viscosity resulting from the models. Note that ν_t is constant for the uniform eddy-viscosity model and its normalized value of the eddy-viscosity evaluated at $x/d = 0.75$ is $\nu_t \approx 0.0029$. In this case the stability analysis of the turbulent mean-flow reduces to a laminar calculation carried out using a locally modified Reynolds number Re^* , defined as: $\frac{1}{Re^*} = \frac{1}{Re} + \nu_t$. In the case of mixing-length models, ν_t is a function of the radial position r/d and its value in the hub vortex region is comparable with the one obtained with the uniform eddy-viscosity model.

The described best-fit procedure has been carried out for all the considered streamwise sections, leading to results analogous to the ones presented for the location $x/d = 0.75$. In order to provide further information on the trend of the free model parameters as a function of the streamwise location, x/d , we report in figure 3.21(a) the calibrated values of ν_t and l_m . This figure shows that ν_t and l_m obtained through the calibration procedure grow almost linearly with x/d , implying that the diffusive effects due to turbulence increase moving downstream. This result is in qualitative agreement with the experiments where it was observed that the hub vortex is almost completely diffused for $x/d > 3$ (Iungo *et al.*, 2013). Moreover, for the two mixing-length models, the obtained values for l_m almost coincide since the expression $2\bar{S} : \bar{S}$ is dominated by the term $\partial\bar{U}_x/\partial r$ in the considered flow (compare equation (3.25) with equation (3.26)). Lastly, figure 3.21(b) shows that the profiles of ν_t obtained by the general-

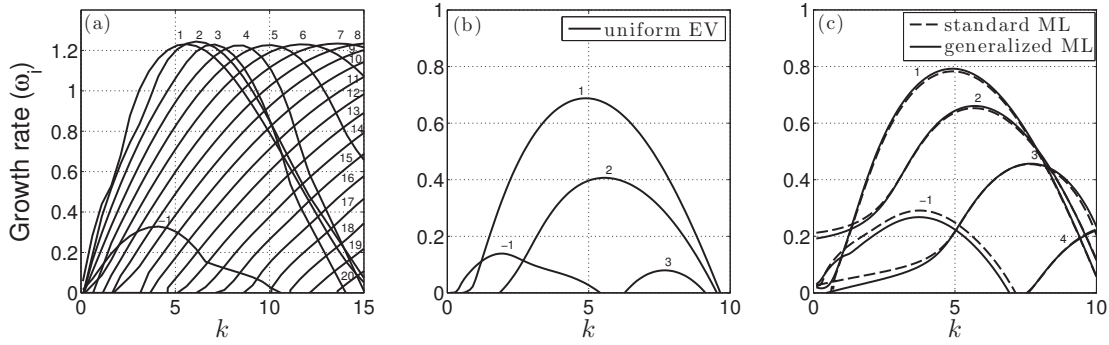


Figure 3.22: Temporal analysis results at section $x/d = 0.5$ (a) without Reynolds stresses, (b) with the uniform eddy-viscosity model, and (c) with the generalized and standard (dashed line) mixing-length models. Growth rates are reported as a function of the axial wavenumber k , and each branch corresponds to a different azimuthal wavenumber m .

ized mixing-length model as a function of the radial position remains similar at the different streamwise sections. In particular, they are characterized by a higher peak located in proximity of the hub vortex position, and a smaller one in correspondence of the tip vortex location. The same conclusions apply for the standard mixing-length model. The eddy-viscosity profiles in figure 3.21 (b) are then introduced in the local linear stability analysis through the term $\nu_t(\bar{\mathbf{U}})$ of equation (3.52).

3.2.5 Stability analysis results

Temporal stability analysis and mode selection

Figure 3.22 depicts the results of temporal stability analysis carried out at the streamwise location $x/d = 0.5$, (a) neglecting the contribution of the Reynolds stresses, (b) using the uniform eddy-viscosity model, and (c) using both the standard and the generalized mixing-length models. For each case the growth rate, ω_i , is reported as a function of the axial wavenumber, k , while each branch corresponds to different azimuthal wavenumbers, m . As in Iungo *et al.* (2013), when Reynolds stresses are neglected, the temporal stability analysis predicts many unstable modes, and it is not possible to identify a single dominant mode as observed in the experiments. Conversely, figure 3.22(b) and 3.22(c) show that, when a model for the turbulent diffusion is introduced, the temporal stability analysis identifies a clearly dominant unstable mode among only four unstable modes detected. Specifically, the higher wavenumber modes are more damped since the diffusion term is proportional with k^2 and m^2 , and the mode with $m = 1$ results the one with the largest growth rate at every considered downstream position. This mode, not shown here for the sake of brevity is the single-helix counter-winding mode characterized experimentally in Iungo *et al.* (2013). Thus, the present results demonstrate the important role of the turbulent diffusion mechanism in the evolution of the perturbation and that even a simple eddy-viscosity model is sufficient to improve the results of the local temporal stability analysis, so as to identify a clearly dominant unstable mode. Moreover,

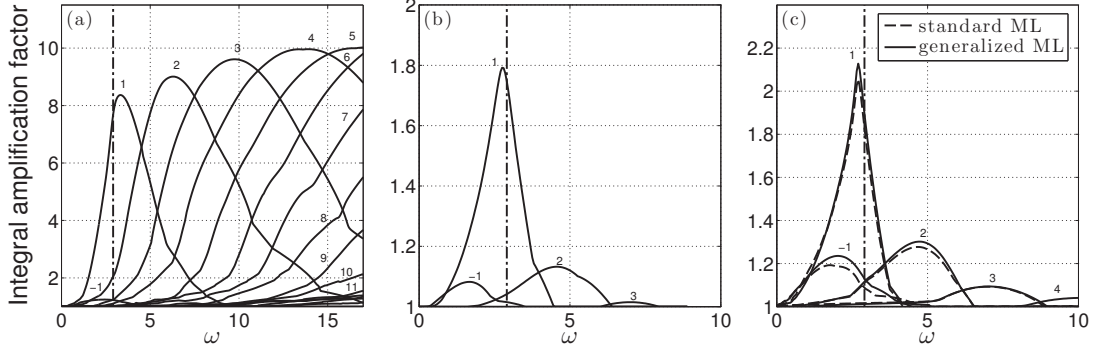


Figure 3.23: Integral amplification factor in the wake (a) without Reynolds stresses, (b) with the uniform eddy-viscosity model, and (c) with the generalized and the standard (dashed line) mixing-length models. Growth rates are reported as a function of the frequency ω , and each branch corresponds to a different azimuthal wavenumber m . The vertical dashdotted line represents the frequency of the hub vortex instability measured experimentally, corresponding to a nondimensional pulsation $\omega_{hub\ vortex} = 2.9$.

figure 3.22(b) and 3.22(c) show that differences among the results obtained by the different closure turbulence models are moderate as concerns the detection of a dominant unstable mode, and that mixing-length models damp slightly less the modes associated to higher frequencies. Similar results have been found for all the analysed streamwise locations.

Spatial stability analysis, integral growth rate and instability frequency prediction

In the framework of local stability analysis of weakly-non-parallel-flows, the integral amplification factor of each unstable mode is determined by integrating in the streamwise direction its spatial growth rate, $-k_i(m, \omega, x)$, which is obtained from dedicated spatial stability analyses. Thus, $-k_i(m, \omega, x)$ is integrated from a given streamwise position, x_0 , up to the downstream position where the mode becomes stable again, x_s :

$$G(m, \omega) = \exp \int_{x_0}^{x_s} -k_i(m, \omega, x') dx' \quad (3.28)$$

$G(\omega, m)$ represents the overall amplification of the mode m at the frequency ω within the wake, after it has undergone its entire amplification process. We remind that $G(m, \omega)$ is a synthesis of the results obtained by local spatial stability analyses carried out at different streamwise sections.

In figure 3.23 the integral amplification factors of the unstable modes are reported as a function of the frequency ω . As shown in figure 3.23(a), when the Reynolds stresses are neglected many unstable modes exist and, as for the temporal analysis, it is not possible to select a dominant mode without considering as additional input the instability frequency detected experimentally. On the other hand, the use of an eddy-viscosity model allows a clear mode identification, as shown in figures 3.23(b) and 3.23(c), and the mode associated to

$m = 1$ is the most spatially amplified one. Its amplification factor has a clear and definitely dominant peak at a frequency ω_f , which is almost coincident with the one measured experimentally ($\omega_{hub\ vortex} = 2.9$ is reported in figure 3.23 as a vertical dash-dotted line). For a more quantitative comparison, the relative error between the experimental instability frequency ($\omega_{hub\ vortex}$) and the predicted frequency ω_f has been computed: a relative error of about 7.1% is obtained for the mixing-length models, and this error is further decreased to 5.3% when the uniform eddy-viscosity model is used.

3.2.6 Conclusions

In this paper eddy-viscosity models are applied in order to take into account turbulence in the stability analysis of the time-averaged flow field past a wind turbine. The work is motivated by a previous investigation, Iungo *et al.* (2013), in which stability analysis was carried out by neglecting the Reynolds stresses. In that study, the characterization of the hub vortex instability was achieved by using as additional input to the stability analysis the instability frequency, which was evaluated via wind tunnel experiments. Here three turbulence closure models have been considered: a constant eddy-viscosity model and two mixing-length models (a standard one and a generalized one for swirling flows). The free parameters of the models have been tuned using the available wind tunnel data. Using the considered models, the number of unstable modes detected via stability analysis is drastically reduced, and the spatially-integrated growth factors clearly indicate one dominant unstable mode, i.e. the single-helix counter-winding mode observed experimentally in Iungo *et al.* (2013). Its instability frequency is also predicted with a very good agreement with the experimental evidence.

The present results show that the use of calibrated turbulence models in the stability analysis of the time-averaged flow field allows not only the characterization of the hub vortex instability, but also the accurate prediction of the associated instability frequency. This result is obtained using simple algebraic closures, properly calibrated, even if the framework proposed here can include more complex RANS models as well. The fact that the mode identification is the result of the sole stability analysis, and that it does not require any additional external information is of crucial importance for many further applications of the proposed method. Specifically, this technique should allow for significant improvements in the prediction of the downstream recovery of wind turbine wakes, and ultimately their control. For this reason, and also for the accuracy observed in the present application, we believe that this strategy and the results discussed in this paper are also of general interest for the stability analysis of turbulent swirling flows.

3.2.7 A note on the mixing-length model

In order to include the effect of turbulent fluctuations in the equation of the coherent perturbation (Eq. (3.52)), the gradient of the eddy-viscosity with respect to the velocity evaluated in the mean flow configuration $\bar{\mathbf{U}}$, needs to be calculated. While it is undetermined and set to zero in the uniform eddy-viscosity model, it is now evaluated for the two mixing-length

models studied in this paper. In the case of standard mixing-length:

$$v_t^e(\langle \mathbf{U} \rangle) = l_m^2 \left| \frac{\partial \langle U_x \rangle}{\partial r} \right| \simeq l_m^2 \left| \frac{\partial \bar{U}_x}{\partial r} \right| + \text{sign} \left(\frac{\partial \bar{U}_x}{\partial r} \right) l_m^2 \frac{\partial \tilde{u}_x}{\partial r} = v_t^e(\bar{\mathbf{U}}) + \nabla_{\mathbf{U}} v_t^e(\bar{\mathbf{U}}) \cdot \tilde{\mathbf{u}} \quad (3.29)$$

Now considering the generalized expression for mixing-length model (see Pope (2000)), in the case of an axisymmetric, locally parallel mean flow:

$$v_t^e(\langle \mathbf{U} \rangle) = l_m^2 (2 \langle S \rangle : \langle S \rangle)^{1/2} = l_m^2 \left[\left(r \frac{\partial \langle U_\theta \rangle}{\partial r} / r \right)^2 + \left(\frac{\partial \langle U_x \rangle}{\partial r} \right)^2 \right]^{1/2} \quad (3.30)$$

Splitting as usual the ensemble averaged flow in the time-averaged flow plus the coherent fluctuation, and recalling that $\sqrt{1+x} = 1 + \frac{1}{2}x + O(x^2)$ for $x \rightarrow 0$:

$$v_t^e(\langle \mathbf{U} \rangle) = l_m^2 (2 \langle S \rangle : \langle S \rangle)^{1/2} \simeq l_m^2 (2\bar{S} : \bar{S})^{1/2} + \frac{l_m^2}{(2\bar{S} : \bar{S})^{1/2}} \left[r \frac{\partial \bar{U}_\theta / r}{\partial r} \left(\frac{\partial \tilde{u}_\theta}{\partial r} + \frac{\tilde{u}_\theta}{r} \right) + \frac{\partial \bar{U}_x}{\partial r} \frac{\partial \tilde{u}_x}{\partial r} \right] = v_t^e(\bar{\mathbf{U}}) + \nabla_{\mathbf{U}} v_t^e(\bar{\mathbf{U}}) \cdot \tilde{\mathbf{u}} \quad (3.31)$$

Note that if $\bar{U}_\theta = 0$, $v_t^e(\bar{\mathbf{U}})$ and $\nabla_{\mathbf{U}} v_t^e(\bar{\mathbf{U}}) \cdot \tilde{\mathbf{u}}$ reduce to the ones of standard mixing-length.

3.3 Instability of wind turbine wakes immersed in the atmospheric boundary layer

F. Viola¹, G.V. Iungo², S. Camarri³, F. Porté-Agel⁴ and F. Gallaire¹

¹ Laboratory of Fluid Mechanics and Instabilities, École Polytechnique Fédérale de Lausanne, Lausanne, CH-1015, Switzerland

² The University of Texas at Dallas, Mechanical Engineering Department, Wind Fluids and Experiments Lab (WindFluX), 75080 Richardson, TX

³ Department of Civil and Industrial Engineering, University of Pisa, Pisa 56122, Italy

⁴ Wind Engineering and Renewable Energy Laboratory, École Polytechnique Fédérale de Lausanne, Lausanne, CH-1015, Switzerland

Journal of Physics: Conference Series. Vol. 625. No. 1. IOP Publishing, 2015.

In this work a technique capable to investigate the near-wake stability properties of a wind turbine immersed in the atmospheric boundary layer is presented. Specifically, a 2D local spatial stability analysis is developed in order to take into account typical flow features of real operating wind turbines, such as the presence of the atmospheric boundary layer and the turbulence heterogeneity of the oncoming wind. This stability analysis can be generally applied on either experimental measurements or numerical data. In this paper it was carried out on wind tunnel experiments, for which a downscaled wind turbine is immersed in a turbulent boundary layer. Through spatial stability analysis, the dominant mode in the near wake, i.e. the most amplified one, is characterized and its frequency matches the hub vortex instability frequency measured in the wind tunnel. As in the case of Viola *et al.* (2014), where an axisymmetric wake condition was investigated, the hub vortex instability results in a single-helical mode.

3.3.1 Introduction

In the wake of wind turbines two main vorticity structures are typically observed: the helical tip vortices and the hub vortex. The tip vortices are shed from the tip of the blades and are rapidly convected downstream because located at the wake periphery where high streamwise velocity is present. The hub vortex is a streamwise-oriented vorticity structure located approximately at the wake centre.

Wind tunnel measurements in the wake produced by a down-scaled wind turbine immersed in a uniform flow showed that these vorticity structures undergo to instabilities in the near-wake and are diffused proceeding downstream Iungo *et al.* (2013); Viola *et al.* (2014). The tip-vortices instability is mainly driven by the mutual inductance between adjacent spirals, in cooperation with short-wave and long-wave instabilities (Widnall (1972); Felli *et al.* (2011)) which favorite the tip-vortices diffusion within one diameter past the turbine (Sarmast *et al.* (2014), Zhang *et al.* (2012)). Conversely, the hub vortex is characterized by oscillations of

3.3. Instability of wind turbine wakes immersed in the atmospheric boundary layer

a frequency equal to roughly 0.34 times the rotational frequency of the wind turbine rotor which are detected up to two diameters downstream, see Medici & Alfredsson (2008) and Iungo *et al.* (2013). In previous works these flow fluctuations were ascribed to wake wandering or meandering, which consists in transversal oscillations of the wind turbine wake. Wake meandering was investigated in detail by Medici & Alfredsson (2008) where it is stated that this phenomenon is mainly excited by the shedding of vorticity structures from the rotor disc acting as a bluff body. In Iungo *et al.* (2013), in the case of uniform oncoming flow, this phenomenon was explained as the appearance of a counter-winding and co-rotating single-helix unstable mode amplified in the wake of the wind turbine. More specifically temporal and spatial linear stability analyses were performed on the time-averaged wind tunnel velocity measurements in order to identify the most amplified vortical structures originating at the hub vortex instability. Furthermore, simultaneous hot-wire measurements confirmed the presence of a helicoidal unstable mode of the hub vortex with a streamwise wavenumber roughly equal to that predicted from the linear stability analysis. This results have been confirmed in the experimental work of Okulov *et al.* (2014) where, through laser doppler anemometry (LDA) and particle image velocimetry (PIV) visualization, these authors found that the wake dynamics is associated with a precession (rotation) of the helical vortex core at a constant Strouhal number. Moreover, Kang *et al.* (2014) carried out LES simulations which included all geometrical details of the wind turbine by a curvilinear immersed-boundary method with evidence of large-scale meandering motions.

In Viola *et al.* (2014) a stability analysis is performed by taking into account the effects of the Reynolds stresses by means of eddy-viscosity models. Other studies in the literature have considered eddy-viscosity models to close the linearized equations for the coherent velocity field in a turbulent flow following the seminal work of Reynolds & Hussain (1972). In Viola *et al.* (2014) three eddy-viscosity models are considered, where the model parameters are calibrated on the wind tunnel data. One model is based on the assumption of a uniform eddy viscosity for each streamwise location, whereas for the other two models a mixing length is estimated. It was shown that with the proposed improved formulation, stability analysis allows not only the unambiguous identification of the hub vortex instability, but also the accurate frequency prediction.

In the present work the analysis is extended to the case of wind turbines immersed in a turbulent atmospheric boundary layer (ABL). The presence of the ABL in the streamwise direction breaks the axisymmetry of the mean flow, thus the harmonic modal expansion in the azimuthal direction is not valid anymore and a 2D local stability analysis has to be carried out. With this formulation the effect of the condition of the ABL such as shear veer or turbulence heterogeneity on the near wake-dynamics can be included within the present analysis. This formulation is here applied to wind tunnel data acquired in the wake of a downscaled wind turbine subjected to a turbulent oncoming boundary layer flow.

This paper is organized as follows: the wind tunnel data are described in section 3.3.2, then the formulation of the stability analysis, which takes the modeled Reynolds stresses into account, and the numerical method are presented in section 3.3.3. The results of the spatial stability analysis of the mean wake flow are then described in section 3.3.4. Finally, conclusions are

drawn in section 3.3.5.

3.3.2 Experimental data

In this work a data-set acquired in the boundary layer wind tunnel of the Wind Engineering and Renewable Energy Laboratory (WIRE) of the Ecole Polytechnique Federale de Lausanne (EPFL) has been considered and investigated by 2D local stability analysis. The experimental facility is a closed loop wind tunnel with an inlet providing a contraction with 5:1 area ratio. Several turbulence devices consisting of coarse meshes and honeycomb flow straighteners are used to increase flow quality. The wind turbine down-scaled model used is a three-bladed GWS/EP-6030x3 anticlockwise. The rotor, with a diameter, d , of 152 mm, is connected to a DC motor with a diameter of 10 mm. The wind turbine model is mounted with a stem of height 127 mm and is directly installed on the wind tunnel floor. By considering its frontal area, the blockage ratio is less than 0.5%, which is very small to neglect possible effects due to the size of the wind tunnel. More details about a similar experimental setup can be found in Jungo *et al.* (2013). For the tests considered here, the tip speed ratio of the turbine (TSR), which is the ratio between the speed of the blade tip and the oncoming velocity at hub height, U_{hub} , is 4.7. For these tests the mean rotational frequency, f_{hub} , was 62 Hz. The velocity at hub height is 6.3 m/s and the turbulence level is equal to 7%. A Reynolds number of 70000 is obtained by considering U_{hub} as reference velocity, and the rotor diameter, d , as reference length.

Measurements of three components of the velocity were performed with a customized Cobra probe produced by Turbulent Flow Instrumentation, which is a four-hole pressure probe. This probe, with an external diameter of 1.5 mm, can measure velocity fluctuations characterized by frequencies lower than 300Hz.

The reference frame used has its origin placed just behind the hub of the wind turbine, with the x -axis corresponding to the streamwise direction, positive pointing downstream. The z -axis is along the vertical direction, positive from the bottom towards the top, while the y -axis is along the spanwise direction oriented so as to produce a right-handed Cartesian coordinate system. Velocity measurements were performed from a downstream distance of $0.375d$ up to $4d$. In figure 4.2 the three velocity components of the time averaged mean flow field at the streamwise position in the wake $x/d = 0.375$ are shown. In figure 4.2(a) the streamwise component, U_x is characterized by a strong velocity deficit which is progressively recovered further downstream. The streamwise velocity is higher at the top periphery of the wake than in the lower due to the presence of the ABL and of the sting supporting the turbine. The significant peaks of the spanwise velocity components U_y and U_z (fig. 4.2(b) and (c) respectively) are detected for radial positions $r/d \approx 0.15$, which are connected to the rotational velocity induced by the hub vortex. In other words the spanwise components correspond to the azimuthal velocity of the hub vortex projected in the cartesian reference frame. The corresponding tangential components of the Reynolds stress tensor are shown in figure 3.25.

3.3. Instability of wind turbine wakes immersed in the atmospheric boundary layer

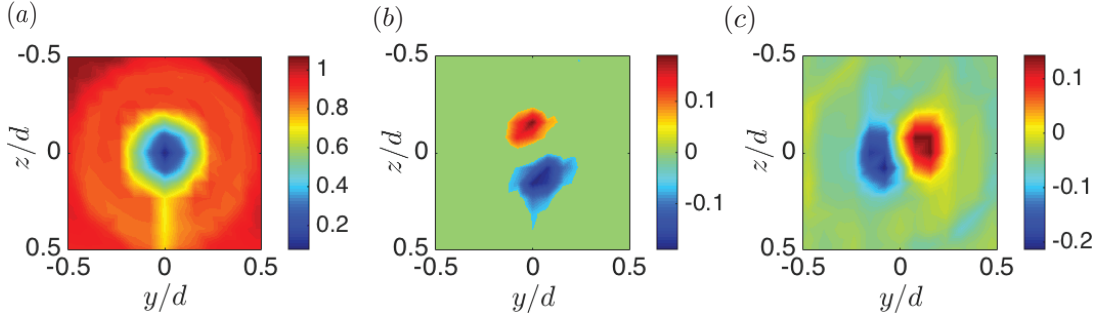


Figure 3.24: Non-dimensional time averaged mean flow at the streamwise position $x/d = 0.375$. (a) U_x/U_{hub} , (b) U_y/U_{hub} and (c) U_z/U_{hub} .

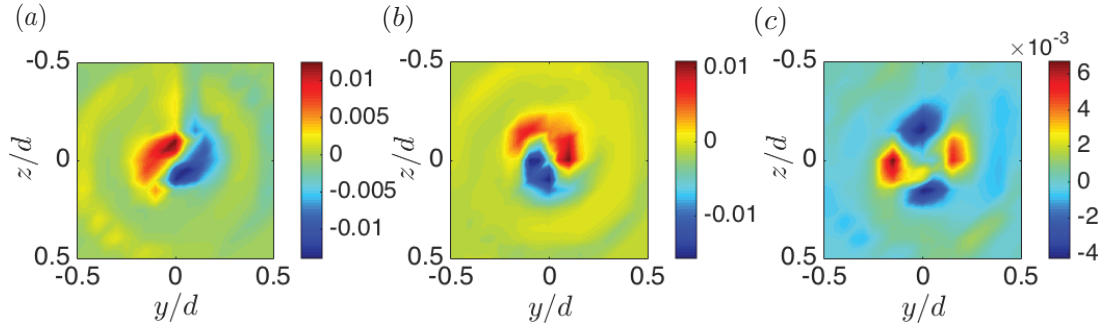


Figure 3.25: Non-dimensional tangential components of Reynolds stress tensor at the streamwise position $x/d = 0.375$. (a) $\overline{u'_x u'_y} / U_{hub}^2$, (b) $\overline{u'_x u'_z} / U_{hub}^2$ and (c) $\overline{u'_y u'_z} / U_{hub}^2$.

3.3.3 Stability analysis, turbulent model and numerical method

Following the approach proposed originally by Reynolds & Hussain (1972) the unsteady flow, $\mathbf{U}(\mathbf{x}, t)$, can be decomposed in three contributions: the time-averaged base-flow, $\overline{\mathbf{U}}(\mathbf{x})$, the coherent fluctuation, $\tilde{\mathbf{u}}(\mathbf{x}, t)$, and the turbulent motion, $\mathbf{u}'(\mathbf{x}, t)$

$$\mathbf{U} = \overline{\mathbf{U}} + \tilde{\mathbf{u}} + \mathbf{u}'$$

Specifically the sum of the time-averaged flow and the coherent fluctuation coincides with the ensemble averaged flow $\langle \mathbf{U} \rangle = \overline{\mathbf{U}} + \tilde{\mathbf{u}}$. Recalling the formulation detailed in Viola *et al.* (2014) the non-linear evolution of the coherent perturbation, $\tilde{\mathbf{u}}$, on top of the time averaged mean flow, $\overline{\mathbf{U}}$, is given by the equation (3.32):

$$\begin{aligned} \nabla \cdot \tilde{\mathbf{u}} &= 0 \\ \frac{\partial \tilde{\mathbf{u}}}{\partial t} + \nabla \tilde{\mathbf{u}} \cdot \overline{\mathbf{U}} + \nabla \overline{\mathbf{U}} \cdot \tilde{\mathbf{u}} &= -\nabla \tilde{p} + \frac{1}{\text{Re}} \Delta \tilde{\mathbf{u}} - \nabla \cdot [\tilde{\mathbf{u}} \tilde{\mathbf{u}} - \overline{\tilde{\mathbf{u}} \tilde{\mathbf{u}}}] - \nabla \cdot [\langle \mathbf{u}' \mathbf{u}' \rangle - \overline{\mathbf{u}' \mathbf{u}'}] \end{aligned} \quad (3.32)$$

where the third and last terms of the rhs are respectively the non-linear term and the difference among the Reynolds stresses obtained by ensemble and time averages. From now on, the equations are made non-dimensional with the turbine diameter d and the velocity at the hub

Chapter 3. Hub vortex instability

U_{hub} . In the linear framework the coherent perturbation is assumed to be small and by using the Boussinesq approximation for the Reynolds stresses, eq. (3.32) is rewritten as follows:

$$\frac{\partial \tilde{\mathbf{u}}}{\partial t} + \nabla \tilde{\mathbf{u}} \cdot \bar{\mathbf{U}} + \nabla \bar{\mathbf{U}} \cdot \tilde{\mathbf{u}} = -\nabla \tilde{p} + \frac{1}{\text{Re}} \Delta \tilde{\mathbf{u}} + \nabla \cdot (\nu_t(\bar{\mathbf{U}}) [\nabla + \nabla^T] \tilde{\mathbf{u}}) + \nabla \cdot ((\nabla_{\mathbf{U}} \nu_t(\bar{\mathbf{U}}) \cdot \tilde{\mathbf{u}}) [\nabla + \nabla^T] \bar{\mathbf{U}}) \quad (3.33)$$

Equation(3.52) is the linear evolution of the coherent perturbation on a turbulent time-averaged mean flow with enforced Boussinesq hypothesis, where the eddy-viscosity terms need to be modeled. As in Viola *et al.* (2014) we adopt here the generalized mixing-length model, hence ν_t is given by:

$$\nu_t = l_m^2 (2\bar{S} : \bar{S})^{1/2} \quad (3.34)$$

where S is the strain rate tensor. The mixing-length l_m is tuned on the experimental data through a best fit procedure on the Boussinesq equation, in a similar way to Viola *et al.* (2014). This is done separately at each streamwise section considered for the local stability analysis, so that the value of l_m varies with x . The term $\nabla_{\mathbf{U}} \nu_t \cdot \tilde{\mathbf{u}}$ represents the eddy-viscosity variation due to the coherent fluctuation and it is given by the linearization of the model around the mean flow:

$$\nabla_{\mathbf{U}} \nu_t(\bar{\mathbf{U}}) \cdot \tilde{\mathbf{u}} = l_m^2 \frac{2\bar{S} : \tilde{s}}{(2\bar{S} : \bar{S})^{1/2}}. \quad (3.35)$$

In the framework of weakly-non-parallel stability analysis, eq. (3.52) is now applied to a parallel flow $\bar{\mathbf{U}} = (\bar{U}_x(y, z), \bar{U}_y(y, z), \bar{U}_z(y, z))$ extracted at a given streamwise location. Note that, the three components of the time averaged mean flow vary in both spanwise directions y and z , consequently the local analysis is bidimensional. In contrast, the x -dependence of the flow is considered by carrying out different stability analysis at different sections in the wake, as typical in local analysis assuming weak variations of the flow in that direction. This allows for a modal expansion of the coherent fluctuation in the following form:

$$\tilde{\mathbf{u}}(x, y, z, t) = \hat{\mathbf{u}}(y, z) \exp(i(kx - \omega t)) \quad (3.36)$$

where k is axial wavenumber and ω is the frequency. When this modal form is substituted in Eq. (3.52), an eigenvalue problem is obtained and eigenfunction solutions exist only if k and ω satisfy a dispersion relation of the form:

$$D[k, \omega] = 0. \quad (3.37)$$

The spatial branches, which describe the amplification of perturbation in space, are obtained by solving the dispersion relation with complex wavenumbers k , and real frequency ω , have been considered here (see Iungo *et al.* (2013)). Given $k = k_r + ik_i$, i being the imaginary unit, the term $-k_i$ is the spatial amplification rate, while k_r corresponds to the streamwise wavenumber of the traveling perturbation with frequency ω . Due to the weakly non-parallelism of the meanflow, $\bar{\mathbf{U}}$, the derivatives in the streamwise direction are of higher order and the

3.3. Instability of wind turbine wakes immersed in the atmospheric boundary layer

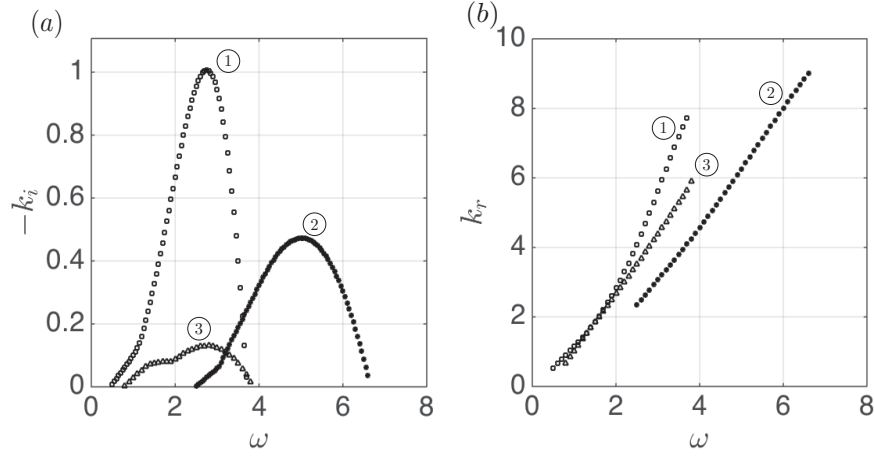


Figure 3.26: Spatial analysis results at the section $x/d = 0.375$. In (a) the growth rates, $-k_i$, are reported as a function of the frequency ω , while in (b) the corresponding axial wavenumbers, k_r , are shown. Each branch corresponds to a different amplified mode.

term $2\bar{S} : \bar{S}$ appearing in equation (3.34) at leading order reduces to:

$$(2\bar{S} : \bar{S})^{1/2} \approx \left[\left(\frac{\partial \bar{U}_x}{\partial y} \right)^2 + \left(\frac{\partial \bar{U}_x}{\partial z} \right)^2 + \left(\frac{\partial \bar{U}_y}{\partial z} + \frac{\partial \bar{U}_z}{\partial y} \right)^2 + 2 \left(\frac{\partial \bar{U}_y}{\partial y} \right)^2 + 2 \left(\frac{\partial \bar{U}_z}{\partial z} \right)^2 \right]^{1/2} \quad (3.38)$$

Similarly the term $2\bar{S} : \tilde{s}$ in the expression of the eddy-viscosity variation due to the coherent fluctuation (3.35) is given by:

$$2\bar{S} : \tilde{s} \approx \left(\frac{\partial \bar{U}_x}{\partial y} \right) \left(\frac{\partial \tilde{u}_x}{\partial y} + \frac{\partial \tilde{u}_y}{\partial x} \right) + \left(\frac{\partial \bar{U}_x}{\partial z} \right) \left(\frac{\partial \tilde{u}_x}{\partial z} + \frac{\partial \tilde{u}_z}{\partial x} \right) + \left(\frac{\partial \bar{U}_y}{\partial z} + \frac{\partial \bar{U}_z}{\partial y} \right) \left(\frac{\partial \tilde{u}_y}{\partial z} + \frac{\partial \tilde{u}_z}{\partial y} \right) + 2 \left(\frac{\partial \bar{U}_y}{\partial y} \right) \left(\frac{\partial \tilde{u}_y}{\partial y} \right) + 2 \left(\frac{\partial \bar{U}_z}{\partial z} \right) \left(\frac{\partial \tilde{u}_z}{\partial z} \right) \quad (3.39)$$

Equations (3.52) together with modal expansion (3.36) are discretized using a staggered pseudo-spectral Chebyshev-Chebyshev collocation method. The three velocity components are defined at the Gauss-Lobatto-Chebyshev (GLC) nodes, whereas the pressure is staggered on a different grid, which is generated with Gauss-Chebyshev nodes (GC). In both y and z directions the algebraic mapping with domain truncation is used, in order to cluster the nodes at the wake center. In the present work $N_y = 40$ and $N_z = 40$ points are used in the axial and radial direction respectively, this resolution having shown to provide the desired convergence of the amplification factors.

3.3.4 Hub vortex instability

The local spatial analysis has been carried out at several streamwise positions in the wake

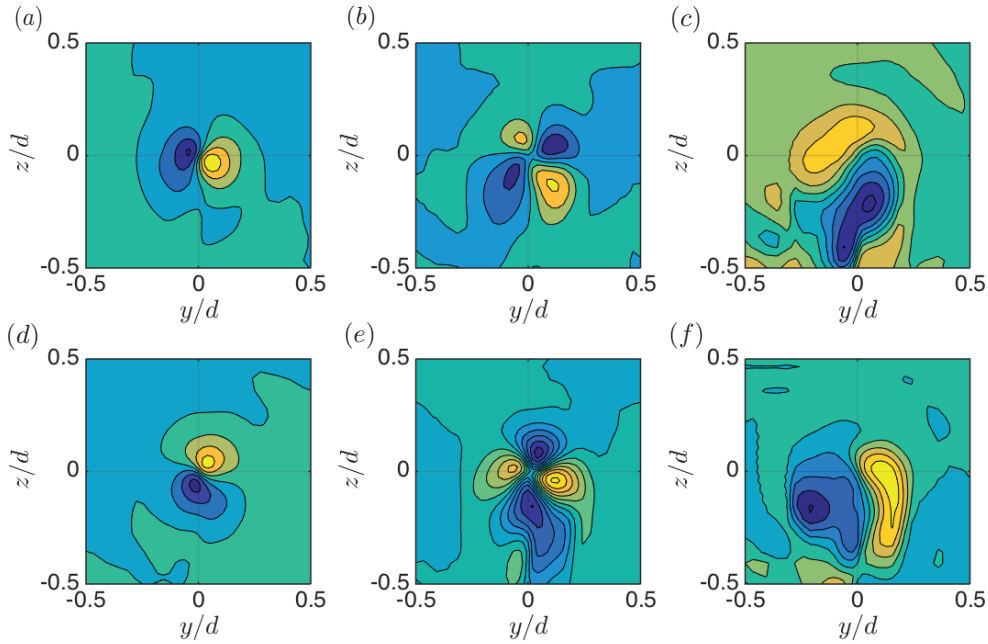


Figure 3.27: Spatial analysis results at the section $x/d = 0.375$. Real (a) and imaginary (d) part of the axial flow of the eigenfunction associated to mode 1 at frequency $\omega = 2.7$. In (b) and (e) the same quantities are shown for mode 2 at frequency $\omega = 5$ and in (c) and (f) for mode 3 at frequency $\omega = 2.8$.

of the wind turbine where the experimental data were acquired. In figure 3.26 the results of the spatial analysis at the first available section, $x/d = 0.375$, are reported. In fig. 3.26(a) the spatial growth rates $-k_i$ are depicted as a function of the frequency of the coherent fluctuation ω , while in (b) the associated axial wavenumbers are shown. Three modes, labeled as modes 1, 2 and 3, result to be amplified in the frequency band $0 \leq \omega \leq 7$. In particular, in the frequency range $2.5 \leq \omega \leq 4$ the three modes coexist and three unstable eigenvalues are found when carrying out the stability analysis. Each mode is characterized by a *preferred* frequency, defined as the frequency associated with the higher spatial growth-rate, which is equal approximately to 2.7 for mode 1, to 5 for mode 2 and to 2.8 for mode 3. In figure 3.27 the axial velocity of the eigenmodes 1, 2 and 3 at the respective preferred frequency, are reported, showing that: the detected unstable modes and related branches present different spatial structures. Specifically, in fig. 3.27(a-d) the complex eigenfunction clearly exhibit a dominant single-helical shape, which is in agreement with the stability analysis results in the wake of a wind turbine invested by a uniform oncoming flow (Iungo *et al.* (2013); Viola *et al.* (2014)) even though in this analysis no modal expansion is imposed in the azimuthal direction and eigenfunctions can have a generic shape in the $y - z$ plane. The eigenfunction of mode 2 in fig. 3.27(b-e) represents a double-helical mode. Lastly, the mode 3 in (c-f) is dominated by a single-helical symmetry, but more diffused respect to mode 1.

By observing the spatial growth rates in fig. 3.26(a), the most amplified perturbation at $x/d = 0.375$ is the single-helical mode 1 at the dominant frequency $\omega = 2.7$. The same analysis

3.3. Instability of wind turbine wakes immersed in the atmospheric boundary layer

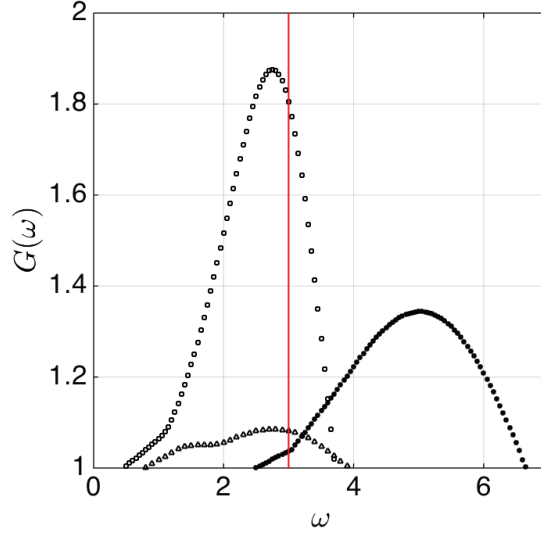


Figure 3.28: Integral amplification factor of coherent perturbations in the wake as a function of the frequency ω . Three modes, labeled as mode 1, mode 2 and mode 3 are amplified through the domain. The vertical red line represents the frequency of the hub vortex instability measured experimentally, corresponding to a non-dimensional pulsation $\omega_{hubvortex} = 3$.

has been carried out in the other streamwise sections in the wind turbine wake and a similar scenario is obtained, with the single helix mode 1 more amplified at the low frequency range. However proceeding downstream the spatial growth rates reduce due to the recovery of the wake deficit and the increase of the turbulence intensity which favors the diffusion of the vortex structures.

In order to determine the most amplified coherent fluctuation through the wake and its frequency, the local spatial growth rates are integrated in the streamwise direction according to:

$$G(\omega) = \exp \int_{x_i}^{x_s} -k_i(\omega, x) dx. \quad (3.40)$$

The global gain represents the integral measure of the amplification in the wake between the first section available, $x_i = 0.375d$, and x_s which is the streamwise position where the mode becomes stable. $G(\omega)$ is reported in figure 3.28 as a function of the frequency ω , where the three modes amplified in the wake are labeled as before. Therefore mode 1 results to be the most amplified mode overall and its dominant frequency is in good agreement with the hub vortex instability frequency measured in the wind tunnel, whose non-dimensional value is $\omega \approx 3$ and is depicted by the red line in fig. 3.28. The limited deviation in the frequency prediction is believed to be related to a non-linear modulation which can not be captured by this linear stability approach. The velocity field of the coherent perturbation at a given frequency ω is given by equation (3.41)

$$\tilde{\mathbf{u}}(x, y, z, t) = Re \left\{ \hat{\mathbf{u}}(x; y, z) e^{i(\int_{x_i}^x k(x', \omega) dx' - \omega t)} \right\}. \quad (3.41)$$

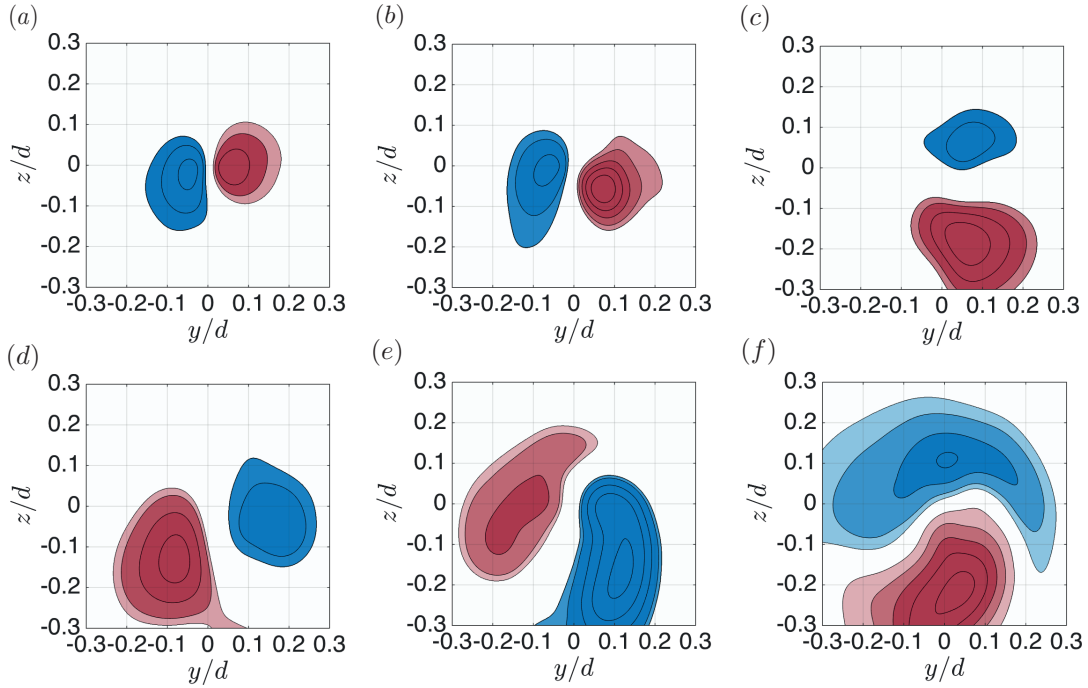


Figure 3.29: Axial velocity of the most amplified coherent perturbation (mode 1 with frequency $\omega = 2.7$) at different streamwise positions. (a) $x/d = 0.375$, (b) $x/d = 0.50$, (c) $x/d = 0.75$, (d) $x/d = 1.00$, (e) $x/d = 1.50$ and (f) $x/d = 2.00$.

Hence, at a given time the term $e^{i \int_{x_i}^x k_r(x') dx'}$, where $k_r(x)$ is the local wavenumber, is setting the phase of the local complex eigenfunction $\hat{\mathbf{u}}(x; y, z)$. Since the $k_r(x)$ are positive quantities, the phase increases proceeding downstream, providing different orientations to the local velocity field yielding the typical helical shape of the hub vortex instability, see Jungo *et al.* (2013). Consequently, the unsteady term $e^{-i\omega t}$ consists in a uniform change of phase in time, resulting in a constant rate rotation of the perturbation around its axis. The axial velocity of mode 1 at frequency $\omega = 2.7$, which is the most amplified coherent perturbation according to spatial analysis, is reported in figure 3.29 at different streamwise positions in the wind turbine wake. In all the considered sections the single-helical symmetry is the dominant one. Moreover, by moving downstream, the eigenfunction is less concentrated around the hub vortex core due to turbulent diffusion, as known by experimental evidence. Hence, also in this case of wind turbine immersed in the atmospheric boundary layer the hub vortex instability is associated with an helical precession of the vortex-core. Moreover, it is interesting to notice that while proceeding downstream, the helicoidal structure observed is slightly displaced downwards. This feature can be related to the presence of the boundary layer. This general lowering of the wake vorticity structures is also typically observed for wakes produced by bluff bodies immersed in a boundary layer, as for the case for a triangular prism in Buresti & Jungo (2010).

3.3.5 Conclusions

A method suitable for local stability analysis in the near wake of wind turbine wakes has been developed and here presented. The method is based on the triple decomposition of the flow field, where an equation describing the dynamics of the coherent perturbations on the time-averaged flow and taking into account the turbulent diffusion is provided. Due to the weakly non parallelism of the flow in the case of wind turbine wakes, a local stability approach has been adopted. More specifically, at a given streamwise position in the wake, x , both y and z directions are discretized by using Chebyshev polynomials and the spatial amplification of perturbations as a function of the frequency are computed. Thus, in this method no modal expansion is imposed to the geometry of the perturbation in the azimuthal direction and the modes investigated are allowed to have a generic shape in the $y - z$ plane. Conversely, a complex wavenumber k is given, where its real and imaginary part define respectively the axial wavelength of the perturbation and its spatial amplification.

In this framework the effect on the near-wake dynamics of typical flow features of the incoming wind, such as the atmospheric boundary layer, turbulence heterogeneity, veer and shear, can be included in the stability analysis. Hence, real operating wind turbines conditions can be investigated with the present tool.

The analysis has been here applied on wind tunnel data, where the mean wind direction is aligned with the wind turbine axis. In particular, the mean wake flow acquired in the wind tunnel is used directly in the stability analysis and the measured Reynolds stresses are used to tune the mixing-length model, which is adopted to take into account turbulent diffusion in the dynamics of the hub vortex instability. The local spatial growth rates are computed at every streamwise position in the wake as a function of the frequency of the perturbation. Three modes, which manifest a dominant helical shape, are found to be amplified in the wake. Specifically, the single helical mode 1 is more unstable in the low frequency range $0 \leq \omega \leq 4$, conversely the double helical mode 2 resonates in the higher frequency interval $4 \leq \omega \leq 6.5$. Finally mode 3 results to be less amplified than modes 1 and 2 in all the frequency range. The dominant mode in the wind turbine wake, and its frequency, are detected by means of the integral amplification factor, which is obtained by integrating the spatial growth rates for the different downstream locations. The spatial shape of this resonating vorticity structure results mode 1, i.e. a single-helix in agreement with previous works which is a remarkable result recalling that no azimuthal modal expansion has been applied to the perturbation field. Moreover, the frequency predicted for the most unstable mode is in good agreement with the one measured in the wind tunnel.

The applicability of this 2D spatial local stability analysis is very general since it is suitable to be directly used to investigate the wake stability of wind turbine flows experimentally measured in the wind tunnel, wind LiDARs, or simulated by RANS or LES approaches.

3.4 Global stability and harmonic response to forcing of the hub vortex: an axisymmetric point of view

3.4.1 Introduction

In the previous three sections, the hub vortex instability has been investigated in a local framework, which relies on the weakly non-parallelism of the mean flow. However, a global approach is also possible, where the direction of advection of the flow has to be discretized. For this reason, the global analysis that is here applied is more suitable to describe flows rapidly evolving in the streamwise direction. For weakly non-parallel flows the two approaches have been compared for the canonical Batchelor wake in chapter 2 but we take here advantage of three components PIV data in a plane to cross check our previous results.

The experimental data used in this section have been acquired in a facility different from the one used in the previous sections and are shortly described in section 3.4.2. The global stability analysis and the global resolvent are then presented in section 3.4.3. Final conclusions and discussion are given in section 3.4.4.

3.4.2 Experiments

Experimental setup

The experimental data used here have been acquired in the boundary layer wind tunnel at the Saint Anthony Falls Laboratory of the University of Minnesota and presented in Zhang *et al.* (2012). We thank these authors for providing their three components PIV measurements in the 2D vertical streamwise ($x - z$) plane, where x and z are the streamwise and vertical direction respectively. In this experiment, a neutrally stratified turbulent boundary layer was developed by using a tripping mechanism at the entrance of the wind-tunnel test section. The free-stream turbulence intensity was approximately 2% at a flow velocity of 2.5 m/s outside the boundary layer.

A three-blade downscaled turbine GWS/EP-5030 x 3 was placed in the lowest one-third of the boundary layer. The turbine tower was 10.5 cm and the rotor diameter d was 13 cm, with the bottom tip of the turbine was placed at the height about 0.6 times the turbine radius. The rotor operates at 18.3 Hz with a tip speed ratio $TSR = \pi f d / U_{hub}$ of approximately 3.7, where $U_{hub} = 2$ m/s was the oncoming flow velocity at the hub height. The corresponding Reynolds number based on U_{hub} and the rotor diameter is $Re = 18000$. The thrust and the power coefficient were estimated to be of 0.42 and 0.37, respectively.

We refer the reader to Zhang *et al.* (2012) for more details about the experimental setup.

Time averaged flow and spectral analysis

Figure (3.30) shows time averaged three velocity component in the central wake plane ($y = 0$). In figure (3.30)(a) the streamwise component, U_x , is characterized by a strong velocity

3.4. Global stability and harmonic response to forcing of the hub vortex

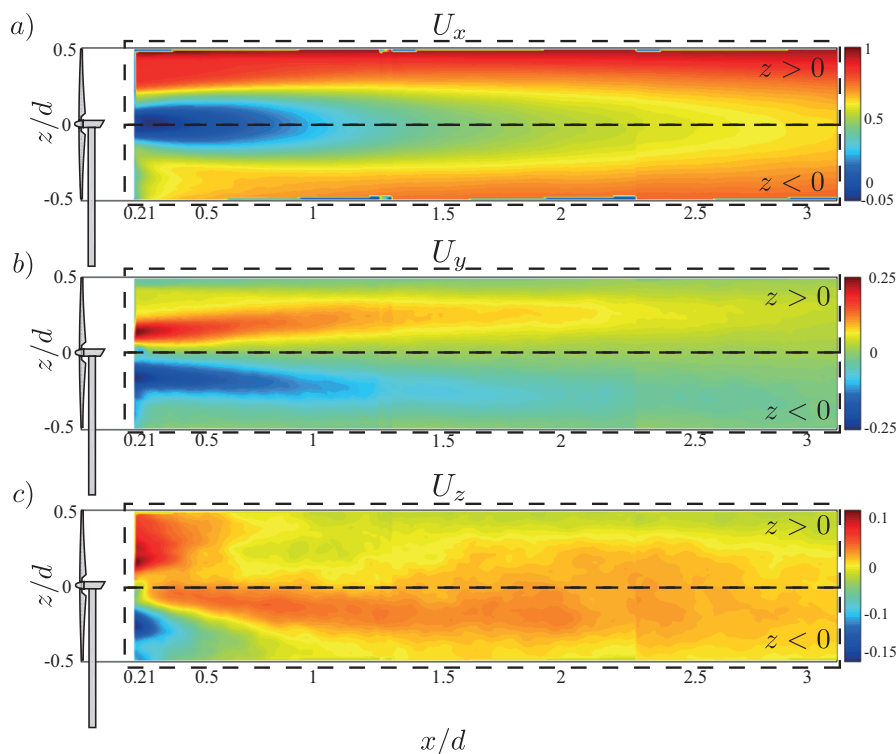


Figure 3.30: Non-dimensional time averaged mean flow in the 2D vertical streamwise ($x - z$) plane. (a) U_x/U_{hub} , (b) U_y/U_{hub} and (c) U_z/U_{hub} .

deficit, with flow reversal in the region $x/d < 0.4$, which is progressively recovered further downstream. The flow field is not symmetric with respect the plane $z = 0$ due to the presence of the atmospheric boundary layer. In particular, the streamwise velocity is higher at the top periphery of the wake than in the lower one. The elongated peaks of the spanwise velocity U_y at $z/d \approx \pm 0.15$ (Fig.(3.30)(b)) are connected to the rotational velocity induced by the hub vortex. In other words the spanwise velocity component U_y corresponds to the azimuthal velocity of the hub vortex projected in the cartesian reference frame. On the other hand, the vertical velocity U_z in (c) is smaller than the other two velocity components and is associated to the streamwise evolution of the flow. It corresponds to the radial velocity of the wake projected on the $x - z$ coordinate system, i.e. in the $y = 0$ plane.

As documented in Zhang *et al.* (2012), hot-wire anemometer (HWA) was used to measure the instantaneous streamwise and wall-normal velocity components with a frequency of acquisition of 1000 Hz. The spectral analysis on the HWA data acquired at the wake periphery revealed an intense fluctuation at a frequency of 55 Hz that is equal to three times the rotational frequency of the turbine. This frequency contribution results from the shedding of so-called tip-vortices from the tip of the three turbine blades. In addition, the power spectra at the wake centerline shows a strong low frequency peak at about 6 Hz, see Figure (3.31), and it is consistent with previous work by Medici & Alfredsson (2006) who attributed it to the meandering of the wake and to Iungo *et al.* (2013); Viola *et al.* (2014) who unraveled a helical

instability of the hub vortex. This low frequency corresponds to a nondimensional pulsation of $2\pi 6 \text{ Hz} * d / U_{hub} = 2.5$.

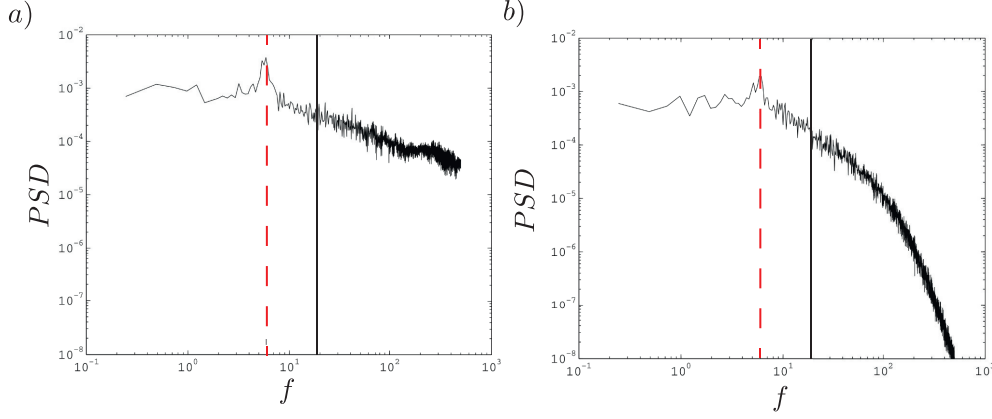


Figure 3.31: Figure adapted from Zhang *et al.* (2012). Power spectrum of the vertical velocity fluctuation at the wake centerline; (a) $x/d = 1$ and (b) $x/d = 2$. The red dashed line indicates the low frequency detected close the hub vortex, that is equal to approximately one third of the wind turbine rotational frequency (black vertical line).

3.4.3 Global analyses

In order to investigate the origin of the hub vortex low-frequency observed in the experiments, we carry out a global stability and a resolvent analysis on the time-averaged flow. Due to the presence of the atmospheric boundary layer, the mean flow in Figure (3.30) is not axisymmetric. However, since the three velocity components are available only in the central wake-plane, a fully three-dimensional stability analysis is not possible. For this reason, we have carried out two distinct axisymmetric stability analyses by considering both the *upper*

$$U_x = U_x(z > 0) \quad U_\theta = U_y(z > 0) \quad U_r = U_z(z > 0) \quad (3.42)$$

and the *lower* part of the flow

$$U_x = U_x(z < 0) \quad U_\theta = U_y(z < 0) \quad U_r = U_z(z < 0). \quad (3.43)$$

In other word, we have considered here two independent axisymmetric mean flows, as shown in Figure 3.32. Here U_x , U_θ and U_r are the streamwise, azimuthal and radial velocity components projected on the radial coordinate system x, r, θ , where $r - \theta$ are the polar coordinates of the rotor plane.

3.4. Global stability and harmonic response to forcing of the hub vortex

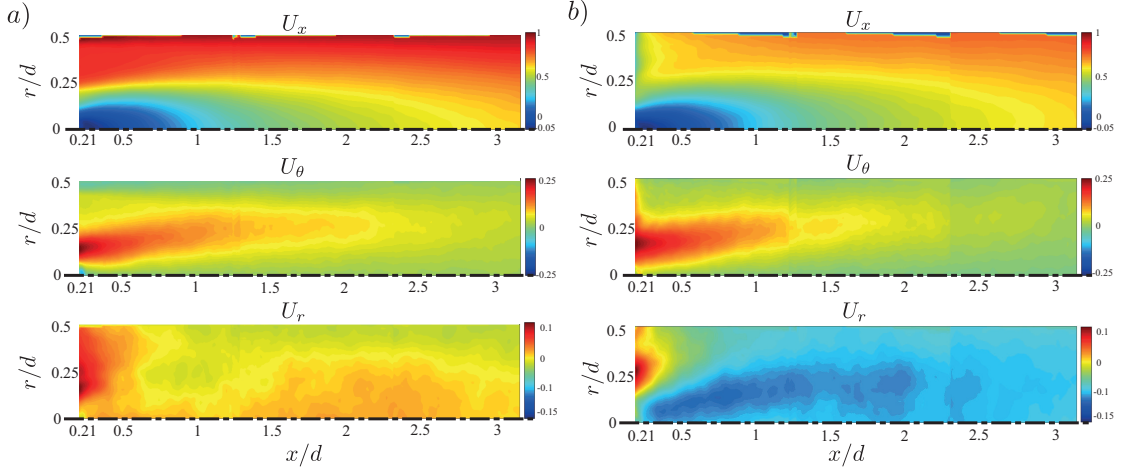


Figure 3.32: Streamwise, azimuthal and radial velocity components of the a) upper and b) lower axisymmetric mean flows, as defined in equations (3.42) and (3.43).

Stability analysis

The dynamics of small perturbations in velocity \mathbf{u} and pressure p about a steady mean flow \mathbf{U} is governed by the following nondimensional equation

$$\frac{\partial \mathbf{u}}{\partial t} + \mathbf{U} \cdot \nabla \mathbf{u} + \mathbf{u} \cdot \nabla \mathbf{U} = -\nabla p + \frac{1}{Re} \nabla^2 \mathbf{u}, \quad \nabla \cdot \mathbf{u} = 0, \quad (3.44)$$

where Re is the Reynolds number based on the oncoming velocity at the hub, U_{hub} and the rotor diameter d . Since the mean flow \mathbf{U} is axisymmetric and independent of time we can decompose the perturbation $\mathbf{q} = (\mathbf{u}, p)$ on normal modes

$$\mathbf{q} = \hat{\mathbf{q}} e^{i(m\theta - \omega t)} \quad (3.45)$$

where the integer m is the azimuthal wavenumber and ω is a complex quantity. In particular, the frequency of the perturbation is given to the real part of ω , ω_r , while the imaginary part, ω_i , is the growth rate. Thus, if $\omega_i > 0$ the perturbation grows exponentially in time, vice versa when $\omega_i < 0$ it decays with damping factor ω_i .

By injecting the modal expansion (3.45) in the equations (3.44) a generalized eigenvalue problem of the form

$$-i\omega \mathbf{B} \hat{\mathbf{q}} = \mathbf{L} \hat{\mathbf{q}}, \quad (3.46)$$

where \mathbf{B} is the mass matrix, \mathbf{L} is the linearized Navier-Stokes operator defined in section 2. Equation (3.46) is discretized by using the staggered pseudospectral Chebyshev-Chebyshev collocation method presented in section 2. Here the computational domain corresponds to the flow region where the PIV data are available, i.e. $0.21 < x/d < 3.1$ and $-0.5 < r/d < 0.5$, with homogenous Dirichlet condition at the inlet, null stresses at the outlet and lateral boundary and compatibility conditions on the axis (Batchelor & Gill, 1962). The number of points used

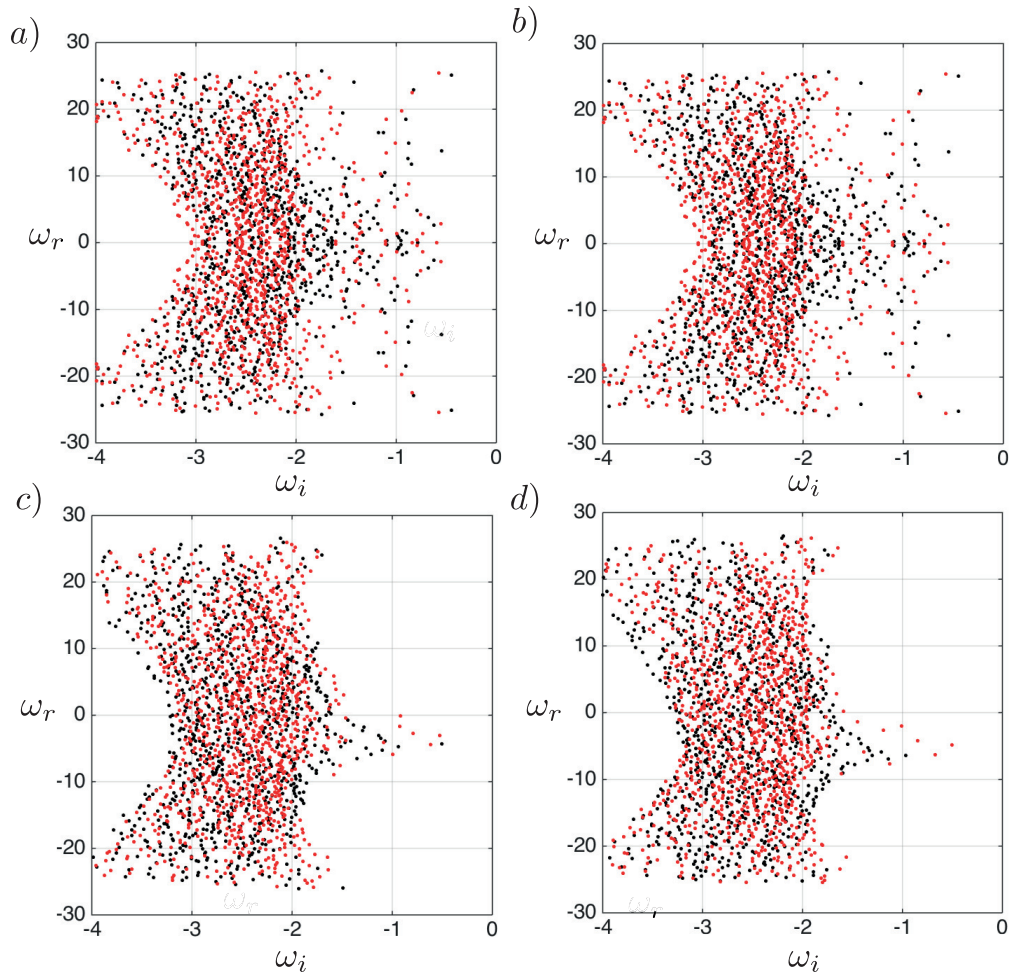


Figure 3.33: Global stability spectrum for (a) $m = 0$, (b) $m = 1$, (c) $m = 2$ and (d) $m = 3$. The black and red markers correspond to the eigenvalues of the upper ($z > 0$) and lower ($z < 0$) mean flow.

in the axial and radial direction is $N_x = 60$ and $N_y = 40$, respectively.

The eigenvalue problem (3.46) is solved for several values of m by using the Matlab function *eigs*. Figure 3.33 shows the closest hundreds eigenvalues to the target $\omega = 0$ for the azimuthal wavenumbers (a) $m = 0$, (b) $m = 1$, (c) $m = 2$ and (d) $m = 3$. The black markers correspond to the global stability spectrum when the upper portion ($z > 0$) of the experimental data is used as mean flow in equation (3.44). On the other hand, when the axisymmetric stability analysis is carried out on the lower part of the flow field ($z < 0$) the red-marked spectrum is obtained. It results that both the upper and lower mean flows are stable for all azimuthal wavenumbers and the least stable mode is an $m = 1$ with a frequency $\omega_r = 0.41$ which is significantly different from the one detected in the experiment that is equal to 2.5. Hence, the hub vortex low frequency observed in the experiment can not explained as a global instability of the flow triggered by globally unstable eigenmode.

3.4. Global stability and harmonic response to forcing of the hub vortex

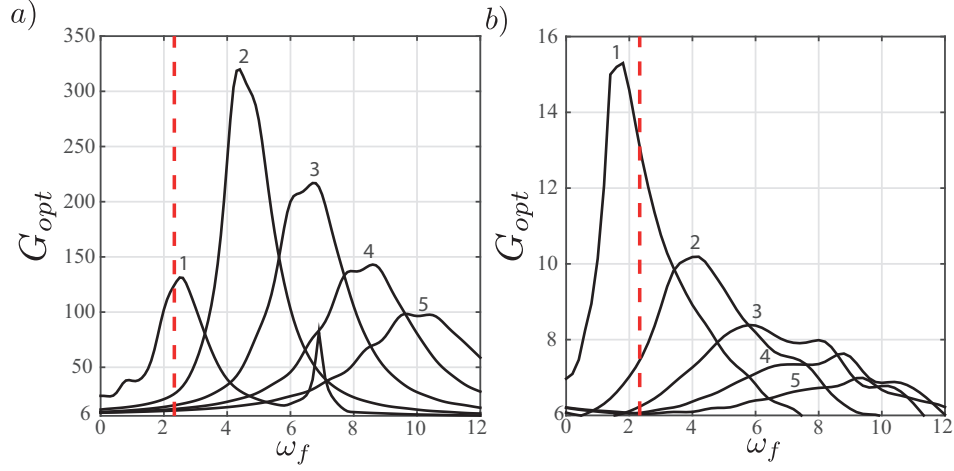


Figure 3.34: Optimal gains versus forcing frequency ω_f , for the (a) upper and (b) lower mean flow. Each branch corresponds to a different azimuthal wavenumber.

Resolvent analysis

In this section, we carry out a pseudo-resonance analysis in order to determine the *preferred* mode in the flow, i.e. the mode corresponding to the largest energy amplification. Following Garnaud *et al.* (2013); Viola *et al.* (2016a) the linear response to an harmonic body forcing \mathbf{f} is given by

$$\frac{\partial \mathbf{u}}{\partial t} + \mathbf{U} \cdot \nabla \mathbf{u} + \mathbf{u} \cdot \nabla \mathbf{U} = -\nabla p + \frac{1}{Re} \nabla^2 \mathbf{u} + \mathbf{f}, \quad \nabla \cdot \mathbf{u} = 0, \quad (3.47)$$

In the case the body forcing is harmonic with frequency ω_f , $\mathbf{f} = \hat{\mathbf{f}} e^{-i\omega_f t}$, and using the normal mode expansion (3.45) setting $\omega = \omega_f$, the linearized system of equations with embedded boundary conditions reads:

$$-i\omega_f \mathbf{B} \hat{\mathbf{q}} = \mathbf{L} \hat{\mathbf{q}} + \mathbf{B}_f \hat{\mathbf{f}}, \quad (3.48)$$

where \mathbf{B} and \mathbf{L} are the same operators used in the stability analysis (3.46) and \mathbf{B}_f is the so-called prolongation operator that maps the boundary forcing onto the interior degrees of freedom. The response to a given forcing $\hat{\mathbf{f}}(x=0, r)$ pushing at the inlet harmonically with frequency ω_f is directly obtained by solving the linear system in equation (3.48). Note that in principle the matrix $(-i\omega_f \mathbf{B} - \mathbf{L})$ can be inverted as long as ω_f is not an eigenvalue of the non-forced system. The kinetic energy gain of the response respect to the forcing is defined as:

$$G^2(m, \omega_f) = \frac{\int_{\Omega} |\hat{\mathbf{u}}|^2 r dr dx}{\int_{\Omega} |\hat{\mathbf{f}}|^2 r dr dx} = \frac{\|(\mathbf{L} + i\omega_f \mathbf{B})^{-1} \mathbf{B}_f \hat{\mathbf{f}}\|_E^2}{\|\hat{\mathbf{f}}\|_E^2}, \quad (3.49)$$

where $(\mathbf{L} + i\omega_f \mathbf{B})^{-1}$ is known as the resolvent.

The preferred mode is defined as the mode corresponding to the largest energy gain. Given

Chapter 3. Hub vortex instability

the forcing frequency, ω_f , and the azimuthal wavenumber, m , the optimal forcing corresponding to the maximum energy amplification is defined in discrete form as:

$$G_{opt}^2(\omega_f, m) = \max_{\hat{\mathbf{f}}} \frac{\|\hat{\mathbf{q}}\|_E^2}{\|\hat{\mathbf{f}}\|_E^2} = \max_{\hat{\mathbf{f}}} \frac{\|(\mathbf{L} + i\omega_f \mathbf{B})^{-1} \mathbf{B}_f \hat{\mathbf{f}}\|_E^2}{\|\hat{\mathbf{f}}\|_E^2}, \quad (3.50)$$

As explained in detail in Marquet & Sipp (2010); Garnaud *et al.* (2013) the optimization defined in equation (3.50) is equivalent to the following eigenvalue problem, where $G_{opt}^2(\omega_f)$ corresponds to the eigenvalue λ :

$$\mathbf{Q}_f^{-1} \mathbf{B}_f^H (\mathbf{L} + i\omega_f \mathbf{B})^{-H} \mathbf{Q}^H (\mathbf{L} + i\omega_f \mathbf{B})^{-1} \mathbf{B}_f \hat{\mathbf{f}} = \lambda \hat{\mathbf{f}}, \quad (3.51)$$

\mathbf{Q} and \mathbf{Q}_f are the weight matrices of the discretized energy norm and the norm of the forcing, and defined as Viola *et al.* (2016a).

Figure 3.34 shows the optimal gains, $G_{opt}(\omega_f, m)$, as a function of the forcing frequency, where each branch corresponds to a different azimuthal wavenumber. In both a) the upper mean flow and b) the lower mean flow case the single helical mode is the most amplified mode at the hub vortex frequency which is depicted by the vertical dashed line. However, the mode that better resonates in the upper mean flow analysis is a $m = 2$ mode at a frequency $\omega_f = 4.3$ which differs from the hub vortex frequency measured in the experiments, that is equal to 2.5. As in the case of the local spatial analysis carried out by Lungo *et al.* (2013) and reported in section 3.1, it is not possible to select a dominant mode without considering as additional input the instability frequency detected experimentally.

Resolvent analysis for turbulent flows

In analogy to the work of Viola *et al.* (2014), presented in section 3.2 we now carry out a resolvent analysis that includes the effect of the small scale turbulence which has been neglected in the previous section. This analysis leverages on the so-called triple decomposition proposed by Reynolds & Hussain (1972), where the unsteady flow is decomposed as the sum of the time-averaged base-flow, $\mathbf{U}(\mathbf{x})$, the coherent fluctuation, $\tilde{\mathbf{u}}(\mathbf{x}, t)$, and the turbulent motion, $\mathbf{u}'(\mathbf{x}, t)$. Recalling the formulation detailed in section 3.2 the linear evolution of the coherent perturbation, $\tilde{\mathbf{u}}$, on top of the time averaged flow, \mathbf{U} , is given by the equation (3.32):

$$\frac{\partial \tilde{\mathbf{u}}}{\partial t} + \nabla \tilde{\mathbf{u}} \cdot \mathbf{U} + \nabla \mathbf{U} \cdot \tilde{\mathbf{u}} = -\nabla \tilde{p} + \nabla \cdot ((Re^{-1} + \nu_t)[\nabla + \nabla^T] \tilde{\mathbf{u}}), \quad \nabla \cdot \tilde{\mathbf{u}}, \quad (3.52)$$

where the ν_t is the nondimensional eddy-viscosity which is the proportionality coefficient between the mean strain rate tensor and the deviatoric part of the Reynolds stress tensor in the Boussinesq equation.

$$-\overline{\mathbf{u}'\mathbf{u}'} + \frac{2}{3} \bar{q} I \simeq \nu_t [\nabla + \nabla^T] \bar{\mathbf{U}} \quad (3.53)$$

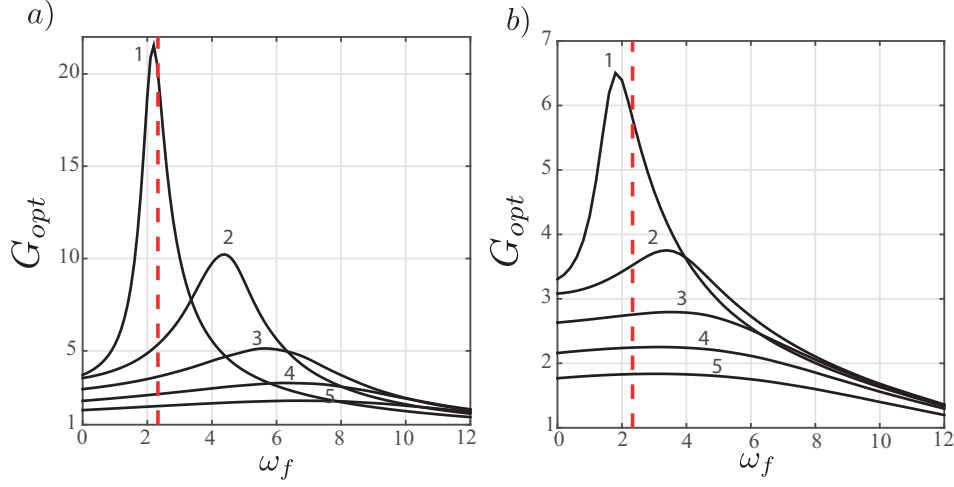


Figure 3.35: Optimal gains versus forcing frequency ω_f with the uniform eddy-viscosity model and, for the (a) upper and (b) lower mean flow. Each branch corresponds to a different azimuthal wavenumber.

where q is the turbulent kinetic energy (TKE) and I is the 3x3 identity matrix. In this preliminary analysis we adopt a simple uniform eddy-viscosity analysis which was found to correctly predict the hub vortex frequency in the local spatial analysis carried out in Viola *et al.* (2014). The value of the eddy viscosity ν_t is here calibrated by using the statistics of the experimental velocity data gently provided by Zhang *et al.* (2012). Specifically, a *best fit* strategy minimizing the norm of the difference between the lhs and rhs of the Boussinesq equation (3.53) is used, in a similar fashion to what explained in section 3.2. We obtained an eddy viscosity equal to $\nu_t = 1.4 \cdot 10^{-4}$. Thus, in the case of uniform eddy viscosity model, the resolvent analysis (3.47) simply reduces to lower the Reynolds number to an equivalent Reynolds number defined as $Re^* = (Re^{-1} + \nu_t)^{-1} = 700$.

Figure 3.35 shows the optimal gains, $G_{opt}(\omega_f, m)$, as a function of the forcing frequency in the case of uniform eddy viscosity model. Accounting for the small scale turbulent effect in the resolvent analysis allows to a clear mode identification, as shown in (b) and (c) for the upper and lower mean flow. The single helical mode $m = 1$ it is seen to be the preferred mode in the wind turbine wake, i.e. the most amplified one. Its amplification factor has a clear and definitely dominant peak at a frequency, which is almost coincident with the one measured experimentally (equal to 2.5 and reported in figure 3.35(a) and (b) as a red vertical line).

3.4.4 Conclusions

In this section, we have tried to take benefit of three components 2D PIV data in a vertical plane by Zhang *et al.* (2012) to use a direct global method to determine the stability and response to harmonic forcing of the swirling wake behind a model turbine. While this avoids to make any weakly non-parallel assumptions, it still requires an important and obviously questionable hypothesis: the flow is assumed axisymmetric to avoid conducting a 3D stability

Chapter 3. Hub vortex instability

analysis.

We here compared the global stability properties of the axisymmetric upper and lower flows that were measured. In absence of turbulence models, there are considerable differences between both analyses since the preferred mode is found to be $m = 2$, $\omega = 4.2$ and $m = 1$, $\omega = 1.8$ respectively. The addition of the simplest possible turbulence model, a constant eddy viscosity however damps higher modes and frequencies, reconciling the amplification properties deduced from the analysis of the upper and lower flow fields: the preferred mode is $m = 1$ at a frequency that well matched the one of the hub vortex instability measured in the experiments.

4 Flow control of weakly non-parallel flows

Flow control of weakly non-parallel flows: application to trailing vortices

F. Viola¹, E. Pezzica¹, G.V. Iungo², S. Camarri³ and F. Gallaire¹

¹ Laboratory of Fluid Mechanics and Instabilities, École Polytechnique Fédérale de Lausanne, Lausanne, CH-1015, Switzerland

² The University of Texas at Dallas, Mechanical Engineering Department, Wind Fluids and Experiments Lab (WindFluX), 75080 Richardson, TX

³ Department of Civil and Industrial Engineering, University of Pisa, Pisa 56122, Italy

In revision in *Journal of Fluid Mechanics*.

A general formulation is proposed to control the integral amplification factor of harmonic disturbances in weakly non-parallel amplifier flows. The sensitivity of the local spatial stability spectrum to a base-flow modification is first determined, generalizing the results of Bottaro *et al.* (2003). This result is then used to evaluate the sensitivity of the overall spatial growth to a modification of the inlet flow condition. This formalism is applied to a non-parallel Batchelor vortex which is a well-known model for trailing vortices generated by a lifting wing. The resulting sensitivity map indicates the optimal modification of the inlet flow condition enabling to stabilize the most amplified helical mode. It is shown that the control, formulated using a single linearization of the flow dynamics carried out on the uncontrolled configuration, successfully reduces the integral spatial gain of the instability.

4.1 Introduction

In the framework of linear stability analysis, open flows showing self-sustained oscillations, such as spiral vortex-breakdown (Ruith *et al.*, 2003; Qadri *et al.*, 2013), are globally unstable

and are called oscillators. In contrast, stable flows which exhibit a strong response to external disturbances are named amplifiers. Trailing vortices generated by a lifting wing are a classical example of amplifier flows in aeronautics (Spalart, 1998).

The stability properties of open flows depend in a complex way on multiple factors, such as the advection rate, the presence of localized forces, turbulence level, fluid properties, domain geometry, initial and boundary conditions. Thus, a modification of one of these factors yields a variation of the linearized operators of the stability analysis which turns into a modification of the eigenvalues in the stability spectrum. The dependence of the stability properties on one or more of these factors is commonly called *sensitivity*. Chomaz (2005) explained that the sensitivity may become large when the linear stability operator is non-normal, which is usually the case in hydrodynamics. For this reason several studies have been devoted along the years to sensitivity analyses.

Giannetti & Luchini (2007) defined the so-called structural sensitivity, which is the sensitivity to a spatially localized feedback and showed that the combined analysis of the global mode and its adjoint mode allows the identification of the wavemaker of the stability, i.e. the core region where the self-excited instability mechanism takes place. Bottaro *et al.* (2003) were the first to study the sensitivity to a base-flow modification and they identified the regions of the parallel Couette flow where a base flow modification has the most significant effect on temporal stability. Such base-flow variations can be the result of a passive control acting on the flow. Using a variational technique, Marquet *et al.* (2008) derived a general expression of the base-flow sensitivity valid for oscillator flows. In the case of amplifiers, the flow response to an external forcing is given by the resolvent analysis (Chomaz, 2005) and its sensitivity with respect to a base-flow modification was derived analytically by Brandt *et al.* (2011). They focused on the variation of the resolvent norm in the case of the Blasius boundary layer subjected to a harmonic body force where both component-wise and convective non-normalities are present. This analysis was applied by Boujo & Gallaire (2015) to the backward-facing step flow and extended to the case of inlet forcing and time-stochastic perturbation.

However, when the base flow evolves *slowly* in the advection direction these global approaches overlook the physical amplification mechanism, which is the convective growth of perturbation which can be related to the local stability properties of the flow. Indeed, the WKB asymptotic approach reveals that the linear spatial amplification of perturbations in amplifier flows is well captured by the spatial stability branches which are solutions of the local stability analysis, see Huerre & Rossi (1998). This raises the question if it is possible to determine a systematic way to control the amplification gain of a given mode, i.e. its global amplification, resulting from the integration of the local spatial growth along the streamwise direction. The objective of this paper is to provide a general framework so as to solve the mentioned control problem. The method proposed here generalizes to the case of weakly non-parallel amplifier flows the adjoint-based strategies usually employed for controlling oscillators (see Camarri (2015) for a review). Noise amplifiers comprise many fundamental flows as for instance boundary layers, convectively unstable wakes, trailing vortices, thus the proposed method is general and has many direct engineering applications. In this paper we present only a particular prototypical application of academic interest, which consists in

4.2. Sensitivity of the local spatial stability spectrum

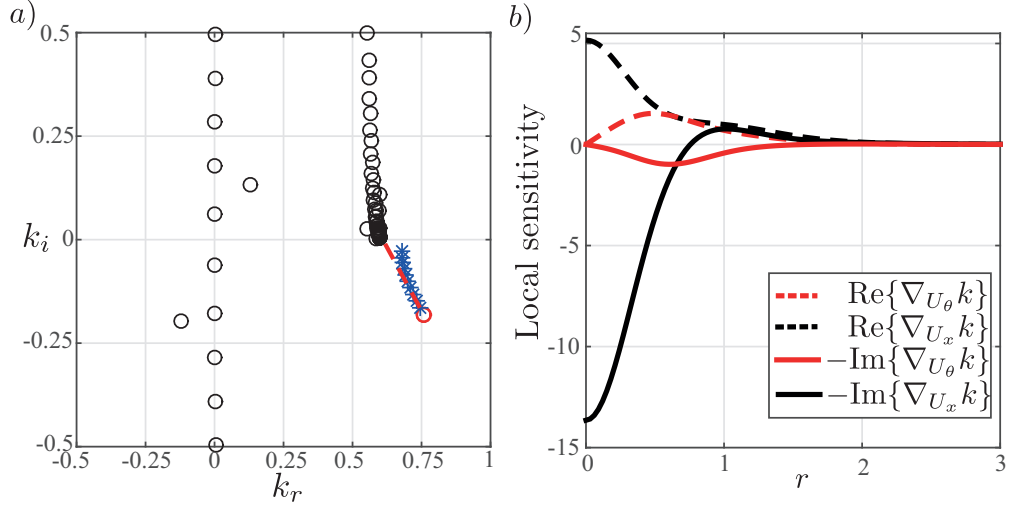


Figure 4.1: In (a) the circles are the eigenvalue spectrum of the parallel Batchelor vortex with $\alpha = 0.667$, $S = 0.333$, $Re = 100$, $m = 1$ and $\omega = 0.6$. The red circle indicates the most unstable physical eigenvalue. The blue asterisks mark the variation of the dominant eigenvalue (red circle) due to a modification of the base-flow (see text) is shown by the blue asterisks. The red line is the linear prediction based on the sensitivity map, whose components are reported in (b).

controlling the spatial instability of the non-parallel Batchelor vortex, well characterized in the literature, using a perturbation of the velocity profile generating the vortex. The particular selected test case, which is aimed at showing an example of flow control, is loosely applicable to disturbances suppression in trailing vortices (Spalart, 1998) and in wind turbine wakes (Iungo *et al.*, 2013). To this purpose we need first to address in section 4.2 the sensitivity of the local spatial stability problem in the parallel flow framework. Successively, on the basis of the previous result, the sensitivity of the integral gain to a generic modification of the velocity profile generating the vortex is derived in section 4.3.

4.2 Sensitivity of the local spatial stability spectrum

Although the formalism used here applies to all kind of convectively unstable shear flows, we consider now a Batchelor vortex profile with dimensionless velocity components

$$U_r = 0, \quad U_\theta = S(1 - e^{-r^2})/r, \quad U_x = 1 - \alpha e^{-r^2}, \quad (4.1)$$

where r , θ and x are the cylindrical coordinates. The wake and swirl parameters are set to $\alpha = 0.667$ and $S = 0.333$, respectively, and the Reynolds number based on the vortex core radius and the free-stream axial velocity, is equal to $Re = 100$. The behaviour of infinitesimal three-dimensional disturbances, $\mathbf{q}(x, r, \theta; t) = (\mathbf{u}, p)$, superimposed on top of the base-flow is

described by the linearized Navier-Stokes equations

$$\frac{\partial \mathbf{u}}{\partial t} + \mathbf{U} \cdot \nabla \mathbf{u} + \mathbf{u} \cdot \nabla \mathbf{U} = -\nabla p + \frac{1}{Re} \Delta \mathbf{u}, \quad \nabla \cdot \mathbf{u} = 0, \quad (4.2)$$

where \mathbf{u} and p are the disturbance velocity and pressure. In the case of parallel axisymmetric base-flow, these perturbations can be decomposed in the standard form:

$$\mathbf{q}(x, r, \theta; t) = \hat{\mathbf{q}}(r) e^{i(kx + m\theta - \omega t)}, \quad (4.3)$$

where m is the azimuthal wavenumber and $\hat{\mathbf{q}}(r) = (\hat{\mathbf{u}}, \hat{p})$. Our test-case vortex was shown to be convectively unstable by Viola *et al.* (2016a), calling for a spatial stability analysis, where the frequency ω is real and wavenumber k complex. The real part of k , k_r , corresponds to the streamwise wavenumber of the traveling perturbation and the imaginary part of k , in particular $-k_i$, is the spatial amplification rate. The governing equations (4.1), together with the normal mode expansion (4.3), can be recast in a quadratic eigenvalue problem of the following type

$$k^2 \mathcal{C}_2(\mathbf{U}, \omega) \hat{\mathbf{q}} + k \mathcal{C}_1(\mathbf{U}, \omega) \hat{\mathbf{q}} + \mathcal{C}_0(\mathbf{U}, \omega) \hat{\mathbf{q}} = 0, \quad (4.4)$$

where the linear operators $\mathcal{C}_0, \mathcal{C}_1, \mathcal{C}_2$, together with boundary conditions are reported in the appendix 4.5.

Figure 4.1 depicts the spatial spectrum for $\omega = 0.6$, where unstable perturbations propagating downstream are characterized by a positive phase velocity, ω/k_r , and a negative growth rate, k_i . Thus, the eigenvalues of interest are located in the fourth quadrant, i.e. $k_r > 0$ and $k_i < 0$. The red circle depicts the non-spurious eigenvalue associated with the largest spatial growth rate.

4.2.1 Generic sensitivity analysis of the local stability problem

The sensitivity of a given eigenvalue k to generic perturbations of the linear operators in equation (4.4) is here derived by a standard expansion procedure. A small variation of the linear operators $\mathcal{C}'_0 = \mathcal{C}_0 + \delta \mathcal{C}_0, \mathcal{C}'_1 = \mathcal{C}_1 + \delta \mathcal{C}_1, \mathcal{C}'_2 = \mathcal{C}_2 + \delta \mathcal{C}_2$ yields a small variation of the eigenvector $\hat{\mathbf{q}}' \sim \hat{\mathbf{q}} + \delta \hat{\mathbf{q}}$ together with a small variation in the eigenvalue $k' \sim k + \delta k$. At first order we have:

$$\delta k = - \frac{(\mathbf{q}^\dagger, [\delta \mathcal{C}_0 + k \delta \mathcal{C}_1 + k^2 \delta \mathcal{C}_2] \hat{\mathbf{q}})}{(\mathbf{q}^\dagger, [\mathcal{C}_1 + 2k \mathcal{C}_2] \hat{\mathbf{q}})}, \quad (4.5)$$

where the round brackets designate a suitable scalar product and $\mathbf{q}^\dagger = (\mathbf{u}^\dagger, p^\dagger)$ is the adjoint vector associated with the defined scalar product. From now on we will use the Hermitian inner product defined as $(\mathbf{q}_A, \mathbf{q}_B) = \int_0^\infty \mathbf{q}_A^H \mathbf{q}_B r dr$, where the symbol H indicates the trans-conjugate and \mathbf{q}_A and \mathbf{q}_B are two complex vector fields. In this case, the adjoint vector satisfies

the following adjoint spatial problem:

$$k^{*2} \mathcal{C}_2^\dagger \mathbf{q}^\dagger + k^* \mathcal{C}_1^\dagger \mathbf{q}^\dagger + \mathcal{C}_0^\dagger \mathbf{q}^\dagger = 0, \quad (4.6)$$

where the superscript $*$ designates the complex conjugate and the adjoint operators \mathcal{C}_0^\dagger , \mathcal{C}_1^\dagger and \mathcal{C}_2^\dagger are reported in the Appendix 4.5. The adjoint vector \mathbf{q}^\dagger is defined up to a multiplicative factor and from now the chosen normalization is such that the denominator of the expression (4.5) is equal to 1. Equation (4.5) is the generalization of the sensitivity of a standard eigenvalue problem explained in Chomaz (2005), which would correspond to the case $\mathcal{C}_2 = 0$.

4.2.2 Sensitivity of the local spatial stability properties to base flow modifications

We are now interested in determining the sensitivity of k to a generic base-flow modification $\delta \mathbf{U} = (\delta U_r = 0, \delta U_\theta, \delta U_x)$, where the restriction $\delta U_r = 0$ is dictated by the local analysis setting. A perturbation at the base-flow level in the linearized equation (4.2) yields to a perturbation of the linear operators $\delta \mathcal{C}_0, \delta \mathcal{C}_1, \delta \mathcal{C}_2$ such that $\delta \mathcal{C}_2 = 0$ and

$$[\delta \mathcal{C}_0 + k \delta \mathcal{C}_1] \hat{\mathbf{q}} = \begin{pmatrix} im \hat{u}_r \delta U_\theta / r + ik \hat{u}_r \delta U_x - 2 \hat{u}_\theta \delta U_\theta / r \\ \hat{u}_r \partial \delta U_\theta / \partial r + im \hat{u}_\theta \delta U_\theta / r + ik \hat{u}_r \delta U_x + \hat{u}_r \delta U_\theta / r \\ \hat{u}_r \partial \delta U_x / \partial r + im \hat{u}_x \delta U_\theta / r + ik \hat{u}_x \delta U_x \\ 0 \end{pmatrix}. \quad (4.7)$$

Substituting equation (4.7) in equation (4.5) and integrating by parts we can transfer the differential operators from the vector $\delta \mathbf{U}$ to the adjoint vector \mathbf{u}^\dagger . If the base-flow modification does not occur at the domain boundaries, the boundary terms coming from the integration by parts are null and equation (4.5) reads:

$$\delta k = (\nabla_{\mathbf{U}} k, \delta \mathbf{U}), \quad (4.8)$$

where the complex vector

$$\nabla_{\mathbf{U}} k = \begin{pmatrix} 0 \\ im(u_x^\dagger \hat{u}_x^H + u_r^\dagger \hat{u}_r^H + u_\theta^\dagger \hat{u}_\theta^H) + \partial u_\theta^\dagger / \partial r \hat{u}_r^H + u_\theta^\dagger \partial \hat{u}_r^H / \partial r + 2u_r^\dagger \hat{u}_\theta^H / r \\ ik(u_x^\dagger \hat{u}_x^H + u_r^\dagger \hat{u}_r^H + u_\theta^\dagger \hat{u}_\theta^H) + \partial u_x^\dagger / \partial r \hat{u}_r^H + u_x^\dagger \partial \hat{u}_r^H / \partial r + u_x^\dagger \hat{u}_r^H / r \end{pmatrix} \quad (4.9)$$

is the sensitivity of the considered spatial eigenvalue (k) to a base-flow modification. The azimuthal and streamwise components of $\nabla_{\mathbf{U}} k$ are the sensitivities of the complex eigenvalue k to an azimuthal and streamwise base-flow modification. Since $\nabla_{\mathbf{U}} k$ is a complex vector and $\delta \mathbf{U}$ is a real quantity, the real part of $\nabla_{U_\theta} k$ and $\nabla_{U_x} k$, which are reported with dashed lines in figure 4.1 (b), are sensitivities of k_r to a generic base-flow modification. On the other hand, the sensitivity of the spatial growth rate is given by the imaginary part of expression (4.9), whose components are shown in figure 4.1 (b) by plane lines for the most unstable spatial eigenvalue of the parallel Batchelor vortex with $\alpha = 0.667$, $S = 0.333$, $m = 1$ and $\omega = 0.6$. The radial component of the sensitivity to base-flow is null consistently within the parallel flow

assumption of the local analysis.

From the sensitivity maps, it is seen that a base-flow modification with positive azimuthal and streamwise components superimposed to the reference base-flow (4.1) leads k_r to increase. Moreover, a swirl increase and a decrease of the wake deficit yield to a lower spatial growth-rate $-k_i$. Hence, equation (4.8) allows us to determine the direction of displacement of the spatial eigenvalues in the complex k -plane corresponding to a given base-flow modification. In order to verify the sensitivity maps we study the effect of a specific base-flow modification $\delta U_x = ae^{-r^2}$, on the most unstable spatial eigenvalue in Figure 4.1 (a). The considered base-flow modification mimics a variation or uncertainty on the wake parameter α in equation (4.1) and its effect on the spatial stability is determined by solving the spatial stability analysis (4.4) with the modified base flow component $U_x + ae^{-r^2}$. Results are shown in figure 4.1(b) for a ranging from 3% to 30% of α . The true path followed by the selected eigenvalue in the complex plane as the parameter a is varied is indicated with blue asterisks. The same path is approximated by the red straight line using the sensitivity analysis carried out on the unperturbed flow. It is seen that the perturbed eigenvalue positions, which migrates towards the stability region as a is increased, are well aligned with the linear prediction provided by sensitivity analysis, especially when a is small, thus validating the method and its implementation. For larger base-flow modifications, nonlinearities neglected in the linearized relation (4.5), become more important and lead to a progressively increasing discrepancy between the predicted and the true eigenvalue trajectory.

Equation (4.9) is an extension to the spatial analysis of a concept that was originally developed by Bottaro *et al.* (2003) for temporal analysis. It should be also noted that the two non-null components of $\nabla_U k$ are equal to the azimuthal and axial components of the vector

$$-\mathbf{u}^\dagger \cdot (\nabla \hat{\mathbf{u}})^H + \hat{\mathbf{u}}^* \cdot \nabla \mathbf{u}^\dagger, \quad (4.10)$$

which is formally similar to the sensitivity to base flow modifications of a global mode found by Marquet *et al.* (2008). The use of eq. (4.10) in a spatial framework requires $\hat{\mathbf{u}}$ to be the direct spatial mode while \mathbf{u}^\dagger is the spatial adjoint vector which satisfies the spatial adjoint problem (4.6). Moreover, the streamwise and azimuthal derivatives have to be replaced by the Fourier derivatives, according to the modal expansion (4.3). Finally, the radial component of (4.10), which would give the sensitivity to a radial velocity modification in a global framework, does not bear any meaning in the local spatial analysis.

4.3 Sensitivity of the integral growth factor in weakly nonparallel flows

Rather than parallel flows, we now consider weakly non-parallel amplifier flows which slowly evolve in the streamwise direction, resulting in variations of the local stability properties. The non-parallel Batchelor vortex with inlet condition (4.1) and free-stress condition at the outlet and radial far-field boundaries represents a suitable prototype flow. Its velocity components and pressure $\mathbf{Q} = (\mathbf{U}, P)$ are found by solving the discrete Navier-Stokes equations (4.11) in

4.3. Sensitivity of the integral growth factor in weakly nonparallel flows

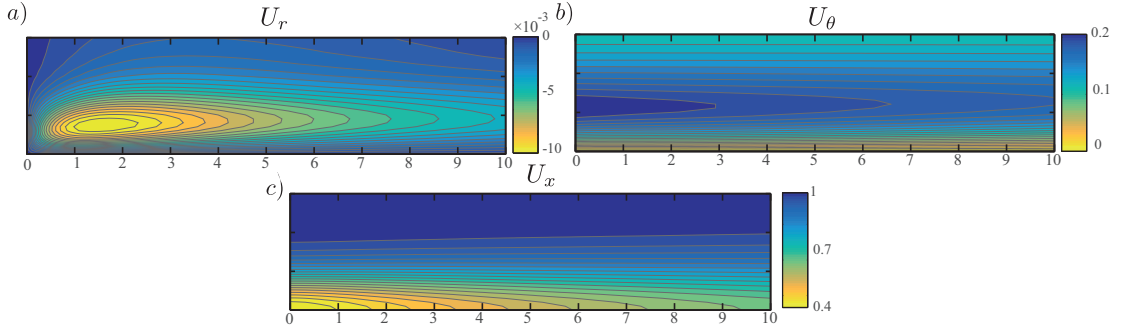


Figure 4.2: (a) Radial, (b) azimuthal and (c) streamwise velocity components of the non-parallel Batchelor vortex at $Re = 100$ with inlet condition given by the velocity profile in equation (4.1).

cylindrical coordinates:

$$\mathbf{N}(\mathbf{Q}, \mathbf{U}_0) = \begin{pmatrix} \mathbf{U} \cdot \nabla \mathbf{U} + \nabla P - \frac{1}{Re} \Delta \mathbf{U} \\ \nabla \cdot \mathbf{U} \end{pmatrix} = 0, \quad (4.11)$$

where the dependence from the inlet condition \mathbf{U}_0 is emphasized. We have used a staggered pseudospectral Chebyshev-Chebyshev collocation method (Viola *et al.*, 2016a) and the non-linear solution of equation (4.11) at $Re = 100$ is obtained by a Newton-Raphson method. The computational domain is $0 < x < 15$ and $0 < r < 10$ and it has been discretized by using 80 and 40 nodes in the streamwise and radial directions. The resulting velocity field \mathbf{U} is reported in Figure 4.2 (a,b,c). Note as in (a) the radial velocity is significantly smaller than the other two velocity components, thus validating the assumption of weakly non-parallel flow. Proceeding downstream the vortex core gets slightly diffused, as shown in (b), and the axial velocity deficit in (c) gradually recovers.

Asymptotic theory for a weakly non-parallel base flow (Huerre & Rossi, 1998) prescribes that the global mode at leading order takes the following modulated wave form:

$$\mathbf{q}(r, \theta, x; t) \sim \hat{\mathbf{q}}(r, x) \exp \left[i \left(\int_{x_0}^x k(x', \omega) dx' + m\theta - \omega t \right) \right]. \quad (4.12)$$

By adopting the same notation of the previous section, ω is the frequency of the mode, m is its azimuthal wavenumber, $k(x, \omega)$ is the local spatial eigenvalue at the flow location x and $\hat{\mathbf{q}}(r, x) = (\hat{\mathbf{u}}, \hat{p})$ is the corresponding spatial eigenvector. Figure 4.3 shows the streamwise evolution of the unstable spatial eigenvalue k for the reference case $\omega = 0.6$ and $m = 1$. Due to the reduction of the wake deficit, both the axial wavenumber k_r and the spatial growth rate, $-k_i$, decrease while moving downstream.

4.3.1 Lagrangian formulation

The integral spatial amplification of the perturbation (4.12) is given at leading order by $\exp(-\int_{x_0}^{x_{out}} k_i(x') dx')$, where x_{out} is the position of the domain outlet boundary. In this section,

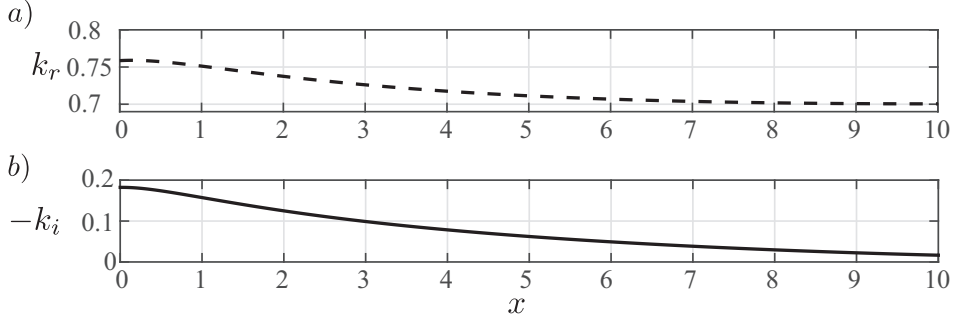


Figure 4.3: Streamwise evolution of the (a) axial wavenumber k_r and of the (b) spatial growth rate $-k_i$ for the spatial branch at $\omega = 0.6$

specifically for control purposes, we are interested in determining the sensitivity of the discrete spatial gain,

$$G = \exp\left(-\sum_{n=1}^{N_x} w_j k_i(x_n)\right), \quad (4.13)$$

to a modification of the inflow conditions \mathbf{U}_0 . In equation (4.13) the coefficients w_j are the integration weights of the standard trapezoidal formula and N_x is the number of locations used to discretize the streamwise direction. This problem can be formulated as an optimization problem where the objective function is the gain itself. Rather than a continuous approach where the continuous optimization problem is defined and then discretized, we will directly apply the Lagrangian technique to the discretized governing equations:

$$\mathcal{L}(\mathbf{Q}, \mathbf{U}_0) = G(\mathbf{Q}) + \boldsymbol{\lambda}^T \mathbf{N}(\mathbf{Q}, \mathbf{U}_0), \quad (4.14)$$

where the superscript T stands for the transpose. The constraint is given by the discretized steady Navier-Stokes equations, $\mathbf{N}(\mathbf{Q}, \mathbf{U}_0)$, and $\boldsymbol{\lambda}$ is the vector of Lagrange multipliers or *discrete adjoint*. Thus, the gradient of the spatial gain G with respect to a base-flow inlet modification is derived by considering variations of the Lagrangian \mathcal{L} . Imposing the stationarity of \mathcal{L} with respect to $\boldsymbol{\lambda}$ reduces to the discrete state equation (4.11), which is satisfied by the uncontrolled base-flow \mathbf{Q} . Then, the stationarity of the Lagrangian with respect to the state variable, \mathbf{Q} , yields to an equation which has to be satisfied by the adjoint variable $\boldsymbol{\lambda}$:

$$-\boldsymbol{\lambda}^T \nabla_{\mathbf{Q}} \mathbf{N} = \nabla_{\mathbf{Q}} G, \quad (4.15)$$

where $\nabla_{\mathbf{Q}} \mathbf{N}$ is the Jacobian matrix. Recalling that the local growth rates $-k_i(x_n)$ depend only on the streamwise and azimuthal velocity at the location x_n , the rhs of equation (4.15) can be rewritten as follows

$$\nabla_{\mathbf{Q}} G = -G \sum_{n=1}^{N_x} w_j \left[\nabla_{U_x} k_i(x_n) \nabla_{\mathbf{Q}} U_x(x_n) + \nabla_{U_\theta} k_i(x_n) \nabla_{\mathbf{Q}} U_\theta(x_n) \right], \quad (4.16)$$

4.3. Sensitivity of the integral growth factor in weakly nonparallel flows

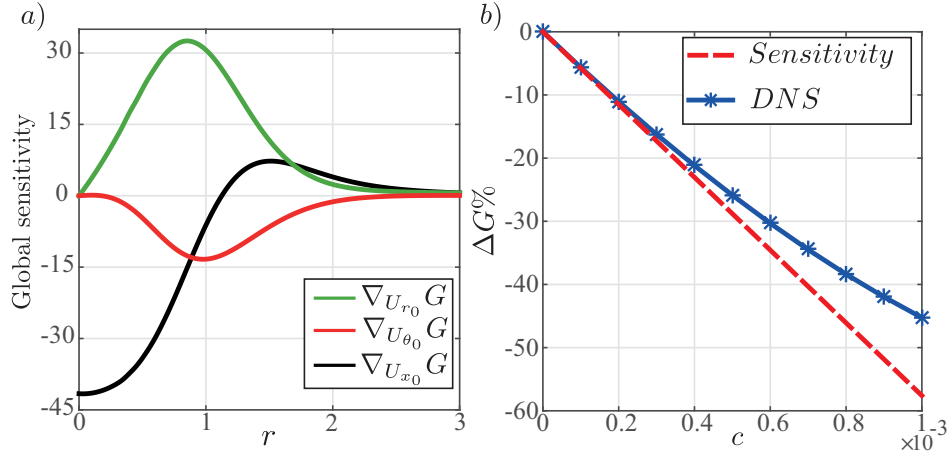


Figure 4.4: In (a) the sensitivity maps to a radial (green), azimuthal (red) and axial (black) inlet velocity modifications. In (b) the true spatial gain modification is reported with blue asterisks as a function of the magnitude of the inlet control c . The red dashed line shows the linear gain modification according to the inlet sensitivity map.

where the terms $\nabla_{U_x} k_i(x_n)$ and $\nabla_{U_\theta} k_i(x_n)$ are the local spatial sensitivities of k_i to a local base-flow modification derived in the previous section. Specifically, the local spatial sensitivities at each section x_n have to be evaluated by injecting the local direct $\hat{\mathbf{u}}(x_n)$ and adjoint $\mathbf{u}^\dagger(x_n)$ modes and the local spatial eigenvalue $k(x_n)$ in equation (4.9). The terms $\nabla_{\mathbf{Q}} \mathbf{U}_x(x_n)$ and $\nabla_{\mathbf{Q}} \mathbf{U}_\theta(x_n)$ are the interpolation matrices which extract from a vector \mathbf{Q} the streamwise and azimuthal velocity components at the streamwise position x_n . Hence, given the local spatial sensitivity analyses, the adjoint variable $\boldsymbol{\lambda}$ can be determined by solving the linear system (4.15).

Finally, the derivative of the Lagrangian \mathcal{L} with respect to the control variable gives the spatial gain modification with respect a small-amplitude generic $\delta \mathbf{U}_0$:

$$\delta G = \frac{dG(\mathbf{Q})}{d\mathbf{U}_0} \delta \mathbf{U}_0 = \boldsymbol{\lambda}^T \nabla_{\mathbf{U}_0} \mathbf{N} \delta \mathbf{U}_0 \quad (4.17)$$

where $\nabla_{\mathbf{U}_0} \mathbf{N}$ is a restriction matrix, which extracts the velocity components at the inlet x_0 from a velocity-pressure vector \mathbf{Q} . Equation (4.17) can be formally rewritten as

$$\delta G = \langle \nabla_{\mathbf{U}_0} G, \delta \mathbf{U}_0 \rangle \quad (4.18)$$

where $\langle \mathbf{u}_A, \mathbf{u}_B \rangle = \mathbf{u}_A^T M \mathbf{u}_B$ is the inner product in the discrete setting, and M is the integration matrix containing the integration weights on its diagonal. The real vector $\nabla_{\mathbf{U}_0} G$ is the spatial gain sensitivity with respect to an inlet modification, and is defined as:

$$\nabla_{\mathbf{U}_0} G = M^{-1} (\nabla_{\mathbf{U}_0} \mathbf{N})^T \boldsymbol{\lambda}. \quad (4.19)$$

For the reference case of $\omega = 0.6$ and $m = 1$, the three components of $\nabla_{\mathbf{U}_0} G$, which correspond to the sensitivity maps to a radial, azimuthal and axial inlet velocity modification, are reported

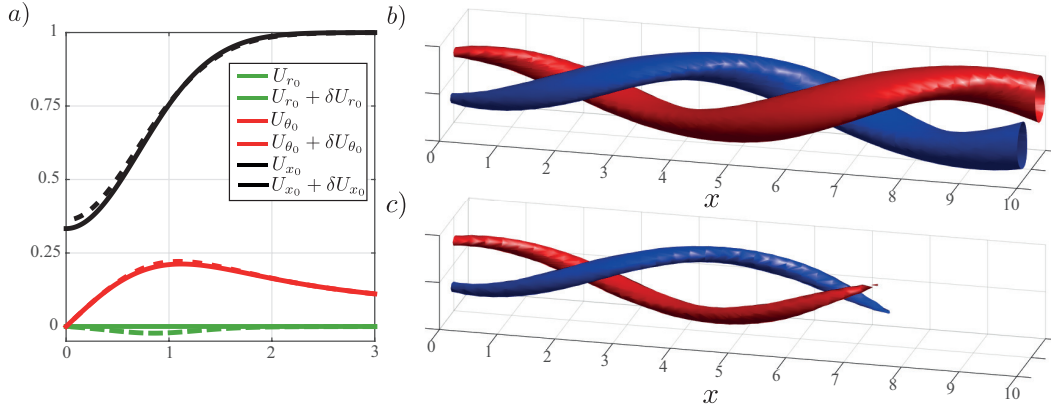


Figure 4.5: (a) Plane lines indicate the velocity components of the uncontrolled inlet condition, which correspond to the Batchelor vortex profile (4.1) with $\alpha = 0.667$ and $S = 0.333$. The velocity components perturbed by the application of the control $\delta \mathbf{U}_0 = 7 \cdot 10^{-4} \nabla_{\mathbf{U}_0} G$ are shown with dashed line. (b) Isosurfaces of $\pm 95\%$ of the maximum axial vorticity of the global spatial mode (4.12) in the (b) uncontrolled and (c) controlled case.

in Figure 4.4. The sensitivity with respect U_{θ_0} reveals that in order to increase the gain, the azimuthal velocity, and therefore the swirl parameter, has to be decreased. Similarly, $\nabla_{U_{x_0}} G$ shows that an increase of the wake deficit and a higher streamwise velocity at the vortex periphery lead to a more intense response to noise. Due to the non-parallelism of the base-flow \mathbf{U} , the spatial gain is also sensitive to a variation of the radial velocity which acts on the local spatial stability properties of the flow through the coupling with the streamwise and azimuthal velocity components in equations (4.11). In particular it is seen that a positive inlet radial velocity, which increases the vortex core diameter and consequently favors the axial deceleration, has a destabilizing effect.

4.3.2 Optimal inlet control

The sensitivity $\nabla_{\mathbf{U}_0} G$ not only predicts the linear modification of the spatial gain due to an inlet modification through (4.18), but it also corresponds to the most destabilizing infinitesimal inlet modification (Camarri, 2015). For this reason, $\nabla_{\mathbf{U}_0} G$ can be used to design an inlet control which stabilizes the global spatial branch. Figure 4.4(b) shows the gain variation due to an inlet modification of the type $\delta \mathbf{U}_0 = -c \nabla_{\mathbf{U}_0} G$, with c the magnitude of the control. The blue line represents the real gain variation with respect to the uncontrolled condition. More precisely, at a given c , the real gain variation (blue asterisk) is computed by (i) solving the non-linear base flow equations (4.11) with the inlet condition $\mathbf{U}_0 - c \nabla_{\mathbf{U}_0} G$, and (ii) carrying out the WKB analysis on the obtained base-flow. Then, (iii) the associated gain $G(c)$ is computed according to the definition (4.13) and the gain variation $\Delta G = 1 - G(c)/G(c=0)$ is obtained, where $G(c=0)$ is the gain of the uncontrolled condition. It is seen that the linear gain variation predicted by equation (4.18), which is depicted by a red line in Fig. 4.4(b), correctly captures the gain variation at small values of c . In contrast, due to the nonlinear dependence of the

gain on the magnitude of the perturbation the error increases at large c . Still, the linearization leading to the sensitivity analysis allows the prediction of even large variations of gain with reasonable accuracy.

As an application, Figure 4.5(a) shows the uncontrolled and the controlled velocity profiles at the inlet for $c = 7 \cdot 10^{-4}$ (see Fig. 4.4(b)). Although the inlet condition differs very slightly from the uncontrolled case, the effect of this variation on the considered instability is substantial as shown in Fig. 4.5(b) and (c) where the axial vorticity of the spatial branch (4.12) with $\omega = 0.6$ and $m = 1$ is reported. In the first case the helical perturbation is convectively unstable in all the flow domain and is continuously amplified while propagating. When the control is applied, the spatial branch is damped for $x > 7$ and the global spatial gain experiences a significant reduction of 35% with respect to the uncontrolled flow.

4.4 Conclusions

In this work a general formulation is proposed which allows the application of systematic adjoint-based techniques for the control of the integral amplification factor of the selected modes in weakly non-parallel amplifier flows. The method is based on the sensitivity analysis of the local stability properties of the flow, which was here derived by adjoint methods. In particular, firstly the sensitivity of the spatial stability spectrum to a generic local modification of the stability operators is found. The results are successively used to study the case of a generic control which implies the modification of the base-flow. Although the method can be easily extended to cover very general cases, we presented here its application to a test case of academic interest, i.e. the control of the spatial instability in an evolving Batchelor vortex based on the perturbation of the velocity profile generating the vortex itself. The particular type of control considered here implies the optimization of the inlet boundary conditions in the simulation of the vortex evolution. We show that the local spatial sensitivities are the building blocks of the sensitivity to generic modifications of the inlet velocity profile. The resulting sensitivity map indicated the optimal modification of the inlet velocity profile so as to stabilize the single helical spatial mode of a non-parallel Batchelor vortex, which is locally convectively unstable. It is shown that the control, formulated using only one linearization of the flow dynamics carried out on the uncontrolled configuration, successfully reduces the global spatial gain of the instability.

The information provided by the control map is valid only for small control amplitudes perturbing the uncontrolled configuration. However, the control design method proposed here can be easily extended to include larger control amplitudes, by employing the sensitivity map in a standard iterative gradient method, as done for instance by Bottaro *et al.* (2003) for temporal analysis on parallel flow.

We conclude underlying that the systematic framework proposed here to control the integral amplification factor in amplifier flows has potential impact in many cases of interest. To name two examples which have inspired this work, the method proposed could be applied to control the wake instability related to the hub vortex in wind turbines (Iungo *et al.*, 2013) or, referring

to the work in Zuccher *et al.* (2006), for the identification of optimally stabilizing disturbances in boundary layers.

4.5 Local spatial stability of swirling flows

We report here the linear operators of the direct (4.4) and adjoint (4.6) QEPs:

$$\mathcal{E}_0 = \begin{bmatrix} imU_\theta/r - \frac{1}{Re}\Delta_{m,r\theta} + i\omega & -2U_\theta/r + \frac{1}{Re}\frac{2im}{r^2} & 0 & \frac{\partial}{\partial r} \\ \frac{\partial U_\theta}{\partial r} + U_\theta/r - \frac{1}{Re}\frac{2im}{r^2} & imU_\theta/r - \frac{1}{Re}\Delta_{m,r\theta} + i\omega & 0 & \frac{im}{r} \\ \frac{\partial U_x}{\partial r} & 0 & imU_\theta/r - \frac{1}{Re}\Delta_m + i\omega & 0 \\ \frac{1}{r} + \frac{\partial}{\partial r} & \frac{im}{r} & 0 & 0 \end{bmatrix}$$

$$\mathcal{E}_0^\dagger = \begin{bmatrix} -imU_\theta/r - \frac{1}{Re}\Delta_{m,r\theta} - i\omega & \frac{\partial U_\theta}{\partial r} + U_\theta/r + \frac{1}{Re}\frac{2im}{r^2} & \frac{\partial U_x}{\partial r} & \frac{\partial}{\partial r} \\ -2U_\theta/r - \frac{1}{Re}\frac{2im}{r^2} & -imU_\theta/r - \frac{1}{Re}\Delta_{m,r\theta} - i\omega & 0 & \frac{im}{r} \\ 0 & 0 & -imU_\theta/r - \frac{1}{Re}\Delta_m - i\omega & 0 \\ \frac{1}{r} + \frac{\partial}{\partial r} & \frac{im}{r} & 0 & 0 \end{bmatrix}$$

$$\mathcal{E}_1 = \begin{bmatrix} iU_x & 0 & 0 & 0 \\ 0 & iU_x & 0 & 0 \\ 0 & 0 & iU_x & i \\ 0 & 0 & i & 0 \end{bmatrix}, \quad \mathcal{E}_1^\dagger = \begin{bmatrix} -iU_x & 0 & 0 & 0 \\ 0 & -iU_x & 0 & 0 \\ 0 & 0 & -iU_x & i \\ 0 & 0 & i & 0 \end{bmatrix}, \quad \mathcal{E}_2 = \mathcal{E}_2^\dagger = \begin{bmatrix} \frac{1}{Re} & 0 & 0 & 0 \\ 0 & \frac{1}{Re} & 0 & 0 \\ 0 & 0 & \frac{1}{Re} & 0 \\ 0 & 0 & 0 & 0 \end{bmatrix}$$

with $\Delta_m = \left(\frac{1}{r}\frac{\partial}{\partial r} + \frac{\partial^2}{\partial r^2} - \frac{m^2}{r^2}\right)$ and $\Delta_{m,r\theta} = \Delta_m - \frac{1}{r^2}$. Homogeneous Neumann conditions on the lateral boundary and regularity conditions on the axis (Batchelor & Gill, 1962) are imposed in both problems. We refer to Viola *et al.* (2016a) for a detailed explanation of the numerical codes and convergence analysis.

5 Axisymmetric vortex breakdown: linear and nonlinear mechanisms

5.1 Introduction

Vortex breakdown is a widespread phenomenon that affects vortices with axial flow such as leading-edge vortices over delta wings, flame holders in combustion devices and atmospheric tornadoes. It consists of an abrupt change in the flow topology where the flow decelerates and diverges as if a solid obstacle was present in the flow. The onset of the vortex breakdown happens when the swirl number S , that compares the magnitude of the azimuthal and axial velocity components, exceeds a critical value. The structure of the vortex varies slowly in the streamwise direction and then, suddenly, the structure changes drastically with the formation of an axisymmetric recirculation region.

In addition to the axisymmetric breakdown form involving a steady bubble enclosing a finite region of recirculating fluid, there exist spiral breakdown states characterized by well-defined helical patterns and rotational frequencies. As observed experimentally by Lambourne & Bryer (1961) Sarpkaya (1971), Faler & Leibovich (1977) and Escudier & Zehnder (1982) in tube experiments, helical instabilities can develop in the lee of the vortex bubble due to strong deceleration of the flow which favors centrifugal waves to become unstable.

This type of vortex breakdown is actually best interpreted as a secondary bifurcation of the axisymmetric vortex breakdown structure and has been largely investigated in the last years using the weakly non parallel assumptions, see Qadri *et al.* (2013) and Gallaire *et al.* (2006) or in the fully non parallel regime, see Qadri *et al.* (2013) and Meliga *et al.* (2012a). Furthermore Meliga *et al.* (2012a) have analyzed helical vortex breakdown in the framework of weakly non-linear but fully non-parallel analysis carrying out a multi scale expansion yielding an amplitude equation. Henceforth a deep understanding of the appearance of these helical instabilities has been gained, and the stability analysis results of Gallaire *et al.* (2006) and Meliga *et al.* (2012a) have been validated against the DNS provided by Ruith *et al.* (2003).

However, although many efforts have been devoted to the description of the initial axisymmetric breakdown state, the transition between the columnar to the breakdown state is still not fully understood. Several explanations have been proposed over the years (see Hall (1972)), but so far none of them has been properly validated against experiments or DNS, and the present

analysis is no different. In order to get some insight and new ideas about the fascinating formation of the axisymmetric vortex breakdown, we have carried out axisymmetric DNS by varying both the swirl number, S , and the Reynolds number Re . Motivated by the results of the DNS, some explanations of the breakdown formation from the literature are revisited under a new light and other possible mechanisms are proposed and discussed.

In contrast to Rusak's approach (Wang & Rusak, 1996*a,b*), which is inviscid in nature, we consider viscous flow from the beginning and do not aim to consider Re^{-1} as a small deviation from inviscid flow. We also consider the swirling jet/wake as it evolves in free space and not in a pipe.

5.2 Governing equations and numerical method

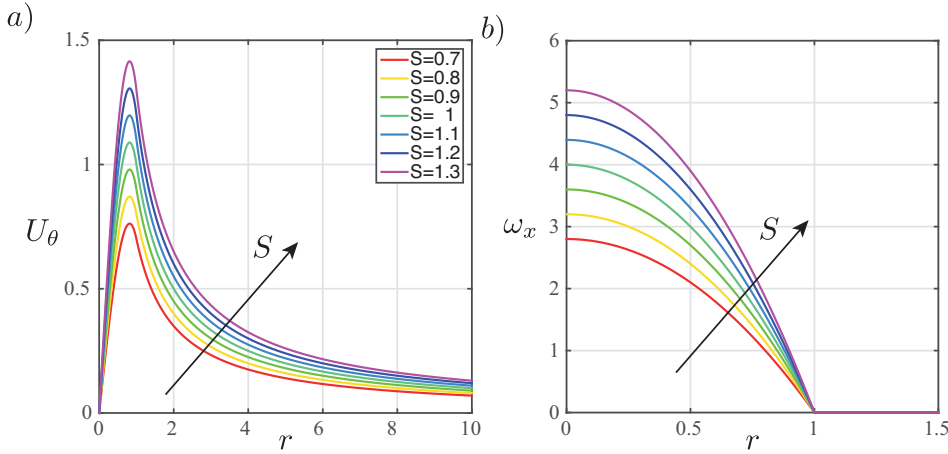


Figure 5.1: (a) Azimuthal velocity and (b) axial vorticity of the Grabovsky and Berger vortex at the inlet. Each line corresponds to a different value of the swirl parameter S as reported in the legend.

In the following, we use standard cylindrical coordinates r , θ and x directions to investigate the dynamics of a non-parallel Grabovski and Berger vortex with inlet condition

$$u_r = 0, \quad u_\theta(r \leq 1) = Sr(2 - r^2), \quad u_\theta(r > 1) = S/r, \quad u_x = 1. \quad (5.1)$$

Here u_r , u_θ and u_x are the non-dimensional radial, azimuthal and axial velocity components made nondimensional using the uniform oncoming velocity and the vortex characteristic core radius as reference scales. The (a) azimuthal velocity and (b) axial vorticity of the vortex inlet profile (5.1) are reported in Figure 5.1. As depicted in (b), the axial vorticity is concentrated in the inner region and is null in the outer one. Thus, the vortex dynamics is governed by the

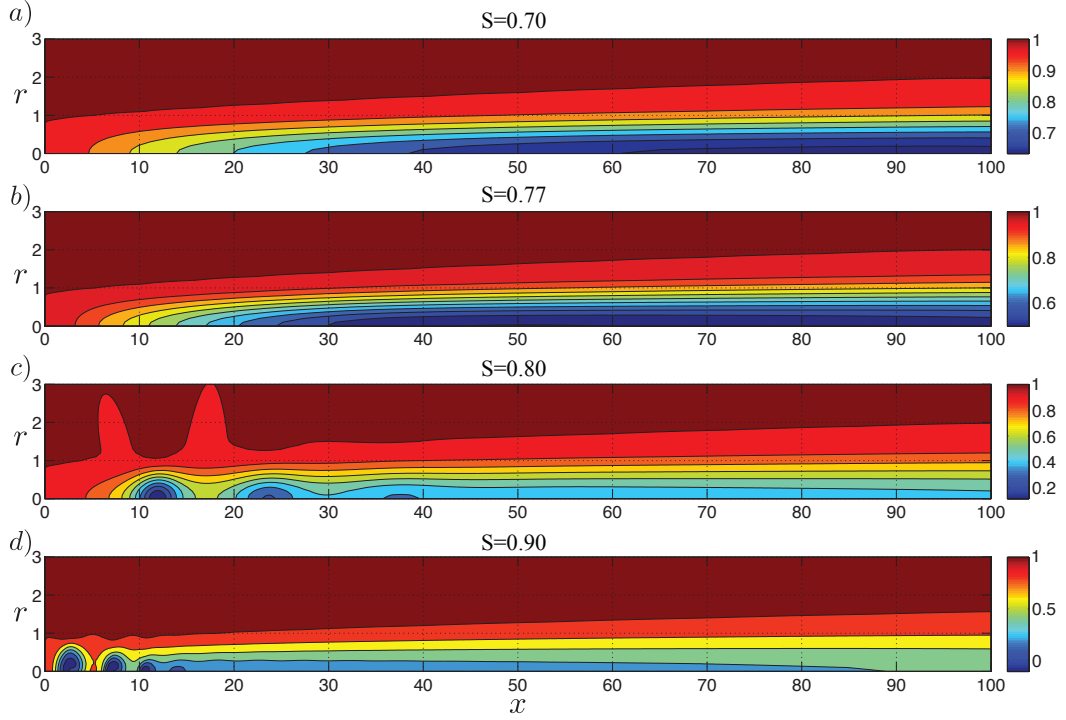


Figure 5.2: Streamwise velocity of the axisymmetric Grabovsky and Berger vortex at $Re = 1000$ computed with Nek5000 for (a) $S = 0.70$, (b) $S = 0.77$, (c) $S = 0.80$ and (d) $S = 0.90$.

steady 3D axisymmetric Navier-Stokes equations

$$\begin{aligned}
 \frac{1}{r} \frac{\partial r u_r}{\partial r} + \frac{\partial u_x}{\partial x} &= 0, \\
 u_r \frac{\partial u_x}{\partial r} + u_x \frac{\partial u_x}{\partial x} &= -\frac{\partial p}{\partial x} + \frac{1}{Re} \left[\frac{1}{r} \frac{\partial}{\partial r} \left(r \frac{\partial u_x}{\partial r} \right) + \frac{\partial^2 u_x}{\partial x^2} \right], \\
 u_r \frac{\partial u_r}{\partial r} + u_x \frac{\partial u_r}{\partial x} - \frac{u_\theta^2}{r} &= -\frac{\partial p}{\partial r} + \frac{1}{Re} \left[\frac{\partial}{\partial r} \left(\frac{1}{r} \frac{\partial r u_r}{\partial r} \right) + \frac{\partial^2 u_r}{\partial x^2} \right], \\
 u_r \frac{\partial u_\theta}{\partial r} + u_x \frac{\partial u_\theta}{\partial x} + \frac{u_r u_\theta}{r} &= \frac{1}{Re} \left[\frac{\partial}{\partial r} \left(\frac{1}{r} \frac{\partial r u_\theta}{\partial r} \right) + \frac{\partial^2 u_\theta}{\partial x^2} \right],
 \end{aligned} \tag{5.2}$$

where p is the nondimensional pressure. The steady solution of equations (5.2) is obtained by time-marching the unsteady axisymmetric equations with the spectral element code Nek5000 (Fischer *et al.*, 2008). The flow is considered steady when the L_2 -norm of the difference between two consecutive solutions is less than 10^{-12} . The computational domain is generally $0 \leq x \leq 100$ and $0 \leq r \leq 10$ (see section 5.7 for a discussion on the influence of the streamwise extension of the domain). In addition to the inlet condition (5.1), a free-stress boundary condition is imposed at the lateral boundary along with symmetry conditions at the axis. In order to ensure convergence at high swirl number, the convective boundary condition $\frac{\partial \mathbf{u}}{\partial t} + U_c \frac{\partial \mathbf{u}}{\partial x} = 0$ has been implemented, where U_c is a nondimensional convective velocity which was set to one.

5.3 Numerical results

In Figure 5.2 the effect of the swirl number on the streamwise velocity field at $Re = 1000$ is shown. At (a) swirl $S = 0.70$, the flow field is very regular and only evolves slowly in the x -direction due to viscous diffusion. When the swirl number is increased from $S = 0.70$ to $S = 0.77$, the flow has a similar topology with the minimum of U_x that migrates upstream. In contrast, at (c) $S = 0.8$ the velocity fields changes abruptly and the vortex flow is not columnar anymore: the flow suddenly decelerates and accelerates several times before gradually recovering a columnar evolution further downstream. A further slightly increase of the swirl to (d) $S = 0.90$, leads to an even different flow configuration with one additional decelerating/accelerating pattern and the entire wave-field migrates towards the inlet section. Note how the breakdown state in (c) happens without the appearance of counterflow. Thus, the recirculation region with two stagnation points (like in (d)) that is invoked by some authors in the literature to define the onset of vortex breakdown, appears only at a later stage.

In order to better understand the transition from the columnar to the breakdown state,

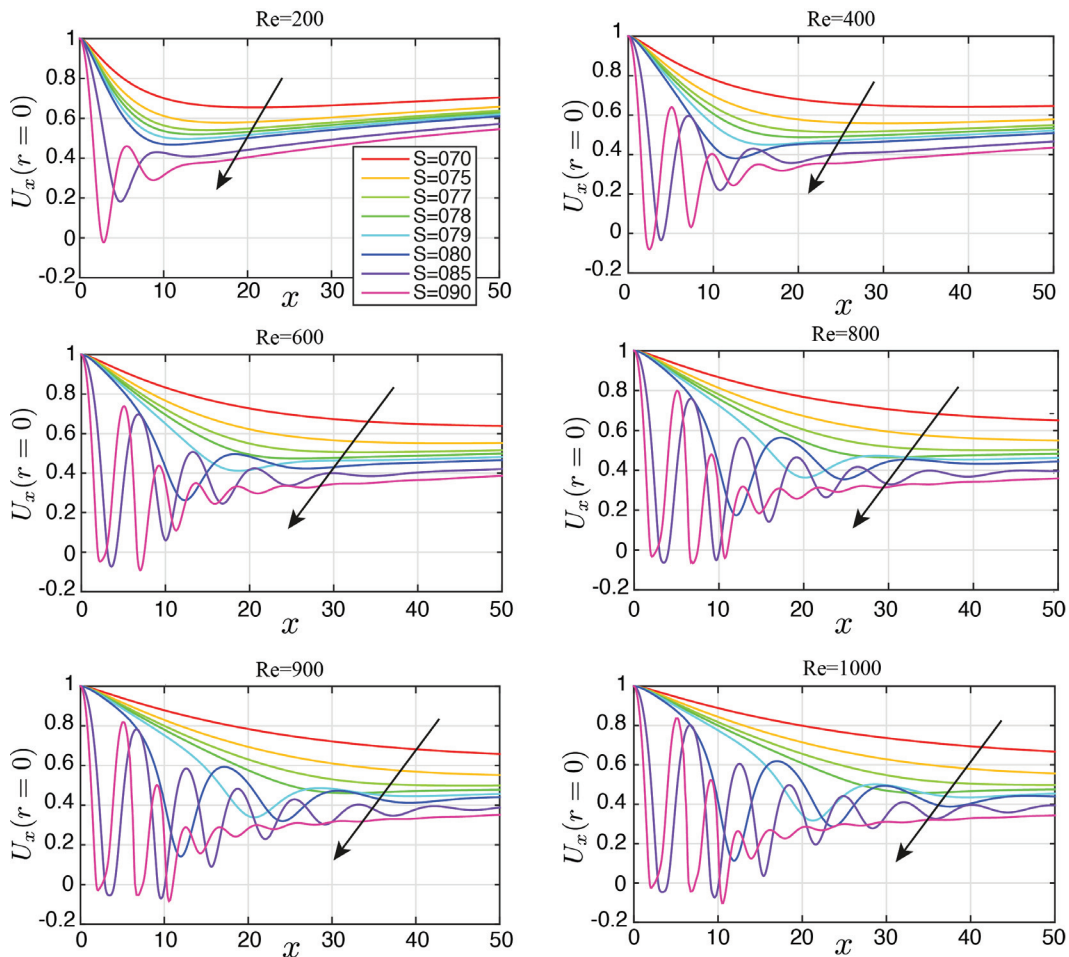


Figure 5.3: Streamwise velocity at the axis of the axisymmetric Grabovsky and Berger vortex as a function of the swirl parameter. Each subplot refers to a different Reynolds number.

5.4. Separation of the quasi-cylindrical equations

several simulations have been carried out varying the two nondimensional parameter of the problem: the swirl parameter S and the Reynolds number Re . The results are reported in Figure 5.3, where the streamwise velocity at the axis is shown and each line refers to a different swirl number; each subplot corresponds to a different Reynolds number. For all the Reynolds number considered, the flow appears very regular at low swirl number manifesting a smooth deceleration and a sequent gradual acceleration. By increasing the swirl number, the minimum of the streamwise velocity decreases and its x -position moves upstream. At a certain swirl number, which depends on the Reynolds number, the transition from columnar to breakdown state suddenly happens with the formation of a slow flow region close to the inlet. By further increasing S , the flow periodically decelerates and accelerates and the velocity eventually becomes negative generating recirculation regions. It is important to remark that in these simulations the axisymmetry inhibits helical instabilities which are seen to occur downstream the recirculation regions (Ruith *et al.*, 2003).

Figure 5.4 reports the minimum of the streamwise velocity on the axis as a function of

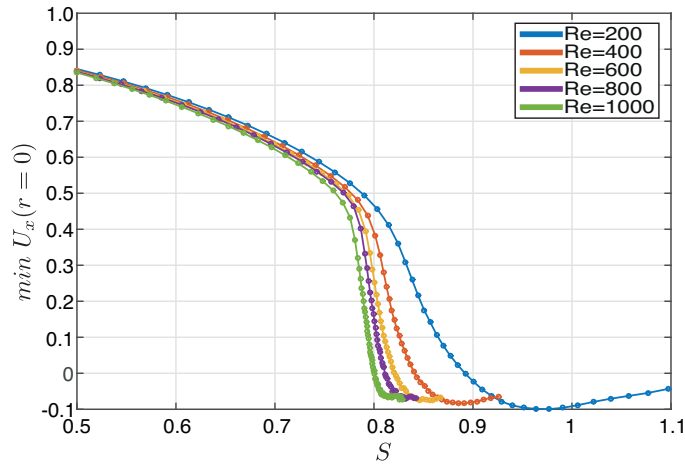


Figure 5.4: Evolution of the minimum axial velocity at the axis when increasing the swirl parameter S and the Reynolds number Re .

S for various Reynolds number. The minimum velocity slightly decreases by increasing the swirl parameter in the columnar regime. Then, an abrupt decrease is observed in correspondence of the onset of the breakdown state. This variation becomes more intense at increasing the Reynolds number and could suggest the possible presence of a saddle-node bifurcation at higher Re , as observed by Meliga & Gallaire (2011) in the case of axisymmetric vortex breakdown in a constricted pipe already at $Re = 500$.

5.4 Separation of the quasi-cylindrical equations

The DNS results reported in Figure 5.3 are now shown in Figure 5.5 by grouping them in subplots according to the swirl number, S . Hence, in a given subplot, each line corresponds to a different Reynolds number. It is seen that at high Reynolds number the transition happens

between $S = 0.77$ and $S = 0.78$. Furthermore, at moderate swirl, see $S = 0.75$ or $S = 0.77$

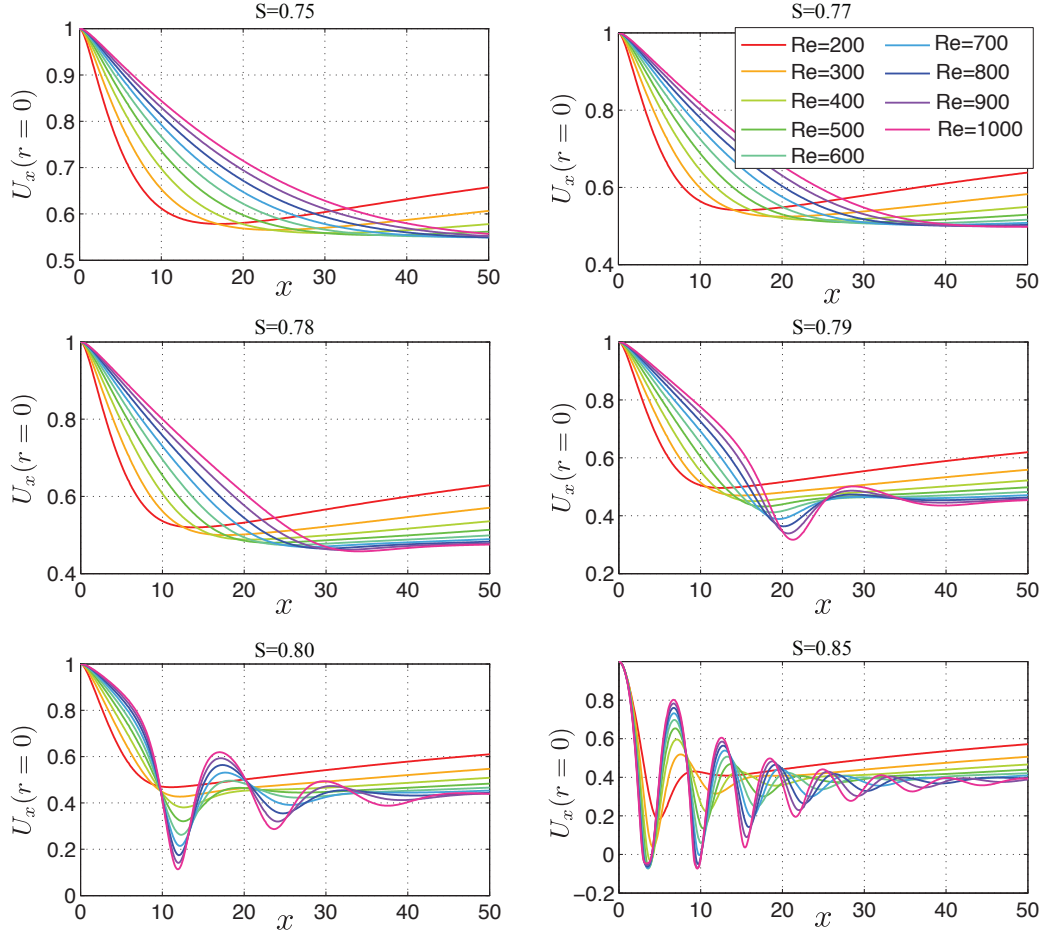


Figure 5.5: Streamwise velocity at the axis of the axisymmetric Grabovsky and Berger vortex as a function of the Reynolds number. Each subplot refers to a different swirl number.

for instance, $U_x(r = 0)$ is Reynolds dependent and seems to have a self-similar shape that is only stretched when the Reynolds number is varied. In contrast, at higher swirl number (see $S = 0.85$) the *wavy* vortex flow does not manifest a significant dependence on the Reynolds number with a typical wavelength between consecutive deceleration regions that is observed for $Re > 500$.

This scenario is reversed if the x -coordinate is rescaled with the Reynolds number, as in Figure 5.6. In this case, the curves at moderate swirl number overlap, especially at higher Reynolds number, whereas at high swirl number the curves do not collapse anymore. This observation can be explained by recalling that the flow before the onset of the breakdown state varies only gradually in the axial direction and the axial gradients are small compared with the radial gradients. Thus, the pre-breakdown flow can be calculated by imposing the

5.4. Separation of the quasi-cylindrical equations

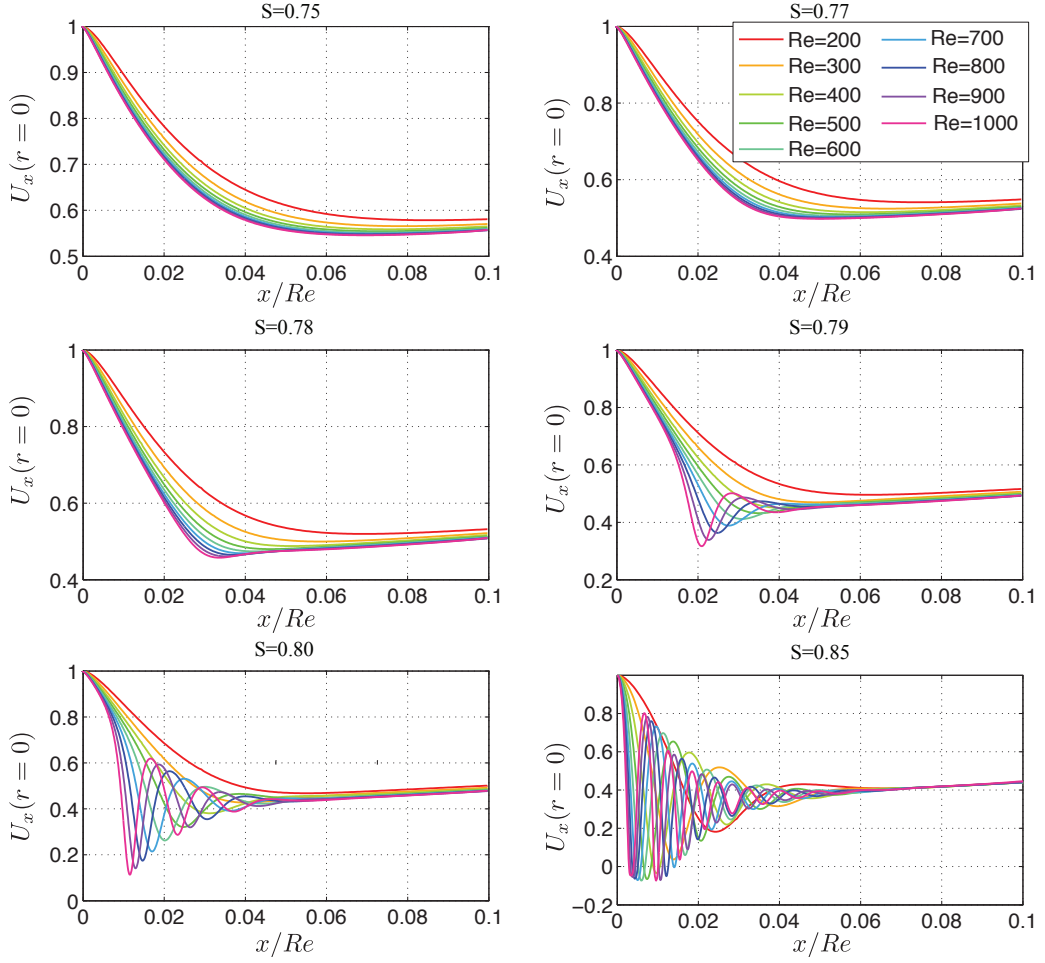


Figure 5.6: As in Figure 5.5 but the x -direction is rescaled by the Reynolds number.

boundary layer approximation $\frac{\partial}{\partial x} \ll \frac{\partial}{\partial r}$ and $u_r \ll u_x$ yielding to the simplified equations

$$\begin{aligned}
 \frac{1}{r} \frac{\partial r u_r}{\partial r} + \frac{\partial u_x}{\partial x} &= 0, \\
 u_r \frac{\partial u_x}{\partial r} + u_x \frac{\partial u_x}{\partial x} &= -\frac{\partial p}{\partial x} + \frac{1}{Re} \left[\frac{1}{r} \frac{\partial}{\partial r} \left(r \frac{\partial u_x}{\partial r} \right) + \frac{\partial^2 u_x}{\partial x^2} \right], \\
 u_r \frac{\partial u_r}{\partial r} + u_x \frac{\partial u_r}{\partial x} - \frac{u_\theta^2}{r} &= -\frac{\partial p}{\partial r} + \frac{1}{Re} \left[\frac{\partial}{\partial r} \left(\frac{1}{r} \frac{\partial r u_r}{\partial r} \right) + \frac{\partial^2 u_r}{\partial x^2} \right], \\
 u_r \frac{\partial u_\theta}{\partial r} + u_x \frac{\partial u_\theta}{\partial x} + \frac{u_r u_\theta}{r} &= \frac{1}{Re} \left[\frac{\partial}{\partial r} \left(\frac{1}{r} \frac{\partial r u_\theta}{\partial r} \right) + \frac{\partial^2 u_\theta}{\partial x^2} \right].
 \end{aligned} \tag{5.3}$$

This system of equations is referred to as *quasi-cylindrical* equations since the streamsurfaces of its solutions are approximately cylindrical (Batchelor, 1964; Hall, 1972). Note that the

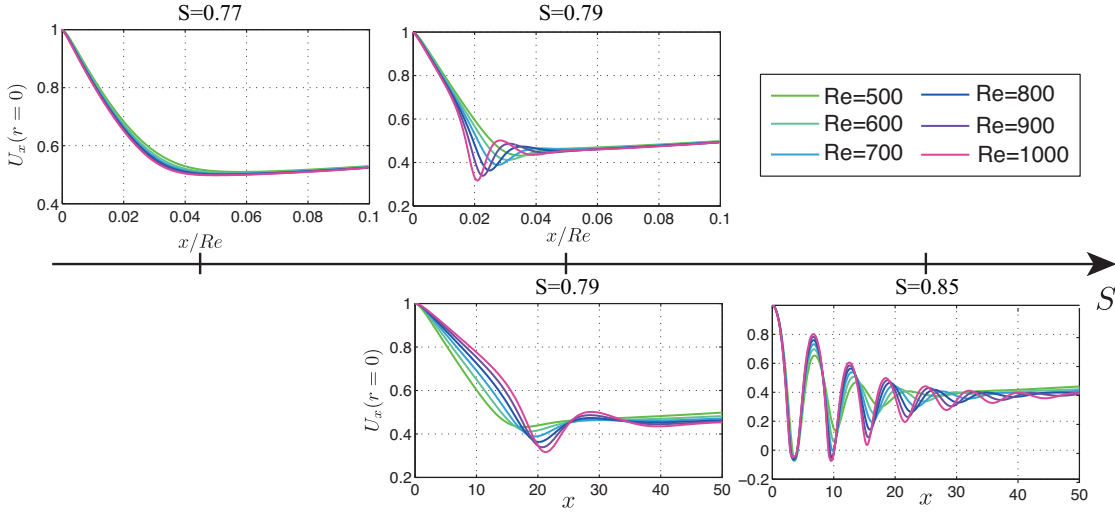


Figure 5.7: Pre-breakdown state (left picture), that follows the boundary layer scaling (x/Re), and post-breakdown solution (right picture), with a typical wavenumber independent from the Reynolds number. The central pictures refer to the transition state at intermediate swirl, corresponding to the on-set of vortex breakdown.

Reynolds number dependence in equations 5.4 vanishes by rescaling

$$x \rightarrow x/Re, \quad u_r \rightarrow Reu_r. \tag{5.4}$$

This means that the Reynolds dependence of the solution of equations can be factorized and the solution at a certain Reynolds number is simply obtained by rescaling x and u_r according to the transformation (5.4), in this way explaining the curves collapse in Figure 5.6.

From the results of the DNS, we can conclude that vortex breakdown occurs when the boundary layer scaling is violated. More precisely, the vortex breakdown can be probably explained as a transition between a columnar solution which is self-similar when the streamwise direction is scaled with the Reynolds number (x/Re) and a flow state that supports axisymmetric waves, whose wavenumber does not depend on the Reynolds number, see Figure 5.7.

This observation is in line with Hall (1972) who explained vortex breakdown as the failure of the quasi-cylindrical equations. Indeed, when the swirl number exceeds a certain value (namely $S = 0.77$), not only the axial gradient become important invalidating the quasi-cylindrical equations, but more importantly the solution ceases to exist. Henceforth Figure 5.8(a) shows how the minimum $U_x(r = 0)$ computed through the quasi-cylindrical equations (blue line), is in good agreement with the real value of Navier-Stokes equations (black line) until $S = 0.77$. Then, for larger swirl parameter, equations (5.4) breaks down and no solution is found. This behavior has a strong analogy with the separation of a two-dimensional boundary layer where the boundary layer equations are not solvable when the adverse pressure gradient becomes too large (Falkner & Skan, 1930; Landau & Lifshitz, 1987).

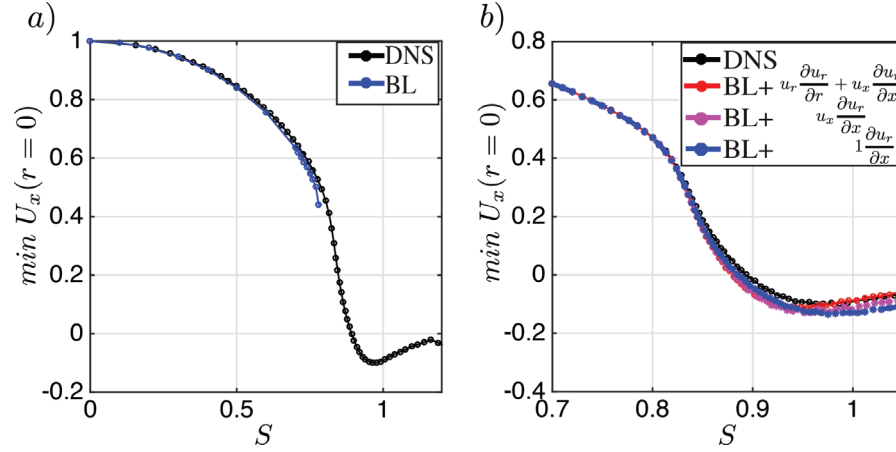


Figure 5.8: In (a) the minimum of the axial velocity at the axis for $Re = 200$ from DNS (black line) is compared with the results of the quasi-cylindrical equations (blue line). In (b) the DNS data (black line) are shown against the modified quasi-cylindrical equations (see text).

5.4.1 What is the missing term in the quasi-cylindrical equations?

Interested in the failure of the quasi-cylindrical equation at high swirl, we decided in collaboration with Pierre-Yves Lagr e to provide a better understanding of this phenomenon and to propose a modification to the quasi-cylindrical equations in such a way to account for the breakdown vortex state.

In the quasi-cylindrical equations (5.4), six terms have been neglected from the full Navier-Stokes equations (5.2) on behalf of the boundary layer approximation. However, when the quasi-cylindrical equations are seen to fail, Navier-Stokes equations still admit a flow solution (breakdown state). We would like here to determine which of the six missing terms has to be retained in the quasi-cylindrical equations in order to have a flow solution at high swirl.

To do so, we have developed a pseudospectral Chebyshev-Chebyshev solver with Newton-Raphson algorithm to find steady solutions of the axisymmetric Navier-Stokes equations (5.2). The code has been validated against Nek5000 results. By its structure, our in-house Navier-Stokes solver allows to easily access and modify the governing equations. Hence, *ad-hoc* numerical simulations have been carried out by dropping one after the other the six terms from the Navier-Stokes equations and checking if a solution to the modified equations still exists.

We have found that for a solution to exist at $S > 0.77$, it is necessary to include the convective term in the radial momentum equations. On the other hand, the viscous terms are seen not to be crucial for the existence of the solution. In other words, at high swirl the balance between the radial pressure gradient $\partial p/\partial r$ and the centrifugal term u_θ^2/r is incorrect. In a similar fashion to Lagr e *et al.* (2005) and Chouly & Lagr e (2012), we now propose reduced Navier-Stokes equations (or extended quasi-cylindrical equations) to correctly account for the vortex breakdown state. The first set of reduced Navier-Stokes equations (RNS1) consists in adding

to the quasi-cylindrical equations the nonlinear convective term in the radial momentum

$$\begin{aligned}
 \frac{1}{r} \frac{\partial r u_r}{\partial r} + \frac{\partial u_x}{\partial x} &= 0, \\
 u_r \frac{\partial u_x}{\partial r} + u_x \frac{\partial u_x}{\partial x} &= -\frac{\partial p}{\partial x} + \frac{1}{Re} \frac{1}{r} \frac{\partial}{\partial r} \left(r \frac{\partial u_x}{\partial r} \right), \\
 u_r \frac{\partial u_r}{\partial r} + u_x \frac{\partial u_r}{\partial x} - \frac{u_\theta^2}{r} &= -\frac{\partial p}{\partial r}, \\
 u_r \frac{\partial u_\theta}{\partial r} + u_x \frac{\partial u_\theta}{\partial x} + \frac{u_r u_\theta}{r} &= \frac{1}{Re} \frac{\partial}{\partial r} \left(\frac{1}{r} \frac{\partial r u_\theta}{\partial r} \right).
 \end{aligned} \tag{5.5}$$

The solution to the reduced Navier Stokes equations (5.5) is seen to exist at swirl number larger than $S > 0.77$ and well matches the solution of full Navier-Stokes equations (5.2). See for instance Figure 5.8(b) where the minimum value of $U_x(r = 0)$ at $Re = 200$ computed through full Navier-Stokes equations (black line) is compared with the results from RNS1 (5.5) (red line).

Moreover, we have found that only the term connected with the streamwise advection of the radial velocity is important in the modified equations. Thus, a second set of reduced equation (RNS2) is proposed

$$\begin{aligned}
 \frac{1}{r} \frac{\partial r u_r}{\partial r} + \frac{\partial u_x}{\partial x} &= 0, \\
 u_r \frac{\partial u_x}{\partial r} + u_x \frac{\partial u_x}{\partial x} &= -\frac{\partial p}{\partial x} + \frac{1}{Re} \frac{1}{r} \frac{\partial}{\partial r} \left(r \frac{\partial u_x}{\partial r} \right), \\
 u_x \frac{\partial u_r}{\partial x} - \frac{u_\theta^2}{r} &= -\frac{\partial p}{\partial r}, \\
 u_r \frac{\partial u_\theta}{\partial r} + u_x \frac{\partial u_\theta}{\partial x} + \frac{u_r u_\theta}{r} &= \frac{1}{Re} \frac{\partial}{\partial r} \left(\frac{1}{r} \frac{\partial r u_\theta}{\partial r} \right),
 \end{aligned} \tag{5.6}$$

which can be further simplified (RNS3) in the hypothesis of strong flow advection $u_x \approx 1$ as follows

$$\begin{aligned}
 \frac{1}{r} \frac{\partial r u_r}{\partial r} + \frac{\partial u_x}{\partial x} &= 0, \\
 u_r \frac{\partial u_x}{\partial r} + u_x \frac{\partial u_x}{\partial x} &= -\frac{\partial p}{\partial x} + \frac{1}{Re} \frac{1}{r} \frac{\partial}{\partial r} \left(r \frac{\partial u_x}{\partial r} \right), \\
 1 \frac{\partial u_r}{\partial x} - \frac{u_\theta^2}{r} &= -\frac{\partial p}{\partial r}, \\
 u_r \frac{\partial u_\theta}{\partial r} + u_x \frac{\partial u_\theta}{\partial x} + \frac{u_r u_\theta}{r} &= \frac{1}{Re} \frac{\partial}{\partial r} \left(\frac{1}{r} \frac{\partial r u_\theta}{\partial r} \right).
 \end{aligned} \tag{5.7}$$

The solution of the modified quasi-cylindrical equations RNS2 and RNS3 are seen to be in good agreement with the results of the full equations for $S > 0.77$ (see magenta and blue lines in Figure 5.8) pointing to the fundamental importance of the term $u_x \frac{\partial u_r}{\partial x}$ in the on-set of the vortex breakdown state which is strongly non-parallel.

5.5 Possible linear mechanisms

5.5.1 Local analysis: standing waves and subcritical state

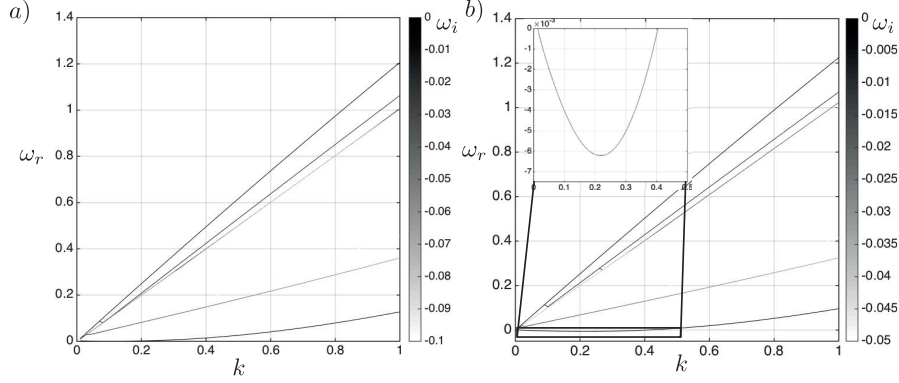


Figure 5.9: Frequencies ω_r versus streamwise wavenumber k of the axisymmetric viscous eigenmodes for (a) $S = 0.78$, $Re = 1000$, $x = 35$ and (b) $S = 0.78$, $Re = 2500$, $x = 60$. The grayscale shows the damping rate ω_i . In a) the flow is supercritical since the group velocity $\partial\omega_r/\partial k$ is always positive whereas in b) the flow supports upstream-propagating waves (see inset) and is subcritical.

During the '60s and '70s several interpretations of vortex breakdown based on the local stability properties have been proposed. Squire (1960) interpreted the vortex breakdown state as originated by inviscid standing waves over a base-state. He found three swirl distributions that support standing waves when the swirl velocity is larger than the axial flow. However, in the experiment of Sarpkaya (1971) the breakdown state with swirl velocity less the axial one was observed, thus invalidating Squire's criterion. Moreover, Benjamin (1962) pointed out that the group velocity of Squire's standing waves was directed downstream and could not be associated with the recirculation region observed in the experiment. Then Benjamin proposed an explanation based on the existence of a transition between a supercritical flow region which cannot support standing waves to a subcritical region which can. This criterion has an evident analogy with the phenomenon of hydraulic jump which is associated with an abrupt variation of the water-air freesurface (Rayleigh, 1914). Nevertheless, Benjamin's proposal does not offer a prediction of the occurrence or position of the breakdown and no validation against experiments or DNS has been showed. It has to be remarked that Benjamin's argument on the existence of a region of subcritical flow implies that the flow supports wavepackets with zero group velocity (Fig. 5.9(b)). This has strong analogy with the absolute stability criterion of Huerre & Monkewitz (1990) although it can not be strictly applied here because the waves are always weakly damped ($\omega_i < 0$).

Here, we have investigated the local stability properties of the swirling flow solutions obtained in our DNS. In particular, we are interested in the axisymmetric viscous local modes

$$\mathbf{u}(x, r, t) = \hat{\mathbf{u}}e^{i(kx - \omega t)}, \quad (5.8)$$

Chapter 5. Axisymmetric vortex breakdown

with real wavenumber k and complex frequency ω . See chapter 2 and Fabre *et al.* (2006) for more details on the notation and methods to compute numerically the dispersion relation. Figure 5.9(a) displays the real frequency ω_r computed for $S = 0.78$ and $Re = 1000$ at the streamwise position where the minimum of the streamwise velocity is observed ($x = 35$). The wave phase velocity, ω_r/k , and group velocity $\partial\omega_r/\partial k$ are always positive, meaning that no standing waves are supported by the flow (Squire's criterion) and that the vortex is locally supercritical in the sense of Benjamin. Moreover, the damping rates ω_i , which are shown by the grayscale, are always negative, meaning that these supercritical waves decays in time. In Figure 5.9(b) the same quantities are shown in the case of $S = 0.78$ and $Re = 2500$ at the streamwise position $x = 60$. As also depicted by the inset, a set of waves with negative group velocity exists: the flow is subcritical because it supports upstream-propagating waves. Furthermore, the phase velocity is null at $k = 0.4$ (standing wave) and a zero group-velocity is observed at $k = 0.22$. However, as indicated by the grayscale all waves are stable since $\omega_i < 0$.

The local stability analysis presented above for two representative cases, has been carried

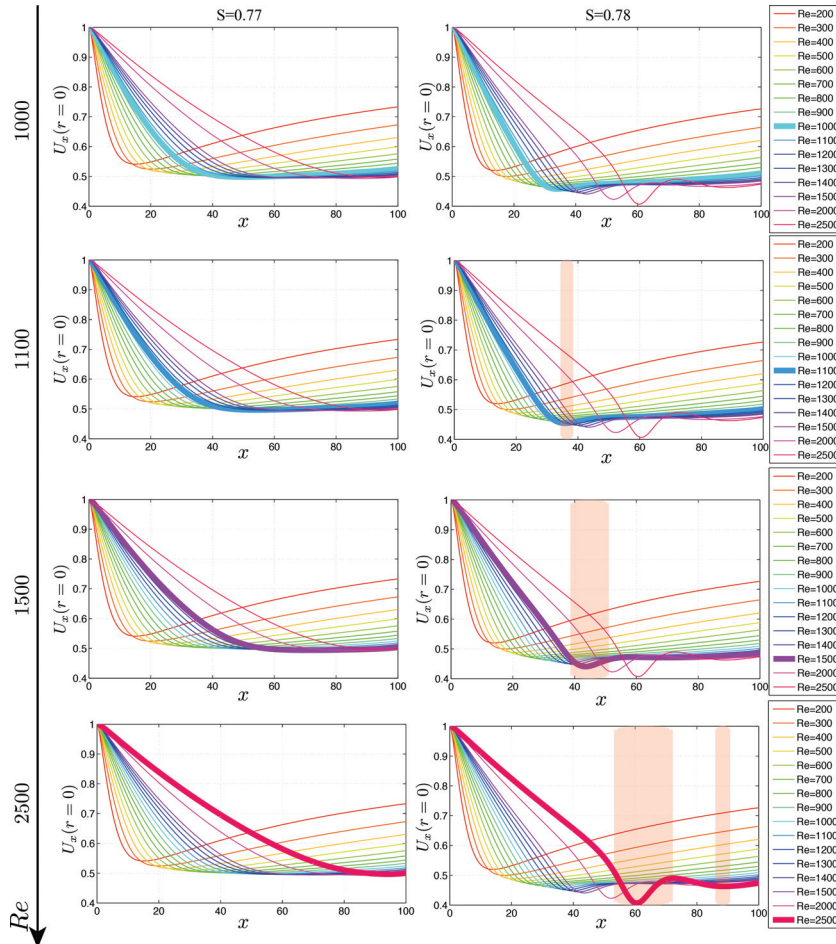


Figure 5.10: The subcritical flow regions are shaded by red rectangles. Two values of swirl are considered, namely $S = 0.77$ (left column) and $S = 0.78$ (right column), for increasing values of Reynolds number: $Re = 1000, 1100, 1500, 2500$.

out for several streamwise positions and Reynolds numbers, see Figure 5.10. Since the transition to the breakdown state at high Reynolds number seems to happen for $0.77 < S < 0.78$, we have restricted ourselves to $S = 0.77$ (left column) and $S = 0.78$ (right column). The red rectangles over the streamwise velocity profile distinguish subcritical flow regions from the rest of the flow domain that is supercritical. In the range of Reynolds number investigated, the flow field is seen to be everywhere supercritical at $S = 0.77$. On the other hand, a narrow region of subcritical flow is present for $S = 0.78$ at $Re = 1100$ which increases its elongation when the Reynolds number is increased. Specifically, a second subcritical region appears at $Re = 2500$ in correspondence of a second flow deceleration region. Hence, it is seen that Benjamin's argument of a super/subcritical transition is correctly correlated with the *bumpy* breakdown solution. However, it does not seem to yield a prediction on the critical swirl parameter and breakdown position and a quantitative comparison on the streamwise wavenumber has not been possible. Moreover, it is not possible to conclude if the super/subcritical transition is the mechanism or a consequence (or both) of the breakdown state.

5.5.2 Global analysis: instability

Rather than a local stability analysis, we investigate now the global stability properties of the columnar and breakdown solutions. Let consider axisymmetric incompressible Navier-Stokes equations and let make them nondimensional by using the freestream velocity U_∞ and the characteristic vortex radius. In vectorial form

$$\frac{\partial \mathbf{u}}{\partial t} + \mathbf{u} \cdot \nabla \mathbf{u} = -\nabla p + \frac{1}{Re} \Delta \mathbf{u}, \quad \nabla \cdot \mathbf{u} = 0. \quad (5.9)$$

with inlet condition

$$u_r = 0, \quad u_\theta(r \leq 1) = Sr(2 - r^2), \quad u_\theta(r > 1) = S/r, \quad u_x = 1. \quad (5.10)$$

By defining the state vector $\mathbf{q} = (\mathbf{u}, p)$, the system of equations (5.25) together with boundary conditions can be written as

$$\mathcal{N}(\mathbf{q}, S) = \mathbf{0}. \quad (5.11)$$

In order to study the stability at a given swirl number S_0 we expand the flow field q as

$$\mathbf{q} \sim \mathbf{q}_0 + \epsilon \mathbf{q}_1(t) \quad (5.12)$$

where \mathbf{q}_0 is the base state and $\epsilon \mathbf{q}_1$ is the axisymmetric unsteady perturbation of size ϵ . By injecting the expansion (5.12) in the governing equations (5.10) at leading order we retrieve the steady nonlinear Navier-Stokes equations at swirl $S = S_0$

$$\epsilon^0: \quad \mathcal{N}(\mathbf{q}_0, S_0) = \mathbf{0}. \quad (5.13)$$

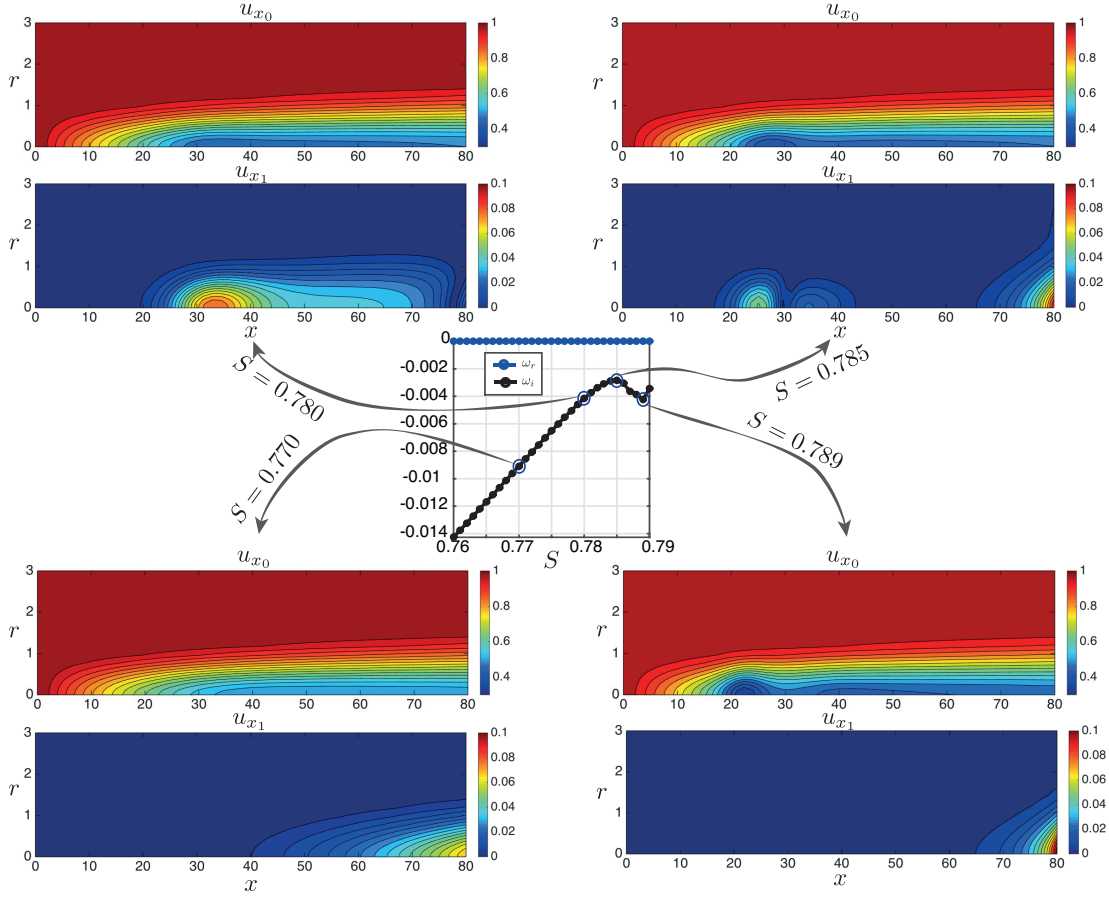


Figure 5.11: In the central plot the frequency, ω_r , and the growth rate, ω_i , of the least stable eigenmode at $Re = 1000$ is shown as a function of S . The outer pictures show the streamwise velocity of the base-flow u_{x_0} and of the least stable mode u_{x_1} for swirl numbers: $S = 0.770$ (bottom-left), $S = 0.780$ (top-left), $S = 0.785$ (top-right), $S = 0.789$ (bottom-right).

This equation is satisfied by the steady nonlinear Navier-Stokes \mathbf{q}_0 which is obtained by DNS and showed in the previous section. At the next order we have the global stability problem

$$\epsilon^1: \quad \mathcal{L}(\mathbf{q}_0, S_0)\mathbf{q}_1 = \mathbf{0} \quad (5.14)$$

where \mathcal{L} is the Jacobian, i.e. the linearized operator $\nabla_{\mathbf{q}} \mathcal{N}$. Since the base flow is axisymmetric, \mathbf{q}_1 takes the form of normal modes

$$\mathbf{q}_1 = \hat{\mathbf{q}}_1 e^{i\omega t}, \quad (5.15)$$

where ω is complex and its real part, ω_r , is the frequency of the perturbation whereas its imaginary part, ω_i , is the growth rate. Thus, the first order system (5.14) can be rewritten as an eigenvalue problem

$$\epsilon^1: \quad (i\omega\mathcal{B} - \mathcal{A}(\mathbf{q}_0, S_0))\hat{\mathbf{q}}_1 = \mathbf{0}, \quad (5.16)$$

where ω is the eigenvalue and

$$\mathcal{A}(\mathbf{q}_0, S_0) = \begin{bmatrix} \nabla() \cdot \mathbf{u}_0 + \mathbf{u}_0 \cdot \nabla() - Re^{-1} \Delta & \nabla \\ \nabla^T & 0 \end{bmatrix}, \quad \mathcal{B} = \begin{bmatrix} I & 0 \\ 0 & 0 \end{bmatrix}. \quad (5.17)$$

Figure 5.11 reports the frequency and growth rate of the least stable mode as a function of the swirl number for Reynolds number equal to $Re = 1000$. For all S the frequency is null and the damping rate is negative, this meaning that the mode is steady and stable. Hence, the transition to a breakdown state, which occurs here for $0.77 < S < 0.79$, can not be explained as a supercritical bifurcation with the destabilization of steady mode.

However, it has to be remarked that the flow gets only weakly stable when the swirl is increased and the least stable mode is very close to marginal stability ($S = 0.785$). Furthermore, the eigenmode penetrates upstream into the domain for S close to a the critical swirl S_0 . Indeed, in the range $0.775 < S < 0.785$ the weakly stable mode is localized in the flow domain at $20 < x < 40$ which is the position of onset of the breakdown. Hence, the linear mode can not explain the breakdown state but is probably closely connected to it.

5.6 Possible nonlinear mechanisms

5.6.1 Weakly nonlinear resolvent: a regular asymptotic expansion approach

Let now scale u_r and u_x in the axisymmetric Navier-Stokes equations by the freestream velocity U_∞ and u_θ by the swirl velocity SU_∞ . In vectorial form we have

$$\underbrace{\widetilde{\mathbf{u}} \cdot \nabla \widetilde{\mathbf{u}}}_{\mathbf{u} \cdot \nabla \mathbf{u}} - S^2 \frac{u_\theta^2}{r} \mathbf{e}_r = -\nabla p + \frac{1}{Re} \Delta \mathbf{u}, \quad \nabla \cdot \mathbf{u} = 0. \quad (5.18)$$

where the swirl parameter only appears in the centrifugal term which is written explicitly. Thus, the swirl dependence disappears in the inlet condition which reads

$$u_r = 0, \quad u_\theta(r \leq 1) = r(2 - r^2), \quad u_\theta(r > 1) = 1/r, \quad u_x = 1. \quad (5.19)$$

By defining the state vector $\mathbf{q} = (\mathbf{u}, p)$, the system of equations (5.18) along with boundary conditions can be written as

$$\mathcal{N}(\mathbf{q}, S) = \mathbf{0}. \quad (5.20)$$

We now consider a certain swirl number S_0 corresponding to a pre-breakdown state and we aim to investigate the appearance of the breakdown state due to a small increase of the swirl parameter

$$S = S_0 + \epsilon \Delta S. \quad (5.21)$$

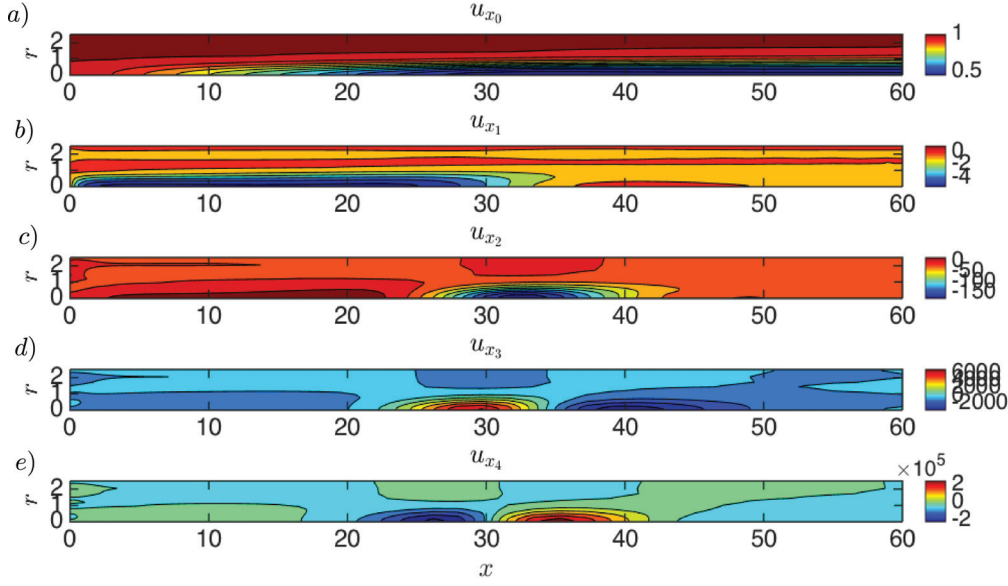


Figure 5.12: (a) Zero, (b) first, (c) second, (d) third and (e) fourth order streamwise velocity according to the expansion (5.22)

In the framework of weakly nonlinear analysis, the flow field \mathbf{q} is expanded as follows

$$\mathbf{q} = \mathbf{q}_0 + \epsilon \mathbf{q}_1 + \epsilon^2 \mathbf{q}_2 + O(\epsilon^3). \quad (5.22)$$

At leading order we retrieve the nonlinear Navier-Stokes equations at swirl $S = S_0$

$$\epsilon^0: \quad \mathcal{N}(\mathbf{q}_0, S_0) = \mathbf{0}. \quad (5.23)$$

which is satisfied by \mathbf{q}_0 that has been obtained by DNS (see previous section). At the next orders we get a hierarchy of non-homogeneous linear problems

$$\begin{aligned} \epsilon^1: \quad & \mathcal{L}(\mathbf{q}_0, S_0) \mathbf{q}_1 = 2S_0 \Delta S \frac{u_{\theta_0}^2}{r} \mathbf{e}_r, \\ \epsilon^2: \quad & \mathcal{L}(\mathbf{q}_0, S_0) \mathbf{q}_2 = \left(\Delta S^2 \frac{u_{\theta_0}^2}{r} + 4S_0 \Delta S \frac{u_{\theta_0} u_{\theta_1}}{r} + S_0^2 \frac{u_{\theta_1}^2}{r} \right) \mathbf{e}_r - \widetilde{\mathbf{u}_1 \cdot \nabla \mathbf{u}_1}, \\ \epsilon^3: \quad & \mathcal{L}(\mathbf{q}_0, S_0) \mathbf{q}_3 = \left(2\Delta S^2 \frac{u_{\theta_0} u_{\theta_1}}{r} + 2S_0 \Delta S \frac{u_{\theta_1}^2 + u_{\theta_0} u_{\theta_2}}{r} + S_0^2 \frac{u_{\theta_1} u_{\theta_2}}{r} \right) \mathbf{e}_r - \widetilde{\mathbf{u}_1 \cdot \nabla \mathbf{u}_2} - \widetilde{\mathbf{u}_2 \cdot \nabla \mathbf{u}_1} \\ & \dots \end{aligned} \quad (5.24)$$

where \mathcal{L} is the Jacobian, i.e. the linearized operator $\nabla_{\mathbf{q}} \mathcal{N}$. The unknowns \mathbf{q}_1 , \mathbf{q}_2 , \mathbf{q}_3 , ... are determined by solving the associated linear system since the \mathcal{L} is non-degenerate as discussed above. Hence, at every order we compute a global resolvent calculation, see chapter 2 for more details. Then, the flow solution at $S = S_0 + \epsilon \Delta S$ is obtained by summing up the contribution at

the various orders according to eq. (5.22).

This weakly nonlinear analysis is here applied to the case of $Re = 1000$ and $S_0 = 0.78$. Figure 5.12 shows the axial velocity at (a) leading order (solution of Navier-Stokes equations) and (b-e) at the next four orders (obtained by global resolvent). Note that the first order solution in Fig. 5.12(a) manifest a 'slow' flow region at $5 \ll x \ll 25$, that corresponds to the decelerated region observed in the breakdown state at higher swirl number (see the plot for swirl number $S = 0.79$ in Figure 5.5). Furthermore, in Fig. 5.12(b) and (c) two region of deceleration are observed, similarly to the case of breakdown state at higher swirl number ($S = 0.80$ in Fig. 5.5). Figure 5.13 reports the streamwise velocity on the axis at the swirl number $S = S_0 + \epsilon \Delta S = 0.79$ computed with DNS (orange line) and the one obtained by the asymptotic analysis at fourth order (blue line). Although the agreement is not satisfactory, a decelerated flow region is present in the asymptotic solution which is at the same position of the one observed in the DNS.

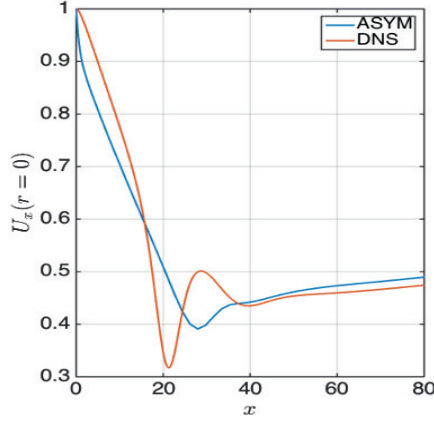


Figure 5.13: Streamwise velocity on the axis at $Re = 1000$ and $S = 0.79$ according to DNS (orange line) and asymptotic analysis (blue line).

5.6.2 Weakly nonlinear stability: a compatibility condition approach

As for the weakly nonlinear resolvent, we consider axisymmetric incompressible Navier-Stokes equations and we make them nondimensional by using the freestream velocity U_∞ as characteristic velocity scale for u_r and u_x and SU_∞ for u_θ , thereby the governing equations read

$$\underbrace{\overline{\mathbf{u} \cdot \nabla \mathbf{u}} - S^2 \frac{u_\theta^2}{r} \mathbf{e}_r}_{\mathbf{u} \cdot \nabla \mathbf{u}} = -\nabla p + \frac{1}{Re} \Delta \mathbf{u}, \quad \nabla \cdot \mathbf{u} = 0. \quad (5.25)$$

$$u_r = 0, \quad u_\theta(r \leq 1) = r(2 - r^2), \quad u_\theta(r > 1) = 1/r, \quad u_x = 1 \quad \text{at } x = 0.$$

We now consider a certain swirl number S_0 corresponding to a pre-breakdown state and we aim to investigate the appearance of the breakdown state due to a small increase of the swirl

parameter

$$S = S_0 + \epsilon^2 \Delta S \quad (5.26)$$

In the framework of weakly nonlinear analysis, the flow field q is expanded as follows

$$\mathbf{q} = \mathbf{q}_0 + \epsilon \mathbf{q}_1 + \epsilon^2 \mathbf{q}_2 + O(\epsilon^3), \quad (5.27)$$

and in the spirit of multiple scales, we also introduce the slow time scale $T = \epsilon t$.

At leading order we have the nonlinear Navier-Stokes equations at swirl $S = S_0$

$$\epsilon^0: \quad \mathcal{N}(\mathbf{q}_0, S_0) = \mathbf{0}. \quad (5.28)$$

which is satisfied by \mathbf{q}_0 that has been obtained by DNS (see previous section).

At first order we retrieve the linear global stability problem:

$$\epsilon^1: \quad \mathcal{L}\mathbf{u}_1 = \mathbf{0}. \quad (5.29)$$

As discussed in section 5.5.2, this problem has an eigenvalue with zero frequency and a small, but non-zero, damping rate σ . The solution of equation (5.29) has the normal form

$$\mathbf{u} = A(T)e^{-\sigma t}\hat{\mathbf{u}}_1, \quad (5.30)$$

where the amplitude $A(T)$ only depends on the slow time scale T and it has to be determined at next order.

The second order consists in a non-homogeneous linear problem

$$\epsilon^2: \quad \mathcal{L}\mathbf{u}_2 = -e^{-\sigma t}\hat{\mathbf{u}}_1 \frac{\partial A}{\partial T} - e^{-2\sigma t}\hat{\mathbf{u}}_1 \cdot \nabla \hat{\mathbf{u}}_1 A^2 + 2S_0 \Delta S \frac{v_{\theta_0}^2}{r} \mathbf{e}_r. \quad (5.31)$$

This equation is almost singular because it has an eigenvalue σ which is small. Thus, its particular solution, which is given by the global resolvent, can be large. In particular, if $\sigma = \epsilon \tilde{\sigma}$ the particular solution could be of the same order of the first order solution, in this way violating the hypothesis of the asymptotic scheme. Henceforth, we need to impose a compatibility condition in order to have a particular solution to (5.31) of the kind

$$\mathbf{u}_2 = e^{-\sigma t}\hat{\mathbf{u}}_2 \quad (5.32)$$

which is similar to the first order problem solution and that decays at large time. By substituting this ansatz in equation (5.31) we have

$$\epsilon^2: \quad \mathcal{L}\hat{\mathbf{u}}_2 = -\hat{\mathbf{u}}_1 \frac{\partial A}{\partial T} - e^{-\sigma t}\hat{\mathbf{u}}_1 \cdot \nabla \hat{\mathbf{u}}_1 A^2 + 2S_0 \Delta S \frac{v_{\theta_0}^2}{r} e^{\sigma t} \mathbf{e}_r, \quad (5.33)$$

and by recalling that $\sigma t = \underbrace{\tilde{\sigma}}_T \epsilon t$ and that the forcing term in the right hand side (rhs) of equation (5.33) now only depends on the slow time scale we have

$$\epsilon^2 : \quad \mathcal{L}\hat{\mathbf{u}}_2 = -\hat{\mathbf{u}}_1 \frac{\partial A}{\partial T} - e^{-\tilde{\sigma}T} \hat{\mathbf{u}}_1 \cdot \nabla \hat{\mathbf{u}}_1 A^2 + 2S_0 \Delta S e^{\tilde{\sigma}T} \frac{v_{\theta_0}^2}{r} \mathbf{e}_r. \quad (5.34)$$

In order to have a solution to this equation, its rhs has to live in the image of the operator \mathcal{L} : this implies that the rhs has to be orthogonal to the adjoint space (Fredholm alternative). Since the operator \mathcal{L} has rank $N - 1$ the adjoint space has dimension 1. Hence, the rhs has to be orthogonal to the adjoint vector, \mathbf{u}^\dagger , which satisfies $\mathcal{L}^\dagger \mathbf{u}^\dagger = \mathbf{0}$. So projecting eq. (5.34) on the adjoint vector we get:

$$\underbrace{(\mathbf{u}^\dagger, \mathcal{L}\hat{\mathbf{u}}_2)}_{=0} = -(\mathbf{u}^\dagger, \hat{\mathbf{u}}_1) \frac{\partial A}{\partial T} - e^{-\tilde{\sigma}T} (\mathbf{u}^\dagger, \hat{\mathbf{u}}_1 \cdot \nabla \hat{\mathbf{u}}_1) A^2 + 2S_0 \Delta S e^{\tilde{\sigma}T} (\mathbf{u}^\dagger, \frac{v_{\theta_0}^2}{r} \mathbf{e}_r). \quad (5.35)$$

Thus an equation for the amplitude $A(T)$ is obtained:

$$\frac{\partial A}{\partial T} + \alpha e^{-\tilde{\sigma}T} A^2 + \beta \Delta S e^{\tilde{\sigma}T} = 0 \quad (5.36)$$

where,

$$\alpha = \frac{(\mathbf{u}^\dagger, \hat{\mathbf{u}}_1 \cdot \nabla \hat{\mathbf{u}}_1)}{(\mathbf{u}^\dagger, \hat{\mathbf{u}}_1)}, \quad \beta = -2S_0 \frac{(\mathbf{u}^\dagger, \frac{v_{\theta_0}^2}{r} \mathbf{e}_r)}{(\mathbf{u}^\dagger, \hat{\mathbf{u}}_1)}. \quad (5.37)$$

Equation (5.36) admits a solution of the type $A = c e^{\tilde{\sigma}T}$:

$$\alpha c^2 + \tilde{\sigma} c + \beta \Delta S = 0 \quad (5.38)$$

which has a real solution for c if $\tilde{\sigma}^2 > 4\alpha\beta\Delta S$.

Finally, according to the expansion (5.27) the flow at $S = S_0 + \epsilon^2 \Delta S$ is asymptotic to

$$\mathbf{u}(S) = \mathbf{u}(S_0) + \epsilon c \hat{\mathbf{u}}_1 + O(\epsilon^2) \quad (5.39)$$

where $\hat{\mathbf{u}}_1$ is the eigenvector which is stable at order ϵ !

In other words the stable linear mode at S_0 appears with finite amplitude at $S = S_0 + \epsilon^2 \Delta S$ through a weakly non-linear mechanism. The basic idea behind this asymptotic expansion is that the weakly stable mode that lives in the spectrum of the columnar solution is triggered by the nonlinear term when S is large enough and σ is small enough. Hence, before the eigenvalue gets marginally stable the mode manifests itself: this mechanism could explain the reason why the transition to the axisymmetric breakdown state appears without a classical linear instability mechanism. Note that the argument of a finite amplitude transition applies well here because an increasing of the control parameter S is at first order a forcing term synchronized with the weakly stable mode (both are steady). It is not the case for a weakly

Chapter 5. Axisymmetric vortex breakdown

stable system such as the cylinder wake, where at $Re < Re_c$ the mode has a frequency ω and is not sensitive to the steady *forcing* operated by the nonlinear term.

It has to be remarked that the formalism of global weakly nonlinear analysis, including the Fredholm alternative, has been here originally applied to the case of weakly stable first order problem (rather than marginally stable one). The same result can be obtained by using the approach of Meliga *et al.* (2009) where the marginal stability of the first order problem is formally recovered by defining a shift operator which translates the weakly stable eigenvalue to marginal stability condition ($\omega_i = 0$).

This analysis has not been yet finalized and compared against DNS. The computation of the coefficients (5.37), which requires global direct and adjoint calculations is an ongoing work.

5.7 Appendix: Domain sensitivity

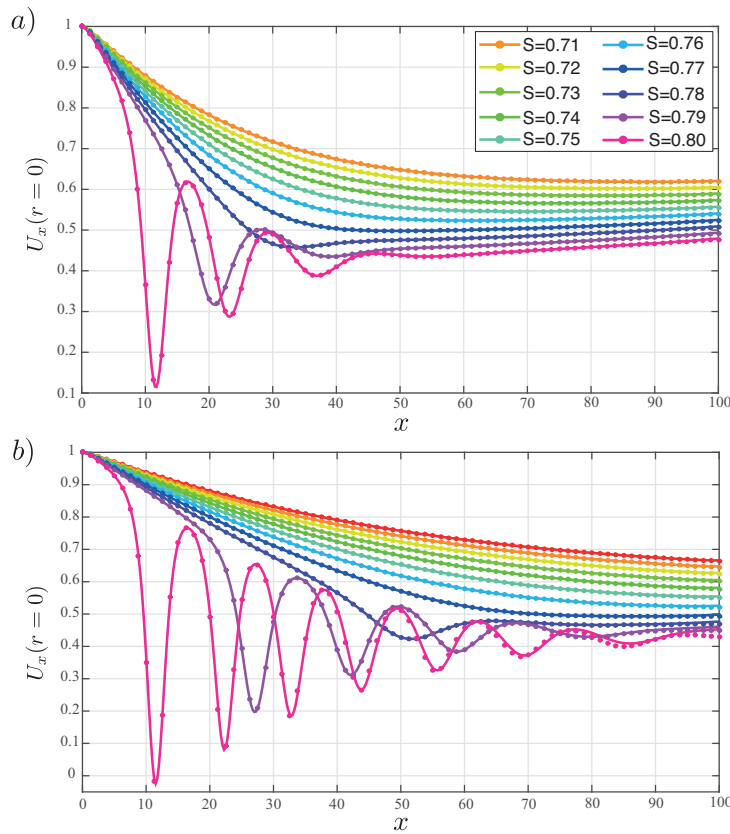


Figure 5.14: Streamwise velocity at the axis for (a) $Re = 1000$ and (b) $Re = 2000$ computed with Nek5000. The line refers to domain size $0 < x < 100$ and the circular markers to $0 < x < 200$.

The sensitivity of the DNS results with respect to the streamwise domain extension has been tested by carrying out simulations with different domain size with Nek5000. Figure 5.14 shows the streamwise velocity at $r = 0$ obtained by using an axial domain size of 100 (solid lines) and 200 (dot markers) units for (a) $Re = 1000$ and (b) $Re = 2000$. The results are seen to be insensitive to the domain size, apart for the case $Re = 2000$ and $S = 0.80$ where a slight

difference is observed. Indeed, when the Reynolds number is increased the domain size has to be increased accordingly. Note that the scaling law (5.4) satisfied by the quasi-cylindrical solutions, suggest that the computational domain has to be increased in the x -direction linearly with the Reynolds number.

5.8 Appendix: Batchelor boundary layer equations

According to Batchelor (1964) when the wake defect in the streamwise flow is small $|u_x - 1| \ll 1$, the quasi-cylindrical equations (5.4) can be further simplified

$$\begin{aligned}
 \frac{1}{r} \frac{\partial r u_r}{\partial r} + \frac{\partial u_x}{\partial x} &= 0, \\
 u_r \frac{\partial u_x}{\partial r} + \underbrace{u_x}_{1} \frac{\partial u_x}{\partial x} &= -\frac{\partial p}{\partial x} + \frac{1}{Re} \left[\frac{1}{r} \frac{\partial}{\partial r} \left(r \frac{\partial u_x}{\partial r} \right) + \frac{\partial^2 u_x}{\partial x^2} \right], \\
 u_r \frac{\partial u_r}{\partial r} + u_x \frac{\partial u_r}{\partial x} - \frac{u_\theta^2}{r} &= -\frac{\partial p}{\partial r} + \frac{1}{Re} \left[\frac{\partial}{\partial r} \left(\frac{1}{r} \frac{\partial r u_r}{\partial r} \right) + \frac{\partial^2 u_r}{\partial x^2} \right], \\
 u_r \frac{\partial u_\theta}{\partial r} + \underbrace{u_x}_{1} \frac{\partial u_\theta}{\partial x} + \frac{u_r u_\theta}{r} &= \frac{1}{Re} \left[\frac{\partial}{\partial r} \left(\frac{1}{r} \frac{\partial r u_\theta}{\partial r} \right) + \frac{\partial^2 u_\theta}{\partial x^2} \right],
 \end{aligned} \tag{5.40}$$

It follows that the dependence on Re and S in equations 5.40 and inlet condition

$$u_r = 0, \quad u_\theta(r \leq 1) = Sr(2 - r^2), \quad u_\theta(r > 1) = S/r, \quad u_x = 1. \tag{5.41}$$

vanishes by rescaling

$$x \rightarrow x/Re, \quad u_r \rightarrow S^2 Re u_r, \quad u_x \rightarrow S^2 u_x, \quad u_\theta \rightarrow S Re u_\theta. \tag{5.42}$$

This means that the Reynolds and swirl parameter dependence of the solution in the equations can be factorized and that the solution at a certain Reynolds and swirl numbers is simply obtained by rescaling x and \mathbf{u} according to the transformation (5.42). Hence, if the solution to the Batchelor boundary layer equations (henceforth BBL) is known for a certain (S, Re) is then known for all S and Re . However, although the quasi-cylindrical equations well approximate the DNS solution in their domain of validity (Figure 5.15(a)), the BBL solutions differ significantly from the DNS curves especially at large S , see Figure 5.15(b). Therefore, the BBL equations provide a computationally cheap solution which is accurate only when the flow is weakly non-parallel (low swirl number).

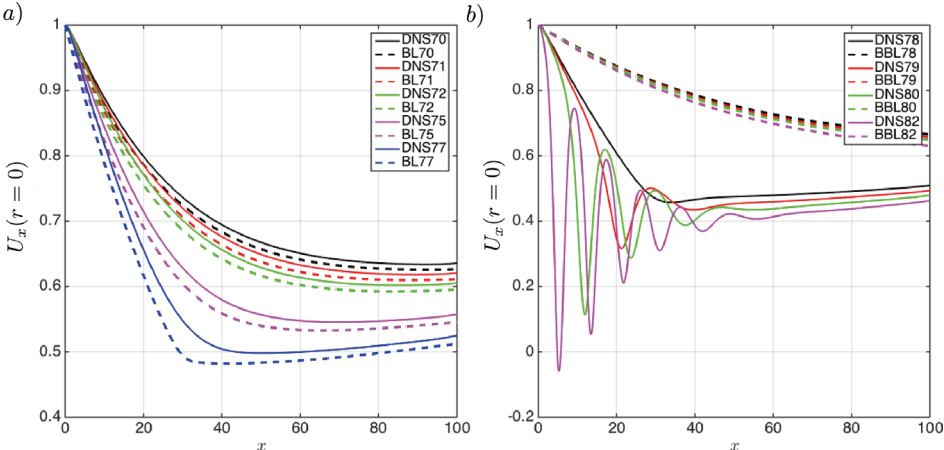


Figure 5.15: Streamwise velocity at the axis computed by (a) DNS (solid lines) and quasi-cylindrical equations (dashed lines) and (b) DNS (solid lines) and Batchelor boundary layer equations (dashed lines)

Nonlinear friction in fluid-solid resonators **Part II**

6 The viscous torsional pendulum

6.1 Introduction

A torsional pendulum consists of a disk-like mass suspended from a thin rod or wire. When the mass is twisted around the axis of the wire, the wire exerts a torque on the mass, tending to rotate it back to its original position. If twisted and released, the mass will oscillate back and forth periodically, and the system's natural frequency can be controlled by accurately tuning the oscillating mass and the restoring force exerted by the wire.

Due to its simple and regular dynamics, the torsional pendulum has been used in numerous precision experiments in electrical science, biophysics, petrology, metallurgy, and various other fields of endeavor (Gillies & Ritter, 1993). In particular, it is a mainstay instrument in gravitational physics because it enables one to isolate and measure weak forces with a magnitude comparable with the background gravitational field of the earth (Gundlach & Merkowitz, 2000; Tan *et al.*, 2015). Indeed, if well balanced, it is possible to place the Earth's gravitational force in an orthogonal relationship to the plane in which the signal of interest occurs. The basic idea in these experimental methods is to study gravitational effects by measuring the influence of masses external to the pendulum on its regular periodic motion.

Torsional pendula are also used in the watch industry as fundamental timing elements. For instance the balance wheel that is the timekeeping device used in mechanical watches, is a peculiar torsional pendulum where the restoring force is provided by a coiled spring rather than a long twisted wire. The balance wheel and hairspring together form a harmonic oscillator, which due to resonance oscillates preferentially at a certain frequency. The watchmakers have made constant progress to ensure linearity of the spring even at large amplitude to ensure both a regular time-beating and a sufficient period of operation.

In each of these settings, the motion of the torsional pendulum needs to be as regular as conceivable. The presence of any damping source in the system can indeed bias and corrupt the measurements or alter the perfect beating of a sophisticated swiss watch. Therefore, depending on the application, mechanical frictions are conveniently suppressed or reduced by using linear torsional springs, lubrication or bearings. However, once the mechanical dissipation sources are dropped, another dissipation mechanism becomes dominant: the

viscous friction exerted by the surrounding fluid on the oscillating mass. This dissipative mechanism originates in the relative motion of the solid and the fluid that sets up viscous stresses, which tend to drag the fluid to move with the disk and, as a consequence, prevent the disk's motion. As a result, the resulting damped motion of the disk becomes not trivial because it depends on the complex motion of the fluid surrounding the disk.

The flow induced by an oscillating disk has been studied extensively since Stokes (1851), who derived an asymptotic solution of the flow field and the torque at the disk's surface that is valid in the limit of high frequency and small amplitude of oscillation, so that the nonlinear effects are neglected. The nonlinear correction to the oscillatory problem was first tackled by Rosenblat (1959) who defined an unsteady inner shear layer at the disk's surface and an outer steady flow region. He reduced the Navier-Stokes equations to a set of one-dimensional ordinary differential equations which correspond to the unsteady version of the classical rotating disk equations solved by Von Karman (1921). By expanding the velocity and pressure in powers of the amplitude, Rosenblat (1959) found an asymptotic solution that approximates the azimuthal velocity and, consequently, the viscous torque at leading order. The same problem has been then studied by Benney (1964), using a multiple scales technique valid over the entire flow domain, while Riley (1965) carried out both the low and the high frequency case by means of a matched asymptotic expansion.

Interested in its fundamental implications, we investigate here the motion of a torsional pendulum consisting of an oscillating disk subjected to viscous friction. The full fluid-structure problem is solved through numerical simulations by coupling the disk's motion to the velocity and pressure field of the fluid, governed by the Navier-Stokes equations. In contrast to classical linear damping theory, we uncover the existence of two different limiting behaviors in dynamics of the system yielding to different scalings for the damping rate. This observation is rationalized theoretically in the framework of boundary layer theory. The gained understanding motivates us to introduce a simple phenomenological model for the viscous relaxation of the torsional pendulum. This predictive model gives an analytic expression for the free decay of the system that is compared with the results of the full numerical simulations.

6.2 Problem description and governing equations

Let consider a plane disk of radius R , height H and density ρ_d , that is surrounded by a fluid of viscosity μ and density ρ . The disk can only rotate about its axis and is connected to a torsional spring exerting a restoring torque, τ_k , on the disk. The spring is assumed to be ideal, meaning that the torque, τ_k , is proportional to the twisting angle, θ , through the elastic coefficient k ,

$$\tau_k = -k\theta. \tag{6.1}$$

Equation (6.1) is the angular version of the Hooke's law. Thus, the disk's position in time is described by a single Lagrangian coordinate, $\theta(t)$, that is the angle of twist of the disk from its equilibrium position. When the disk is twisted by an angle θ_m and then released, the spring exerts a torque on the mass tending to rotate it back to its equilibrium position. As a

6.2. Problem description and governing equations

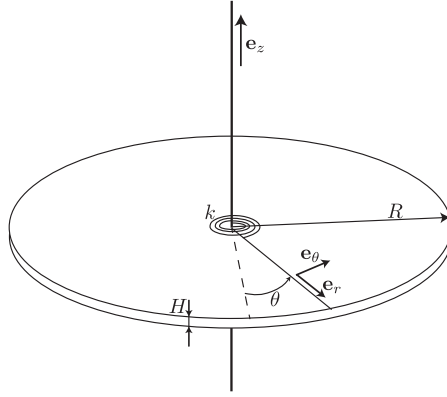


Figure 6.1: Schematic of the torsional pendulum: a thin disk of radius R and thickness H is connected to torsional spring with elastic constant k . The angular distance with respect to the equilibrium position (dashed line) is denoted θ .

consequence, the disk oscillates back and forth in the plane perpendicular to its axis, and the potential energy initially stored in the torsional spring is periodically converted into kinetic energy until dissipation brings the system at rest in the equilibrium position, $\theta = 0$. Thus, the motion of the torsion pendulum is described by Euler's second law

$$I\ddot{\theta} + k\theta = \tau_f, \quad (6.2)$$

where the dot symbol designates double derivation with respect to time and τ_f is the resultant torque exerted by external forces on the disk. The moment of inertia I depends on the mass geometry and in the case of a disk it is equal to

$$I = \frac{\pi H}{2R} \rho_d R^5. \quad (6.3)$$

Equation (6.2) is conveniently made nondimensional by using the inverse of the natural frequency of the system, $\omega = \sqrt{k/I}$, and the disk's radius, R , as characteristic time and length scales

$$\ddot{\theta} + \theta = \epsilon \tau_f, \quad (6.4)$$

where from now all symbols refers to nondimensional quantities. The number ϵ in equation (6.4) depends on the aspect ratio of the disk, $\frac{H}{R}$, and on the density ratio, $\frac{\rho}{\rho_d}$, according to

$$\epsilon = \frac{2 R \rho}{\pi H \rho_d}. \quad (6.5)$$

In the absence of mechanical dissipation, the forcing term τ_f in equation (6.4) corresponds to the viscous torque exerted by the fluid on the disk that prevents the pendulum's oscillations. This term is given by the the integral on the disk surface, Γ_d , of the torque per unit surface

Chapter 6. The viscous torsional pendulum

exerted at a given position $\mathbf{r} = (r, \theta, z)$ by the local normal stress $\boldsymbol{\sigma} \cdot \mathbf{n}$

$$\boldsymbol{\tau}_f = \left(\oint_{\Gamma_d} -\mathbf{r} \wedge (\boldsymbol{\sigma} \cdot \mathbf{n}) d\Gamma \right) \cdot \mathbf{e}_z, \quad (6.6)$$

where \mathbf{n} is the unit normal pointing outward the domain and \mathbf{e}_z is the unit normal aligned with the axis of the disk, see Figure 6.1 . In particular the nondimensional normal stress, $\boldsymbol{\sigma} \cdot \mathbf{n}$, writes

$$\boldsymbol{\sigma} \cdot \mathbf{n} = -p\mathbf{n} + Re^{-1} (\nabla \mathbf{u} + \nabla^T \mathbf{u}) \cdot \mathbf{n}, \quad (6.7)$$

where Re is the Reynolds number based on the characteristic length and time scales, and (\mathbf{u}, p) are the velocity and pressure fields governed by the incompressible axisymmetric Navier-Stokes equations

$$\frac{\partial \mathbf{u}}{\partial t} + \mathbf{u} \cdot \nabla \mathbf{u} = -\nabla p + \frac{1}{Re} \Delta \mathbf{u}, \quad \nabla \cdot \mathbf{u} = 0 \quad (6.8)$$

The system of equation for the fluid phase are complemented by the no-slip boundary condition at the disk's surface

$$\mathbf{u} = \dot{\theta} r \mathbf{e}_\theta, \quad \text{on } \Gamma_d, \quad (6.9)$$

Then, the initial conditions (6.10) correspond to a starting motion from rest with an initial twisting angle equal to $\theta(0) = \theta_m$

$$\begin{aligned} \theta(t=0) &= \theta_m, \quad \dot{\theta}(t=0) = 0 \\ \mathbf{u}(t=0) &= \mathbf{0}. \end{aligned} \quad (6.10)$$

Hence, the problem is completely characterized by the following non-dimensional parameter

$$Re = \frac{\rho \sqrt{k l I} R^2}{\mu}, \quad \frac{H}{R}, \quad \frac{\rho d}{\rho}, \quad \theta_m. \quad (6.11)$$

Numerical method

The system of equations (6.4) and (6.2), together with the coupling conditions (6.6) and (6.9) are solved numerically. In particular, the oscillator equation (6.4) is rewritten as a first order system, by introducing an additional scalar variable y :

$$\begin{aligned} \dot{y} &= -\theta + \epsilon \tau_f \\ \dot{\theta} &= y \end{aligned} \quad (6.12)$$

The first order differential equations (6.12) are integrated numerically in time by using a fourth order Runge-Kutta scheme. The axisymmetric Navier-Stokes equations in cylindrical coordinates are solved by means of the spectral element solver Nek5000 by Fischer *et al.* (2008).

The computational domain of size $-1 < z < 1$, $0 < r < 2$ is discretized using 1940 elements. Equations (6.2) and the no-slip boundary condition (6.9) are completed with the free-stress boundary condition at the radial and vertical outer boundaries of the domain. Since we use 8th order polynomials, the total number of grid points is equal to 124160 and the time step is kept fixed and equal to $5 \cdot 10^{-4}$.

At each time step, equation (6.12) is solved, then the noslip boundary condition (6.9) is updated according to the new rotational velocity of the disk, and the Navier-Stokes equations are marched one time step forward. Then, the instantaneous torque τ_f is calculated using equation (6.6) and the new angular position of the disk is computed.

6.3 A fluid-solid oscillator

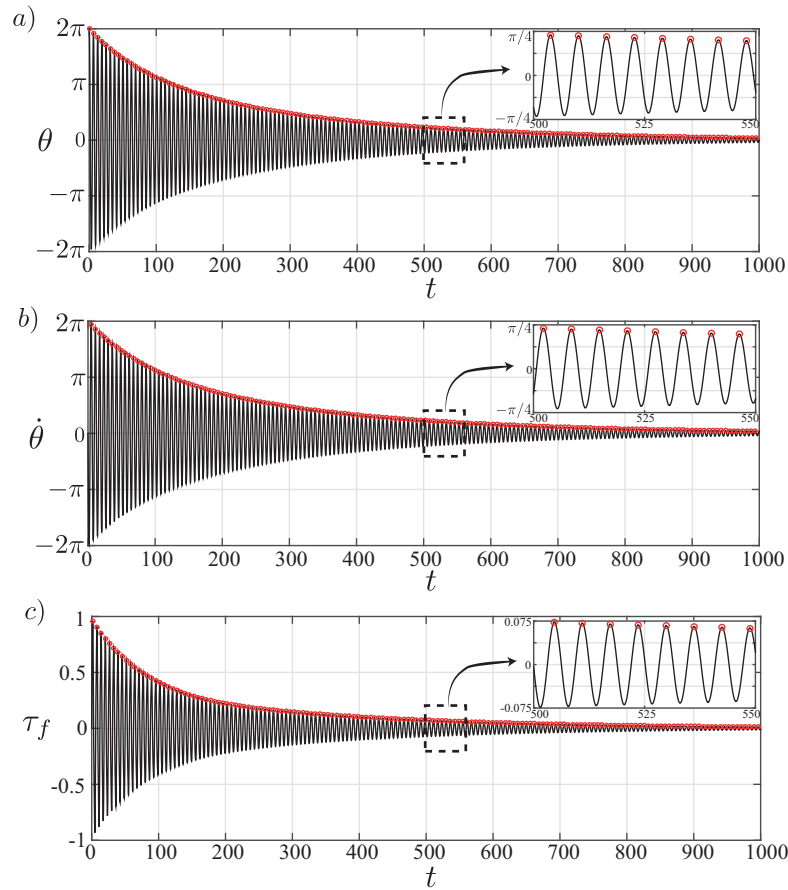


Figure 6.2: (a) Angular position θ , (b) angular velocity $\dot{\theta}$ and (c) viscous torque τ_f as a function of time obtained through full numerical simulation of the fluid-structure system. The red dots depict the local maxima in each cycle, as also shown in the insets.

Here we focus the oscillatory motion of a thin disk of aspect ratio $H/R = 10^{-3}$, which is heavy with respect to the surrounding fluid. The density ratio between the two is set equal to $\rho_d/\rho = 7000$, which is a realistic value for a metal made disk in air, and the corresponding value

Chapter 6. The viscous torsional pendulum

of ϵ in equation (6.4) is $\epsilon = 0.09$. The spring constant, k , is such that the Reynolds number is equal to $Re = 1000$. The motion is initiated by twisting the disk of an angle $\theta_m = 2\pi$, and then releasing it without any initial spinning. The following motion oscillating motion is determined through full numerical simulation of the governing equations introduced in the previous section.

The resulting twisting angle, θ , and the corresponding angular velocity, $\dot{\theta}$, are reported in Figure (6.2) (a) and (b) as a function of the non-dimensional time, t . The free decay of the disk motion appears very regular, as also pointed out by the insets, and the disk periodically oscillates in a sinusoidal fashion. The motion is slowly damped by the viscous torque, see Fig. (6.2) (c), and after 1000 nondimensional time units (corresponding to 160 cycles) the oscillation amplitude is roughly equal to 2% of the initial one, $\theta_m = 2\pi$.

In order to extract quantitative measure on the time variation of the frequency, on the

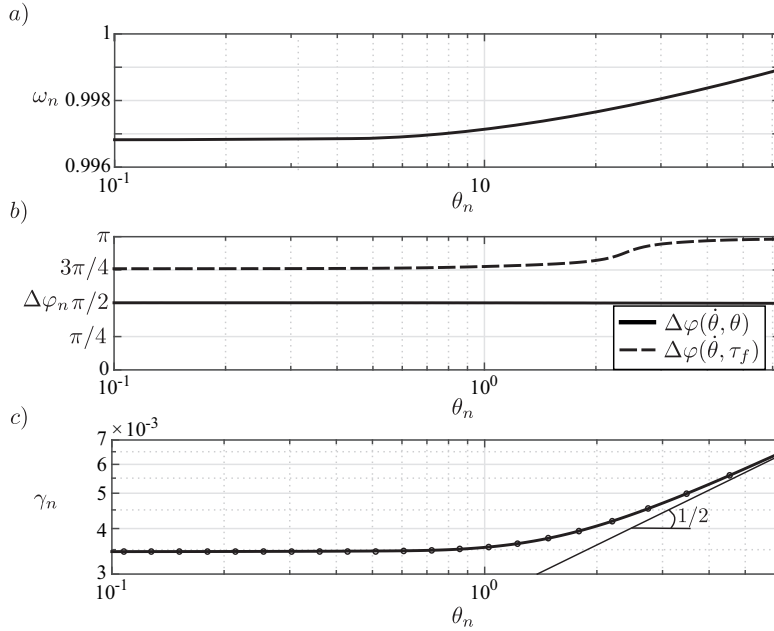


Figure 6.3: (a) Oscillation frequency, ω_n , (b) phase lags, $\Delta\varphi(\dot{\theta}, \theta)$, $\Delta\varphi(\dot{\theta}, \tau_f)$, and (c) damping rate, γ_n , as a function of the oscillation amplitude, θ_n .

phase shift and on the damping rate of the disk motion, we define θ_n , $\dot{\theta}_n$ and τ_{f_n} as the local maximum of the n th period of the signals $\theta(t)$, $\dot{\theta}(t)$ and τ_f . Those quantities are depicted by the red circles in Figure (6.2) (a-c). We refer to time values corresponding to θ_n , $\dot{\theta}_n$ and τ_{f_n} as $t[\theta_n]$, $t[\dot{\theta}_n]$ and $t[\tau_{f_n}]$, respectively. Therefore, the maxima θ_n are a measure of the instantaneous amplitude of the oscillation, and the inverse of the time distance of two consecutive peaks (θ_{n+1} , θ_n) measures the frequency

$$\omega_n = \frac{2\pi}{t[\theta_{n+1}] - t[\theta_n]}. \quad (6.13)$$

Figure 6.3(a) shows the nondimensional oscillation frequency ω_n (linear scale), as a function

of the oscillation amplitude θ_n (logarithmic scale). The frequency is roughly 1, meaning that the disk oscillates constantly at the natural frequency of the undamped system, $\sqrt{k/I}$, and that no significant added mass effect is active. More precisely, a small negative frequency shift of order 0.3% is observed at small amplitude with respect to the frequency at the beginning of the motion.

We now turn the attention towards the phase shift between the twisting angle, θ , the twisting velocity, $\dot{\theta}$, and the viscous torque, τ_f . The phase lag, $\Delta\varphi$, between two time signals $f(t)$ and $g(t)$ is defined as

$$\Delta\varphi_n(f, g) = t[f_n] - t[g_n]. \quad (6.14)$$

Hence, the phase lag between the twisting angle and twisting velocity, $\Delta\varphi(\dot{\theta}, \theta)$, and between the twisting velocity and the viscous torque, $\Delta\varphi(\dot{\theta}, \tau_f)$, are reported in Fig. 6.3(b) versus θ_n . The quantity $\Delta\varphi(\dot{\theta}, \theta)$ does not depend on the oscillation amplitude and is equal to $\pi/2$, which is the phase shift between the angle and the angular velocity of a linear pendulum. In contrast, $\Delta\varphi(\dot{\theta}, \tau_f)$ is roughly equal to π at the beginning of the motion (large amplitudes) and then progressively relaxes reaching a plateau at $3\pi/4$ for small amplitude. Note as when $\Delta\varphi(\dot{\theta}, \tau_f) = \pi$, the viscous torque is in phase opposition with the twisting angle, as typical in a linearly damped oscillator.

In order to have a quantitative measures of the dissipative effect of the viscous torque exerted on the disk by the surrounding fluid, we compute the averaged damping rate over one cycle γ_n , that is defined as the ratio between two consecutive amplitude peaks (θ_{n+1}, θ_n)

$$\gamma_n = -\frac{\log(\theta_{n+1}/\theta_n)}{t_{n+1} - t_n}. \quad (6.15)$$

The damping rate reported in Figure. 6.3(c), is seen to depend on the oscillation amplitude: it is higher at large amplitudes and decreases to a constant value when the amplitude gets smaller. The logarithmic scale for abscissa and ordinata, reveals that γ is roughly proportional to the square root of the amplitude when $\theta_n \gg 1$.

From our numerical results, we can conclude that two limiting regimes are observed: a (i) high amplitude regime where the damping rate $\gamma_n \propto \sqrt{\theta_n}$ and the phase lag $\Delta\varphi(\dot{\theta}, \tau_f) \approx \pi$ and a (ii) low amplitude regime with uniform damping rate and $\Delta\varphi(\dot{\theta}, \tau_f) \approx 3\pi/4$. Between this two regimes a transitional regime exists corresponding to intermediate amplitudes (approximately $0.8 < \theta_n < 2$).

6.4 Nonlinear and linear regimes

In order to get some insight on the high and low amplitude regimes, we start by writing the dimensional Navier-Stokes equations

$$\frac{\partial \mathbf{u}}{\partial t} + \mathbf{u} \cdot \nabla \mathbf{u} = -\frac{1}{\rho} \nabla p + \nu \Delta \mathbf{u}, \quad \nabla \cdot \mathbf{u} = 0. \quad (6.16)$$

Chapter 6. The viscous torsional pendulum

Let scale the equations as follows

$$u_\theta = U_\theta \tilde{u}_\theta, \quad u_r = U_r \tilde{u}_r, \quad u_z = U_z \tilde{u}_z, \quad p = P \tilde{P}, \quad t = \omega^{-1} \tilde{t}, \quad r = R \tilde{r}, \quad z = \delta \tilde{z}, \quad (6.17)$$

where the symbol $\tilde{\cdot}$ designates scaled variables and U_θ , U_r , U_z and P are the characteristic azimuthal, radial and vertical velocities and pressure. In particular, the characteristic azimuthal velocity is set as

$$U_\theta = \theta^* \omega R, \quad (6.18)$$

where θ^* is the typical oscillation amplitude. When the kinematic viscosity, $\nu = \mu/\rho$, is small, the flow is potential everywhere except in a thin layer near the surface of thickness δ where the flow is rotational and viscous effects dominate. In the boundary layer spirit, δ is much smaller than the size of the body that scales with R , i.e. $\delta/R \ll 1$. By inserting the gauges (6.17) in equation (6.16), we can determine a scaling law for the unsteady, convective, pressure and viscous terms

$$\frac{\partial \mathbf{u}}{\partial t} \sim \theta^* \omega^2 R^2, \quad \mathbf{u} \cdot \nabla \mathbf{u} \sim \theta^{*2} \omega^2 R, \quad \frac{1}{\rho} \nabla p \sim \theta^{*2} \frac{\omega^2 R^2}{\delta}, \quad \nu \Delta \mathbf{u} \sim \theta^* \frac{\nu \omega R}{\delta^2}. \quad (6.19)$$

See the appendix for a detailed derivation of these scaling arguments. It follows that two limiting cases are possible depending on the size of the oscillation amplitude θ^* .

6.4.1 Low amplitude model

In the low amplitude regime

$$\theta^* \ll 1 \quad (6.20)$$

the nonlinear term is smaller than the unsteady term which has to be balanced by the viscous term close to the wall. This dominant balance sets the penetration depth of viscous effects in the flow

$$\omega^2 \theta^* R = \frac{\nu \omega R \theta^*}{\delta^2} \rightarrow \delta \sim \delta_s = \sqrt{\frac{\nu}{2\omega}} \quad (6.21)$$

which is the so-called Stokes layer. The pressure adapts in order to have a contribution at leading order and scales as

$$\frac{P^*}{\rho \delta} = \omega^2 \theta^* R \rightarrow P^* = \omega^2 \theta^* R \rho \delta_s. \quad (6.22)$$

In contrast, the convective term is of higher order

$$\omega^2 \theta^{*2} R \ll \omega^2 \theta^* R \rightarrow \theta^* \ll 1. \quad (6.23)$$

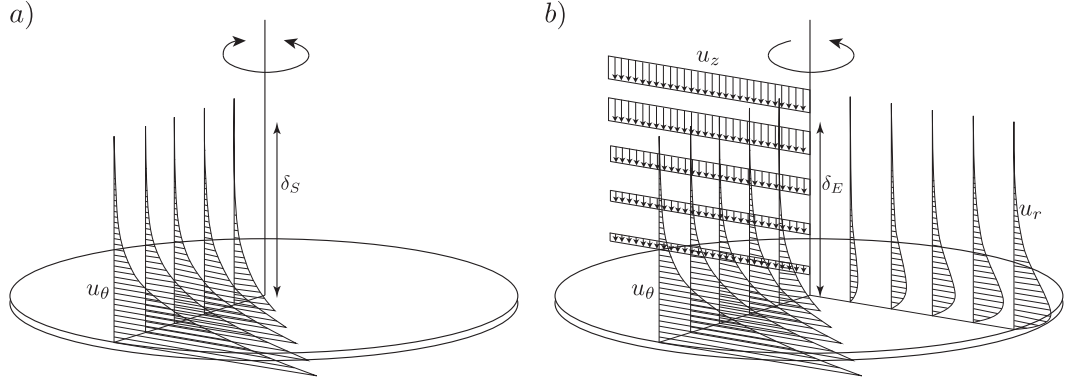


Figure 6.4: Instantaneous velocity profiles in the laboratory frame of a) Stokes flow (oscillating disk) and b) Von Karman solution (rotating disk). In a) the fluid's motion is circular near the disk and the azimuthal velocity, u_θ , decays at a distance δ_S (Stokes layer, eq. (6.21)) far from it. In b) the fluid near the disk spirals outwards inducing a negative axial velocity flux toward the disk that reaches a finite value at a typical distance equal to δ_E (Ekman layer, eq. (6.31)) .

In this regime the governing equations are linear, and in the limit of large radius disk and large Reynolds number, an analytical solution of the governing equations and boundary conditions is available. Indeed, this problem is formally equivalent to the Stokes flow over a disk oscillating about its axis with twisting angle $\theta(t) = \theta^* \cos(\omega t)$ (Stokes, 1851; Landau & Lifshitz, 1987). The flow streamlines are circular near the disk and the penetration length of the motion is given by the Stokes layer, δ_S ,

$$u_r = 0, \quad u_\theta / r = -\omega \theta^* e^{-z/\delta_S} \sin(\omega t - z/\delta_S), \quad u_z = 0, \quad (6.24)$$

see Figure 6.4(a) for a schematic representation. The corresponding nondimensional viscous torque exerted by the fluid is equal to

$$\tau_f = \frac{\pi \theta^*}{\sqrt{Re}} \cos(t - \pi/4). \quad (6.25)$$

Note as according to this analytical solution, which corresponds to the leading order torque in Rosenblat (1959), the phase lag between the viscous torque (6.25) and the twisting velocity, $\dot{\theta}$, is equal to $3\pi/4$, in line with what observed in the low amplitude regime in the numerical simulation, see Figure 6.3(b). By using standard trigonometry, the term $\theta^* \cos(t - \pi/4)$ can be rephrased as a function of the twisting angle and twisting velocity

$$\theta^* \cos(t - \pi/4) = \cos(\pi/4)\theta(t) - \sin(\pi/4)\dot{\theta}. \quad (6.26)$$

Thus, equation (6.25) together with the relation (6.26) provides an analytical expression for the instantaneous viscous torque valid in the low amplitude limit. By substituting eq. (6.25) in the governing equation (6.4) we obtain

$$\ddot{\theta} + \theta = 2\epsilon\sigma(\theta - \dot{\theta}) \quad (6.27)$$

Chapter 6. The viscous torsional pendulum

where the coefficient σ is equal to $\sigma = \pi/\sqrt{8Re}$. By defining θ_l the initial twisting angle of the linear regime we have the analytical solution

$$\theta(t) = \theta_l e^{-\epsilon\sigma t} \cos\left(t\sqrt{1 - 2\epsilon\sigma - \epsilon^2\sigma^2}\right). \quad (6.28)$$

Note as the only term in eq. (6.27) connected to the damping is $2\epsilon\sigma\dot{\theta}$, which also provides a second order frequency shift proportional to $\epsilon^2\sigma^2$. In contrast, the term $2\epsilon\sigma\theta$ does not contribute to the energy dissipation, but sets the dominant frequency shift since it scales as $\epsilon\sigma$.

Figure 6.5 shows the comparison between the full numerical simulation and the low

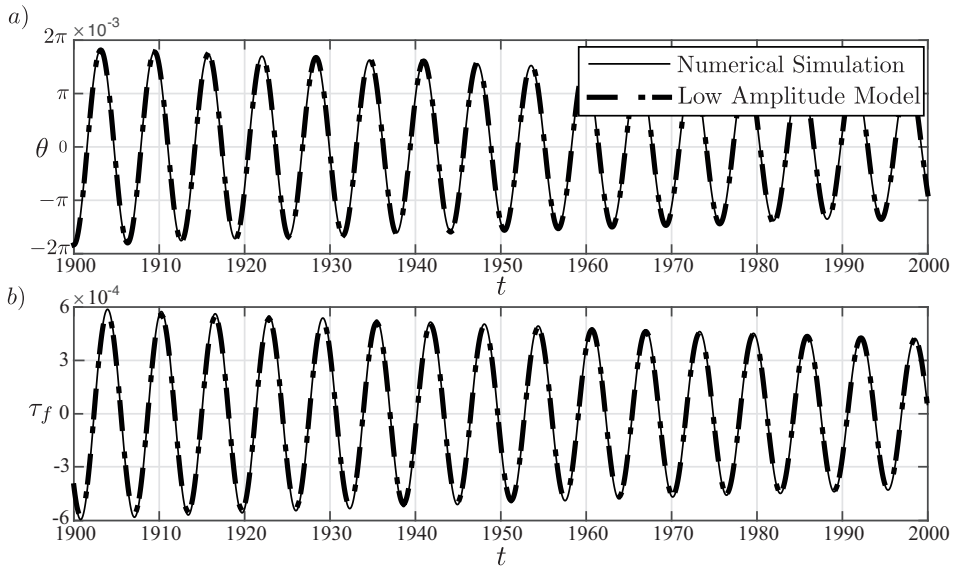


Figure 6.5: Comparison between full numerical simulation (solid line) and low amplitude model (dot-dashed line) at $Re = 1000$. The (a) oscillation amplitude and the (b) viscous torque are shown as a function of time.

amplitude model (6.28). Since the model is only valid for small amplitude the comparison is carried out for large time ($t > 1900$) when the amplitude of oscillation is of order 10^{-3} . More precisely, the initial amplitude condition, θ_l , in equation (6.28) is set equal to the twisting angle from DNS at $t = 1900$. According to eq. (6.28) the oscillation amplitude attenuates following an exponential decay, in agreement with what observed in the numerical simulations in the low amplitude regime (section 6.3). Furthermore, Figure 6.6 reports the damping rate versus oscillation amplitude θ_n obtained through full numerical simulation (solid line) and the one of the low amplitude model (point-dashed line)

$$\gamma_{LAM} = \epsilon\sigma. \quad (6.29)$$

In the low amplitude regime (small θ_n) the deviation between the two is about 7.5% which is attributed to the fact that the analytical expression for the torque (6.25) is deduced by invoking large Reynolds number. In order to verify this hypothesis, we have carried out further

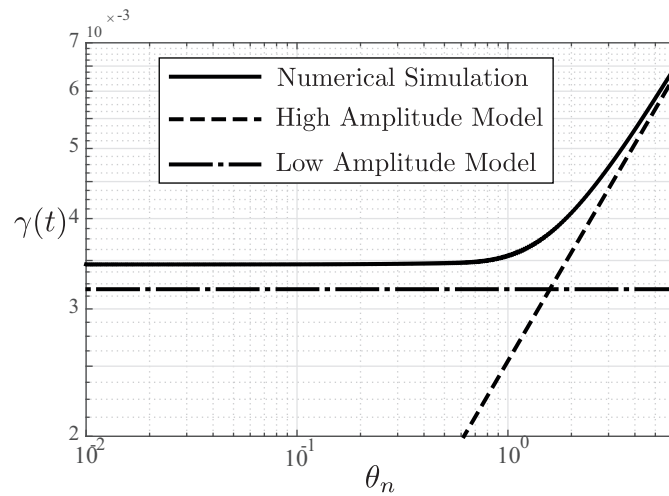


Figure 6.6: Instantaneous damping rate as a function of the oscillation amplitude in logarithmic scale at $Re = 1000$. The solid line refers to the results from the numerical simulations, whereas the dot-dashed and dashed lines refer to damping rate of the low and high amplitude models.

numerical simulations in the low amplitude regime ($\theta_m = 2\pi/100$) at higher Reynolds number. Figure 6.7 shows the percentage deviation between the low amplitude model damping rate $\gamma_{LAM} = \epsilon\pi/\sqrt{8Re}$, and the one obtained through numerical simulation, γ_{DNS} . The accuracy of the low amplitude model on the damping rate increases at higher Reynolds number, reaching a deviation of 2% at Reynolds $Re = 20000$.

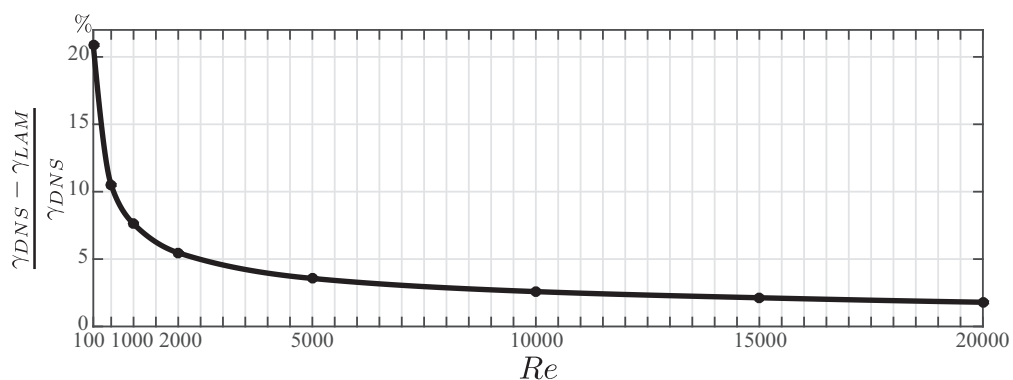


Figure 6.7: Relative error of the damping rate of the low amplitude model, γ_{LAM} , with respect to the value from full numerical simulations, γ_{DNS} , as a function of the Reynolds number, Re .

6.4.2 High amplitude model

In the high amplitude regime

$$\theta^* \gg 1, \quad (6.30)$$

and the nonlinear term dominates because proportional θ^{*2} . Close to the surface the noslip boundary condition imposes the balance between the convective term and the viscous term, setting in this way the depth of penetration of the viscous effects

$$\omega^2 \theta^{*2} R = \frac{\nu \omega R \theta^*}{\delta^2} \rightarrow \delta \sim \delta_E = \sqrt{\frac{\nu}{\theta^* \omega}} \quad (6.31)$$

which corresponds this time to the Ekman layer. The pressure adapts to play in the game with viscous and the convective terms

$$\frac{P^*}{\rho \delta_E} = \omega^2 \theta^{*2} R = \rightarrow P^* = \omega^2 \theta^{*2} R \rho \delta_E. \quad (6.32)$$

In contrast, the unsteady term results negligible

$$\omega^2 \theta^* R^2 \ll \omega^2 \theta^{*2} R \rightarrow 1 \ll \theta^*, \quad (6.33)$$

meaning that the velocity varies only slowly with time. The solution therefore asymptotically matches that of a quasi-steady flow the disk would generate by rotating uniformly at the instantaneous rotational speed.

This result is in agreement with Rosenblat (1959) and Benney (1964) who suggested that the low frequency regime is indeed well approximated by the quasi-steady Von Karman flow

$$u_r/r = -\frac{1}{2}\Omega \frac{dh}{d\zeta}, \quad u_\theta/r = \Omega g(\zeta), \quad u_z = \sqrt{\Omega \nu} h(\zeta). \quad (6.34)$$

This self-similar solution was found by Von Karman (1921) who sought for a flow such that u_r/r , u_θ/r and u_z are all functions of z alone, see Figure 6.4(b). With this ansatz, the full fluid problem reduces to a set of two coupled ODE, that is satisfied by $g(\zeta)$ and $h(\zeta)$ which are function of the self-similar variable $\zeta = z/\delta_E$ (δ_E is the Ekman layer, see eq. (6.31)). Note as in the quasi-steady Von Karman solution, the constant disk's angular velocity Ω is set equal to the instantaneous rotational velocity $\dot{\theta}$.

Furthermore, Riley (1965) probed asymptotically that the quasi-steady Von Karman flow corresponds to the leading order solution in the low frequency regime, except in the neighborhood of a turning point when the angular velocity inverts its sign. At that instant, unsteady terms become comparable to the viscous and inertial terms, and the equations have to be properly expanded in time around $\dot{\theta} = 0$ to account for the time-boundary layer. However, as shown by Schippers (1979), this time nonuniformity weakly affects the shear stresses on the

disk and the instantaneous torque well compares with the one of Von Karman,

$$\tau_f = -\frac{0.616\pi}{\sqrt{Re}}\dot{\theta}^{3/2}. \quad (6.35)$$

Therefore, the expression (6.35) is here used in our problem to model the viscous torque in the high amplitude regime. Note as there is not phase lag between the viscous torque (6.35) and the twisting velocity, $\dot{\theta}$, accordingly with what observed in the high amplitude regime in the numerical simulation, see Figure 6.3(b). By substituting eq. (6.35) in the disk's governing equation (6.4) we obtain

$$\ddot{\theta} + \theta = -\epsilon\alpha\dot{\theta}|\dot{\theta}|^{1/2}, \quad (6.36)$$

where the coefficient α is equal to $0.616\pi/\sqrt{Re}$ and the absolute value is introduced to conveniently treat the negative twisting velocity. Even if equation (6.36) does not have a closed-form analytical solution, still an asymptotic solution can be obtained by using the method of multiple scales (Nayfeh, 2008). Thus, in the limit of small ϵ (here equal to 0.091), we expand $\theta(t)$ asymptotically as

$$\theta = \theta_0(t, T) + \epsilon\theta_1(t, T) + O(\epsilon^2), \quad (6.37)$$

where T is the slow time scale $T = \epsilon t$.

At leading order ϵ^0 , the linear oscillator equation is recovered:

$$\ddot{\theta}_0 + \theta_0 = 0, \quad (6.38)$$

where the dot stands for a derivative with respect to the fast time t . This equation admits oscillatory solutions of the form

$$\theta_0 = \frac{1}{2}a(T)e^{i[t+\beta(T)]} + c.c., \quad (6.39)$$

where the phase β and the nondimensional envelope a depend on the slow time scale T and *c.c.* designates the complex conjugate.

At order ϵ , the nonlinear term, $\alpha\dot{\theta}_0|\dot{\theta}_0|^{1/2}$, enters as a forcing term to the oscillator equation, together with the slow time modulation $\dot{\theta}'_0$:

$$\ddot{\theta}_1 + \theta_1 = -2\dot{\theta}'_0 - \alpha\dot{\theta}_0|\dot{\theta}_0|^{1/2}. \quad (6.40)$$

The prime sign denotes derivation with respect to the slow time scale T . The first term on the rhs is synchronized with the sloshing motion as it oscillates at the natural frequency

$$2\dot{\theta}'_0 = i(a' + ia\beta')e^{i(t+\beta)} + c.c. \quad (6.41)$$

Chapter 6. The viscous torsional pendulum

In contrast, the nonlinear term is not purely harmonic, but through a Fourier series the components oscillating at the natural frequency may be isolated

$$\dot{\theta}_0|\dot{\theta}_0|^{1/2} = a^{3/2}(-\sin(t+\beta))|-\sin(t+\beta)| = a^{3/2} \sum_{n=-\infty}^{\infty} d_n e^{ni(t+\beta)} = a^{3/2} i c_1 e^{i(t+\beta)} + c.c. + NST \quad (6.42)$$

where NST gathers the other Fourier modes. Thus, the Fourier coefficient of the first harmonic oscillating at the natural frequency reads

$$i c_1 = d_1 = \frac{1}{2\pi} \int_0^{2\pi} (-\sin(t+\beta))|-\sin(t+\beta)| e^{-i(t+\beta)} dt = 0.4577i. \quad (6.43)$$

In order to avoid secular terms at first order, the resonant terms in the rhs of equation (6.40) have to cancel out, yielding to the amplitude equation:

$$i[a' + \alpha a^{3/2} c_1] + [-a\beta'] = 0. \quad (6.44)$$

By splitting real and imaginary parts we get,

$$a' + \alpha a^{3/2} c_1 = 0, \quad \beta' = 0 \quad (6.45)$$

with solution

$$a(t) = \left(a_0^{-1/2} + \frac{\alpha c_1}{2} \epsilon t \right)^{-2}, \quad \beta = \beta_0, \quad (6.46)$$

where the constants a_0 and β_0 are set by the initial condition. Thus, in the case of starting motion from rest with a twisting angle θ_m , we have $a_0 = \theta_m$, $\beta_0 = 0$ and the asymptotic solution reads

$$\theta(t) = \left(\theta_m^{-1/2} + \frac{\epsilon \alpha c_1}{2} t \right)^{-2} \cos(t). \quad (6.47)$$

Note as a small frequency shift is present between the high amplitude asymptotic solution (6.47) and the one obtained at small amplitudes, equation (6.28). This frequency shift is equal to $\epsilon\sigma = 0.3\%$ at leading order, that is in agreement with the frequency shift observed in the DNS and reported in Figure (6.3). The asymptotic solution (6.47) is now compared to the full numerical simulation in the high amplitude regime. Figure 6.9 shows (a) the twisting angle and (b) the torque exerted by the surrounding fluid on the disk as a function of the time. Both quantities are well captured by the high amplitude model (6.47). In addition, the attenuation rate of the oscillating motion is given by the slow time amplitude (6.46) that results from our asymptotic analysis. More precisely, the instantaneous damping rate according to the high amplitude model is equal to

$$\gamma_{HAM}(t) = -\frac{d(\log(a(t)/\theta_m))}{dt} = \epsilon \alpha c_1 \sqrt{a(t)}. \quad (6.48)$$

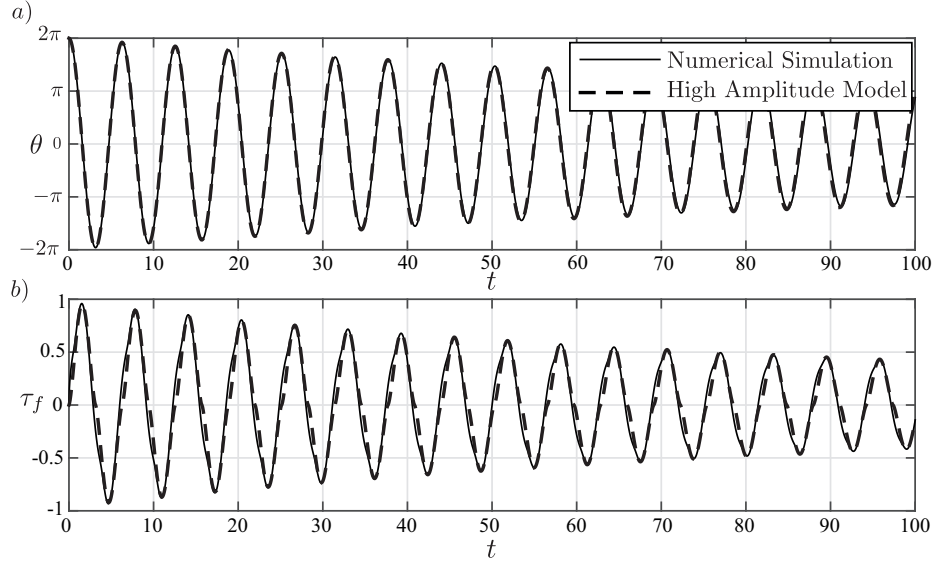


Figure 6.8: Comparison between full numerical simulation (solid line) and high amplitude model (dashed line) at $Re = 1000$. The (a) oscillation amplitude and the (b) viscous torque are shown as a function of time.

and is reported by a dashed line in Figure 6.6. It results that the model (6.47) correctly captures the dependence of the damping rate on the oscillation amplitude $a(t)$ observed in the numerical simulations and discussed in section (6.3).

6.4.3 A phenomenological model for the amplitude decay

The low and high amplitude models described above are seen to well describe the disk's motion in their domain of validity and are complementary. Therefore, a general predictive model for the free decay of a torsional pendulum starting from rest is here proposed.

As shown in Figure (6.6), the instantaneous damping rate computed by full numerical simulations (6.15) is well estimated by the upper envelope of the low and high amplitude model damping rates

$$\gamma_M(t) = \max(\gamma_{LAM}, \gamma_{HAM}) = \max\left(\epsilon\sigma, [(\epsilon\alpha c_1 \sqrt{\theta_m})^{-1} + t/2]^{-1}\right). \quad (6.49)$$

It follows that the twisting angle decay θ_n can be approximated by an exponential decay with a non-uniform damping rate of the type

$$\theta_n = \theta_m e^{-\int \gamma_M(t) dt}. \quad (6.50)$$

Figure 6.9 shows by circular symbols the oscillation amplitude θ_n computed with the phenomenological model (6.50) that well compares with the twisting angle relaxation computed by DNS (solid line). It has to be remarked that no tunable parameter is present in the model

equation (6.48).

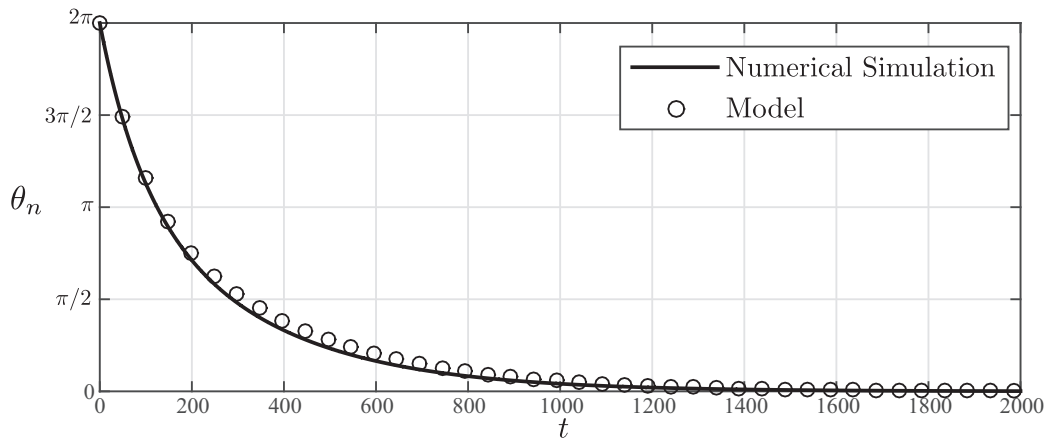


Figure 6.9: Free amplitude decay in time of the torsional pendulum at $Re = 1000$. The prediction of the analytical model (6.50) (circular symbols) is compared with the results of the full numerical simulations (solid line).

6.5 Conclusions

In this work the free decay of a torsional pendulum submitted to viscous friction has been investigated. The system is constituted by a thin disk that is connected to a torsional spring and surrounded by a viscous light fluid.

The full fluid-structure problem is solved numerically by coupling the second Euler's law, that prescribes the disk's rotation, to the Navier-Stokes equations, that governs the fluid's motion. Specifically, the disk rotational speed sets the fluid velocity at the disk's surface whereas the viscous stresses appear as a forcing term in the Euler's equation for the disk. From our numerics, we observe that even if the frequency of the damped system is almost uniform in time and close to the natural frequency of the system, a small frequency shift exist between high and low amplitudes. The phase lag between the twisting velocity and the viscous torque varies with time: it is equal to π , when the motion starts, and reduces to $3\pi/4$ at later time. Furthermore, the instantaneous damping rate is seen to decrease proportionally to the square root of the oscillation amplitude at the beginning of the motion, before reaching a constant value.

This observations have been rationalized theoretically by writing boundary layer equations in the vicinity of disk. Two limiting regimes have been distinguished, (i) a low amplitude linear regime (corresponding to the final time motion decay) and (ii) a high amplitude quasisteady nonlinear regime (early time dynamics). In both scenarios an analytical solution of the viscous torque is available from literature that we have used to build a low and high amplitude predictive models for the free decay of the motion. In the first case, the boundary layer thickness corresponds to the Stokes layer and the resulting model equation can be solved analytically: the system oscillates at a frequency close to the natural one with a phase lag between viscous torque and rotational speed of $3\pi/4$. It is seen to decay exponentially with a

uniform damping rate. In the second case, the boundary layer thickness corresponds to the Ekman layer and the system is governed by a nonlinear equation that is solved asymptotically by means of multiple scales method. In the high amplitude regime, the system oscillate at the natural frequency of the system with a torque-velocity phase lag that is equal to π . Importantly, the instantaneous damping rate is found to be proportional to the square root of the oscillation amplitude.

Motivated by the satisfactory agreement between the full numerical solution and the low and high amplitude models, we have then proposed a simple and general phenomenological model for the free decay of a disk-torsional pendulum. The model is based on considering the upper envelope of the instantaneous damping rates of the low and high amplitude models. An analytical expression for the free decay of the disk torsional pendulum is given which well predicts the results of the numerical simulations without any tunable parameter.

Appendix: Boundary layer on a rotating disk

In this section we derive the boundary layer equations in the case of a rotating disk and we derive the scaling arguments (6.19). Let us consider the unsteady incompressible Navier-Stokes equations in cylindrical coordinates for an axisymmetric flow

$$\begin{aligned}
 \frac{1}{r} \frac{\partial r u_r}{\partial r} + \frac{\partial u_z}{\partial z} &= 0 \\
 \frac{\partial u_z}{\partial t} + u_r \frac{\partial u_z}{\partial r} + u_z \frac{\partial u_z}{\partial z} &= -\frac{1}{\rho} \frac{\partial p}{\partial z} + \nu \left[\frac{1}{r} \frac{\partial}{\partial r} \left(r \frac{\partial u_z}{\partial r} \right) + \frac{\partial^2 u_z}{\partial z^2} \right] \\
 \frac{\partial u_r}{\partial t} + u_r \frac{\partial u_r}{\partial r} + u_z \frac{\partial u_r}{\partial z} - \frac{u_\theta^2}{r} &= -\frac{1}{\rho} \frac{\partial p}{\partial r} + \nu \left[\frac{1}{r} \frac{\partial}{\partial r} \left(r \frac{\partial u_r}{\partial r} \right) + \frac{\partial^2 u_r}{\partial z^2} - \frac{u_r}{r^2} \right] \\
 \frac{\partial u_\theta}{\partial t} + u_r \frac{\partial u_\theta}{\partial r} + u_z \frac{\partial u_\theta}{\partial z} + \frac{u_r u_\theta}{r} &= \nu \left[\frac{1}{r} \frac{\partial}{\partial r} \left(r \frac{\partial u_\theta}{\partial r} \right) + \frac{\partial^2 u_\theta}{\partial z^2} - \frac{u_\theta}{r^2} \right]
 \end{aligned} \tag{6.51}$$

and let scale them with the gauges defined in Equation (6.17). Form the continuity equation we get a relation between the radial and axial characteristic velocities

$$\frac{U_r}{R} \frac{1}{\tilde{r}} \frac{\partial \tilde{r} \tilde{u}_r}{\partial \tilde{r}} + \frac{U_z}{\delta} \frac{\partial \tilde{u}_z}{\partial \tilde{z}} = 0 \Rightarrow \frac{U_r}{U_z} = \frac{\delta}{R}. \tag{6.52}$$

Let us write the azimuthal momentum equation

$$\omega U_\theta \frac{\partial \tilde{u}_\theta}{\partial t} + \frac{U_r U_\theta}{R} \tilde{u}_r \frac{\partial \tilde{u}_\theta}{\partial \tilde{r}} + \frac{U_z U_\theta}{\delta} \tilde{u}_z \frac{\partial \tilde{u}_\theta}{\partial \tilde{z}} + \frac{U_r U_\theta}{R} \frac{\tilde{u}_r \tilde{u}_\theta}{\tilde{r}} = \left[\frac{\nu U_\theta}{R^2} \frac{1}{\tilde{r}} \frac{\partial}{\partial \tilde{r}} \left(\tilde{r} \frac{\partial \tilde{u}_\theta}{\partial \tilde{r}} \right) + \frac{\nu U_\theta}{\delta^2} \frac{\partial^2 \tilde{u}_\theta}{\partial \tilde{z}^2} - \frac{\nu U_\theta}{R^2} \frac{\tilde{u}_\theta}{\tilde{r}^2} \right]. \tag{6.53}$$

The left hand side scales as $U_x U_\theta / \delta$ and the dominant balance between the convective and viscous term yields

$$\frac{U_z U_\theta}{\delta} = \frac{\nu U_\theta}{\delta^2} \Rightarrow U_z = \frac{\nu}{\delta}. \tag{6.54}$$

Chapter 6. The viscous torsional pendulum

Then, by writing the momentum equation in the radial direction

$$\omega U_r \frac{\partial \tilde{u}_r}{\partial t} + \frac{U_r^2}{R} \tilde{u}_r \frac{\partial \tilde{u}_r}{\partial \tilde{r}} + \frac{U_z U_r}{\delta} \tilde{u}_z \frac{\partial \tilde{u}_r}{\partial \tilde{z}} - \frac{U_\theta^2}{R} \frac{\tilde{u}_\theta^2}{\tilde{r}} = -\frac{P^*}{\rho R} \frac{\partial \tilde{p}}{\partial \tilde{r}} + \left[\frac{\nu U_r}{R^2} \frac{1}{\tilde{r}} \frac{\partial}{\partial \tilde{r}} \left(\tilde{r} \frac{\partial \tilde{u}_r}{\partial \tilde{r}} \right) + \frac{\nu U_r}{\delta^2} \frac{\partial^2 \tilde{u}_r}{\partial \tilde{z}^2} - \frac{\nu U_r}{R^2} \frac{\tilde{u}_r}{\tilde{r}^2} \right] \quad (6.55)$$

we get a relation between U_θ and U_z

$$\frac{U_\theta^2}{R} = \frac{\nu U_r}{\delta^2} \Rightarrow U_\theta = U_z. \quad (6.56)$$

By combining the results (6.54) and (6.56) we find that the Reynolds number, $Re = U_\theta R / \nu$, has to be equal to the inverse of the small number $\epsilon = \delta / R$

$$U_\theta = \frac{\nu}{\delta} \Rightarrow 1 = \frac{\nu}{U_\theta \delta} = \frac{1}{Re} \frac{R}{\delta} \Rightarrow \frac{1}{Re} = \epsilon. \quad (6.57)$$

We turn now to determine the scaling law for the pressure. From the azimuthal momentum equation (6.55) and the axial momentum equation

$$\omega U_z \frac{\partial \tilde{u}_z}{\partial t} + \frac{U_r U_z}{R} \tilde{u}_r \frac{\partial \tilde{u}_z}{\partial \tilde{r}} + \frac{U_z^2}{\delta} \tilde{u}_z \frac{\partial \tilde{u}_z}{\partial \tilde{z}} = -\frac{P^*}{\rho \delta} \frac{\partial \tilde{p}}{\partial \tilde{z}} + \left[\frac{\nu U_z}{R^2} \frac{1}{\tilde{r}} \frac{\partial}{\partial \tilde{r}} \left(\tilde{r} \frac{\partial \tilde{u}_z}{\partial \tilde{r}} \right) + \frac{\nu U_z}{\delta^2} \frac{\partial^2 \tilde{u}_z}{\partial \tilde{z}^2} \right] \quad (6.58)$$

it results that for the pressure to appear at leading order in the radial and axial momentum equations it has to scale as $P^* = \rho U_\theta^2$.

As a result, the boundary layer equations for a rotating disk at leading order read

$$\begin{aligned} \frac{1}{r} \frac{\partial r u_r}{\partial r} + \frac{\partial u_z}{\partial z} &= 0 \\ \frac{\partial u_r}{\partial t} + u_z \frac{\partial u_z}{\partial z} &= -\frac{1}{\rho} \frac{\partial p}{\partial z} + \nu \frac{\partial^2 u_z}{\partial z^2} \\ \frac{\partial u_\theta}{\partial t} + u_z \frac{\partial u_r}{\partial z} - \frac{u_\theta^2}{r} &= -\frac{1}{\rho} \frac{\partial p}{\partial r} + \nu \frac{\partial^2 u_r}{\partial z^2} \\ \frac{\partial u_z}{\partial t} + u_z \frac{\partial u_\theta}{\partial z} + \frac{u_r u_\theta}{r} &= \nu \frac{\partial^2 u_\theta}{\partial z^2}, \end{aligned} \quad (6.59)$$

from which it follows that

$$\frac{\partial \mathbf{u}}{\partial t} \sim \omega U_\theta, \quad \mathbf{u} \cdot \nabla \mathbf{u} \sim \frac{U_\theta^2}{R}, \quad \frac{1}{\rho} \nabla p = \frac{U_\theta^2}{\delta}, \quad \nu \Delta \mathbf{u} \sim \nu \frac{U_\theta}{\delta^2}. \quad (6.60)$$

By relating the characteristic azimuthal velocity to the rotational frequency of the disk (see Eq. (6.18)), we finally get the scaling arguments (6.19).

6.6 Appendix: Rosenblat's torque

In the limit of small oscillation amplitude, Rosenblat (1959) found the second order correction of the viscous torque exerted by the fluid on the oscillating disk

$$\tau_f = \rho\pi R^4 \frac{\sqrt{\omega^3\nu}}{\sqrt{2}} [\theta^* (\cos(\omega t) + \sin(\omega t)) + \theta^{*3} (-0.262 \cos(\omega t) + 0.060 \sin(\omega t))]. \quad (6.61)$$

Note that the leading order term corresponds to the torque of the linear Stokes solution (6.25), whereas the cubic part is the second order nonlinear contribution. In the spirit of amplitude equation, the nondimensional torque can be rewritten as a function of the oscillation amplitude. Consequently, the disk's equation in the low amplitude regime with the second order torque reads

$$\ddot{\theta} + \theta = \epsilon 2\sigma(\theta - \dot{\theta}) + 2\sigma a^2(t)(-0.262\theta - 0.060\dot{\theta}). \quad (6.62)$$

As done in section 6.4.2, we seek for an asymptotic solution of the type

$$\theta = \theta_0(t, T) + \epsilon\theta_1(t, T) + O(\epsilon^2), \quad (6.63)$$

where T is the slow time scale $T = \epsilon t$.

At leading order ϵ^0 , the linear oscillator equation is recovered

$$\ddot{\theta}_0 + \theta_0 = 0, \quad (6.64)$$

with solution,

$$\theta_0 = \frac{1}{2}a(T)e^{i[t+\beta(T)]} + c.c.. \quad (6.65)$$

At order ϵ , the nonlinear torque (6.61), enters as a forcing term in the problem, along with the slow time modulation $\dot{\theta}'_0$

$$\ddot{\theta}_1 + \theta_1 = -2\dot{\theta}'_0 + 2\sigma(\theta - \dot{\theta}) + 2\sigma a^2(t)(-0.262\theta - 0.060\dot{\theta}), \quad (6.66)$$

where the prime sign denotes derivation with respect to the slow time scale T . In order to avoid secular terms at first order, the resonant terms in the rhs of equation (6.66) have to cancel out, yielding to the amplitude equation:

$$i[a' + \sigma a + 0.060\sigma a^3] + [-a\beta' + \sigma a - 0.262\sigma a^3] = 0, \quad (6.67)$$

which is satisfied by

$$a(t) = \frac{e^{-\epsilon\sigma t}}{\sqrt{a_0^2 + 0.060(1 - e^{-2\epsilon\sigma t})}}, \quad \beta(t) = \beta_0 - \epsilon\sigma t + \frac{0.262}{2 \cdot 0.060} \log(a_0^2 + 0.060(1 - e^{-2\epsilon\sigma t})), \quad (6.68)$$

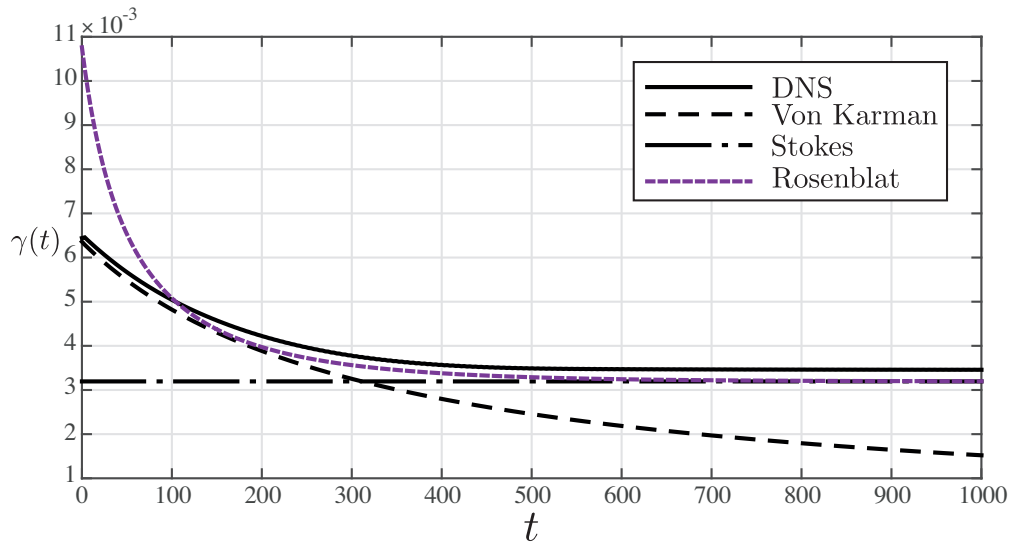


Figure 6.10: Instantaneous damping rate as a function of time at $Re = 1000$. The solid line refers to the results from the numerical simulations, whereas the dashed, dot-dashed, and purple dashed lines refer to damping rate of the quasi-steady Von Karman, Stokes and Rosenblat solution.

with a_0 and β_0 set by the initial condition.

It follows that the instantaneous damping rate is given by a linear contribution, equal to the Stokes damping rate (6.29), and a nonlinear one, associated with the second order correction of the torque

$$\gamma(t) = -\frac{1}{a_0} \frac{da(t)}{dt} = \epsilon\sigma[1 + 0.060a^2(t)]. \quad (6.69)$$

Figure 6.10 reports the instantaneous damping rate from DNS, compared with the ones corresponding to (i) quasi-steady Von Karman, (ii) Stokes and (iii) Rosenblat solution. The latter matches well the full numerical solution in the intermediate region between high and low amplitudes, and collapses on the Stokes solution when the quadratic term in equation (6.69) becomes negligible. However, out of its domain of validity, Rosenblat's asymptotic solution significantly overestimates the damping rate since in the high amplitude regime the viscous torque scales as $\dot{\theta}^{3/2}$ rather than $\dot{\theta}^3$, as correctly captured by the quasi-steady Von Karman solution.

7 Nonlinear friction in sloshing dynamics: total wetting

Foam on troubled water: capillary induced finite-time arrest of sloshing waves

F. Viola¹, P.-T. Brun², B. Dollet³ and F. Gallaire¹

¹ Laboratory of Fluid Mechanics and Instabilities, École Polytechnique Fédérale de Lausanne, Lausanne, CH-1015, Switzerland

² Department of Mathematics, Massachusetts Institute of Technology, Cambridge, Massachusetts 02139, USA

³ Institut de Physique de Rennes, UMR CNRS 6251, Université Rennes 1 Bâtiment 11A, Campus de Beaulieu, 35042 Rennes Cedex, France

Physics of Fluids 28 (2016): 091701

Interfacial forces exceed gravitational forces on a scale small relative to the capillary length - two millimeters in the case of an air-water interface - and therefore dominate the physics of sub-millimetric systems. They are of paramount importance for various biological taxa and engineering processes where the motion of a liquid meniscus induces a viscous frictional force that exhibits a sublinear dependence in the meniscus velocity, i.e. a power law with an exponent smaller than one. Interested in the fundamental implications of this dependence, we use a liquid-foam sloshing system as a prototype to exacerbate the effect of sublinear friction on the macroscopic mechanics of multi-phase flows. In contrast to classical theory, we uncover the existence of a finite-time singularity in our system yielding the arrest of the fluid's oscillations. We propose a minimal theoretical framework to capture this effect, thereby amending the paradigmatic damped harmonic oscillator model. Our results suggest that, although often not considered at the macroscale, sublinear capillary forces govern the friction at liquid-solid and liquid-liquid interfaces.

7.1 Introduction

No one who has glimpsed at Hokusai's iconic wave paintings can fail to notice the truthful yet stylized rendering of the singular nature of such multi-scale flows. On a theoretical point of view, overturning, breaking and atomization are supported by nonlinear terms in the equations prescribing the waves' dynamics at large amplitude, so that finding their exact solution is often arduous. Nonlinearities, however, usually become of negligible relative importance for sufficiently low amplitudes of motion, thereby enabling perturbative linearized approaches (Lamb, 1932). These theoretical linear problems are easier to solve than their nonlinear counterparts and have been extremely successful at predicting the stability, characteristic frequencies and growth rates of a wide range of physical systems arising in natural and industrial settings, a classic example of which is the sloshing of fluid in a container (Ibrahim, 2005). In such a case, the excess of gravitational potential energy associated to the deformation of the free surface is progressively relaxed when periodically turned into kinetic energy and damped by viscous forces (Case & Parkinson, 1957; Ibrahim, 2005). In the small amplitude regime, the fundamental sloshing frequency for a cylindrical container is known to be $\omega_0 = \sqrt{1.84 g/R}$ where g is the acceleration of gravity and R the container radius (Ibrahim, 2005). The classical contributions to the viscous damping rate, σ , have been identified as the dissipation in the oscillating boundary layers near the container walls and the free surface, and the bulk dissipation (Case & Parkinson, 1957). Those dissipative forces have different scalings with respect to the governing parameters (radius R , viscosity μ , density ρ , gravity g), but all depend linearly on the free surface velocity (Case & Parkinson, 1957; Ibrahim, 2005).

Here, we study the effect of a small modification to this classical problem, as we place a thin layer of foam on a volume of water (see Fig. 7.1), and explore the dramatic change in its mechanistic properties. It has been recently shown (Sauret *et al.*, 2015) that sloshing in a rectangular basin could be strongly damped by the addition of a shallow foam layer at the top. While foam is a complex media with visco-elasto-plastic rheological properties (Cantat, 2013), this significant attenuation was attributed to friction between the foam and the wall, which dominates the dissipation in the foam bulk (Sauret *et al.*, 2015). In this work, we focus our attention on the nonlinear nature of the dissipation occurring in the foam layer. This source of dissipation emanates from the relative displacement of the liquid channels separating the foam bubbles, known as *Plateau borders* (Cantat, 2013). The motion of these multiple air-liquid interfaces along the container results in a frictional force that scales nonlinearly with their sliding velocity. Indeed, this force scales like $Ca^{2/3}$, where Ca is the capillary number based on the sliding velocity (Bretherton, 1961; Denkov *et al.*, 2005; Cantat, 2013). Owing to their sublinearity (the exponent on the velocity is smaller than one), these frictional terms are found to dominate all linear contributions for small enough values of Ca , which naturally arise for small amplitudes of motion. Therefore, unlike nonlinearities with exponents greater than one, they cannot be neglected, thereby ruining all linear theoretical approaches. Unlike the picture of a linearly damped oscillator classically used in textbooks to model sloshing, we show experimentally and theoretically that the sloshing of the liquid phase does not relax exponentially. The damping rate in fact increases catastrophically at small amplitude and

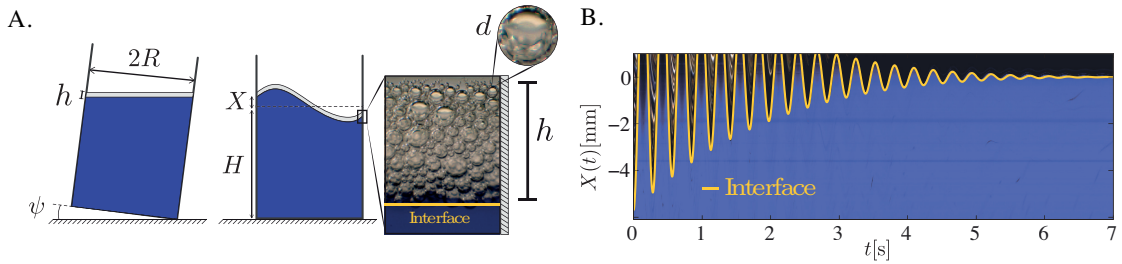


Figure 7.1: (A) Experimental setup: a cylindrical container is tilted by an angle ψ to initiate the sloshing of a volume of water surmounted by foam. The foam layer of thickness $h \ll H$ and $h \ll R$ comprises bubbles of typical radius d . (B) Shown is the spatio-temporal view of the water-foam contact line $X(t)$ captured in a typical experiment.

yields a *finite-time arrest* of the fluid's motion.

7.2 Experiments

The setup consists of a cylindrical Plexiglas container of internal radius $R = 37.05$ mm that is sealed to an aluminum plate connected itself to a hinge. The container is filled with a column of water of height H which is surmounted by a foam layer of thickness h , see Figure 7.1A. The foam is produced when injecting a commercial hand soap (Hypron SA) through a nozzle with a grid with pore size 0.2 mm and has typical bubbles diameter $d = 0.25$ mm. The foam's liquid fraction is measured to be 25% once poured on top of the water column (evaluated using the weight of a volume of foam). This large value relative to dry foams, is due to capillary forces yielding an intake of water effectively enlarging the foam Plateau borders (Cantat, 2013). In the following, the liquid fraction across the foam layer, whose thickness ranges from $h = 2.5$ mm to 6.5 mm, is assumed uniform. Using an oscillating drop tensiometer (Tracker, Teclis), we measured the surface tension, $\gamma = 31.5$ mN/m, of the soap solution. Its viscoelastic surface dilatational modulus, quantifying the relative variation of surface tension upon dilatation and compression, is found below resolution (0.1 mN/m), showing that the interface can be considered as mobile (Denkov *et al.*, 2005) and that free shear boundary conditions apply.

Experiments are initiated by tilting the container of an angle ψ and then releasing it, see Fig. 7.1A. The dynamics following the impact is recorded with a high-speed camera (Phantom Micro M310) operating at 300 Hz. In order to investigate the waves dynamics at small scales, we coupled a Nikon 50 mm lens with an optical bellows obtaining a resolution of $2 \cdot 10^{-2}$ mm per pixel on the water-foam interface displacement. After a short transient regime, the flow response was found to exhibit a single mode of oscillation (see Fig. 7.1B). The frequency of oscillations, 3.50 Hz, matches the theoretical inviscid prediction $\omega_0 = \sqrt{1.84g/R}$ within 1%. This result was expected for $h = 0$ as the deep water condition $H > 2R$ is satisfied and the container size is well above the capillary length (Lamb, 1932), i.e. $\gamma/\rho g R^2 \ll 1$. This frequency is found unchanged when adding foam ($0 < h < 6.5$ mm), as already observed in previous experiments (Sauret *et al.*, 2015) and discussed in section 7.3.2.

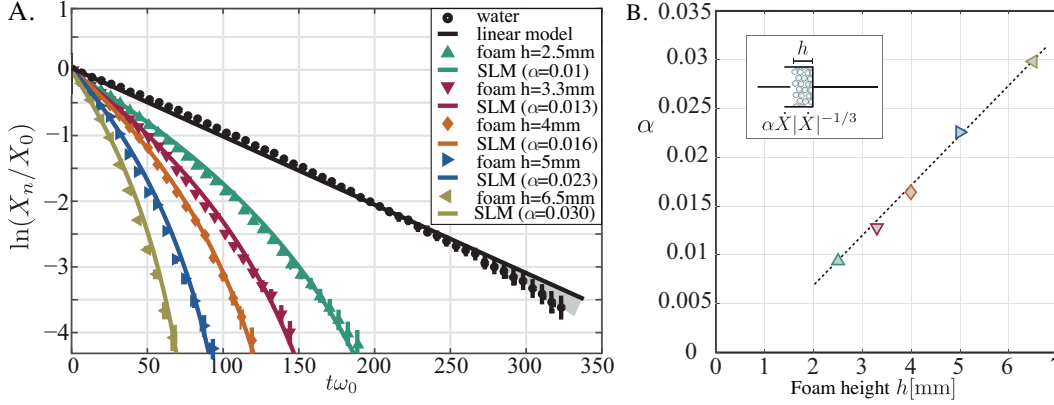


Figure 7.2: (A) Logarithmic decrement, $\mathcal{D} = \ln(X_n/X_0)$, of the sloshing amplitude for foam thicknesses ranging across values $h = 0, 2.5, 3.3, 4, 5, 6.5$ mm. Symbols indicate measurements, while continuous lines represent the envelope solutions of the sublinear model (SLM), with a single fitting parameter α (see $a(t)$ in eq. 7.20). (B) Shown is the dependance of the friction force exerted by the foam layer, F_f , through the friction coefficient α as found in experiments. F_f increases linearly with the foam thickness h , i.e. with the number of layers of oscillating bubbles.

The attenuation of the gravity waves is investigated by recording the motion $X(t)$ of the water-foam interface at the azimuth corresponding to the largest wave oscillation. Using the function 'orthogonal view' in ImageJ, we follow the evolution of a pixel line over time, thereby reconstituting the oscillatory motion $X(t)$ of the contact line at a given location, see Fig. 7.1B. The natural logarithm $\mathcal{D} = \ln(X_n/X_0)$ of the ratio between the amplitude of the n th peak, X_n , and the amplitude of the first peak, systematically chosen to $X_0 = 5$ mm, is used as an instantaneous measure of the growth rate. For the case $h = 0$ (no foam), we recover the classical result of a constant damping rate. The logarithmic decrement is linear in time for most of the dynamics, $\mathcal{D} \propto -\sigma\omega_0 t$, as indicated in Fig. 7.2A (see section 7.4 for a rationalization of the shaded area). We found $\sigma = 0.0098$, which exceeds the theoretical expression (Case & Parkinson, 1957) of the viscous damping rate by a factor 2. This result is in line with other experimental measurements in the literature (Cocciaro *et al.*, 1991) and is commonly attributed to the advancing and receding of the dynamic contact line (Ibrahim, 2005). As soon as a thin foam layer is added in the system, \mathcal{D} is no longer linear, as shown in Fig. 7.2A for values of h ranging from 2.5 mm to 6.5 mm. We find \mathcal{D} to be concave down and negatively correlated to h . In other words, the damping rate is greater with foam as evidenced by previous experiments (Sauret *et al.*, 2015) but also evidently increases as the amplitude of oscillations decreases. In particular this result translates into the fact that the interface does not relax exponentially at a given rate, but instead its decay is progressively hastened. This novel observation suggests the existence of a mechanism submitting smaller oscillations to a stronger damping, that we aim to rationalize.

7.3 A nonlinear fluid oscillator

7.3.1 Equivalent mechanical system

From this point onward, we restrict ourselves to thin layers of foam and we assume the entire layer of height h is oscillating along with the liquid phase. We model the total oscillating mass as $\pi R^2(\rho\lambda + \rho_f h)$, where $\lambda \sim R$ is the penetration length of the wave (Lamb, 1932) and ρ and ρ_f denote the density of water and foam, respectively. Given the physical parameters of the problem we place ourselves in the limit $\rho_f h \ll \rho\lambda$, i.e. we neglect foam's inertia relative to the one of water. Similarly, the restoring gravitational force acting on this volume of fluid may be estimated considering solely the liquid phase: $F_g \sim \rho g \pi R^2 X$, where X is the amplitude of the water-foam interface and g the acceleration of gravity. In absence of foam, according to the seminal work of Case & Parkinson (Case & Parkinson, 1957), three main dissipation sources exist, they acting: (i) at the free surface, (ii) in the fluid bulk and (iii) in the Stokes boundary layer close to the wall. The last contribution has been shown to dominate the other ones (Case & Parkinson, 1957). Denoting by μ and ν the water dynamic and kinematic viscosities, and by \dot{X} the oscillation speed, we model the viscous dissipation as a single force $F_w \sim 2\pi R \lambda \mu \dot{X} / \delta$, where $\delta \sim \sqrt{\nu / \omega_0}$ is the Stokes layer thickness (Case & Parkinson, 1957).

We now turn to model the force F_f associated with capillary effects in the foam layer. Let us consider a single wall Plateau border, i.e. the edge separating neighboring bubbles at the wall, sliding along the container vertical wall with velocity \dot{X} . Damping of its motion originates from the transition region between the wetting film at the wall and the moving wall Plateau border (Cantat, 2013). The matching between the outer meniscus and the transition zone, involving a balance between viscous and capillary forces, defines the friction force per unit length of a wall Plateau border scaling as $\gamma Ca^{2/3}$, where $Ca = \mu \dot{X} / \gamma$ is the capillary number and γ denotes the surface tension (Cantat, 2013). The total length of surface Plateau borders is given by their typical length, d , times the number of Plateau borders in contact with the container that scales as $2\pi R h / d^2$. Thus, the friction force acting at the wall in the foam layer reads

$$F_f \sim \frac{h}{d} R \gamma^{1/3} \mu^{2/3} \dot{X} |\dot{X}|^{-1/3}, \quad (7.1)$$

where the absolute value is introduced to conveniently treat negative speeds. This result is reminiscent to the force acting on a plate pulled out of a bath (Landau & Levich, 1942; Bretherton, 1961) and is valid for a mobile interface, i.e. an interface where a free shear boundary condition applies. This point has been verified for the foam used in our experiments (see section 7.2).

Using the estimation for the volume of fluid effectively oscillating and the forces acting on it, we write Newton's 2nd law:

$$\pi R^2 (\rho \lambda) \ddot{X} = F_g + F_w + F_f. \quad (7.2)$$

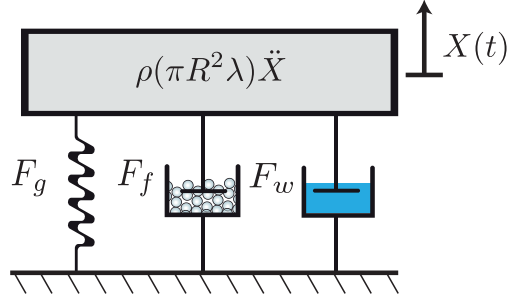


Figure 7.3: A sketch of our reduced model for sloshing. The effects of foam are accounted by the sublinear term $F_f \propto \dot{X}|\dot{X}|^{-1/3}$. This term amends the classical damped oscillator model where the inertial term is balanced by the restoring force, $F_g \propto X$, and the viscous damping, $F_w \propto \dot{X}$.

Equation (7.2) constitutes a nonlinear oscillator where inertia is resisted by the restoring force of gravity and the two dissipative terms, F_w and F_f (see the equivalent mechanical system depicted in Figure 7.3). We note that F_w varies linearly with \dot{X} , while F_f has a sublinear dependence on the interface velocity \dot{X} . As a consequence, F_f is expected to dominate the dynamics when \dot{X} is sufficiently small. After a renormalization by the inertial term, eq. (7.2) yields

$$\ddot{X} + \omega_0^2 X = -2\sigma\omega_0\dot{X} - \alpha\omega_0^{4/3}R^{1/3}\dot{X}|\dot{X}|^{-1/3}, \quad (7.3)$$

where ω_0 is the angular frequency scaling as $\omega_0 \sim \sqrt{g/R}$, and σ is the viscous damping coefficient which is proportional to $\sigma \sim \sqrt{\nu}/(R^{3/4}g^{1/4})$. These scaling arguments are in line with the theoretical results obtained using first principles (Lamb, 1932; Case & Parkinson, 1957). The last term on the right hand side is the nonlinear damping associated with the foam layer, where the prefactor $\omega_0^{4/3}R^{1/3}$ results from the renormalization, and α is the dimensionless coefficient of sublinear damping, which scales as $\alpha \sim hd^{-1}\gamma^{1/3}\mu^{2/3}\rho^{-1}R^{-5/3}g^{-2/3}$.

7.3.2 Asymptotic solution and comparison to experiments

In the limit of negligible capillary effects, $\alpha = 0$, equation (7.3) reduces to a linearly damped harmonic oscillator. This equation is traditionally used to model the free-surface oscillations of a liquid in a tank (Ibrahim, 2005), with solution:

$$X(t) = X_0 e^{-\omega_0\sigma t} \cos(\sqrt{1-\sigma^2}\omega_0 t), \quad (7.4)$$

where X_0 is the initial amplitude. This expression is consistent with the experimental data reported in Fig. 7.2 for $h = 0$ (no foam).

With foam and thus $\alpha \neq 0$, eq. (7.3) does not have a closed-form analytical solution. However, an asymptotic solution can be obtained by using the method of multiple scales as detailed in Nayfeh (Nayfeh, 2008). In the limit of small damping, $\sigma, \alpha \ll 1$, the solution of eq. (7.3) is

asymptotic to $X(t) \sim a(t) \cos(\omega_0 t)$, where the sinusoidal term is the solution of the undamped oscillator ($\sigma = \alpha = 0$ as in the leading order problem in the asymptotic scheme). The slow varying envelope $a(t)$ is determined at the next order by imposing a compatibility condition that involves only the right hand side terms in eq. (7.3) oscillating at the natural frequency of the system ω_0 . $X(t)$ reads:

$$X(t) = \underbrace{\left[X_0^{1/3} - \frac{\alpha}{\sigma} c R^{1/3} (e^{\omega_0 \sigma t / 3} - 1) \right]^3}_{a(t)} e^{-\sigma \omega_0 t} \cos(\omega_0 t). \quad (7.5)$$

See the section 7.5 for a detailed derivation of the asymptotic solution and the definition of the constant c that is the Fourier coefficient of the Fourier component of $\dot{X}|\dot{X}|^{-1/3}$ synchronized to the natural frequency of the system ω_0 . Note that the frequency shift $\sqrt{1 - \sigma^2}$ in eq. (7.4), is not present in the asymptotic solution (7.20) as it belongs to a higher order.

The asymptotic solution (7.20) to the sublinear model (SLM), is now compared and fitted to our experimental results. In Figure 7.2(b) the coefficients ω_0 and σ are set to their reference values obtained experimentally in the $h = 0$ limit ($\omega_0 = 22.00$ rad/s, $\sigma = 9.8 \cdot 10^{-3}$). The sublinear coefficient α is thus the only unknown parameter of the model. Here, α is determined independently for each of the $h \neq 0$ cases by fitting the logarithmic decrement with equation (7.20). We find that our model captures the concave aspect of the linear decrement measured from experiments. Additionally, the larger the film thickness, the stronger the nonlinear damping coefficient. More precisely, our data in Fig. 7.2B shows that the damping coefficient α increases linearly with the foam thickness h , further validating the proposed physical picture: in the range of thin foam layers investigated, the foam acts as collection of Plateau borders, which all equally contribute to the effective dissipative force. The number of contact lines, earlier estimated as the foam thickness to bubble diameter ratio h/d , is thus the relevant scale to evaluate α .

7.3.3 Sublinear friction and its finite-time arrest

Assured that the reduced model (7.3) and its solution (7.20) are a quantitative representation of the sloshing dynamics with foam, we turn to examine the mechanistic impact of the sub-linear damping introduced in our model. In Fig. 7.4A we report the sublinear model (SLM) envelope $a(t)$ in the particular, yet representative, case $h = 4$ mm. Its concave down behavior contrasts with the classical exponential relaxation adopted by previous works (Sauret *et al.*, 2015), indicated by the blue line. This effect is due to an increase of the relative importance of sublinear friction forces compared to the inertial and restoring terms as the amplitude of oscillation decreases. The dominance of interfacial effects is induced by their sublinear dependance in the oscillating velocity. In fact, they diverge in the limit of vanishing oscillations, yielding a finite-time singularity. For the sake of the validation of our asymptotic solution (7.20), we report also in Fig. 7.4A the numerical solution of eq. (7.3) obtained using a third order Runge-Kutta scheme.

Upon examination of the behavior of eq. (7.20) at very small amplitudes, we find the ampli-

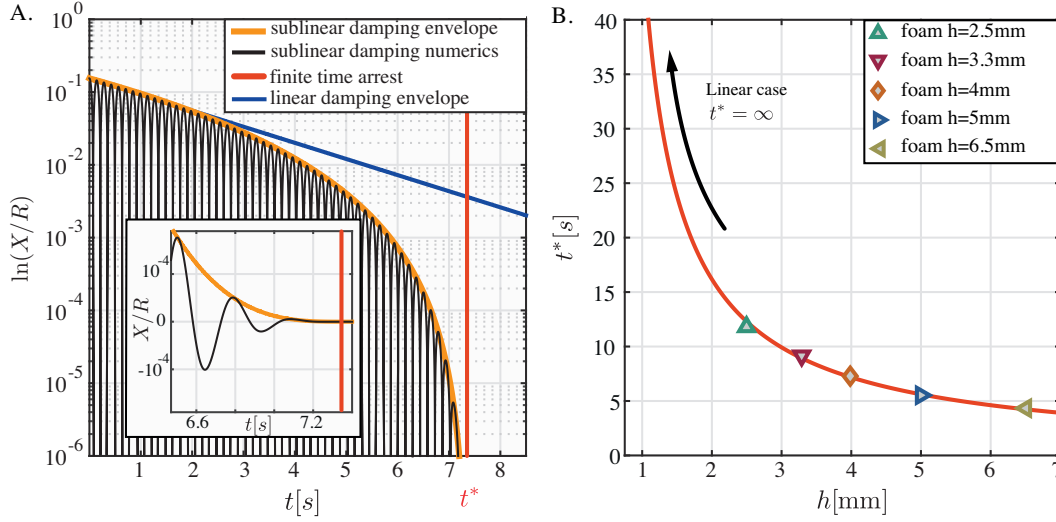


Figure 7.4: (A) Numerical nonlinear solution of eq. (7.3) for $h = 4$ mm (black line), together with its envelope obtained by asymptotic analysis (orange line). The vertical red line indicates the finite-time of arrest t^* . The blue line represents the envelope of the linear model solution starting from the same initial condition. (B) Time of arrest as a function of the foam height h for a single initial condition (from eq.(7.6) with $\alpha(h)$ reported in Fig. 7.2B). Symbols correspond to the values deduced from the experiments.

tude of sloshing to be exactly nil for time $t = t^*$, where t^* is the time of arrest. This behavior contrasts the classical linear theory giving rise to an exponential decay for which $t^* = \infty$. In our model, t^* is finite and using eq. (7.20), we can derive its analytical expression:

$$t^* = \frac{3}{\sigma\omega_0} \ln \left[1 + c^{-1} \frac{\sigma}{\alpha(h)} \left(\frac{X_0}{R} \right)^{1/3} \right]. \quad (7.6)$$

In Fig. 7.4B we show the variation of t^* with h and report the values corresponding to our experiments (as deduced from the fit of our experimental data using the SLM). The time of arrest t^* diverges in the limit where $h = 0$, as expected since this case corresponds to an exponential relaxation in our theoretical framework (see eq. (7.4)). A small foam layer ($h = 2.5$ mm) is sufficient to bring this time to a finite and relatively small value ($t^* \simeq 12$ s). Other values of t^* corresponding to larger values of h are of the same order (the smallest is 5 s) and decrease if the foam thickness h increases.

7.4 Conclusions

In our experiments we found that adding foam to a liquid dramatically damps its oscillatory motion but hardly affects its sloshing frequency. Without foam, sloshing is well approximated by a linearly damped harmonic oscillator relaxing exponentially with characteristic time $t_\mu = 1/(\sigma\omega_0)$, thereby predicting an arrest of motion for $t^* = \infty$. In contrast, owing to its cellular structure, foam introduces sublinear capillary forces, which, in turn, lead to a finite-time

arrest of the fluid's motion. Equation (7.6) provides the expression for the time of arrest t^* , highlighting the importance of the ratio between the viscous damping $\sigma \sim \nu^{1/2} g^{-1/4} R^{-3/4}$ and the sublinear damping $\alpha \sim h d^{-1} \gamma^{1/3} \mu^{2/3} R^{-5/3} g^{-2/3} \rho^{-1}$ coefficients. The time of arrest t^* is negatively correlated to α/σ and diverges when this ratio is small (corresponding to a linearly damped oscillator). Specifically, an increase in h , an increase in γ or a decrease in d , all yield a decrease in t^* . The scaling argument for the sublinear coefficient α is in good agreement with the experimental measurements for various foam height h , see section 7.3.2. On the other hand, its dependence on the fluid density, ρ , its viscosity, μ , and surface tension, γ , along with the dependence on the container size, R , and the foam bubble diameter, d , can in principle be probed experimentally by using different fluids, container size and foams and it is a future perspective of this work.

Note that this expression is only valid for small but finite foam layers. Sloshing with a large amount of foam may lead to the situation where only a fraction of the total volume of foam is effectively in motion. The upper part of the foam layer remains still, hence does not participate to the sublinear damping examined in this work. We therefore anticipate that $\alpha(h)$ does not remain linear for arbitrarily large values of h , but instead saturates, in turn giving rise to a plateau for t^* in the limit of large foam thicknesses.

Similarly, the case $d = 0$ and $h = 0$ is ill-defined in our model. For these values, corresponding to a simple liquid-air interface, a liquid meniscus forms at the container walls. During sloshing, this advancing and receding contact line will generate a small, yet nonlinear, friction force (Cantat, 2013), which affects the damping rate measured in the experiments (Cocciaro *et al.*, 1991; Ibrahim, 2005). Evidence of these effects is apparent at very small amplitude as highlighted by the shaded area in Fig. 7.2A for pure water. Although the accuracy of the measurements does not allow for a systematic analysis at this stage, this observation suggests that our work could generalize to a single moving contact line. Accounting for those effects – without foam to exacerbate them – requires a realistic contact line model (Ibrahim, 2005), with features such as contact angle hysteresis and the variations of contact angle with the contact line velocity.

Finally, we note that finite-time arrests are commonly observed in mechanical systems involving solid friction as a consequence of Coulomb's law, but have not frequently been reported in fluidic systems. Their importance in practical situations such as Euler's disk has been the subject of investigations in recent years (Moffatt, 2000). Here, we have demonstrated that the effect of pure fluid dissipation in sub-millimetric menisci at a contact line is sufficient to bring a body of fluid to rest in finite time albeit the fluid's volume is significantly larger than that of the meniscus.

Financial support by ERC grant SimCoMiCs 280117 is gratefully acknowledged.

7.5 Appendix: Asymptotic analysis

Let us consider the nonlinear oscillator

$$\ddot{X} + \omega_0^2 X = -2\sigma\omega_0\dot{X} - \alpha\omega_0^{4/3}R^{1/3}\dot{X}|\dot{X}|^{-1/3}, \quad (7.7)$$

and let make it dimensionless using the frequency ω_0^{-1} and the container radius R as characteristic time and length scales:

$$\ddot{x} + 2\sigma\dot{x} + x + \alpha\dot{x}|\dot{x}|^{-1/3} = 0, \quad (7.8)$$

where $X = Rx$. A dot in the equation denotes a time derivative with respect to the dimensionless time $\tilde{t} = t\omega_0$. This is an oscillator linearly and sublinearly damped, where the two damping coefficients, σ and α , are assumed to be small and of the same order. A single small parameter ϵ can therefore be defined such that the scaled quantities $\bar{\sigma} = \sigma/\epsilon$ and $\bar{\alpha} = \alpha/\epsilon$ are of order one. Accordingly to multiple scale approach, an asymptotic expansion in ϵ is carried out

$$x = x_0(\tilde{t}, T) + \epsilon x_1(\tilde{t}, T) + O(\epsilon^2), \quad (7.9)$$

where T is the slow time scale defined as $T = \epsilon\tilde{t}$. At zero order in ϵ , the linear oscillator equation is recovered:

$$\ddot{x}_0 + x_0 = 0, \quad (7.10)$$

where the dot here stands for a derivative with respect to the fast time t . The solution to this equation is

$$x_0 = \frac{1}{2}\mathcal{A}(T)e^{i[\tilde{t}+\phi(T)]} + c.c., \quad (7.11)$$

where the phase ϕ and nondimensional envelope \mathcal{A} depend on the slow time scale T and $c.c.$ designates the complex conjugate.

At order ϵ , the linear damping term, $2\bar{\sigma}\dot{x}_0$, and its nonlinear counterpart, $\bar{\alpha}\dot{x}_0|\dot{x}_0|^{-1/3}$, enter as forcing terms to the oscillator equation, together with a term resulting from the slow time modulation:

$$\ddot{x}_1 + x_1 = -2\dot{x}'_0 - 2\bar{\sigma}\dot{x}_0 - \bar{\alpha}\dot{x}_0|\dot{x}_0|^{-1/3}. \quad (7.12)$$

The prime signs denote a derivation with respect to the slow time scale T . The first two terms on the r.h.s. are synchronized with the sloshing motion as they oscillate at the natural frequency

$$\begin{aligned} 2\dot{x}'_0 &= i(\mathcal{A}' + i\mathcal{A}\phi')e^{i(\tilde{t}+\phi)} + c.c. \\ 2\bar{\sigma}\dot{x}_0 &= i\bar{\sigma}\mathcal{A}e^{i(\tilde{t}+\phi)} + c.c.. \end{aligned} \quad (7.13)$$

Conversely, the nonlinear term is not purely harmonic, but through a Fourier series the components oscillating at the natural frequency may be isolated:

$$\tilde{\alpha} \dot{x}_0 |\dot{x}_0|^{-1/3} = i \tilde{\alpha} c \mathcal{A}^{2/3} e^{i(\tilde{t} + \phi)} + c.c. + \text{NRT} \quad (7.14)$$

where NRT stands for the nonresonating terms and c is the Fourier coefficient of the resonating harmonic which is given by:

$$c = \frac{1}{2\pi} \int_0^{2\pi} \sin^2(\tilde{t} + \phi) |\sin(\tilde{t} + \phi)|^{-1/3} d\tilde{t} = \frac{2\Gamma(1/3)}{5\Gamma(5/6)\sqrt{\pi}} \approx 0.5356. \quad (7.15)$$

In order to avoid secular terms at first order, the resonant terms in the r.h.s. of eq. (7.12) have to cancel out, yielding to the amplitude equation:

$$i(\mathcal{A}' + i\mathcal{A}\phi') + i\tilde{\sigma}a + i\tilde{\alpha}c\mathcal{A}^{2/3} = 0. \quad (7.16)$$

By splitting real and imaginary parts, we obtain an equation for the slow phase modulation,

$$\phi' = 0 \Rightarrow \phi = \phi_0 \quad (7.17)$$

and another one for the amplitude

$$\mathcal{A}' + \tilde{\sigma}\mathcal{A} + \tilde{\alpha}c\mathcal{A}^{2/3} = 0, \quad (7.18)$$

with solution

$$\mathcal{A}(\tilde{t}) = e^{-\sigma\tilde{t}} \left[\mathcal{A}_0^{1/3} - \frac{c\alpha}{\sigma} (e^{\sigma\tilde{t}/3} - 1) \right]^3, \quad (7.19)$$

where the constants a_0 and ϕ_0 are set by the initial position, X_0/R , and initial velocity $\dot{X}_0/(\omega_0 R)$ according to: $\phi_0 = -\tan^{-1}[\dot{X}_0/(\omega_0 X_0)]$ and $a_0 = X_0/(R \cos \phi_0)$. In the case of starting motion from rest the dimensional asymptotic solution to equation (7.7) is given by:

$$X(t) = \underbrace{\left[X_0^{1/3} - \frac{\alpha}{\sigma} c R^{1/3} (e^{\omega_0 \sigma t / 3} - 1) \right]^3}_{a(t)} e^{-\sigma \omega_0 t} \cos(\omega_0 t), \quad (7.20)$$

where $a(t)$ is the dimensional envelope function $a(t) = R\mathcal{A}(\omega_0^{-1}\tilde{t})$.

8 Nonlinear friction in sloshing dynamics: partial wetting

Contact line hysteresis in sloshing dynamics yields finite time arrest

F. Viola¹, P.-T. Brun² and F. Gallaire¹

¹ Laboratory of Fluid Mechanics and Instabilities, École Polytechnique Fédérale de Lausanne, Lausanne, CH-1015, Switzerland

² Department of Mathematics, Massachusetts Institute of Technology, Cambridge, Massachusetts 02139, USA

Submitted to *Journal of Fluid Mechanics*.

In mechanics, sloshing constitutes an archetypal damped oscillator, with frequency derived in the potential flow limit (Lamb, 1932). The damping rate results from the viscous dissipation at the wall, in the bulk and at the free surface, respectively (Case & Parkinson, 1957). However, the classic theoretical prediction significantly underestimates the damping rate when compared to careful laboratory experiments. In addition, theory provides a unique value of the damping rate, while experiments revealed that the damping increases as the sloshing amplitude decreases.

Here, we demonstrate theoretically that the enhanced damping and its dependence on the sloshing amplitude is in fact due to capillary forces at the contact line between the liquid and the container walls. To this end, we model inviscid waves using a nonlinear contact line empiric law, which presents hysteresis. The resulting system of equations is solved by means of a global weakly nonlinear analysis using the method of multiple scales. Capillary effects have a dramatic influence on the calculated damping rate, especially when the sloshing amplitude gets smaller: this nonlinear interfacial term stops the fluid dynamics after a finite time. In contrast to viscous damping, where the wave motion decays exponentially, the contact angle hysteresis acts as Coulomb solid friction yielding a *finite time arrest*.

8.1 Introduction

It is sufficient to casually shake a glass of water to raise a tempest in it. However, if the initial amplitude of the fluid motion is small enough, its sloshing is very regular: the gravity waves are quantized into modes owing to the action of the container walls. The confinement exacerbates the viscous dissipation in the fluid, which damps the fluid's oscillations and eventually brings the interface back to rest. In this small amplitude regime, the non-linearities in the governing equations are negligible and the sloshing modes are classically computed in the limit of potential flow (Lamb, 1932). The angular eigenfrequency of the first non-axisymmetric longitudinal mode, ω , depends on gravity, g , surface tension, σ , the fluid density ρ , its height h and the radius R of the cylindrical container through the well-known dispersion relation

$$\omega_n^2 = g\lambda_n \left(1 + \frac{\sigma}{\rho g} \lambda_n^2 \right) \tanh(\lambda_n h), \quad (8.1)$$

where λ_n are the roots of the first derivative of the n_{th} -order Bessel function $J'_n(R\lambda_n) = 0$. During the motion, those capillary-gravity waves are damped by viscous dissipation occurring at the (i) oscillating Stokes layers at the walls, (ii) in the fluid bulk and (iii) at the free-surface. The damping rates associated with these three source of dissipation can be computed with a perturbative approach in the limit of small kinematic viscosity ν . Specifically, Case & Parkinson (1957) showed that the dissipation is more intense at the Stokes layers that scale as $\sqrt{\nu}$, when compared to the dissipation in the bulk that scales linearly with ν . Last, the dissipation at the free surface results in a smaller term scaling as $\nu^{3/2}$, see Ursell (1952). These three damping rates have different scaling with the physical quantities but they all are independent from the oscillation amplitude as their evaluation results from a linear problem.

However, experiments of Benjamin & Ursell (1954); Case & Parkinson (1957); Keulegan (1959) and Cocciaro *et al.* (1991) reveal that the theoretical values of the damping rates significantly underestimate the damping of gravity waves measured in laboratory-size containers. In fact, in controlled conditions with carefully polished brass container are needed to recover experimental values close to theoretical estimates of the damping rate (Case & Parkinson, 1957). Specifically, Keulegan (1959) carried out an extensive experimental campaign to study the damping of surface standing waves with several liquids, container size and materials. He found that the damping depends on the material of the container and is in general higher than the one provided by the aforementioned linear theory, which neglects the key-role of capillary effects on the waves attenuation. Moreover, his pioneer work revealed a dependence of damping on the wave amplitude. The damping at small amplitude after several wave cycles was indeed found higher than the one at larger amplitude. Similar results have, since then, been reported by Cocciaro *et al.* (1991) and Cocciaro *et al.* (1993) who investigated the influence of interfacial effects on the natural frequency and the damping rate of sloshing. This work focuses both on wetting and partial wetting conditions unraveling dissipation mechanisms other than the viscous dissipation in the boundary layers and in the bulk of the fluid.

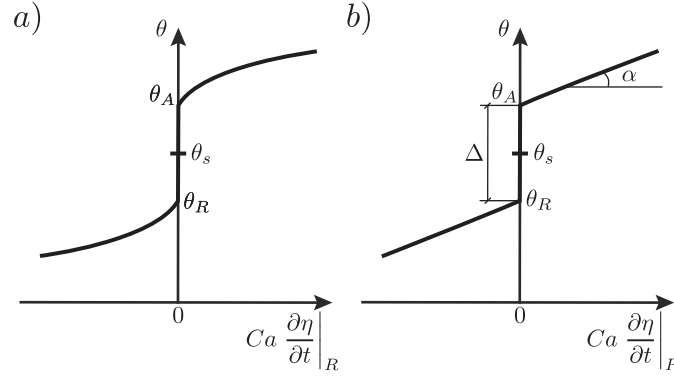


Figure 8.1: Illustrative sketch of contact line models with contact angle, θ , versus the contact line velocity, times the capillary number Ca . In (a) the nonlinear model of Dussan (1979) with the hysteresis range $[\theta_R, \theta_A]$ is shown. (b) reports the nonlinear contact line model used in this work, which corresponds to the linear Hocking law (8.3) with slip coefficient α , plus a symmetric hysteresis range of size Δ .

In fact, in the theoretical work of Case & Parkinson (1957) capillary effects are not accounted for. In particular, the interface is assumed to intersect orthogonally the wall and to freely slip on it (*free-end edge boundary conditions*). This assumption was proven incorrect as experiments reveal that the contact angle θ between the fluid-air interface $\eta(r, \phi, t)$ and the wall is varying throughout the fluid's motion. Additionally, this angle depends on the wetting properties of the wall and the velocity of the contact line $\eta(r = R, \phi, t)$. Miles (1967) modified such capillary effects and their contribution to the damping rate. He assumed that θ is a function of the contact line velocity $\partial\eta/\partial t|_R$, where R denotes the fact that derivative is taken at the wall. For a velocity less than a critical value Miles assumed a relation of the kind

$$\left. \frac{\partial\eta}{\partial t} \right|_R \propto (\cos\theta - \cos\theta_s), \quad (8.2)$$

where θ_s designates the static equilibrium contact angle. When equation (8.2) is linearized around $\theta_s = \pi/2$, the wetting boundary condition proposed by Hocking (1987) is retrieved

$$\left. \frac{\partial\eta}{\partial t} \right|_R = \alpha \frac{\partial\eta}{\partial r}. \quad (8.3)$$

The contact line velocity is proportional to the contact angle, $\theta \approx \pi/2 - \partial\eta/\partial r$, through the slip coefficient α . Hocking (1987) showed that imposing model (8.3) as a boundary condition in the inviscid sloshing problem yields a finite damping rate, resulting solely from capillary effects (recall that the model is potential). By setting arbitrarily α , he obtained damping values qualitatively in line with the experimental measurements of Benjamin & Ursell (1954), Case & Parkinson (1957) and Keulegan (1959). Note that the capillary contribution to damping vanishes for the two limiting cases $\alpha = \infty$ and $\alpha = 0$ which correspond to the free-end and pinned-end edge conditions, respectively. The dependence of the damping rate on the slip coefficient, α , and on the static contact angle, θ_s , was addressed for circular container by

Kidambi (2009) solving iteratively an eigenvalue problem. Cocciaro *et al.* (1993) carried out experiments in order to measure α for surface gravity-capillary waves in a cylindrical container with static contact angle $\theta_s = 62^\circ$. They demonstrated that α is not constant during the sloshing motion and it increases with the contact line velocity. These aspects were also discussed by Keulegan (1959) and Jiang *et al.* (2004). As a consequence of these observations, Cocciaro *et al.* (1993) proposed a slip coefficient that depends explicitly on the amplitude of oscillations. This assumption violates the principles of linear problems and is incompatible with the classic eigenvalues formulations.

In summary experiments indicate the need for a theoretical framework including a model of the contact line richer than the semiempirical relations (8.2) and (8.3). Particular attention should be given to the nonlinear dependence of contact angle with velocity or hysteresis: in the framework of a unidirectional flow over a flat plate at low Reynolds number, Dussan (1979) observed that the dynamic contact-angle at the contact line is a function of the contact line velocity. Additionally, he evidenced the existence of a range $[\theta_R, \theta_A]$ such that if θ lies within this interval then the contact line does not SloshWaterAppeAr to move (contact-angle hysteresis), see Figure 8.1a. Such a behaviour has been observed in the case of silicone oil drops sliding down a glass plate at low velocities by Rio *et al.* (2005); Le Grand *et al.* (2005); De Gennes *et al.* (2002).

Only a handful of contributions in the literature make use of this fact in the context of oscillating flows. The case of an oscillating solid plate at the interface of a bath was investigated theoretically by Young & Davis (1987); Hocking (2003) who demonstrated that the fixed contact angle assumption may lead to physically unrealistic contact line speed responses. They noted that the contact-angle hysteresis and the steepening of the contact angle occurring while increasing the contact-line speed leads to dissipative effects. The same system has been studied experimentally by Ting & Perlin (1995) in order to derive an empirical boundary-condition model for the contact line in oscillatory flow.

The purpose of this work is to investigate theoretically the effect of contact line hysteresis on the sloshing motion and provide a theoretical framework rationalizing the dependence of damping on the amplitude of motion. To this end we consider inviscid waves subjected to a realistic nonlinear contact line law, which we derive in the next section. The resulting system of equations is solved by means of a global weakly nonlinear analysis using the method of multiple scale Stuart (1958). We finally derive a general asymptotic formulation that accounts for nonlinear interfacial effects at the contact line.

The paper is organized as follows. The governing equations, including the contact line model with hysteresis, are presented in § 2. The weakly non linear stability analysis is formulated in § 3, where we compute the fundamental sloshing global mode and derive the governing amplitude equation. In § 4, results are discussed, focusing on the dissipative effect of the contact angle hysteresis. Conclusions and perspectives are finally outlined in § 5.

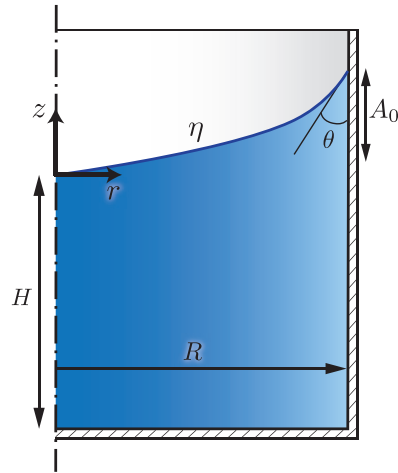


Figure 8.2: Geometry of the circular basin of internal radius R which is filled with a depth of liquid H . The interface η intersects the vertical wall with the dynamic contact angle θ . The amplitude A_0 is the maximum initial interface displacement.

8.2 Governing equations

Let us consider a cylindrical container of radius R filled to a depth H with a liquid of density ρ . A cylindrical coordinate system is defined, where z is the vertical direction corresponding to the axis of the container, and the zero is set at the unperturbed interface position at the centerline, r is the radial direction and ϕ is the azimuth (see Figure 8.2). The fluid motion associated to a displacement of the interface, η , is irrotational outside the viscous boundary layers at the walls and at the interface. In the inviscid limit, the fluid velocity is derived from a velocity potential Φ , which satisfies the continuity equation

$$\Delta\Phi = 0, \quad (8.4)$$

together with symmetry condition on the axis ($\Phi|_{r=0} = 0$) and the no penetration condition at the walls:

$$\left. \frac{\partial\Phi}{\partial r} \right|_{r=R} = 0, \quad \left. \frac{\partial\Phi}{\partial z} \right|_{z=-H/R} = 0. \quad (8.5)$$

In the following, quantities are made nondimensional by the radius, R , and the characteristic velocity \sqrt{gR} . At $z = \eta$, the kinematic boundary condition is such that no flow is allowed through the interface:

$$\frac{\partial\eta}{\partial t} = -\frac{\partial\Phi}{\partial r} \frac{\partial\eta}{\partial r} - \frac{1}{r^2} \frac{\partial\Phi}{\partial\phi} \frac{\partial\eta}{\partial\phi} + \frac{\partial\Phi}{\partial z} \quad \text{at } z = \eta, \quad (8.6)$$

and Laplace law prescribes the relation between the pressure, p , and the local curvature, $\chi(\eta)$, namely:

$$-p|_{\eta} = \frac{\chi(\eta)}{Bo} \quad \text{at } z = \eta, \quad (8.7)$$

where the Bond number prescribes the relative magnitude of interfacial effects and gravity $Bo = \rho g R^2 / \sigma$, where σ is the surface tension.

We turn to define the boundary condition at the contact line $\eta(r = 1, \phi, t)$, which plays a central role in our problem. Rather than the classic free-end edge condition $\partial\eta/\partial r|_{r=1} = 0$ or the Hocking law in eq. (8.3), we adopt a realistic contact line model with hysteresis, which is depicted in Figure 8.1b. Specifically, a range of hysteresis contact angle is added to the linear relation between dynamic contact angle, θ and contact line velocity $\partial\eta/\partial t|_{r=1}$:

$$\theta - \theta_s = \begin{cases} \alpha_A Ca \left. \frac{\partial\eta}{\partial t} \right|_{r=1} + \Delta/2 & \text{if } \left. \frac{\partial\eta}{\partial t} \right|_{r=1} > 0 \\ \alpha_R Ca \left. \frac{\partial\eta}{\partial t} \right|_{r=1} - \Delta/2 & \text{if } \left. \frac{\partial\eta}{\partial t} \right|_{r=1} < 0 \end{cases}, \quad (8.8)$$

where Δ is the size of the hysteresis and α_A and α_R are the slip coefficients of the advancing and receding meniscus. The contact angle is related to the interface through the geometrical relation:

$$\left. \frac{\partial\eta}{\partial r} \right|_{r=1} = \cot(\theta). \quad (8.9)$$

This model proposed by Dussan (1979) accounts for the dependence of the dynamic contact angle θ on the contact line velocity through the Capillary number $Ca = \mu\sqrt{Rg}/\gamma$ as observed in unidirectional flow experiments. Specifically, Rio *et al.* (2005); Le Grand *et al.* (2005) measured the dynamic contact angle at the contact line of sliding drops for various velocities and considering a wide range of silicone oil viscosity (10 – 1000cP). The experimental data for the low viscosity silicone oil 10cP are in good agreement with eq. (8.8) using the following values $\alpha_A = 45$ and $\alpha_R = 104$. Similar experiments on water drops were carried out by Puthenveetil *et al.* (2013) this time reporting $\alpha_A = 58$ and $\alpha_R = 108$. With a different experimental setup, Winkels *et al.* (2011) measured the receding contact angle in the dewetting phase of water in the immersion lithography yielding in $\alpha_R = 67$.

The contact angle hysteresis depends in on the roughness and chemical contamination of the solid surface, the presence of surfactants and polymers in the liquid, see De Gennes (1985) and Leger & Joanny (1992). In fact, Δ varies from few degrees to more than hundred depending on the application. We refer the reader to Samuel *et al.* (2011) and Law & Zhao (2016) for a comprehensive review on contact angle hysteresis.

For the sake of spinelessness, we set $\alpha = \alpha_R = \alpha_A$, meaning that the contact angle increases when the contact line advances exactly as the opposite as the contact angle decreases when the contact line recedes. We hope that this choice will help highlight the role of Δ in the problem (by opposition of differences between α_R and α_A). In this limit, equation (8.8) can be

written in the following compact form:

$$\theta - \theta_s = \alpha Ca \left. \frac{\partial \eta}{\partial t} \right|_{r=1} + \frac{\Delta}{2} \operatorname{sgn} \left(Ca \left. \frac{\partial \eta}{\partial t} \right|_{r=1} \right), \quad (8.10)$$

where sgn denotes the sign function that is negative one for negative argument and one for positive argument. Equation (8.10) reduces to the Hocking law (8.3) when the contact angle hysteresis Δ is set to zero. A similar model has also been proposed by Ting & Perlin (1995) and Jiang *et al.* (2004) to model the contact line hysteresis observed in their sloshing experiments. Note that even if the flow is considered inviscid in the domain, viscous forces balance capillary forces at the contact line. As a consequence, eq. (8.10) depends on the capillary number, $Ca = \mu \sqrt{Rg}/\sigma$. In the following, we use equation (8.10) to model the sloshing of capillary-gravity waves in a cylindrical basin.

8.3 Weakly nonlinear analysis

The system of equations introduced in the previous section is nonlinear and can not be solved analytically. We present here a weakly nonlinear analysis valid in the limit of small contact angle hysteresis, $\Delta = \epsilon^2 \hat{\Delta}$ and small $\alpha Ca = \epsilon \hat{\alpha}$. Let us consider the following asymptotic expansion:

$$\begin{aligned} \Phi &= \Phi_0 + \epsilon \Phi_1 + \epsilon^2 \Phi_2 + O(\epsilon^3), \\ \eta &= \eta_0 + \epsilon \eta_1 + \epsilon^2 \eta_2 + O(\epsilon^3), \\ p &= p_0 + \epsilon p_1 + \epsilon^2 p_2 + O(\epsilon^3), \\ \theta &= \theta_0 + \epsilon \theta_1 + \epsilon^2 \theta_2 + O(\epsilon^3). \end{aligned} \quad (8.11)$$

Substituting the expansion (8.11) in (8.4), (8.6), (8.7) and (8.10), a series of system of equations are obtained at the various orders in ϵ . At order ϵ^0 , the nonlinear problem associated with the shape of the static meniscus will be obtained. At order ϵ we recover the classic linear eigenvalue problem for the sloshing modes. Their frequencies correspond to the eigenvalues of this first order system. At the higher order ϵ^2 , an amplitude equation is obtained: $A(T)$ is a slow-time modulation that provides the weakly nonlinear correction to the first order solution accounting for our the contact line model. Moreover, in the spirit of multiple scales technique, a *slow* time scale is introduced which is related to the physical *fast* time scale according to: $T = \epsilon t$.

8.3.1 Order ϵ^0

At order ϵ^0 , the static base-state is retrieved. The potential Φ_0 is null everywhere in the domain and the pressure is hydrostatic, $p = -z$ in our non-dimensional scheme. The dynamic boundary condition (8.7) reduces to the equation for the static meniscus in radial coordinates,

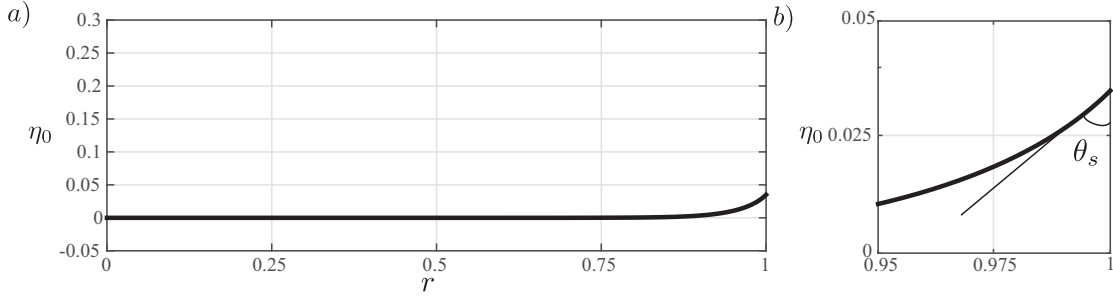


Figure 8.3: In (a) the static meniscus, η_0 , is shown as a function of the radial coordinate. In (b) the static contact line region is detailed.

which prescribes the zero-order interface deformation due to capillary effects:

$$-\eta_0 = -\frac{1}{Bo} \chi(\eta_0), \tag{8.12}$$

where $\chi(\eta_0) = (\eta_{0,rr} + \eta_{0,r}(1 + \eta_{0,r}^2)/r)(1 + \eta_{0,r}^2)^{-3/2}$ is the curvature of η_0 , which does not depend on the azimuth. The second-order equation (8.12) is completed with two boundary conditions. At the centerline, the static meniscus regularity condition

$$\left. \frac{\partial \eta_0}{\partial r} \right|_{r=0} = 0 \tag{8.13}$$

holds owing to axisymmetry. The contact line model (8.10), prescribes the boundary condition at $\eta_0(r = 1)$:

$$\theta_0 = \theta_s, \tag{8.14}$$

which sets

$$\left. \frac{\partial \eta_0}{\partial r} \right|_{r=1} = \cot(\theta_s). \tag{8.15}$$

Equation (8.12) is nonlinear in η_0 and is solved using an iterative Newton method, see Appendix 8.7.1 for details on the numerical method.

Figure 8.3(a) shows the static meniscus $\eta_0(r)$ in the case of $\theta_s = \pi/4$ and $Bo = 500$, which typically corresponds to the value one would obtain for $g = 9.81 \text{ m/s}^2$ with a glass (here $R = 0.05 \text{ m}$) filled with water ($\rho = 10^3 \text{ kg/m}^3$, $\mu = 10^{-3} \text{ kg/(ms)}$, $\sigma = 70 \text{ mN/m}$). The interface does not depend on H and is basically flat in the domain aside from a region close to the wall spanning over at a distance of the order of the capillary length, $\sqrt{\sigma/\rho g} \approx 0.05 R$ here. In Fig. 8.3(b) equal axis are used to show that η_0 intersect the wall with the prescribed static contact angle $\theta_s = \pi/4$. We now turn to the next order.

8.3.2 Order ϵ

At order ϵ the potential, Φ_1 , satisfies the first order continuity equation:

$$\Delta\Phi_1 = 0, \quad (8.16)$$

with symmetry condition on the axis and no penetration condition at the vertical and bottom walls. From the unsteady Bernoulli equation, the first order dynamic condition (8.7) flattened at η_0 is given by:

$$\left. \frac{\partial\Phi_1}{\partial t} + \eta_1 - \frac{1}{Bo} \frac{\partial\chi(\eta)}{\partial\eta} \right|_{\eta_0} \eta_1 = 0 \quad \text{at } z = \eta_0, \quad (8.17)$$

where the last term is the first-order variation of the curvature $\chi(\eta)$ associated with a small perturbation $\epsilon\eta_1$:

$$\left. \frac{d\chi(\eta)}{d\eta} \right|_{\eta_0} \eta_1 = \underbrace{\frac{(1 + \eta_{0,r}^2) - 3r\eta_{0,r}\eta_{0,rr}}{(1 + \eta_{0,r}^2)^{5/2}}}_{a(r)} \frac{1}{r} \frac{\partial\eta_1}{\partial r} + \underbrace{\frac{1}{(1 + \eta_{0,r}^2)^{3/2}}}_{b(r)} \frac{\partial^2\eta_1}{\partial r^2} + \underbrace{\frac{1}{(1 + \eta_{0,r}^2)^{1/2}}}_{c(r)} \frac{1}{r^2} \frac{\partial^2\eta_1}{\partial\phi^2}. \quad (8.18)$$

Then, the first order kinematic boundary condition reads:

$$\left. \frac{\partial\eta_1}{\partial t} = - \frac{\partial\Phi_1}{\partial r} \right|_{\eta_0} \frac{\partial\eta_0}{\partial r} + \left. \frac{\partial\Phi_1}{\partial z} \right|_{\eta_0} \quad \text{at } z = \eta_0, \quad (8.19)$$

where the radial and the vertical derivative of the potential Φ_1 correspond to the radial and vertical velocity at $z = \eta_0$. The term $\partial\eta_0/\partial r$ is the radial derivative of the zero-order interface obtained at previous order. The contact line condition at ϵ is $\theta_1 = 0$, which implies:

$$\left. \frac{\partial\eta_1}{\partial r} \right|_{r=1} = 0, \quad (8.20)$$

and corresponds to the free-edge boundary condition.

By defining the state variable $\mathbf{q}_1 = (\Phi_1, \eta_1)$, the system of equations can be written in compact form using equations (8.16) and (8.17) as state equations:

$$(\partial_t \mathcal{B} - \mathcal{A}) \mathbf{q}_1 = \mathbf{0}, \quad (8.21)$$

where the linear operators are defined by:

$$\mathcal{B} = \begin{pmatrix} 0 & 0 \\ I_\eta & 0 \end{pmatrix}, \quad \mathcal{A} = \begin{pmatrix} \Delta & 0 \\ 0 & I - \frac{1}{Bo} \left. \frac{\partial\chi(\eta)}{\partial\eta} \right|_{\eta_0} \end{pmatrix}. \quad (8.22)$$

Equation (8.21) is subject to the boundary conditions at the interface (8.19) and at the contact line (8.20). In addition, the axisymmetry condition $\Phi_1 = 0|_{r=0}$ is imposed on the axis, along with the no penetration condition at the solid walls, ($\left. \frac{\partial\Phi_1}{\partial r} \right|_{r=1} = 0$ and $\left. \frac{\partial\Phi_1}{\partial z} \right|_{z=-H} = 0$). The

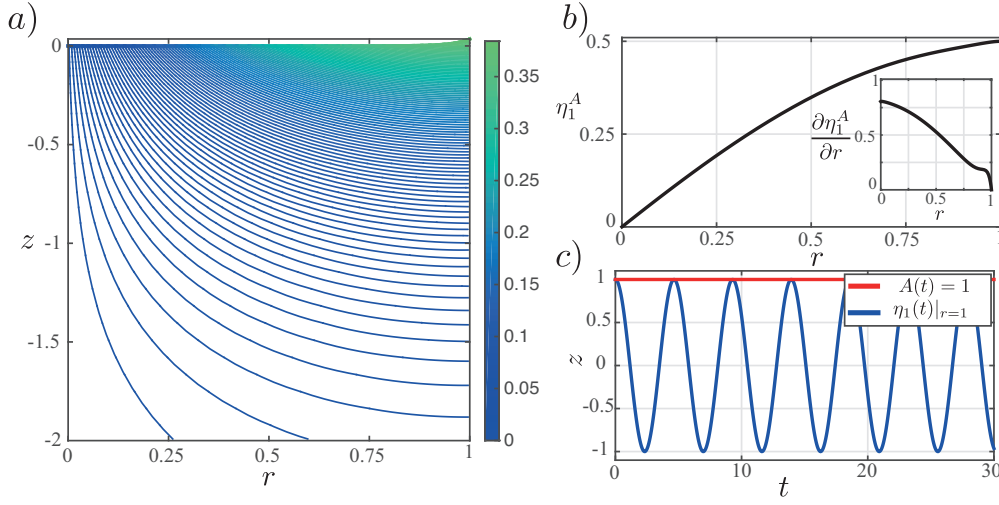


Figure 8.4: First order problem solution for the reference case. (a) shows hundred isolines of the potential Φ_1^A are shown. In (b) the first order interface η_1^A is shown along with its radial derivative in the inset. The first order contact line motion is reported in (c), where the amplitude has been set to one.

solution of eq. (8.21) then reads:

$$\mathbf{q}_1 = A(T)\mathbf{q}_1^A e^{i\omega t} e^{in\phi} + c.c., \quad (8.23)$$

where *c.c.* stands for the complex conjugate. The amplitude $A(T)$ is a slow modulation of the flow which depends on the slow time scale T , and will be determined at the next order. The integer n is the azimuthal wavenumber, and the eigenvalue $i\omega$ is associated with the eigenvector \mathbf{q}_1^A such that:

$$(i\omega\mathcal{B} - \mathcal{A})\mathbf{q}_1^A = \mathbf{0}, \quad (8.24)$$

with $\mathbf{q}_1^A = (\Phi_1^A, \eta_1^A)$. The linear operators \mathcal{B} and \mathcal{A} are discretized by mean of Chebyshev collocation method, where a two-dimensional mapping is used to map the computational space to the physical space that has a curved boundary due to the static meniscus η_0 . We refer to Appendix 8.7.2 for details on the numerical method and the associated convergence study.

In figure 8.4(a) the potential Φ_1^A is shown for the reference case of $Bo = 500$, $\theta_s = \pi/4$, $H = 3R$ and $n = 1$. We observe that the spatial gradients of Φ_1^A , which are connected with the spatial variation of the velocity, are higher at the meniscus region where the domain curves. In contrast, the potential becomes smooth far from the interface in agreement with classic sloshing theory, which predicts an exponential decay of the wave velocity moving away from the interface. Note that the values reported in the colorbar depends on the normalization of the eigenvector \mathbf{q}_1^A defined up to a multiplicative factor. Without loss of generality, the eigenvector is normalized here by imposing that $\eta_1^A(1) = 0.5$, hence η_1^A a real vector and Φ_1^A is a purely imaginary field. In Figure 8.4(b) the interface η_1^A is shown. According to the boundary conditions at the centerline and at the wall, η_1^A is zero at the centerline and intersects the

container walls orthogonally.

Figure 8.4(c) shows the contact line motion for the case where the slow evolving amplitude $A(T)$ has been arbitrarily set to one (and will be determined in the next section). Since the flow is inviscid, the contact line keeps oscillating without ever being damped as there is no dissipation mechanism at play yet. The eigenvalue ω is thus a real number, which corresponds to the frequency of sloshing. In our reference case we find $\omega = 1.35$ and the imaginary part is zero to machine precision. This frequency differs slightly from the one computed with the analytical formula (8.1) for $n = 1$ ($\omega_{\theta_s=\pi/2} = 1.36$) as the static contact angle is different from $\pi/2$, see Appendix 8.7.2 for further discussions.

8.3.3 Order ϵ^2

At order ϵ^2 , the second-order continuity equation reads:

$$\Delta\Phi_2 = 0, \quad (8.25)$$

where Φ_2 is the second-order velocity potential, which is symmetric with respect to the axis and satisfies the no-penetration condition at the container boundaries. This equation is similar to the first order governing equation (8.16) due to the linearity of the continuity equation (8.4). In contrast, the dynamic condition (8.7) applied to η_2 differs from the one at the previous order:

$$\left. \frac{\partial\Phi_2}{\partial t} + \eta_2 - \frac{1}{Bo} \frac{\partial\chi(\eta)}{\partial\eta} \right|_{\eta_0} \eta_2 = -\frac{\partial\Phi_1}{\partial T} + NRT, \quad (8.26)$$

where forcing terms SloshWaterAppeAr on the right hand side (rhs). According to the definition of $\mathbf{q}_1 = (\Phi_1, \eta_1)$ in eq. (8.23), the term $\partial\Phi_1/\partial T$ is the slow time variation of the first order solution which oscillates at system natural frequency determined at the previous order. The terms coming from second-order corrections of both the curvature and the pressure do not resonate. They are quadratic thus not relevant for the further analysis. Consequently, these non resonant terms are not explicitly written in (8.26) but instead are denoted NRT . We anticipate that, in order to determine the complex amplitude $A(T)$ at this order, a compatibility condition involving only the resonating terms will be used. Similarly to what was done for the dynamic condition (8.26), we derive the kinematic condition

$$\left. \frac{\partial\eta_2}{\partial t} + \frac{\partial\Phi_2}{\partial r} \right|_{\eta_0} \eta_{0,r} - \left. \frac{\partial\Phi_2}{\partial z} \right|_{\eta_0} = -\frac{\partial\eta_1}{\partial T} + NRT, \quad (8.27)$$

where $\partial\eta_1/\partial T$ is the slow time modulation of the interface motion and NRT gathers all the non resonating terms. At this point, the nonlinear contact angle correction due to the contact line model enters in the analysis:

$$\theta_2 = \hat{\alpha} \frac{\partial\eta_1}{\partial t} + \frac{\hat{\Delta}}{2} \operatorname{sgn} \left(\frac{\partial\eta_1}{\partial t} \right) \Big|_{r=1}, \quad (8.28)$$

Chapter 8. Nonlinear friction in sloshing dynamics: partial wetting

where $\hat{\Delta}$ is the rescaled size of the contact angle hysteresis, $\Delta = \epsilon^2 \hat{\Delta}$, and $\hat{\alpha}$ is the rescaled slip coefficient, $\alpha Ca = \epsilon \hat{\alpha}$. The second-order angle correction θ_2 in equation (8.28) is related to η_2 and to the static contact angle, θ_s , through the geometrical relation:

$$\left. \frac{\partial \eta_2}{\partial r} \right|_{r=1} = \frac{-\theta_2}{\sin^2(\theta_s)}. \quad (8.29)$$

In order to impose a compatibility condition, that is needed to determine the amplitude $A(T)$ in equation (8.23), the terms oscillating at the natural frequency in the contact line model (8.28) have to be considered, as done for the dynamic and kinematic conditions (8.26)–(8.27). However the sign function is nonlinear and not purely harmonic, but through the Fourier series its ω -harmonic may be isolated (see Nayfeh (2008)):

$$\text{sgn}\left(\frac{\partial \eta_1}{\partial t}\right) = \text{sgn}\left(i\omega A \eta_1^A e^{i\omega t + n\phi} + c.c.\right) = \sum_{k=-\infty}^{\infty} d_k(\phi) e^{ik\omega t} \quad (8.30)$$

The complex amplitude and η_1^A can be decomposed in module and phase, namely: $A(T) = |A(T)|e^{i\beta(T)}$ and $\eta_1^A = |\eta_1^A|e^{i\beta_\eta}$. By defining the quantity $\xi = \omega t + n\phi + \frac{\pi}{2} + \beta_\eta + \beta(T)$, the coefficient d_k is given by:

$$d_k(\phi) = \frac{\omega}{2\pi} \int_{-\frac{4\pi}{\omega}}^{\frac{4\pi}{\omega}} \text{sgn}(\cos(\xi)) e^{-ik\omega t} dt = e^{ik(n\phi + \pi/2 + \beta_\eta + \beta(T))} \underbrace{\frac{1}{2\pi} \int_{-\pi}^{\pi} \text{sgn}(\cos(\xi)) e^{-ik\xi} d\xi}_{c_k}. \quad (8.31)$$

Consequently, the nonlinear term reads:

$$\text{sgn}\left(\frac{\partial \eta_1}{\partial t}\right) = \sum_{k=-\infty}^{\infty} c_k e^{ik\xi} = c_1 e^{i(\omega t + n\phi + \pi/2 + \beta_\eta + \beta(T))} + c.c. + NRT, \quad (8.32)$$

where we have isolated the harmonic oscillating at the sloshing natural frequency. The Fourier coefficient c_1 is equal to:

$$c_1 = \frac{1}{2\pi} \int_{-\pi}^{\pi} \text{sgn}(\cos(\xi)) e^{-i\xi} d\xi = \frac{2}{\pi}. \quad (8.33)$$

By substituting equation (8.32) in the ϵ -order contact line model (8.29) we have

$$\left. \frac{\partial \eta_2}{\partial r} \right|_{r=1} = -\frac{\hat{\alpha}}{\sin^2(\theta_s)} i\omega \eta_1^A A e^{i\omega t} e^{in\phi} - \frac{i\hat{\Delta}}{\pi \sin^2(\theta_s)} \frac{\eta_1^A}{|\eta_1^A|} \frac{A}{|A|} e^{i\omega t} e^{in\phi} \Big|_{r=1} + c.c. + NRT, \quad (8.34)$$

where the first term on the rhs is associated to the linear part of the contact line model (8.10) and provides a correction to the dynamic contact angle that is found proportional to the contact line velocity. The second term in the rhs is nonlinear with respect of the contact line velocity. Its origin is attributed to the contact angle hysteresis. Specifically, this term only depends on the phase of the velocity, a result consistent with the use of the sgn function that only depends on the sign of its argument. As a result, this term provides a different correction if the interface is advancing or receding.

In compact form, the second order problem is written as:

$$(\partial_t \mathcal{B} - \mathcal{A}) \mathbf{q}_2 = \mathcal{F}_2, \quad (8.35)$$

where \mathcal{A} is here subjected to the non-homogeneous boundary conditions (8.27) and (8.34). The forcing term on the rhs is:

$$\mathcal{F}_2 = - \left(\begin{array}{c} 0 \\ \partial \Phi_1 / \partial T |_{\eta_0} \end{array} \right) = - \underbrace{\frac{\partial A}{\partial T} \left(\begin{array}{c} 0 \\ \Phi_1^A |_{\eta_0} \end{array} \right)}_{\mathcal{F}_2^A} e^{i\omega t} e^{in\phi} + c.c. \quad (8.36)$$

This forcing term, along with the forcing terms in the boundary conditions (8.27) and (8.34), can resonate and induce a flow response that diverges as time increases. Hence, a compatibility condition has to be imposed in order to have a non-resonating particular solution to (8.36) of the type $\mathbf{q}_2 = \hat{\mathbf{q}}_2 e^{i\omega t} e^{in\phi} + c.c.$ and therefore preserve the asymptotic expansion scheme. By substituting this expression in the second order problem (8.35) we get:

$$(i\omega \mathcal{B} - \mathcal{A}) \hat{\mathbf{q}}_2 = \mathcal{F}_2^A. \quad (8.37)$$

This equation has a non-trivial solution if and only if \mathcal{F}_2^A is orthogonal to the adjoint mode \mathbf{q}^\dagger , according to Fredholm alternative. The adjoint global mode \mathbf{q}^\dagger is the solution of the adjoint equations:

$$(\partial_t \mathcal{B}^\dagger - \mathcal{A}^\dagger) \mathbf{q}^\dagger = \mathbf{0}, \quad (8.38)$$

where the linear operators \mathcal{A}^\dagger and \mathcal{B}^\dagger are derived by integrating by parts the system of equations (8.21). We refer to Appendix 8.6 for the complete derivation of the adjoint equations and the definition of the adjoint mode. The resulting compatibility condition reads:

$$\langle \mathbf{q}^\dagger, (\partial_t \mathcal{B} - \mathcal{A}) \hat{\mathbf{q}}_2 \rangle = \langle \mathbf{q}^\dagger, \mathcal{F}_2^A \rangle. \quad (8.39)$$

where the brackets $\langle \rangle$ define the Hermitian scalar product (8.52). By substituting the expression for \mathcal{F}_2^A from (8.36), we obtain

$$\langle \mathbf{q}^\dagger, \mathcal{F}_2^A \rangle = - \frac{\partial A}{\partial T} \int_{\eta_0} \bar{\eta}^\dagger \Phi_1^A d\eta_0, \quad (8.40)$$

where the symbol \int_{η_0} denotes a surface integral on the zero-order surface $\eta_0(r)$ with $d\eta_0 = r dz \sqrt{1 + \eta_{0,r}^2}$, as detailed in Appendix 8.6. Furthermore, the lhs of equation (8.39) is non-zero because the kinematic and the contact line conditions are not homogeneous at second order:

$$\langle \mathbf{q}^\dagger, (\partial_t \mathcal{B} - \mathcal{A}) \hat{\mathbf{q}}_2 \rangle = \underbrace{\langle (\partial_t \mathcal{B}^\dagger - \mathcal{A}^\dagger) \mathbf{q}^\dagger, \hat{\mathbf{q}}_2 \rangle}_{=0} + \int_{\eta_0} \bar{\Phi}^\dagger \frac{\partial A \eta_1^A}{\partial T} d\eta_0 - \frac{\sin^3 \theta_s}{Bo} \eta^\dagger \frac{\partial \eta_2}{\partial r} \Big|_{r=1},$$

(8.41)

where the integral on the free surface η_0 comes from the slow time derivative in the second-order kinematic condition (8.27), and the last term is associated with the contact line model. The detailed calculation yielding these boundary and corner terms are reported in Appendix 8.6.

8.3.4 Amplitude equation

Introducing finally the auxiliary constant κ and the two real damping coefficients ζ and χ , defined as

$$\kappa = (\bar{\eta}^\dagger \eta_1^A)_{r=1} / \int_{\eta_0} \bar{\eta}^\dagger \Phi_1^A + \Phi_1^\dagger \eta_1^A d\eta_0, \quad \zeta = \frac{\omega \sin(\theta_s) \hat{\alpha} \kappa}{Bo}, \quad \chi = \frac{\sin(\theta_s) \hat{\Delta} \kappa}{\pi Bo |\eta_1^A|}, \quad (8.42)$$

the substitution of expression (8.34) in equation (8.41) yields the compatibility condition (8.39)

$$\frac{\partial A}{\partial T} + \zeta A + \chi A/|A| = 0, \quad (8.43)$$

This nonlinear amplitude equation is the main result of this paper: it dictates the relaxation dynamics caused by the contact line dissipation. The effective damping SloshWaterAppeArs as the sum of a linear contribution, weighted by the linear damping coefficient ζ , resulting from the linear part of the contact line model and a nonlinear contribution, scaled by the nonlinear damping coefficient χ , originating in the contact line hysteresis.

By decomposing the complex amplitude in module and phase, $A(T) = |A(T)|e^{i\beta(T)}$, equation (8.43) can be integrated analytically:

$$|A(T)| = \left(A_0 + \frac{\chi}{\zeta} \right) e^{-\zeta T} - \frac{\chi}{\zeta}, \quad \beta(T) = \beta_0, \quad (8.44)$$

where A_0 and β_0 depend on the initial condition. Equation (8.44) represents the weakly non linear correction to the first-order solution (8.23) associated with the contact line model (8.10), yielding the contact line motion:

$$\eta_1|_{r=1} = 2\epsilon |A(t)| |\eta_{1|r=1}^A| \cos(\omega t + \beta_0 + n\phi + \beta_\eta). \quad (8.45)$$

Specifically, $|A(t)|$ is the nonlinear correction on the amplitude, and β_η is the phase of $\eta_{1|r=1}^A$, which is nil due to way the eigenmode \mathbf{q}_1^A has been normalized. It should be noted that η_1^A , β_η and $A(t)$ depend on the normalization of the direct mode, albeit the final result η_1 does not.

We next consider, as a illustrative example, the dynamics of the fundamental sloshing mode, $n = 1$, following an initial deflection of the interface of amplitude $A_0 = 0.1$ from rest ($\beta_0 = 0$) for the set of representative parameters chosen throughout this section. The Bond number and the static contact angle are equal to $Bo = 500$ and $\theta_s = \pi/4$, and the contact line

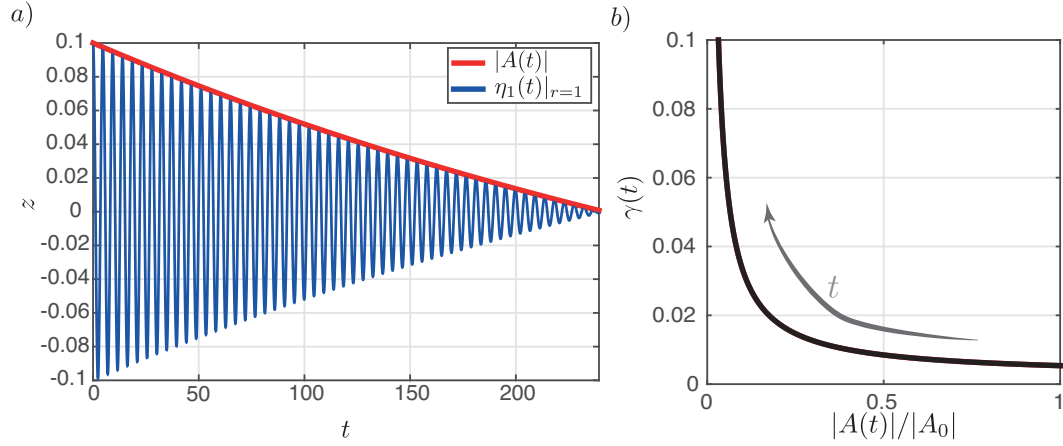


Figure 8.5: Contact line motion (blue line) modulated by the slow time amplitude (red line) is shown in a). In b) the corresponding capillary damping versus the wave amplitude.

model parameters are set to $Ca = 0.01$, $\alpha = 60$ and $\Delta = 10^\circ$. Figure 8.5a shows the second order contact line motion by a blue line, whereas the red line corresponds to the envelope $|A(t)|$. One can first note that the sloshing frequency is not modified at leading order by the nonlinear contact line dynamics. Regarding the amplitude, in contrast to the first order solution (Figure 8.4c), the contact line motion is damped. Moreover, the wave attenuation is not uniform during the sloshing time and the instantaneous damping rate

$$\gamma(t) = -\frac{d \log(|A(t)|/A_0)}{dt} = \frac{e\zeta}{1 - e^{e\zeta t}/(1 + A_0\zeta/\chi)}, \quad (8.46)$$

that is reported in Figure 8.5b depends on the wave amplitude, as typical in nonlinear systems.

8.4 Discussion

The theoretical multiple scale analysis presented in the previous section has revealed the nonlinear nature of the sloshing motion associated to the contact line hysteretic dynamics. In this section, we take advantage of this theoretical framework and study the dynamics of the fundamental sloshing mode, $n = 1$, following an initial perturbation A_0 of the interface (Fig. 8.2) as a function of several macroscopic parameters.

8.4.1 Effect of contact angle hysteresis

We focus here on the influence of the contact angle hysteresis Δ on both $|A(t)|$ and $\gamma(t)$. To this end, the governing parameters of the system, namely the Bond number, Bo , the static contact angle, θ_s , the slip coefficient, α , the initial contact line deflection, A_0 , and the capillary number, Ca , are set to the reference values used in section 8.3. Therefore, only the value of the contact angle hysteresis Δ is varied.

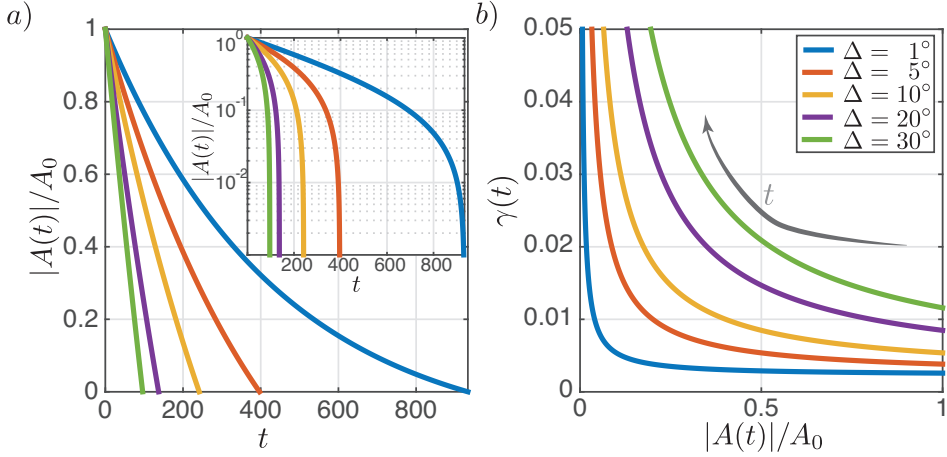


Figure 8.6: a) Amplitude modulation versus time. Each note correspond to a specific contact angle hysteresis ranging from 1° to 30° . In the inset the same quantities are reported in logarithmic scale to emphasize their singular behavior. b) Shown is the damping rate originating from capillary effects, plotted as a function of the oscillation amplitude relative to the initial perturbation.

Figure 8.6a shows the relative sloshing amplitude $|A(t)|/A_0$ as a function of time for different values of the contact angle hysteresis Δ . As evident from the logarithmic decrement $\log(|A(t)|/A_0)$ (inset) two regimes may be identified. At first the amplitude decays roughly exponentially, as evidenced by the linear aspect of the plot, with an initial damping rate

$$\gamma(t=0) = -c\zeta - \frac{\epsilon\chi}{A_0}. \quad (8.47)$$

There are therefore two contributions to the damping rate prevailing at initial times: in addition to the expected source of damping associated to the linear contact line friction, which is proportional to α through ζ , the contact line hysteresis also contributes to damp the motion already from the beginning of the motion through a contribution which is proportional to the contact angle hysteresis Δ through χ and inversely proportional to the initial amplitude A_0 . The limiting behavior close to $A = 0$ can also be analyzed: eq. (8.46) reveals that exists a finite time t^* such that the damping rate diverges

$$\gamma(t=t^*) \rightarrow \infty, \quad (8.48)$$

with,

$$t^* = \frac{1}{c\zeta} \log\left(1 + \frac{\zeta}{\chi} A_0\right). \quad (8.49)$$

Moreover, it is seen from eq. (8.44) that the finite time singularity of the damping rate yields the sloshing amplitude to vanishes and becomes exactly zero at t^* . By recalling that $\chi \propto \Delta$ (see eq. (8.42)), we can conclude that the hysteresis is at the origin of the finite time arrest of the motion. Indeed, if Δ is set to zero the system relaxes exponentially with damping rate

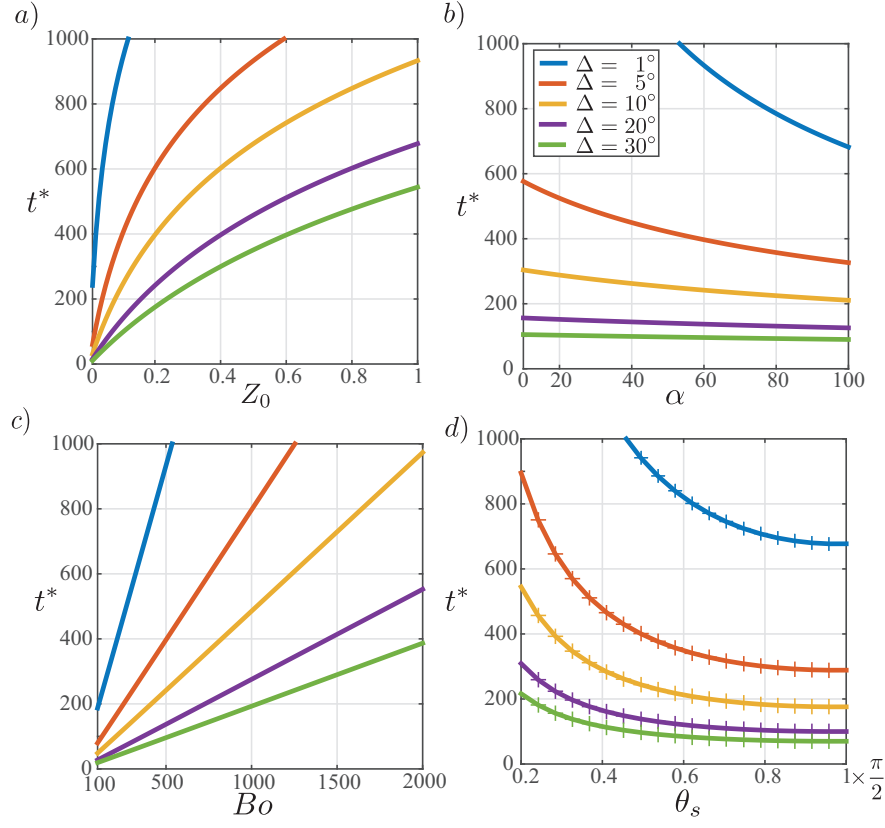


Figure 8.7: Finite time of arrest t^* is reported as a function of a) the Bond number, b) the static contact angle, c) the slip coefficient and d) the initial contact line displacement. The + symbols displayed in (d) correspond to t^* computed with a finer mesh (see Appendix 8.7), showing convergence with respect to grid resolution.

$\epsilon\zeta$ and t^* diverges. On the other hand, even a small a value of the contact angle hysteresis as small as 1° is enough to introduce a significant dissipative effect that largely impacts the dynamics, in particular leading its arrest in finite time. The contact angle hysteresis therefore both contributes to increase the initial damping rate and to hasten the finite time arrest.

8.4.2 Time of arrest: parametric study

We now turn to investigate the parametric dependence of the time of arrest, t^* on the physical parameters of the problem. To this end, we use the configuration introduced in section 8.3 as a reference and subsequently vary the Bond number, Bo , the static contact angle, θ_s , as well as the contact line model parameters, αCa and Δ , and the set of the initial condition, A_0 . Using our previous results from section 8.3 we anticipate that the first order solution depends only on the static contact angle θ_s and on the Bond number Bo . On the other hand, the contact line model parameters αCa and Δ , and the initial condition A_0 only affect the solution at second

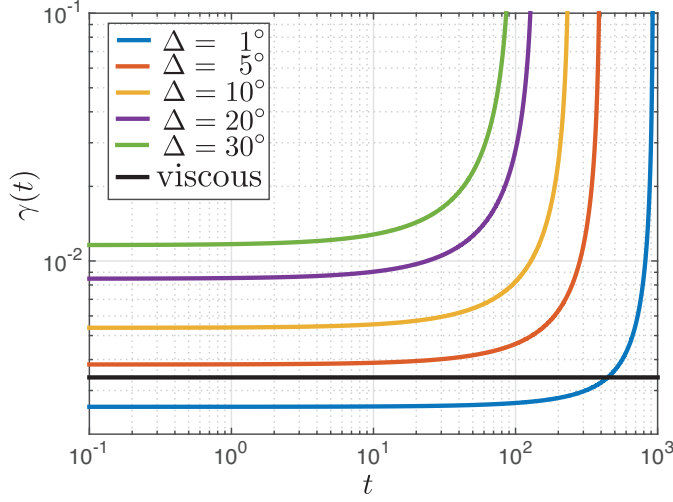


Figure 8.8: Comparison between the capillary damping rate versus time for different contact angle hysteresis and the viscous damping (horizontal black line).

order.

Using the definition of ζ and χ in equation (8.49), we obtain a scaling law for t^* :

$$t^* \propto \frac{Bo}{\omega \kappa \sin(\theta_s)} \frac{1}{\alpha Ca} \log \left(1 + e \frac{\alpha Ca \omega A_0}{\Delta} \right). \quad (8.50)$$

In Fig. 8.7 we show the variation of t^* as a function of the key parameters of the problem. The time of arrest evidently increases with the initial interface deflection A_0 . In effect, A_0 sets the initial energy of the system, which has to be entirely dissipated in order to reach the rest configuration. Therefore, a higher A_0 requires a longer time before the interface comes back to rest. However, due to the logarithmic dependence of t^* with respect to A_0 in eq. (8.50), the time of arrest increases less than linearly with A_0 as evident from the concave down curves reported in Fig. 8.7a. Regarding the slip coefficient, α , an increase of its value α yields an increase of the damping rate and in turn a decrease of t^* . This result remains true for all the values of Δ considered (see Fig. 8.7b).

Since the frequency ω and the scalar quantity κ (see eq. (8.42)) arise from the first order problem, they both depend in a complex way on the static angle, θ_s , and the Bond number, Bo . For this reason, the scaling law for t^* with respect to θ_s and Bo cannot be in principle immediately deduced from equation (8.50). However, we have found that both ω and κ do not vary significantly with respect to θ_s and Bo , as illustrated by figure 8.7c, which shows a linear dependence of t^* with the Bond number and corroborated by figure 8.7d, which suggests that the time of arrest decreases when the static contact angle θ_s is decreased, according to the ratio $Bo/\sin(\theta_s)$ in equation (8.50).

Finally, from the respective position of all curves in Figure 8.7 relative to the value of hysteresis parameter Δ , we deduce that an increase of the contact angle hysteresis always anticipate the arrest of sloshing, in consistence with expression (8.50).

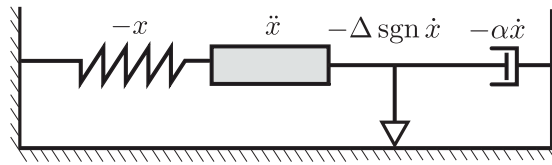


Figure 8.9: Schematic of the sloshing system with hysteresis.

8.4.3 Comparison with the theory of Case & Parkinson (1957)

Our approach to sloshing demonstrates that capillary effects at the contact line and, in particular, the hysteresis of the contact angle have a dissipative effect on the dynamics of sloshing in a container. This result is in line with experimental evidence (Keulegan, 1959; Cocciaro *et al.*, 1991) where the measured damping rate significantly exceeds the viscous damping rate of Case & Parkinson (1957). In Figure 8.8 the capillary damping for the reference case introduced in section 8.3 is shown for different values of Δ spanning from 1° to 30° . We recall that here the slip coefficient $\alpha = 60$ has been set according to the available experimental data for unidirectional steady flow. In the same figure, the horizontal black line depicts the corresponding viscous damping rate, which in the case of deep-water tank is given by $\gamma_\mu = 0.56\omega\sqrt{Ca/Bo}$, see Ibrahim (2005). As observed in section 8.3.4, the capillary damping is roughly constant at early time where the wave amplitude is large and its magnitude increases with contact angle hysteresis. A contact line hysteresis of Δ as small as 5° is already sufficient to surpass the pure viscous damping, dominated by the contribution of the wall Stokes layers Case & Parkinson (1957). In addition, the capillary damping significantly increases at later time when the amplitude of oscillation diminishes. Even for small values of Δ , there exists a time such that the capillary damping becomes larger to the usual viscous damping leading to the arrest of the motion.

8.5 Conclusions

In this work we have presented a novel weakly nonlinear formulation which takes into account the effect of contact angle hysteresis on inviscid surface capillary-gravity waves in a circular cylinder. To this aim, a contact line model which was derived experimentally in the framework of unidirectional flows (Dussan (1979); Rio *et al.* (2005); Le Grand *et al.* (2005)) is adopted as boundary condition at the contact line. In our asymptotic expansion the static meniscus shape in a cylindrical geometry is given at zero order. At next order the linear problem satisfied by the sloshing gravity-capillary waves is obtained. The resulting global modes are neutrally stable because any dissipation source is present at zero and first order. Thus in the spirit of multiple scale analysis, a slow amplitude and phase modulations are obtained at second order which correspond to the weakly nonlinear correction accounting for the capillary effects at the contact line. The phase modulation is not affected at first order, meaning that capillary effects do not affect significantly the sloshing frequency. This result is in line with experimental

observation of Keulegan (1959) and Cocciaro *et al.* (1991, 1993). Capillary effects however have a dramatic influence on damping rate: the amplitude modulation results in a significant attenuation of the first order waves. Indeed, according to the amplitude equation (8.43) the capillary dissipation has two contributions: (i) a nonlinear one related with the contact angle hysteresis and (ii) a linear part due to the linear dependence between the contact angle and the contact line velocity. The capillary damping rate in our analysis depends on the wave amplitude consistently with the experimental observation of Keulegan (1959); Cocciaro *et al.* (1991) and is practically uniform when the wave amplitude is large: it results from the combined action of the linear dynamical contact angle law and the hysteresis. The damping rate eventually increases significantly at small amplitudes, as a consequence of the hysteresis contribution.

In contrast to the viscous damping where the wave motion decays until infinite time, the capillary damping yields a *finite time arrest*, i.e. the capillary damping stops the fluid sloshing after a finite amount of time. A similar result has been found in the case of sloshing biphasic system, where the fluid column is surmounted by a thin layer of foam Viola *et al.* (2016b). We have determined an explicit approximated formula expressing the time of arrest as a function of the Bond number, the Capillary number, the static contact angle and the contact line model parameters is a result of the asymptotic analysis. Specifically the time of arrest is positively correlated with the Bond number and with the initial deflection of the contact line. The time of arrest decreases when the static contact angle increases (keeping constant the other parameters of the contact line model, namely α and Δ). On the other hand, an increase of the slip coefficient α and the contact angle hysteresis Δ are both associated with an augmented damping rate which anticipates the time of arrest.

The origin of this time arrest can be explained by noticing that the system behaves as an oscillator damped by viscous and solid friction, see Figure 8.9. Indeed, the amplitude equation (8.43) describes the oscillation x ruled by the equation:

$$\ddot{x} + x + \alpha \dot{x} + \Delta \operatorname{sgn} \dot{x} = 0, \quad (8.51)$$

with the friction coefficients α and Δ of the order of a small parameter ϵ . This means that the hysteresis term acts as Coulomb solid friction. An equation similar to (8.51) has been used by Noblin *et al.* (2004) to model the contact line dynamics of sessile drop subjected to vibrations. Our current work aims at analyzing the role of the contact line dynamics on harmonically forced sloshing dynamics by quantifying its effect on the nonlinear transfer function.

We finally note that the weakly nonlinear stability analysis carried out here provides a general framework to account for capillary effects in the surface gravity-capillary waves in a container. Indeed, contact line models other from the one used here can be introduced in the formulation.

8.6 Appendix: Adjoint equations

In this section we determine the adjoint equations to the first order problem (8.24), associated with the Hermitian scalar product:

$$\langle \mathbf{q}_\alpha, \mathbf{q}_\beta \rangle = \int_{\Omega} \overline{\Phi}_\alpha \Phi_\beta d\Omega + \int_{\eta_0} \overline{\eta}_\alpha \eta_\beta d\eta_0, \quad (8.52)$$

where the overline symbol designates the complex conjugate. The first term is a weighted volume integral with $d\Omega = r dr dz$. The second one corresponds to a surface integral on the zero-order surface $\eta_0(r)$ with $d\eta_0 = r dz \sqrt{1 + \eta_{0,r}^2}$. In this section we will demonstrate that the first-order system of equations and boundary conditions are self-adjoint with respect to the scalar product (8.52).

By definition, the adjoint operator of the direct operator $i\omega\mathcal{B} - \mathcal{A}$, satisfies:

$$\langle \mathbf{q}^\dagger, (i\omega\mathcal{B} - \mathcal{A})\mathbf{q} \rangle = \langle (i\omega_0^\dagger\mathcal{B}^\dagger - \mathcal{A}^\dagger)\mathbf{q}^\dagger, \mathbf{q} \rangle. \quad (8.53)$$

where $\mathbf{q}^\dagger = (\Phi^\dagger, \eta^\dagger)$ is a vector. Hence, the adjoint operator $i\omega_0^\dagger\mathcal{B}^\dagger - \mathcal{A}^\dagger$ is derived by integration by parts, transferring the differential operators from the vector \mathbf{q} to the vector \mathbf{q}^\dagger . The boundary conditions for the adjoint operator are chosen so as to nullify the boundary integrals coming from the integration by parts. The rhs of equation (8.53) reads:

$$\int_{\Omega} \overline{\Phi}^\dagger \Delta\Phi d\Omega + \int_{\eta_0} \overline{\eta}^\dagger \left(i\omega\Phi + \eta - \frac{1}{Bo} \left[\frac{a(r)}{r} \frac{\partial\eta}{\partial r} + b(r) \frac{\partial^2\eta}{\partial r^2} + \frac{c(r)}{r^2} \frac{\partial^2\eta}{\partial\theta^2} \right] \right) \frac{d\eta_0}{\sqrt{1 + \eta_{0,r}^2}} = 0, \quad (8.54)$$

and integrating by parts we get:

$$\begin{aligned} & \int_{\Omega} \Delta\overline{\Phi}^\dagger \Phi d\Omega + \int_{\partial\Omega} \overline{\Phi}^\dagger \nabla\Phi \cdot \mathbf{n} dS - \int_{\partial\Omega} \Phi \nabla\overline{\Phi}^\dagger \cdot \mathbf{n} dS \\ & + \int_{\eta_0} -i\omega\overline{\eta}^\dagger \Phi r dr + \int_{\eta_0} \left(\overline{\eta}^\dagger - \frac{1}{Bo} \left[\frac{a(r)}{r} \frac{\partial\overline{\eta}^\dagger}{\partial r} + b(r) \frac{\partial^2\overline{\eta}^\dagger}{\partial r^2} - \frac{n^2 c(r)}{r^2} \overline{\eta}^\dagger \right] \right) \eta r dr \\ & - \frac{1}{Bo} \left[r b(r) \left(\overline{\eta}^\dagger \frac{\partial\eta}{\partial r} - \frac{\partial\overline{\eta}^\dagger}{\partial r} \eta \right) \right]_{r=0}^{r=1} = 0. \end{aligned} \quad (8.55)$$

The first integral comes from the integration of continuity equation, and it is nullified by imposing the adjoint potential $\Delta\Phi^\dagger = 0$ to be harmonic. The integrals on the domain boundary $\partial\Omega$ involving the normal velocity $\nabla\Phi \cdot \mathbf{n}$ are the boundary terms resulting in the integration by parts of the continuity equation. These terms vanish at the solid wall because of the no-penetration condition,

$$\left. \frac{\partial\Phi}{\partial r} \right|_{r=1} = \left. \frac{\partial\Phi}{\partial z} \right|_{z=-h} = \left. \frac{\partial\Phi^\dagger}{\partial r} \right|_{r=1} = \left. \frac{\partial\Phi^\dagger}{\partial z} \right|_{z=-h} = 0, \quad (8.56)$$

Chapter 8. Nonlinear friction in sloshing dynamics: partial wetting

and at the axis because of the symmetry condition:

$$\Phi|_{r=0} = \Phi^\dagger|_{r=0} = 0. \quad (8.57)$$

At the free interface the domain is curved, and the normal vector is $\mathbf{n} = \frac{(-\frac{\partial\eta_0}{\partial r}, 1)}{\sqrt{(1+\eta_{0,r}^2)}}$. By using the kinematic boundary conditions (8.19) equation (8.55) reads:

$$\begin{aligned} & \int_{\eta_0} \left(-i\omega\eta^\dagger + \eta_{0,r} \frac{\partial\bar{\Phi}^\dagger}{\partial r} - \frac{\partial\bar{\Phi}^\dagger}{\partial z} \right) \Phi \frac{d\eta_0}{\sqrt{1-\eta_{0,r}^2}} + \\ & + \int_{\eta_0} \left(-i\omega\Phi^\dagger + \bar{\eta}^\dagger - \frac{1}{Bo} \left[\frac{a(r)}{r} \frac{\partial\bar{\eta}^\dagger}{\partial r} + b(r) \frac{\partial^2\bar{\eta}^\dagger}{\partial r^2} + \frac{c(r)}{r^2} \frac{\partial^2\bar{\eta}^\dagger}{\partial\phi^2} \right] \right) \eta \frac{d\eta_0}{\sqrt{1-\eta_{0,r}^2}} \\ & - \frac{1}{Bo} \left[r b(r) \left(\bar{\eta}^\dagger \frac{\partial\eta}{\partial r} - \frac{\partial\bar{\eta}^\dagger}{\partial r} \eta \right) \right]_{r=0}^{r=1} = 0. \end{aligned} \quad (8.58)$$

From the first two terms in equation (8.58) the adjoint kinematic and dynamic interface conditions are retrieved:

$$\begin{aligned} & -i\omega\eta^\dagger + \eta_{0,r} \frac{\partial\Phi^\dagger}{\partial r} - \frac{\partial\Phi^\dagger}{\partial z} = 0 \\ & -i\omega\Phi^\dagger + \eta^\dagger - \frac{1}{Bo} \left[\frac{a(r)}{r} \frac{\partial\eta^\dagger}{\partial r} + b(r) \frac{\partial^2\eta^\dagger}{\partial r^2} + \frac{c(r)}{r^2} \frac{\partial^2\eta^\dagger}{\partial\phi^2} \right] = 0. \end{aligned} \quad (8.59)$$

To complete the adjoint system of equations the last term in equation (8.58), which comes from the integration by part of the capillary pressure in the direct dynamic condition, has to be nullified. In $r = 0$ this term is null because of the integral argument is weighted by r . In contrast, at the contact line $b(r = 1) = \sin^3(\theta_s)$ and the condition:

$$-\frac{\cos^3(\theta_s)}{Bo} \left(\bar{\eta}^\dagger \frac{\partial\eta}{\partial r} - \frac{\partial\bar{\eta}^\dagger}{\partial r} \eta \right) \Big|_{r=1} = 0 \quad (8.60)$$

defines the natural boundary condition at the contact line. In the case of free-end edge interface:

$$\frac{\partial\eta}{\partial r} \Big|_{r=1} = \frac{\partial\eta^\dagger}{\partial r} \Big|_{r=1} = 0. \quad (8.61)$$

It should be noted that also the pinned boundary condition $\eta = \eta^\dagger = 0$ is also a natural boundary condition of the problem. Hence the direct problem at order ϵ is self-adjoint with the respect to the Hermitian scalar product (8.52):

$$i\omega_0^\dagger \mathcal{B}^\dagger - \mathcal{A}^\dagger = -i\omega\mathcal{B} - \mathcal{A}. \quad (8.62)$$

The vector \mathbf{q}^\dagger which satisfies the adjoint equations $[-i\omega\mathcal{B} - \mathcal{A}]\mathbf{q}^\dagger = 0$ is the adjoint mode.

8.7 Appendix: Numerical code

8.7.1 Static meniscus

At order ϵ^0 the static meniscus shape in a cylindrical basin it has to be determined. The governing equation (8.12) is discretized through Chebyshev collocation method and the Gauss-Lobatto-Chebyshev (GLC) collocation grid $s \in [-1, 1]$ is mapped into the physical space $r \in [0, R]$ through the linear mapping $r = R(s + 1)/2$. Hence the solution to the nonlinear equation is obtained by mean of an iterative Newton method which is made of the following steps:

1. Find an approximate guess solution η_0 which satisfies the boundary conditions (8.13) and (8.15).
2. Solve for $\delta\eta_0$ the linear system:

$$\left. \frac{d\chi(\eta)}{d\eta} \right|_{\eta_0} \delta\eta_0 = -\chi(\eta_0) \quad (8.63)$$

with homogeneous boundary conditions, where the Jacobian $d\chi(\eta)/d\eta$ is defined in equation (8.18).

3. Set $\eta_0 = \eta_0 + \delta\eta_0$
4. Compute the L_2 -norm of $\delta\eta_0$. If $\|\eta_0\|_{L_2} > 10^{-12}$ go to step (b)
5. Set the static meniscus to η_0

8.7.2 Global stability analysis

At order ϵ^1 the linear eigenvalue problem (8.24) has to be solved and the equations together with the boundary conditions are discretized through Chebyshev collocation in a similar fashion to Viola *et al.* (2016a). The physical domain is in general not rectangular due to the presence of the static meniscus η_0 . For this reason the physical domain with coordinates (r, z) has to be mapped into the Chebyshev space (s, t) through the transformation:

$$r = \frac{R}{2}(s + 1), \quad z = (t + 1) \left(\frac{H}{2} + \frac{\eta_0(s)}{2} \right) - H, \quad (8.64)$$

where η_0 is the static meniscus. The partial derivatives in the physical space are related to the derivative in the physical space according to the relations:

$$\begin{aligned} \frac{\partial u}{\partial r} &= \frac{1}{r,s} u_{,s} - \frac{z,s}{r,s z,t} u_{,t} & \frac{\partial u}{\partial y} &= \frac{1}{z,t} u_{,t} \\ \frac{\partial^2 u}{\partial r^2} &= \frac{1}{r,s^2} u_{,ss} + \frac{z,s^2}{r,s^2 z,t^2} u_{,tt} - \frac{z,t z,ss - 2z,s z,st}{r,s^2 z,t^2} u_{,t} - \frac{2z,s}{r,s^2 z,t} u_{,st} & \frac{\partial^2 u}{\partial y^2} &= \frac{1}{z,t^2} u_{,tt} \end{aligned} \quad (8.65)$$

Chapter 8. Nonlinear friction in sloshing dynamics: partial wetting

where the derivatives of the physical coordinates with respect depend on the mapping function, see Heinrichs (2004). In our case:

$$\begin{aligned} r_{,s} &= R & r_{,ss} &= 0 & r_{,t} &= 0 & r_{,st} &= 0 & r_{,tt} &= 0 \\ z_{,s} &= \frac{t+1}{2}\eta_{,s} & z_{,ss} &= \frac{t+1}{2}\eta_{,ss} & z_{,t} &= \frac{H}{2} + \frac{\eta(s)}{2} & z_{,st} &= \frac{\eta_{,s}}{2} & z_{,tt} &= 0 \end{aligned} \quad (8.66)$$

The integrals `SloshWaterAppEaring` in equations (8.42) are computed with Clenshaw-Curtis quadrature formula, where the quadrature weights are adapted to the mappings used following the method presented in Sommariva (2013). The number of nodes in the radial and vertical direction is $N_r = N_z = 60$ which ensures convergence of the results. In Figure 8.7(d) the time of arrest as a function of θ_s and Δ computed with the finer grid $N_r = N_z = 80$ is reported as proof of convergence.

9 Conclusions and perspectives

In this thesis the resonant behavior of swirling wakes and sloshing waves has been studied. First, we have considered the response to forcing of trailing and wind turbine hub vortices, with special emphasis on convective non-normalities and mode selection. Then, the effect of capillary sublinearities in the free decay of sloshing waves has been explored, both in the total and partial wetting regimes.

In **chapter 2** we have studied how trailing vortices respond to a harmonic forcing. Full 3D numerical simulation of a non-parallel Batchelor vortex, reveal that a large variety of helical responses are excited and amplified through the flow field when an inlet or body forcing is applied. Single and double helical structures are excited at low frequency, whereas higher azimuthal wavenumber modes resonate at higher frequencies, see Figure 9.1.

With the aim of understanding the mode selection mechanism as a function of the forcing frequency, both a WKB analysis, in the framework of weakly-non-parallel flows, and a global resolvent approach are carried out. It is found that the appearance of a preferred helical shape at a given frequency is directly connected to the local stability properties of the flow which is everywhere convectively unstable. Indeed, the mode selection predicted by the linear optimal forcing analysis well matches the one observed in full nonlinear DNS computation. Regarding the energy gain of the response, the single helix mode is found to have the largest nonlinear amplification to a harmonic in time and random in space inlet forcing. Moreover, due to its peculiar azimuthal symmetry, the single-helix mode is the most sensitive to disturbances forcing the flow at the centerline and resonates in a broader frequency range due to possible nonlinear interaction mechanisms between neighboring modes.

These techniques have been then translated in **chapter 3** to investigate the physical origin of the coherent fluctuation of the hub vortex in wind turbine wakes that has been observed experimentally (Medici & Alfredsson, 2006; Chamorro & Porté-Agel, 2010; Jungo *et al.*, 2013). Local and global stability analysis on the time-averaged wind tunnel measurements revealed that this oscillation is related the appearance of a counter-winding and co-rotating single-helix mode. Thus, a novel formulation has been introduced to properly account for the turbulent

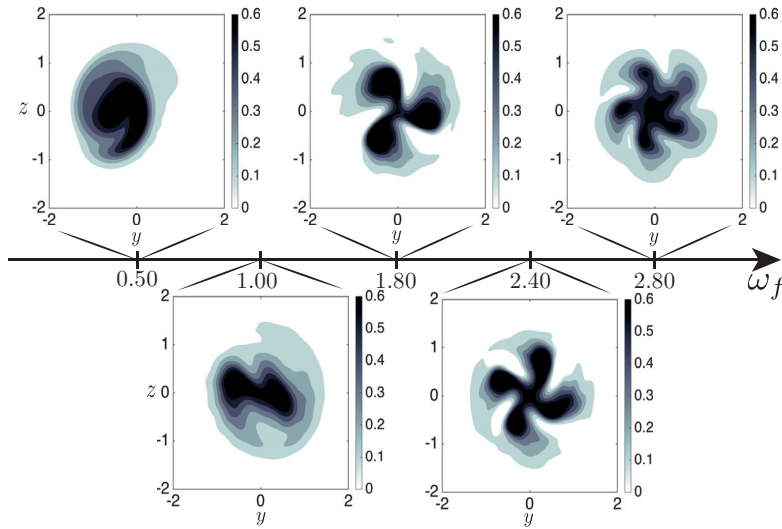


Figure 9.1: Mode selection in a harmonically forced trailing vortex (isocontours of axial vorticity). When the forcing frequency, ω_f increases higher wavenumber modes resonate.

effects in the stability analysis by means of eddy-viscosity models tuned on the Reynolds stresses available from experiments. With our stability analysis, we were able to predict the frequency of instability of the hub vortex and the streamwise wavenumber of the helicoidal mode which successfully match with experiments.

Furthermore, we extended the stability analysis to wind turbines immersed in a turbulent atmospheric boundary layer. In this case, the mean wake can not be considered as axisymmetric and 2D local stability analysis has been carried out, confirming that, for the considered operational conditions of the turbine, the single-helix mode visualized in Figure 9.2 resonates.

Aiming at controlling the helical modes arising in trailing and hub vortices, we developed in **chapter 4** a general adjoint-based technique for the control of disturbances amplification in weakly non-parallel amplifier flows. The method is based on the sensitivity of the spatial stability spectrum to a generic local baseflow modification, that is by itself a novel contribution to classical Hydrodynamic stability theory. These local sensitivities are concurrently used in a Lagrangian formulation to determine the optimal control capable to reduce the energy response of amplifier flow. The technique has been applied to the case of an evolving Batchelor vortex: by using only one linearization of the flow dynamics carried out on the uncontrolled configuration, we successfully determined the optimal linear control to reduce the global amplification of helical modes in the flow domain.

Finally, in **chapter 5** we revisited with a modern perspective the classical, but still not completely understood, phenomenon of vortex breakdown. Based on our numerical simulations carried out at different Reynolds and swirl number, we observed that the breakdown state corresponds to a transition state between two different flow solutions. While the pre-breakdown state corresponds to a self-similar columnar solution which respects the classical boundary layer scaling in agreement to Hall (1972), the self-similarity is lost for post-breakdown solutions. However, this transition can not be explained as a supercritical bifurcation because the

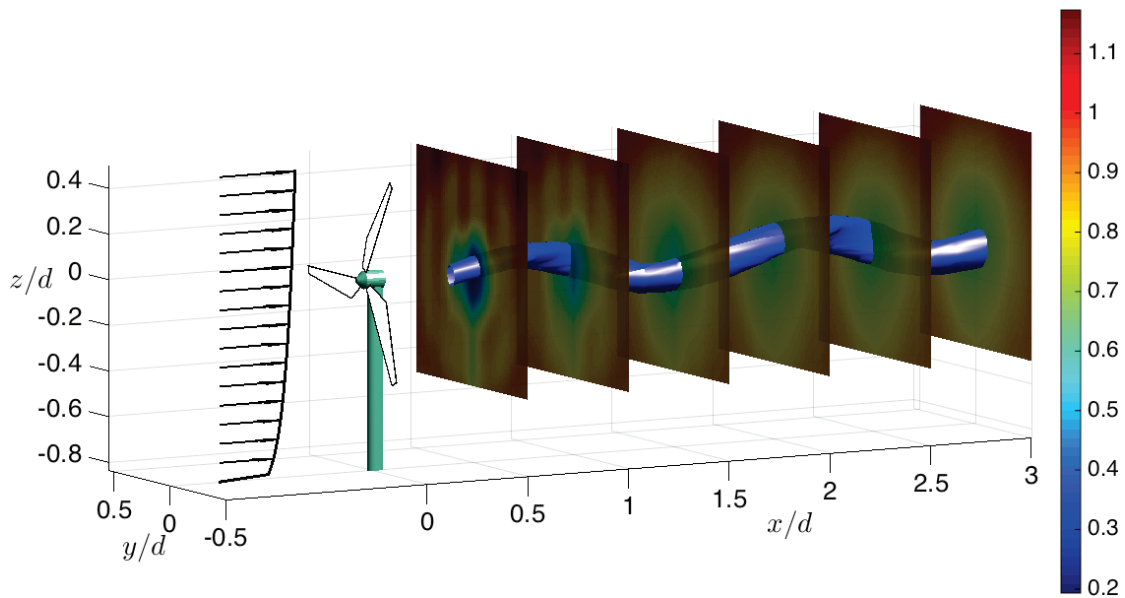


Figure 9.2: Reconstruction of the global mode resonating in the hub vortex instability (isosurface of axial vorticity). The arrows depict the atmospheric boundary layer in the oncoming flow and the streamwise planes in the wind turbine wake report the mean flow axial velocity.

flow is seen to remain always globally stable to axisymmetric steady perturbations. Still, a weakly damped steady mode with a topology similar to the breakdown state is present in the spectrum. Thus, we have shown asymptotically that this mode could be triggered by nonlinear effects even if linearly stable. Finally, a set of reduced Navier-Stokes equations that correctly account for the vortex breakdown state with a cheaper computational cost has been derived.

As we have just summarized, new results on the amplification mechanisms and mode selection in swirling wakes have been obtained. Nevertheless, interesting open questions remain on this topic and, with the insights gained from our investigation, several extensions of this work are possible.

In particular, the mode selection in the wind turbine hub vortex has not been yet fully explained, since the physical mechanism leading to the single-helix instability is still not clear. Since all the measured slices of fluid domain are convectively unstable our main point is that the single-helix is the most unstable mode in both temporal and spatial analysis at the instability frequency given from experiments (in a similar way to Oberleithner *et al.* (2011)). We further claimed that, even if there was a region of absolute instability in the very near wake, this region would be very small and most likely not elongated enough to act as wavemaker and trigger a global mode. On the other hand, if the flow acts as an amplifier, then a forcing is necessary to trigger a significant response, which raises the following fundamental question: **where is this forcing coming from?** We argue probably from the wind turbine itself. In fact in Felli *et al.* (2011) the instability of the hub vortex occurs at the same frequency of rotation of the wind-turbine, like in a transfer function relation between the input and output of linear

systems. In our experiments and in agreement with Chamorro & Porté-Agel (2010) and Zhang *et al.* (2012) the low-spectral component connected to wake instability is equal to approximately 0.34 times the hub rotational frequency. The flow response is at a frequency close to 1/3 of the upstream forcing suggesting an explanation through **nonlinear subharmonic resonance**: since the flow is quite insensitive at the frequency of the forcing (it is actually locally stable!), the response is located in the resonance range where a certain subharmonic resonates well. In the case of Felli *et al.* (2011) we can conjecture the existence of some modes with large amplification close to the propeller rotation frequency such that the response of the flow is synchronized with the forcing.

In this conception, stability features of the flow play the role of a filter. They only allow a certain range of frequencies in the flow response, where locally unstable and globally sufficiently amplified modes are found. This argument could be better investigated performing experiments varying continuously the flow parameters (such as the tip speed ratio) in such a way that the ratio among the frequency instability and the rotational frequency of the turbine will vary from 0.34, as in our case, to 1, as in Felli *et al.* (2011). According to the theory of amplifier flows a clear switch among the dominant frequency and its subharmonics can be expected varying the operational condition of the turbines and, as a consequence, the flow parameters.

In this respect, the phenomenon of the hub vortex instability seems to be quite robust in the sense that it has been detected in several wind tunnel experiments and more recently in numerical simulations. However, wind turbine wakes are greatly affected by the atmospheric conditions and their operational regimes. Indeed, pitch and yaw angles of a turbine are continuously adjusted as a function of the wind velocity and direction. Hence, a natural extension of this work would be to study **how the mode selection depends on incoming wind turbulence, thrust coefficient, tip speed ratio and blade lift distribution of the wind turbine**. The mean flow, which varies from case to case, could be obtained in dedicated wind turbine experiments or Reynolds Averaged Navier Stokes simulations.

Another interesting aspect is the enhancement of the turbulent mixing and flow entrainment in the wake caused by the spiralling motion of the hub vortex due to the instability. Therefore, its **control with the objective of hasten the wake recovery**, is of great interest for maximizing wind farm energy harvesting. With this motivation, the control strategy for amplifier flows developed in this thesis could be employed to determine the region of the wind turbine wakes more receptive to a mean flow modification and to design an optimal control to act on the instability. The effectiveness of the designed control strategy could be tested in wind-tunnel experiment to verify the increase (or decrease) of the hub vortex instability amplification.

Another extension of the work would be the investigation of the **vortex meandering phenomenon** observed in trailing-vortex experiments (Devenport *et al.*, 1996; Jacquin *et al.*, 2001; Iungo *et al.*, 2009), in the light of spatial stability analysis. The random-like precession of the vortex core could be maybe explained as the result of the convectively unstable spatial modes, eventually excited by turbulent fluctuations. Moreover, the particle image velocimetry measurements of Roy & Leweke (2008) revealed that the most energetic helical perturbation

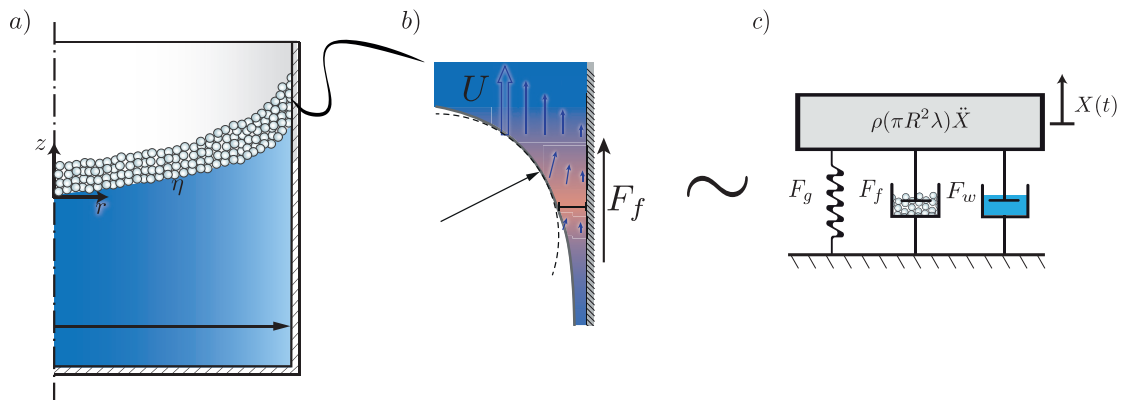


Figure 9.3: Sleshooting of (a) foam-water waves in a cylindrical basin where the (b) motion of the surface Plateau borders originates a sublinear friction force, F_f . The equivalent mechanical system is sketched in (c), where the inertial term proportional to the interface acceleration, \ddot{X} , is balanced by the restoring force of gravity, F_g , the viscous friction in the liquid phase, F_w , and the sublinear force in the foam phase, F_f .

present in their meandering experiments is the single-helix displacement mode that corresponds to the most nonlinearly amplified mode in our numerical simulations on the harmonic response of trailing vortices.

Lastly, regarding the **axisymmetric vortex breakdown**, the **weakly nonlinear mechanisms** proposed in this work could give a new understanding of this intriguing phenomenon and are currently one of my ongoing projects.

The second part of the thesis has been devoted to nonlinear friction effects on the dynamics of fluid-solid resonators. Nonlinearities have been classified as superlinear or sublinear, according to their power law dependence on the fluid velocity. Namely, nonlinear terms with an exponent greater than one, such as the convective term in the Navier-Stokes equations, dominate the dynamics at large amplitudes, thereby enabling linearized approaches at small scales. In contrast, sublinear terms, i.e. with an exponent less than one, become of paramount importance at small oscillation amplitudes.

In **chapter 6** the motion of a torsional pendulum consisting of an oscillating disk subjected to a superlinear and linear friction has been studied. The full fluid-structure problem has been solved through numerical simulations by coupling the disk's motion to the fluid's velocity and pressure fields. It was seen that even if the frequency of the damped system is almost uniform in time and close to the natural frequency, a small frequency shift exists between high and low amplitudes. We observed furthermore the existence of two different regimes in the dynamics of the pendulum yielding to different scalings for the damping rate: it decreases proportionally to the square root of the oscillation amplitude at the beginning of the motion before reaching a constant value.

These observations have been explained in the framework of boundary layer theory where two limiting regimes have been distinguished: (i) a low amplitude linear regime where an oscillating Stokes layer takes place (Stokes, 1851) and (ii) a high amplitude nonlinear regime

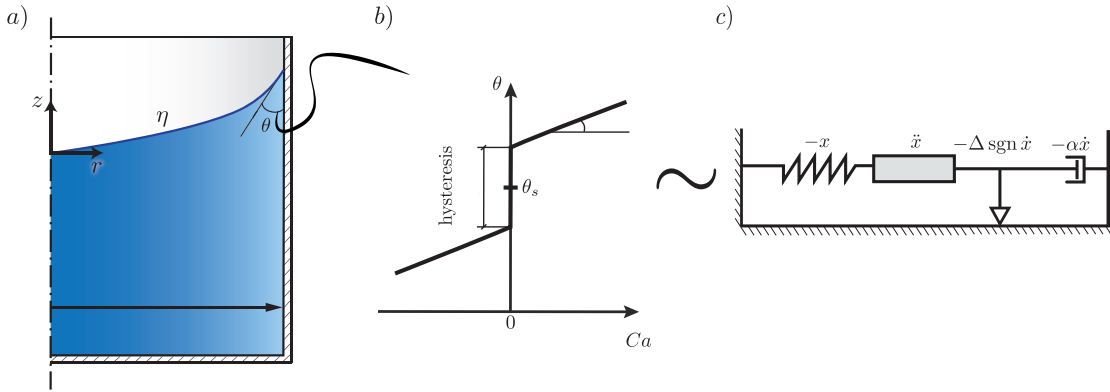


Figure 9.4: (a) Sloshing of water waves in a cylindrical basin, where the dynamic contact angle θ depends on the capillary number $Ca = \mu U / \gamma$ based on the contact line velocity U through the nonlinear model in (b). The hysteresis acts as a solid friction and the equivalent mechanical system is sketched in (c).

that is well described by the quasi-steady Von Karman solution (Von Karman, 1921). These analytical solutions motivated us to introduce a simple phenomenological model for the viscous relaxation of the torsional pendulum. This predictive model gives an analytic expression for the free decay of the system compares well with the results of the full numerical simulations.

In **chapter 7** we uncovered previously unseen sublinear effects in a liquid-foam sloshing system designed at desktop scale. We showed experimentally and theoretically that when a layer of foam is placed on top of a liquid, the sloshing of the liquid phase does not relax exponentially. Indeed, the motion of the several contact lines embedded in the cellular structure of the liquid foam generates a sublinear friction at the container's wall, see Figure 9.3. Thus, this sublinear force yields the damping rate of the sloshing motion to increase catastrophically at small amplitude, thereby stopping the fluid's oscillations in a finite time. This result is in strong contrast with the classical linear exponential relaxation ending at infinite time. We rationalized our observations deriving a minimal theoretical model accounting for the sublinear interfacial effects in the total wetting regime which evidences the predominance of interfacial effects in macroscopic dynamical systems comprising contact lines.

Then, in **chapter 8** a single phase liquid sloshing in partial wetting conditions is considered. In this case no precursor film along the container's wall is present, so that the oscillating interface is effectively in contact with the container. The contact angle depends nonlinearly on the contact line velocity and a contact angle hysteresis range exists when the interface velocity is null (Dussan, 1979). In order to account for this nonlinear effect on the dynamics of inviscid sloshing waves, we carried out a weakly nonlinear analysis based on global stability. We showed theoretically that capillary effects have a dramatic influence on the damping rate. Specifically, the damping rate induced by the motion of the liquid meniscus depends on the wave amplitude, consistently with the experimental observation (Keulegan, 1959; Cocciaro *et al.*, 1991): this rate is practically uniform when the wave amplitude is large and increases significantly at small amplitudes due to the presence of hysteresis. Similarly to the foam case, the damping rate diverges at small amplitudes yielding a finite time arrest of the motion. This

phenomenon was explained by noticing that at leading order the sloshing mode behaves as an oscillator damped by viscous and solid friction, meaning that the hysteresis term acts as Coulomb solid friction as depicted in Figure 9.4.

These new contributions to the study of the nonlinear dynamics of sloshing waves motivate various follow-up projects.

For instance, one of the main outcomes of the theoretical model we have introduced for the water-foam sloshing is an analytical expression of the finite time of arrest, which has different scalings with the different physical parameters. At this stage, only its dependence on the foam thickness has been verified experimentally, whereas **the dependence on the fluid density, viscosity, surface tension, container size and foam bubble diameter** should also be probed with new experiments.

Furthermore, in our experiments only the free decay of sloshing waves has been studied by monitoring their relaxation. It remains, however, to investigate the impact of the sublinear term on the response to forcing. Thus, a complementary experiment to what done here, would be to **measure the amplitude of the free surface response when a small harmonic forcing is applied to the container**. By varying the forcing frequency and the foam layer thickness, the resonance curve is expected to differ from the classical Lorentzian shape far from the resonance condition, where the amplitude of the response is smaller and sublinear effects more intense.

In our weakly nonlinear analysis in chapter 8 we accounted for contact angle hysteresis in inviscid capillary-gravity waves. In particular, an empirical contact line model has been used as boundary condition at the contact line. The next natural step is to perform a **quantitative comparison between the capillary damping rates obtained by the asymptotic analysis and the ones measured experimentally**. Note that since the model parameters strongly depend on the wetting condition and on the roughness of the solid wall, they have to be measured in the particular experimental condition and provided as input in the formulation.

On the fundamental level, the model sketched in Figure 9.4 has been validated experimentally in the case of unidirectional flows but has not been extensively verified in the oscillatory regime. Hence, **precise measurements of the contact line law of a periodically advancing and receding interface** could reveal a different behaviour with respect to unidirectional flow, especially at high frequency. This constitutes a natural continuation of this study, as well as a formidable experimental challenge with a possible impact on the study of dissipative mechanisms at play in the sloshing phenomenon. In this spirit, our weakly nonlinear formulation can be in general extended to other contact line laws at the interface.

Another interesting continuation of this work would be to account for the **viscous effects at leading order**, i.e. to determine the effect of the contact angle hysteresis on the viscous sloshing mode rather than the inviscid one. Preliminary results reveal that this formulation is **ill-posed** since at the contact line the noslip boundary condition imposes the velocity to be null whereas the contact line mode allows for the interface to slide. This paradox, that is not present in the inviscid formulation where slip condition is prescribed at the wall, is usually

Chapter 9. Conclusions and perspectives

overcome in unidirectional flows by introducing a **slip length** (Eggers, 2005). Hence, viscous sloshing modes could be treated by replacing the noslip condition at the wall with a Navier condition. However, this requires to introduce another parameter in the formulation, the slip length, that depends on the specific wetting condition of the problem.

As a final note, the global **weakly nonlinear analysis could be in principle extended to total wetting condition** (see section 1.3.2 in the introduction chapter). However, this case appears as non-trivial since the static contact angle is zero yielding a diverging slope (a cusp) of the static meniscus, that enters in the global analysis at first order. Not only that, the thin wetting film present in the case of a fully wetting fluids has to be discretized and included in the flow domain.

Bibliography

- ÅKERVIK, E., EHRENSTEIN, U., GALLAIRE, F. & HENNINGSON, D. S. 2008 Global two-dimensional stability measures of the flat plate boundary-layer flow. *European Journal of Mechanics-B/Fluids* **27** (5), 501–513.
- ALFREDSSON, P. H. & DAHLBERG, J. A. 1979 A preliminary wind tunnel study of windmill wake dispersion in various flow conditions. Technical Note AU-1499, Part 7, FFA. Stockholm, Sweden.
- ALIZARD, F., CHERUBINI, S. & ROBINET, J.-C. 2009 Sensitivity and optimal forcing response in separated boundary layer flows. *Physics of Fluids* **21** (6), 064108.
- ANTKOWIAK, A. 2005 Short-term dynamics of an isolated vortex. PhD thesis, IMFT - Université Paul Sabatier.
- ARRATIA, C. M. & GALLAIRE, F. 2013 Weakly non-parallel approximation of resolvents for convectively unstable flows. In *Trends in Open Shear Flow Instability - Euromech Colloquium* 547.
- BARKLEY, D. 2006 Linear analysis of the cylinder wake mean flow. *Europhysics Letters* **37** (5), 5.
- BATCHELOR, G. K. 1964 Axial flow in trailing line vortices. *Journal of Fluid Mechanics* **20** (4), 645–658.
- BATCHELOR, G. K. & GILL, A. E. 1962 Analysis of the stability of axisymmetric jets. *Journal of Fluid Mechanics* **14**, 529–551.
- BENJAMIN, T. B. 1962 Theory of the vortex breakdown phenomenon. *Journal of Fluid Mechanics* **14** (04), 593–629.
- BENJAMIN, T. B. & URSELL, F. 1954 The stability of the plane free surface of a liquid in vertical periodic motion. *Proceedings of the Royal Society of London. Series A, Mathematical and Physical Sciences* pp. 505–515.
- BENNEY, D. J. 1964 The flow induced by a disk oscillating in its own plane. *Journal of Fluid Mechanics* **18** (03), 385–391.

Bibliography

- BILLANT, P., CHOMAZ, J.-M. & HUERRE, P. 1998 Experimental study of vortex breakdown in swirling jets. *Journal of Fluid Mechanics* **376**, 183–219.
- BOTTARO, A., CORBETT, P. & LUCHINI, P. 2003 The effect of base flow variation on flow stability. *Journal of Fluid Mechanics* **476**, 293–302.
- BOTTARO, A., SOUEID, H. & GALLETTI, B. 2006 Formation of secondary vortices in turbulent square-duct flow. *AIAA Journal* **44** (4), 803–811.
- BOUJO, E. & GALLAIRE, F. 2014 Controlled reattachment in separated flows: a variational approach to recirculation length reduction. *Journal of Fluid Mechanics* **742**, 618–635.
- BOUJO, E. & GALLAIRE, F. 2015 Sensitivity and open-loop control of stochastic response in a noise amplifier flow: the backward-facing step. *Journal of Fluid Mechanics* **762**, 361–392.
- BRANDT, L., SIPP, D., PRALITS, J. O. & MARQUET, O. 2011 Effect of base-flow variation in noise amplifiers: the flat-plate boundary layer. *Journal of Fluid Mechanics* **687**, 503–528.
- BRETHERTON, F. P. 1961 The motion of long bubbles in tubes. *Journal of Fluid Mechanics* **10** (2), 166–188.
- BURESTI, G. & IUNGO, G. V. 2010 Experimental investigation on the connection between flow fluctuations and vorticity dynamics in the near wake of a triangular prism placed vertically on a plane. *Journal of Wind Engineering and Industrial Aerodynamics* **98** (6), 253–262.
- BURTON, T., SHARPE, D., JENKINS, N. & BOSSANYI, N. 2001 *Wind energy handbook*. John Wiley and Sons.
- BUTLER, K. M. & FARRELL, B. F. 1992 Three-dimensional optimal perturbations in viscous shear flow. *Physics of Fluids* **4** (8), 1637–1650.
- CAMARRI, S. 2015 Flow control design inspired by linear stability analysis. *Acta Mechanica* **226** (4), 979–1010.
- CAMARRI, S., FALLENIOUS, B. E. G. & FRANSSON, J. H. M. 2013 Stability analysis of experimental flow fields behind a porous cylinder for the investigation of the large-scale wake vortices. *Journal of Fluid Mechanics* **715**, 499–536.
- CANTAT, I. 2013 Liquid meniscus friction on a wet plate: Bubbles, lamellae, and foams. *Physics of Fluids* **25** (3), 031303.
- CANUTO, C., HUSSAINI, M. Y., QUARTERONI, A. & ZANG, T. A. 2007 *Spectral methods: evolution to complex geometries and applications to fluid dynamics*. Springer Science & Business Media.
- CASE, K. M. & PARKINSON, W. C. 1957 Damping of surface waves in an incompressible liquid. *Journal of Fluid Mechanics* **2** (02), 172–184.

- CHAMORRO, L. P. & PORTÉ-AGEL, F. 2009 A wind-tunnel investigation of wind-turbine wakes: boundary-layer turbulence effects. *Boundary-Layer Meteorology* **132** (1), 129–149.
- CHAMORRO, L. P. & PORTÉ-AGEL, F. 2010 Effects of thermal stability and incoming boundary-layer flow characteristics on wind-turbine wakes: a wind-tunnel study. *Boundary-Layer Meteorology* **136** (3), 515–533.
- CHARRU, F. 2011 *Hydrodynamic Instabilities*. Cambridge University Press.
- CHOMAZ, J.-M. 2005 Global instabilities in spatially developing flows: non-normality and nonlinearity. *Annual Review of Fluid Mechanics* **37**, 357–392.
- CHOULY, F. & LAGRÉE, P.-Y. 2012 Comparison of computations of asymptotic flow models in a constricted channel. *Applied Mathematical Modelling* **36** (12), 6061–6071.
- COCCIARO, B., FAETTI, S. & NOBILI, M. 1991 Capillarity effects on surface gravity waves in a cylindrical container: wetting boundary conditions. *Journal of Fluid Mechanics* **231**, 325–343.
- COCCIARO, B., FAETTI, S., NOBILI, M. & FESTA, C. 1993 Experimental investigation of capillarity effects on surface gravity waves: non-wetting boundary conditions. *Journal of Fluid Mechanics* **246**, 43–66.
- CORBETT, P. & BOTTARO, A. 2000 Optimal perturbations for boundary layers subject to stream-wise pressure gradient. *Physics of Fluids* **12** (1), 120–130.
- COSSU, C. & CHOMAZ, J.-M. 1997 Global measures of local convective instabilities. *Physical Review Letters* **78** (23), 4387.
- COSSU, C., PUJALS, G. & DEPARDON, S. 2009 Optimal transient growth and very large-scale structures in turbulent boundary layers. *Journal of Fluid Mechanics* **619**, 79–94.
- COUAIRO, A. & CHOMAZ, J.-M. 1999 Fully nonlinear global modes in slowly varying flows. *Physics of Fluids* **11** (12), 3688–3703.
- COX, R. G. 1986 The dynamics of the spreading of liquids on a solid surface, part2, surfactants. *Journal of Fluid Mechanics* **168**, 195–220.
- CRIGHTON, D. G. & GASTER, M. 1976 Stability of slowly diverging jet flow. *Journal of Fluid Mechanics* **77**, 397–413.
- CROUCH, J. D., GARBARUK, A. & MAGIDOV, D. 2007 Predicting the onset of flow unsteadiness based on global instability. *Journal of Computational Physics* **224** (2), 924–940.
- CROUCH, J. D., MILLER, G. D. & SPALART, P. R. 2001 Active-control system for breakup of airplane trailing vortices. *AIAA journal* **39** (12), 2374–2381.
- CROUCH, J. D. & SPALART, P. R. 2000 Active system for early destruction of trailing vortices. US Patent 6,082,679.

Bibliography

- CROW, S. C. & CHAMPAGNE, F. H. 1971 Orderly structure in jet turbulence. *Journal of Fluid Mechanics* **48** (3), 547–591.
- DE GENNES, P.-G. 1985 Wetting: statics and dynamics. *Reviews of Modern Physics* **57** (3), 827.
- DE GENNES, P.-G., BROCHARD-WYART, F., QUÉRÉ, D., FERMIGIER, M. & CLANET, C. 2002 *Gouttes, bulles, perles et ondes*. Belin Paris.
- DEL ÀLAMO, J.C. & JIMENEZ, J. 2006 Linear energy amplification in turbulent channels. *Journal of Fluid Mechanics* **559**, 205–213.
- DEL PINO, C., PARRAS, L., FELLI, M. & FERNANDEZ-FERIA, R. 2011 Structure of trailing vortices: Comparison between particle image velocimetry measurements and theoretical models. *Physics of Fluids* **23** (1), 013602.
- DELBENDE, I., CHOMAZ, J.-M. & HUERRE, P. 1998 Absolute/convective instabilities in the Batchelor vortex: a numerical study of the linear impulse response. *Journal of Fluid Mechanics* **355**, 229–254.
- DELBENDE, I. & ROSSI, M. 2005 Nonlinear evolution of a swirling jet instability. *Physics of Fluids* **17**, 229–254.
- DENKOV, N. D., SUBRAMANIAN, V., GUROVICH, D. & LIPS, A. 2005 Wall slip and viscous dissipation in sheared foams: Effect of surface mobility. *Colloids and Surfaces A* **263** (1), 129–145.
- DEVENPORT, W. J., RIFE, M. C., LIAPIS, S. I. & FOLLIN, G. J. 1996 The structure and development of a wing-tip vortex. *Journal of Fluid Mechanics* **312**, 67.
- DRAZIN, P. G. & REID, W. H. 2004 *Hydrodynamic stability*. Cambridge University Press.
- DUŠEK, J., LE GAL, P. & FRAUNIE, P. 1994 A numerical and theoretical study of the first hopf bifurcation in a cylinder wake. *Journal of Fluid Mechanics* **264**, 59–80.
- DUSSAN, E. B. 1979 On the spreading of liquids on solid surfaces: static and dynamic contact lines. *Annual Review of Fluid Mechanics* **11** (1), 371–400.
- ECKHOFF, K. S. 1984 A note on the instability of columnar vortices. *Journal of Fluid Mechanics* **145**, 417–421.
- EGGERS, J. 2005 Existence of receding and advancing contact lines. *Physics of Fluids* **17** (8), 082106.
- EHRENSTEIN, U. & GALLAIRE, F. 2005 On two-dimensional temporal modes in spatially evolving open flows: the flat-plate boundary layer. *Journal of Fluid Mechanics* **536** (7), 209–218.
- EHRENSTEIN, U. & GALLAIRE, F. 2008 Two-dimensional global low-frequency oscillations in a separating boundary-layer flow. *Journal of Fluid Mechanics* **614**, 315–327.

- ESCUDIER, M. & ZEHNDER, N. 1982 Vortex-flow regimes. *Journals of Fluid Mechanics* **115**, 105–121.
- ESPAÑA, G., AUBRUN, S., LOYER, S. & DEVINANT, P. 2011 Spatial study of the wake meandering using modelled wind turbines in a wind tunnel. *Wind Energy* **14** (7), 923–937.
- FABRE, D. & JACQUIN, L. 2004 Viscous instabilities in trailing vortices at large swirl numbers. *Journal of Fluid Mechanics* **500**, 239–262.
- FABRE, D., SIPP, D. & JACQUIN, L. 2006 Kelvin waves and the singular modes of the lamb-oseen vortex. *Journal of Fluid Mechanics* **551**, 235–274.
- FALER, J. & LEIBOVICH, S. 1977 Disrupted states of vortex flow and vortex breakdown. *Physics of Fluids* **20**, 1385–1400.
- FALKNER, V. M. & SKAN, S. W. 1930 *Some approximate solutions of the boundary layer equations*. HM Stationery Office.
- FELLI, M., CAMUSSI, R. & DIFELICE, F. 2011 Mechanisms of evolution of the propeller wake in the transition and far fields. *Journal of Fluid Mechanics* **682**, 5–53.
- FISCHER, P. F., LOTTES, J. W., STEFAN & G., KERKEMEIER 2008 nek5000 Web page <http://nek5000.mcs.anl.gov>.
- GALLAIRE, F. & CHOMAZ, J. M. 2003 Mode selection in swirling jet experiments: a linear stability analysis. *Journal of Fluid Mechanics* **494**, 222–224.
- GALLAIRE, F., RUIH, M., MEIBURG, E., CHOMAZ, J.-M. & HUERRE, P. 2006 Spiral vortex breakdown as a global mode. *Journal of Fluid Mechanics* **549**, 71–80.
- GARNAUD, X., LESSHAFFT, L., SCHMID, P. J. & HUERRE, P. 2013 The preferred mode of incompressible jets: linear frequency response analysis. *Journal of Fluid Mechanics* **716**, 189–202.
- GASTER, M. 1962 A note on the relation between temporally-increasing and spatially-increasing disturbances in hydrodynamic instability. *Journal of Fluid Mechanics* **14**, 222–224.
- GASTER, M., KIT, E. & WYGNANSKI, I. 1985 Large-scale structures in a forced turbulent mixing layer. *Journal of Fluid Mechanics* **150**, 22–39.
- GIANNETTI, F., CAMARRI, S. & LUCHINI, P. 2010 Structural sensitivity of the secondary instability in the wake of a circular cylinder. *Journal of Fluid Mechanics* **651**, 319.
- GIANNETTI, F. & LUCHINI, P. 2007 Structural sensitivity of the first instability of the cylinder wake. *Journal of Fluid Mechanics* **581** (1), 167–197.
- GILLIES, G. T. & RITTER, R. C. 1993 Torsion balances, torsion pendulums, and related devices. *Review of scientific instruments* **64** (2), 283–309.

Bibliography

- GRABOWSKI, W. J. & BERGER, S. A. 1976 Solutions of the navier-stokes equations for vortex breakdown. *Journal of Fluid Mechanics* **75** (03), 525–544.
- GUNDLACH, J. H. & MERKOWITZ, S. M. 2000 Measurement of newton's constant using a torsion balance with angular acceleration feedback. *Physical Review Letters* **85** (14), 2869.
- GUPTA, B. P. & LOEWY, R. G. 1974 Theoretical analysis of the aerodynamic stability of multiple, interdigitated helical vortices. *AIAA J.* **12**, 1381–1387.
- HALL, M. G. 1972 Vortex breakdown. *Annual Review of Fluid Mechanics* **4** (1), 195–218.
- HEATON, C. J. 2007 Optimal growth of the batchelor vortex viscous modes. *Journal of Fluid Mechanics* **592**, 495–505.
- HEATON, C. J., NICHOLS, J. W. & SCHMID, P. J. 2009 Global linear stability of the non-parallel Batchelor vortex. *Journal of Fluid Mechanics* **629**, 139–160.
- HEINRICHS, W. 2004 Spectral collocation schemes on the unit disc. *Journal of Computational Physics* **199** (1), 66–86.
- HOCKING, L. M. 1987 The damping of capillary-gravity waves at a rigid boundary. *Journal of Fluid Mechanics* **179**, 253–266.
- HOCKING, L. M. 2003 Contact angles and inertia for liquid bounded by an oscillating plate. *The Quarterly Journal of Mechanics and Applied Mathematics* **56** (2), 271–288.
- HUERRE, P. & MONKEWITZ, P. A. 1990 Local and global instabilities in spatially developing flows. *Annual Review of Fluid Mechanics* **22** (1), 473–537.
- HUERRE, P. & ROSSI, M. 1998 Hydrodynamic instabilities in open flows. *Collection alea saclay monographs and texts in statistical physics* **1** (3), 81–294.
- HWANG, Y. & CHOI, H. 2006 Control of absolute instability by basic-flow modification in a parallel wake at low reynolds number. *Journal of Fluid Mechanics* **560**, 465–475.
- IBRAHIM, R. A. 2005 *Liquid Sloshing Dynamics: Theory and Applications*. Cambridge University Press.
- IUNGO, G. V. & LOMBARDI, E. 2011 A procedure based on proper orthogonal decomposition for time-frequency analysis of time series. *Experiments in fluids* **51** (4), 969–985.
- IUNGO, G. V., SKINNER, P. & BURESTI, G. 2009 Correction of wandering smoothing effects on static measurements of a wing-tip vortex. *Experiments in fluids* **46** (3), 435–452.
- IUNGO, G. V., VIOLA, F., CAMARRI, S., PORTÉ-AGEL, F. & GALLAIRE, F. 2013 Linear stability analysis of wind turbine wakes performed on wind tunnel measurements. *Journal of Fluid Mechanics* **737**, 499–526.

- IVANELL, S., MIKKELSEN, R., SØRENSEN, J. N. & HENNINGSON, D. 2010 Stability analysis of the tip vortices of a wind turbine. *Wind Energy* **13**, 705–715.
- IVANELL, S., SØRENSEN, J. N., MIKKELSEN, R. & HENNINGSON, D. 2009 Analysis of numerically generated wake structures. *Wind Energy* **12**, 63–80.
- JACQUIN, L., FABRE, D., GEFFROY, P. & COUSTOLS, E. 2001 The properties of a transport aircraft wake in the extended near field - An experimental study. *Aerospace Sciences Meetings* .
- JIANG, L., PERLIN, M. & SCHULTZ, W. W. 2004 Contact-line dynamics and damping for oscillating free surface flows. *Physics of Fluids* **16** (3), 748–758.
- JOUKOWSKI, N. E. 1912 Vortex theory of a rowing screw. *Trudy Otdeleniya Fizicheskikh Nauk Obshchestva Lubitelei Estestvoznaniya* **1**, in Russian.
- JUNIPER, M. P., TOMMISOLA, O. & LUNDELL, F. 2011 The local and global stability of confined planar wakes at intermediate Reynolds number. *Journal of Fluid Mechanics* **686**, 218–238.
- KANG, S., YANG, X. & SOTIROPOULOS, F. 2014 On the onset of wake meandering for an axial flow turbine in a turbulent open channel flow. *Journal of Fluid Mechanics* **744**, 376–403.
- KERSWELL, R. R. & DAVEY, A. 1996 On the linear instability of elliptic pipe flow. *Journal of Fluid Mechanics* **316**, 307–324.
- KEULEGAN, G. H. 1959 Energy dissipation in standing waves in rectangular basins. *Journal of Fluid Mechanics* **6** (01), 33–50.
- KHORRAMI, M. 1991 On the viscous modes of instability of a trailing line vortex. *Journal of Fluid Mechanics* **225**, 197–212.
- KIDAMBI, R. 2009 Capillary damping of inviscid surface waves in a circular cylinder. *Journal of Fluid Mechanics* **627**, 323–340.
- KITSIOS, V., CORDIER, L., BONNET, J.-P., OOI, A. & SORIA, J. 2010 Development of a nonlinear eddy-viscosity closure for the triple-decomposition stability analysis of a turbulent channel. *Journal of Fluid Mechanics* **664**, 74–107.
- KITSIOS, V., CORDIER, L., BONNET, J.-P., OOI, A. & SORIA, J. 2011 On the coherent structures and stability properties of a leading-edge separated aerofoil with turbulent recirculation. *Journal of Fluid Mechanics* **683**, 395–416.
- KLEIN, R., MAJDA, A. J. & DAMODARAN, K. 1995 Simplified equations for the interaction of nearly parallel vortex filaments. *Journal of Fluid Mechanics* **288**, 201–248.
- LAGRÉE, P.-Y., BERGER, E., DEVERGE, M., VILAIN, C. & HIRSCHBERG, A. 2005 Characterization of the pressure drop in a 2d symmetrical pipe: Some asymptotical, numerical, and experimental comparisons. *ZAMM-Journal of Applied Mathematics and Mechanics/Zeitschrift für Angewandte Mathematik und Mechanik* **85** (2), 141–146.

Bibliography

- LAMB, H. 1932 *Hydrodynamics*. Cambridge University Press.
- LAMBOURNE, N.C. & BRYER, D.W. 1961 The bursting of leading-edge vortices: some observations and discussion of the phenomenon. *Aero. Res. Counc. R & M* **3282**, 1–35.
- LANDAU, L. D. & LEVICH, B. 1942 Dragging of a liquid by a moving plate. *Acta Physicochim. URSS* **17**, 42.
- LANDAU, L. D. & LIFSHITZ, E. M. 1987 *Fluid Mechanics: Vol 6*. Pergamon Press.
- LAW, K.-Y. & ZHAO, H. 2016 *Surface wetting*. Springer.
- LE GRAND, N., DAERR, A. & LIMAT, L. 2005 Shape and motion of drops sliding down an inclined plane. *Journal of Fluid Mechanics* **541**, 293–315.
- LEGER, L. & JOANNY, J. F. 1992 Liquid spreading. *Reports on Progress in Physics* **55** (4), 431.
- LEIBOVICH, S. & STEWARTSON, K. 1983 A sufficient condition for the instability of columnar vortices. *Journal of Fluid Mechanics* **126**, 335–356.
- LEONTINI, J. S., THOMPSON, M. C. & HOURIGAN, K. 2010 A numerical study of global frequency selection in the time-mean wake of a circular cylinder. *Journal of Fluid Mechanics* **645**, 435.
- LEVY, H. & FORSDYKE, A. G. 1928 The steady motion and stability of a helical vortex. *Proc. Roc. Soc. Lond. A* **120**, 670–690.
- LIGHTHILL, J. 1978 *Waves in fluids*. Cambridge University Press.
- LU, H. & PORTÉ-AGEL, F. 2011 Large-eddy simulation of a very large wind farm in a stable atmospheric boundary layer. *Physics of Fluids* **23** (6), 065101.
- LUDWIG, H. 1962 Zur erklärung der instabilität der über angestellten deltaflügeln auftretenden freien wirbelkerne. *Z. Flugwiss* **10** (6), 242–249.
- MALIK, M. R., ZANG, T. A. & HUSSAINI, M. Y. 1985 A spectral collocation method for the navier-stokes equations. *Journal of Computational Physics* **61**, 64–88.
- MANTIČ-LUGO, V., ARRATIA, C. & GALLAIRE, F. 2015 A self-consistent model for the saturation dynamics of the vortex shedding around the mean flow in the unstable cylinder wake. *Physics of Fluids* **27** (7), 074103.
- MANTIČ-LUGO, V. & GALLAIRE, F. 2016 Self-consistent model for the saturation mechanism of the response to harmonic forcing in the backward-facing step flow. *Journal of Fluid Mechanics* **793**, 777–797.
- MARQUET, O., LOMBARDI, M., CHOMAZ, J.-M., SIPP, D. & JACQUIN, L. 2009 Direct and adjoint global modes of a recirculation bubble: lift-up and convective non-normalities. *Journal of Fluid Mechanics* **622**, 1–21.

- MARQUET, O. & SIPP, D. 2010 Global sustained perturbations in a backward-facing step flow. *Seventh IUTAM Symposium on Laminar-Turbulent Transition*.
- MARQUET, O., SIPP, D. & JACQUIN, L. 2008 Sensitivity analysis and passive control of cylinder flow. *Journal of Fluid Mechanics* **615**, 221–252.
- MASSOUH, F. & DOBREV, I. 2007 Exploration of the vortex wake behind of wind turbine rotor. *Journal of Physics: Conference Series* **75** (012036).
- MAYER, E. W. & POWELL, K. G. 1992 Viscous and inviscid instabilities of a trailing vortex. *Journal of Fluid Mechanics* **245**, 91–114.
- MEDICI, D. & ALFREDSSON, P.H. 2006 Measurements on a wind turbine wake: 3D effects and bluff body vortex shedding. *Wind Energy* **9** (3), 219–236.
- MEDICI, D. & ALFREDSSON, P. H. 2008 Measurements behind model wind turbines: further evidence of wake meandering. *Wind Energy* **11**, 211–217.
- MELIGA, P., CHOMAZ, J.-M. & SIPP, D. 2009 Global mode interaction and pattern selection in the wake of a disk: a weakly nonlinear expansion. *Journal of Fluid Mechanics* **633**, 159–189.
- MELIGA, P. & GALLAIRE, F. 2011 Control of axisymmetric vortex breakdown in a constricted pipe: nonlinear steady states and weakly nonlinear asymptotic expansions. *Physics of Fluids* **23** (8), 084102.
- MELIGA, P., GALLAIRE, F. & CHOMAZ, J.-M. 2012*a* A weakly nonlinear mechanism for mode selection in swirling jets. *Journal of Fluid Mechanics* **699**, 216–262.
- MELIGA, P., PUJALS, G. & SERRE, E. 2012*b* Sensitivity of 2-D turbulent flow past a D-shaped cylinder using global stability. *Physics of Fluids* **24**.
- MILES, J. W. 1967 Surface-wave damping in closed basins. In *Proceedings of the Royal Society of London A: Mathematical, Physical and Engineering Sciences*, , vol. 297, pp. 459–475. The Royal Society.
- MOFFATT, H. K. 2000 Euler's disk and its finite-time singularity. *Nature* **404** (6780), 833–834.
- MONKEWITZ, P. A. 1988 A note on vortex shedding from axisymmetric bluff-bodies. *Journal of Fluid Mechanics* **192**, 561–575.
- MONOKROUSOS, A., ÅKERVIK, E., BRANDT, L. & HENNINGSON, D. S. 2010 Global three-dimensional optimal disturbances in the blasius boundary-layer flow using time-steppers. *Journal of Fluid Mechanics* **650**, 181–214.
- MOORE, C. J. 1977 The role of shear-layer instability waves in jet exhaust noise. *Journal of Fluid Mechanics* **80** (02), 321–367.
- NAYFEH, A. H. 2008 *Perturbation Methods*. John Wiley & Sons.

Bibliography

- NOBLIN, X., BUGUIN, A. & BROCHARD-WYART, F. 2004 Vibrated sessile drops: Transition between pinned and mobile contact line oscillations. *The European Physical Journal E: Soft Matter and Biological Physics* **14** (4), 395–404.
- OBERLEITHNER, K., SIEBER, M., NAYERI, C. N., PASCHEREIT, C. O., PETZ, C., HEGE, H.-C., R., NOACK B. & WYGNANSKI, I. 2011 Three-dimensional coherent structures in a swirling jet undergoing vortex breakdown: stability analysis and empirical mode construction. *Journal of Fluid Mechanics* **679**, 383–414.
- OKULOV, V. L. 2004 On the stability of multiple helical vortices. *Journal of Fluid Mechanics* **521**, 319–342.
- OKULOV, V. L., NAUMOV, I. V., MIKKELSEN, R. F., KABARDIN, I. K. & SØRENSEN, J. N. 2014 A regular strouhal number for large-scale instability in the far wake of a rotor. *Journal of Fluid Mechanics* **747**, 369–380.
- OKULOV, V. L. & SØRENSEN, J. N. 2007 Stability of helical tip vortices in a rotor far wake. *Journal of Fluid Mechanics* **576**, 1–25.
- OLENDRARU, C. & SELLIER, A. 2002 Viscous effects in the absolute/convective instability of the Batchelor vortex. *Journal of Fluid Mechanics* **459**, 371–396.
- OLENDRARU, C., SELLIER, A., ROSSI, M. & HUERRE, P. 1999 Inviscid instability of the Batchelor vortex: Absolute-convective transition and spatial branches. *Physics of Fluids* **11**, 1805–1820.
- ORTEGA, J. M., BRISTOL, R. L. & SAVAS, Ö. 2003 Experimental study of the instability of unequal-strength counter-rotating vortex pair. *Journal of Fluid Mechanics* **474**, 35–84.
- PETIT, L., HULIN, J.-P. & GUYON, É. 2012 *Hydrodynamique physique*. EDP Sciences.
- PIER, B. & HUERRE, P. 2001 Nonlinear synchronization in open flows. *J. Fluids Struct.* **15**, 471–480.
- POPE, S. B. 2000 *Turbulent Flows*. Cambridge University Press.
- PORTÉ-AGEL, F., WU, Y.-T., LU, H. & CONZEMIUS, R.J. 2011 Large-eddy simulation of atmospheric boundary layer flow through wind turbines and wind farms. *Journal of Wind Engineering and Industrial Aerodynamics* **99** (4), 154–168.
- PROVANSAL, M., MATHIS, C. & BOYER, L. 1987 Bénard-von karman instability: transient and forced regimes. *Journal of Fluid Mechanics* **182**, 1–22.
- PUTHENVEETIL, B. A., SENTHILKUMAR, V. K. & HOPFINGER, E. J. 2013 Motion of drops on inclined surfaces in the inertial regime. *Journal of Fluid Mechanics* **726**, 26–61.
- QADRI, U. A., M., D. & JUNIPER, M. P. 2013 Structural sensitivity of spiral vortex breakdown. *Journal of Fluid Mechanics* **720**, 558–581.

- RAYLEIGH, LORD 1914 On the theory of long waves and bores. *Proceedings of the Royal Society of London. Series A, Containing Papers of a Mathematical and Physical Character* **90** (619), 324–328.
- REAU, N. & TUMIN, A. 2002 On harmonic perturbations in a turbulent mixing layer. *European Journal of Mechanics - B/Fluids* **21** (2), 143–155.
- REYNOLDS, W. C & HUSSAIN, K. M. 1972 The mechanics of an organized wave in turbulent shear flow. Part 3. theoretical models and comparisons with experiments. *Journal of Fluid Mechanics* **54**, 263–288.
- RILEY, N. 1965 Oscillating viscous flows. *Mathematika* **12** (02), 161–175.
- RIO, E., DAERR, A., ANDREOTTI, B. & LIMAT, L. 2005 Boundary conditions in the vicinity of a dynamic contact line: experimental investigation of viscous drops sliding down an inclined plane. *Physical Review Letters* **94** (2), 024503.
- ROSENBLAT, S. 1959 Torsional oscillations of a plane in a viscous fluid. *Journal of Fluid Mechanics* **6** (02), 206–220.
- ROY, C. & LEWEKE, T. 2008 Experiments on vortex meandering. European project FAR-Wake (AST4-CT-2005-012238). . *Tech. Rep. TR 1.1.1-4* pp. Available at: <http://far-wake.irphe.univ-mrs.fr>.
- RUITH, M. R., CHEN, P., MEIBURG, E. & MAXWORTHY, T. 2003 Three-dimensional vortex breakdown in swirling jets and wakes: direct numerical simulation. *Journal of Fluid Mechanics* **486**, 331–378.
- SAMUEL, B., ZHAO, H. & LAW, K.-Y. 2011 Study of wetting and adhesion interactions between water and various polymer and superhydrophobic surfaces. *The Journal of Physical Chemistry C* **115** (30), 14852–14861.
- SARMAST, S., DADFAR, R., MIKKELSEN, R. F., SCHLATTER, P., IVANELL, S., SØRENSEN, J. N. & HENNINGSON, D. S. 2014 Mutual inductance instability of the tip vortices behind a wind turbine. *Journal of Fluid Mechanics* **755**, 705–731.
- SARPKAYA, T. 1971 On stationary and travelling vortex breakdowns. *Journal of Fluid Mechanics* **45**, 545–559.
- SAURET, A., BOULOGNE, F., CAPPELLO, J., DRESSAIRE, E. & STONE, H. A. 2015 Damping of liquid sloshing by foams. *Physics of Fluids* **27** (2), 022103.
- SCHIPPERS, H. 1979 Analytical and numerical results for the non-stationary rotating disk flow. *Journal of Engineering Mathematics* **13** (2), 173–191.
- SCHITO, P. 2012 Large eddy simulations of wind turbines: interaction with turbulent flow. PhD thesis, Politecnico di Milano, Department of mechanical engineering.

Bibliography

- SCHMID, P. J. 2007 Nonmodal stability theory. *Annual Review of Fluid Mechanics* **39**, 129–162.
- SCHMID, P. J. & HENNINGSON, D. S. 2001 *Stability and transition in shear flows*. Springer.
- SHERRY, M., SHERIDAN, J. & LOJACONO, D. 2010 Horizontal axis wind turbine tip and root vortex measurements. In *15th Int. Symp. on Applications of Laser Techniques to Fluid Mechanis.*
- SIPP, D. & LEBEDEV, A. 2007 Global stability of base and mean flows: a general approach and its applications to cylinder and open cavity flows. *Journal of Fluid Mechanics* **593**, 333–358.
- SIPP, D., MARQUET, O., MELIGA, P. & BARBAGALLO, A. 2010 Dynamics and control of global instabilities in open-flows: a linearized approach. *Applied Mechanics Reviews* **63** (3), 030801.
- SNOEIJER, J. H. & ANDREOTTI, B. 2013 Moving contact lines: scales, regimes, and dynamical transitions. *Annual Review of Fluid Mechanics* **45**, 269–292.
- SOMMARIVA, A. 2013 Fast construction of Fejér and Clenshaw–Curtis rules for general weight functions. *Computers & Mathematics with Applications* **65** (4), 682–693.
- SØRENSEN, J. N. 2011 Instability of helical tip vortices in rotor wakes. *Journal of Fluid Mechanics* **682**, 1–4.
- SPALART, P. R. 1998 Airplane trailing vortices. *Annual Review of Fluid Mechanics* **30** (1), 107–138.
- SQUIRE, H. B. 1960 *Analysis of the vortex breakdown phenomenon*. Imperial College of Science and Technology, Aeronautics Department.
- STOKES, G. G. 1851 *On the effect of the internal friction of fluids on the motion of pendulums*. Pitt Press.
- STONE, H. A. 2010 Interfaces: in fluid mechanics and across disciplines. *Journal of Fluid Mechanics* **645**, 1–25.
- STUART, J. T. 1958 On the non-linear mechanics of hydrodynamic stability. *Journal of Fluid Mechanics* **4**, 1–21.
- TAN, Y.-J., HU, Z.-K. & SHAO, C.-G. 2015 Noise limit of a torsion pendulum under optomechanical control. *Physical Review A* **92** (3), 032131.
- TING, C.-L. & PERLIN, M. 1995 Boundary conditions in the vicinity of the contact line at a vertically oscillating upright plate: an experimental investigation. *Journal of Fluid Mechanics* **295**, 263–300.
- TREFETHEN, L., TREFETHEN, A., REDDY, S. & DRISCOLL, T. 1993 Hydrodynamic stability without eigenvalues. *Science* **261** (5121), 578–584.
- TREFETHEN, L. N. 2008 Is Gauss Quadrature Better than Clenshaw–Curtis? *SIAM Review* **50** (1), 67–87.

- URSELL, F. 1952 Edge waves on a sloping beach. In *Proceedings of the Royal Society of London A: Mathematical, Physical and Engineering Sciences*, , vol. 214, pp. 79–97. The Royal Society.
- VAN DYKE, M. 1982 *An album of fluid motion*, , vol. 176. Parabolic Press Stanford.
- VERMEER, L. J., SØRENSEN, J. N. & CRESPO, A. 2003 Wind turbine wake aerodynamics. *Prog. in Aerospace Sci.* **39** (6-7), 467–510.
- VIOLA, F., ARRATIA, C. & GALLAIRE, F. 2016a Mode selection in trailing vortices: harmonic response of the non-parallel batchelor vortex. *Journal of Fluid Mechanics* **790**, 523–552.
- VIOLA, F., BRUN, P.-T., DOLLET, B. & GALLAIRE, F. 2016b Foam over troubled water: finite time arrest of sloshing in a cylindrical container. *to appear in Physics of Fluids* .
- VIOLA, F., IUNGO, G.V., CAMARRI, S., PORTÉ AGEL, F. & GALLAIRE, F. 2014 Prediction of the hub vortex instability in a wind turbine wake: stability analysis with eddy-viscosity models calibrated on wind tunnel data. *Journal of Fluid Mechanics* **750**, R1.
- VOINOV, O. V. 1976 Hydrodynamics of wetting. *Fluid Dynamics* **11** (5), 714–721.
- VON KARMAN, T. 1921 Über laminare und turbulente reibung. *ZAMM-Journal of Applied Mathematics and Mechanics/Zeitschrift für Angewandte Mathematik und Mechanik* **1** (4), 233–252.
- WANG, S. & RUSAK, Z. 1996a On the stability of an axisymmetric rotating flow in a pipe. *Physics of Fluids* **8** (4), 1007–1016.
- WANG, S. & RUSAK, Z. 1996b On the stability of non-columnar swirling flows. *Physics of Fluids* **8** (4), 1017–1023.
- WHALE, J., PAPADOPOULOS, K. H., ANDERSON, C. G., HELMIS, C. G. & SKYNER, D. J. 1996 A study of the near wake structure of a wind turbine comparing measurements from laboratory and full-scale experiments. *Solar Energy* **56** (6), 621–633.
- WIDNALL, S. E. 1972 The stability of helical vortex filament. *Journal of Fluid Mechanics* **54** (4), 641–663.
- WINKELS, K.G., PETERS, I. R., EVANGELISTA, F., RIEPEN, M., DAERR, A., LIMAT, L. & SNOEIJER, J. H. 2011 Receding contact lines: from sliding drops to immersion lithography. *The European Physical Journal Special Topics* **192** (1), 195–205.
- WU, Y.-T. & PORTÉ-AGEL, F. 2011 Large-eddy simulation of wind-turbine wakes: evaluation of turbine parametrisations. *Boundary-Layer Meteorology* **138** (3), 345–366.
- YOUNG, G.W. & DAVIS, S.H. 1987 A plate oscillating across a liquid interface: effects of contact-angle hysteresis. *Journal of Fluid Mechanics* **174**, 327–356.

Bibliography

- ZAOUALI, Y., FILALI, T., AISSIA, H. B. & JAY, J. 2011 Flow structure generated from an axisymmetric natural air jet at a moderate reynolds number. *Fluid Dynamics Research* **43** (3), 035502.
- ZHANG, W., MARKFORT, C. D. & PORTÉ-AGEL, F. 2012 Near-wake flow structure downwind of a wind turbine in a turbulent boundary layer. *Exp. Fluids* **52** (5), 1219–1235.
- ZUCCHER, S., BOTTARO, A. & LUCHINI, P. 2006 Algebraic growth in a blasius boundary layer: Nonlinear optimal disturbances. *European Journal of Mechanics-B/Fluids* **25** (1), 1–17.

Francesco Viola

PhD in Mechanical Engineering

Personal information

Born December 26, 1987, in Rome, Italy
Italian citizenship
francesco.viola@epfl.ch

Research interests

Flow Instabilities, Vortex Dynamics, Free Surface Flows, Computational Fluid Dynamics, Adjoint Optimization and Asymptotic Methods.

Education

Jun 2012 - Oct 2016, PhD in Mechanical Engineering at EPFL, Switzerland.

Research activity in the Laboratory of Fluid Mechanics and Instabilities (LFMI) under the supervision of Prof. F. Gallaire. The thesis focuses on the theoretical and numerical investigation of mode selection in resonating swirling flows and on sloshing waves damped by fluid-solid friction.

Oct 2006 - Jun 2012, Graduate Diploma in Engineering at Scuola Superiore Sant'Anna of Pisa, Italy

The Scuola Superiore Sant'Anna is a special-statute public university operating in the field of applied sciences where the students are selected through a public national competition.

Final Mark: 100/100 *cum laude*

Oct 2009 - Mar 2012, MSc. in Aerospace Engineering at University of Pisa, Italy

Thesis title: "Linear stability analysis of wind turbine wakes",

advisors: Prof. S. Camarri, Prof. F. Gallaire, Prof. G. V. Iungo and Prof. F. Porté-Agel

Final Mark: 110/110 *cum laude*

Sept 2011- Febr 2012, Research Internship at EPFL, Switzerland

Six months project on wind turbine wake instabilities at WIRE (Wind engineering and renewable energy laboratory), in collaboration with LFMI.

Tutored by Prof. F. Porté-Agel, Prof. F. Gallaire and Prof. G. V. Iungo.

July - Sept 2010, Research Internship at Internship Nanolab - UCSB, USA

Three months project on the development of a computational model for the flow simulation in microchannels with an embedded electrode.

Tutored by Prof. S. Pennathur.

Oct 2006 - Oct 2009, BSc. in Aerospace Engineering at University of Pisa, Italy

Thesis title: "Time-frequency analysis of anemometric signals acquired downstream of a low aspect-ratio cylinder", advisors: Prof. G. Buresti and Prof. G. V. Iungo

Final Mark: 110/110 *cum laude*

Sept - Oct 2009, Research internship at LMT-École Normale Supérieure de Cachan, France

Two months project on mechanical vibrations of reticular structures.

Tutored by Prof. O. Allix.

Sep 2001 - Jul 2006, Scientific High School Diploma at A. Righi of Rome, Italy

Final Mark: 100/100.

Additional schools and trainings

7th Summer School Complex Motion in Fluids. University of Twente, Netherland, 2016, June, 19-24.

Fluid Dynamics of Sustainability and the Environment, Summer School on atmospheric and oceanic fluid mechanics. École Polytechnique, Palaiseau, France, 2015, September, 7-18.

Scientific Python programming. EPFL, Switzerland, 2014, May, 5-8

MPI, an introduction to parallel programming. EPFL, Switzerland, 2014, January, 27-31

Aux Rencontres de Peyresq, Summer School on capillary effects and soft matter. Peyresq, France, 2013, June, 2-6

FLOW-NORDITA Summer School on Advanced Instability Methods for Complex Flows. KTH Royal Institute of Technology, Stockholm, Sweden, 2013, May, 6-10.

Languages

- Italian (Native)
- English (Fluent)
- French (B2)

Awards

2011, 2010 and 2009 Scholarship grant awarded by Scuola Superiore Sant'Anna for stages abroad.

2006 Winner of a full-scholarship for the 5-years program in Engineering at Scuola Superiore Sant'Anna, awarded through a national selection (11 scholarships, 227 participants)

2006 Finalist at National Physics Olympiad, Italy.

2006 and 2005 Finalist at National Team Mathematics Olympiad, Italy.

Teaching and Students supervision

Teaching assistant

Fluid flow Bachelor course in Mechanical Engineering at EPFL (2016), 14 total hours.

Hydrodynamics Master course in Mechanical Engineering at EPFL (2014 and 2015), 56 total hours.

Physics II Bachelor course in Mechanical Engineering at EPFL (2013), 28 total hours.

Physics I Bachelor course in Mechanical Engineering at EPFL (2013 and 2014), 56 total hours.

Master Thesis Supervisor

Tutored one visiting student from University of Pisa at EPFL. Title of the project: "Lagrangian-based sensitivity analyses of swirling wakes instabilities: application to wind turbine hub vortices."

Semester projects Supervisor

Tutored four Master students at EPFL. Title of the project: "Optimal flapping and pitching motion of NACA airfoils for thrust generation".

Tutored two Master students at EPFL. Title of the project: "Fluid Sloshing in a glass".

Tutored two Master students at EPFL. Title of the project: "Bath-Tub Vortex: Stability & Sensitivity Analysis"

Publications

Peer-reviewed journal articles

Viola, F., Brun, P.-T., Dollet, B., & Gallaire, F. (2016). Foam on troubled water: capillary induced finite-time arrest of sloshing waves. *Physics of Fluids*, 28, 091701.

Viola, F., Arratia, C., & Gallaire, F. (2016). Mode selection in trailing vortices: harmonic response of the non-parallel Batchelor vortex. *Journal of Fluid Mechanics*, 790, 523-552.

Viola, F., Iungo, G. V., Camarri, S., Porté-Agel, F., & Gallaire, F. (2014). Prediction of the hub vortex instability in a wind turbine wake: stability analysis with eddy-viscosity models calibrated on wind tunnel data. *Journal of Fluid Mechanics*, 750, R1.

Iungo, G. V., Viola, F., Camarri, S., Porté-Agel, F., & Gallaire, F. (2013). Linear stability analysis of wind turbine wakes performed on wind tunnel measurements. *Journal of Fluid Mechanics*, 737, 499-526.

Lenzi, A., Viola, F., Bonotto, F., Frey, J., Napoli, M., & Pennathur, S. (2011). Method to determine the effective ζ potential in a microchannel with an embedded gate electrode. *Electrophoresis*, 32(22), 3295-3304.

Papers under preparation

Viola, F., Pezzica, E., Iungo, G. V., Gallaire, F., & Camarri, S. (2016). Flow control of weakly non-parallel flows: application to trailing vortices. In revision in *Journal of Fluid Mechanics*.

Ashton, R., Viola, F., Camarri, S., Gallaire, F. & Iungo, G. V (2016). Hub vortex instability within wind turbine wakes: effects of wind turbulence, loading conditions and blade aerodynamics. In revision in *Physical Review Fluids*.

Viola, F., Brun, P.-T., & Gallaire, F. (2016). Contact line hysteresis in sloshing dynamics. Submitted to *Journal of Fluid Mechanics*.

Conference papers

Iungo, G. V., Viola, F., Ciri, U., Leonardi, S., & Rotea, M. (2016). Reduced order model for optimization of power production from a wind farm. In 34th Wind Energy Symposium (p. 2200).

Viola, F., Iungo, G. V., Camarri, S., Porté-Agel, F., & Gallaire, F. (2015). Instability of wind turbine wakes immersed in the atmospheric boundary layer. In *Journal of Physics: Conference Series* (Vol. 625, No. 1, p. 012034). IOP Publishing.

Iungo, G. V., Viola, F., Ciri, U., Rotea, M. A., & Leonardi, S. (2015). Data-driven RANS for simulations of large wind farms. In *Journal of Physics: Conference Series* (Vol. 625, No. 1, p. 012025). IOP Publishing.

Ashton, R., Viola, F., Gallaire, F., & Iungo, G. V. (2015). Effects of incoming wind condition and wind turbine aerodynamics on the hub vortex instability. In *Journal of Physics: Conference Series* (Vol. 625, No. 1, p. 012033). IOP Publishing.

Conferences contributed and invited talks

Finite time arrest in sloshing dynamics 11th European Fluid Mechanics Conference (EFMC11), Seville, Spain, September 12-16, 2016.

Contact line hysteresis in sloshing dynamics. 7th summer school Complex Motion in Fluids, Zenderen, Twente, Netherlands, June, 19-24, 2016.

Nonlinear friction in sloshing dynamics. Invited seminar at LadHyX, Ecole Polytechnique, Palaiseau, France, May, 4, 2016.

How to include the nonlinear Cox-Voinov law into sloshing dynamics? 68th Annual Meeting of the APS Division of Fluid Dynamics, Boston, Massachusetts, USA, November, 22-24, 2015.

Mode selection in trailing vortices: harmonic response of the non-parallel Batchelor vortex. Workshop on Fluid-Structure Interactions and Vortex-Dynamics in Aerodynamics 2015, Porquerolles, France, 29 Jun-4 Jul 2015.

Instability of wind turbine wakes immersed in the atmospheric boundary layer. Wake Conference 2015 Visby, Sweden, June, 9-11, 2015.

Near-wake instability and sensitivity analysis of wind turbines immersed in the atmospheric boundary layer. 67th Annual Meeting of the APS Division of Fluid Dynamics, San Francisco, California, USA, November, 23-25, 2014.

Linear response to harmonic forcing of the non-parallel Batchelor vortex. 10th European Fluid Mechanics Conference (EFMC10), Copenhagen, Denmark, September 14-18, 2014.

